RENSIT:
RadioElectronics. NanoSystems. Information Technologies

Journal "Radioelectronics. Nanosystems. Information Technologies" (abbr. RENSIT)
publishes original articles, reviews and brief reports, not previously published, on topical problems in **radioelectronics (including biomedical) and fundamentals of information, nano- and biotechnologies and adjacent areas of physics and mathematics.**

Designed for **researchers, graduate students, physics students of senior courses and teachers**.
It turns out **2 times a year** (that includes 2 issues)

Authors of journal are academicians, corresponding members and foreign members of Russian Academy of Natural Sciences (RANS) and their colleagues,
as well as other russian and foreign authors on presentation of their manuscripts by the members of RANS, which can be obtained by authors before sending articles to editors.
And also after its receiving - on recommendation of a member of editorial board of journal, or another member of Academy of Natural Sciences, that gave her opinion on article at request of editor.
The editors will accept articles in both **Russian and English** languages.

Articles are internally peer reviewed (**double-blind peer review**) by members of the Editorial Board.
Some articles undergo external review, if necessary.

Journal RENSIT is included in the **DB SCOPUS, EBSCO Publishing,** in the international abstracts database - **Ulrich's International Periodicals Directory**,(USA, New York, http://www.ulrichsweb.com), in the **AJ and DB VINITI RAS** (http://www.viniti.ru), and DB **Russian Science Citation Index (RSCI** http://elibrary.ru/project_risc.asp).
Full-text content is posted in the DB of the **Russian Scientific Electronic Library**
- information resource on the Internet http://elibrary.ru and is available for registered users.
And also - in Open Access **CyberLeninka NEB** of Russian Federation http://cyberleninka.ru.
On journal's website http://www.rensit.ru posted metadata publications
and **RENSIT: Radioelectronics. Nanosystems. Infomation Technologies - english version** (cover-to-cover translation) of journal, which is a party to **CrossRef.**

The founder - the **Russian Academy of Natural Sciences**
Publisher - Publishing Center of the Russian Academy of Natural Sciences
Publisher Address: 119002 Moscow, per. Sivtsev Vrazhek 29/16

CONTENTS

RUSSIAN ACADEMY OF NATURAL SCIENCES

DEPARTMENT OF RADIOELECTRONICS, NANOPHYSICS AND INFORMATION TECHNOLOGIES PROBLEMS

RENSIT:

RADIOELECTRONICS. NANOSYSTEMS. INFORMATION TECHNOLOGIES.

2021, Vol. 13, no. 3

FOUNDED IN 2009
4 ISSUES PER YEAR
MOSCOW

ISSN 2414-1267

The journal on-line is registered by the Ministry of Telecom and Mass Cjmmunications of the Russian Federation. Certificate El. no. FS77-60275 on 19.12.2014

EDITORIAL BOARD ADDRESS
218-219 of., 7 b., 11, Mokhovaya str., 125009 MOSCOW, RUSSIAN FEDERATION,
tel. +7 495 629 3368
fax +7 495 629 3678 for Grachev

Analysis of the current state and development prospects of radar system for guided weapons of air targets destruction

Anatoliy R. Ilchuk A.R., Andrey I. Panas, Sergey V. Shcherbakov
RPC "Istok" named after Shokin", https://istokmw.ru/
Fryazino 141190, Moscow region, Russian Federation
E-mail: arilchuk@istokmw.ru, aipanas@istokmw.ru, sherbakov@istokmw.ru

Vladimir I. Merkulov, Vladimir S. Chernov
Vega Concern, https://www.vega.su/
Moscow 121170, Russian Federation
E-mail: from_fn@mail.ru, chernova.45@list.ru
Received May 27, 2921, peer-reviewed June 04, 2021, accepted June 11, 2021

Abstract: **The effectiveness of destruction of air objects (AO) largely depends on the excellence of radar devices, which are called radar homing heads (RHH) of the guided weapons systems (GWS). In the process of GWS AO development, several generations of RHHs were created: semi-active RHHs with a pulsed or continuous target illumination signal; RHHs providing combined guidance; RHHs, providing realization of inertial guidance with radio correction from the weapon control system of the GWS carrier, active guidance, a combination of semi-active and active modes, combined guidance, in which inertial guidance with radio correction, passive and active homing are consistently implemented. Currently, there is a need for an analytical generalization of information about the GHHs, published in various open scientific and technical sources of information. In the course of the analysis, it was found that the main directions for improving the RHHs are: the development of new, more flexible non-stationary homing methods and their information support, which provide the ability to intercept new types of AO in complex signal-jamming multipurpose situations. This predetermines the need to achieve a high level of RHHs protection from natural and intentional interference, the use of trajectory control of observation when aiming at radio-emitting and group objects, improvement of situational awareness, RHHs intellectualization and digitalization, improvement of RHH antenna systems.**

Keywords: **radar homing heads, guided weapons, air object, guidance system**

UDC 621.396.96

For citation: Anatoliy R. Ilchuk, Vladimir I. Merkulov, Andrey I. Panas, Vladimir S. Chernov, Sergey V. Shcherbakov. Analysis of the current state and development prospects of radar systems for guided weapons of air targets destruction. *RENSIT,* 2021, 13(3):227-244. DOI: 10.17725/rensit.2021.13.227.

Contents

1. INTRODUCTION

The radar homing heads **(**RHH), being one of the types of information-and-control systems of the guided weapons systems **(**GWS) **of air objects (**AO), provides the implementation of the homing method and its information support. All indicators of the complex perfection (efficiency, survivability, dynamism) for the destruction of the air objects largely depend on the quality of RHH functioning.

In the process of GWS AO development, several generations of RHHs were created. At the initial stage, semi-active RHHs with a pulsed or continuous target illumination signal were developed. In semi-active pulsed RHHs the AT was irradiated by the onboard radar of GWS carrier, and in the RHH, GWS guidance signals were generated based on information obtained as a result of receiving radio signals reflected from the AO.

To increase the launch range of GWS, GWSs were developed using various guidance methods at different parts of the flight path: at the initial stage inertial-corrected guidance was used, followed by proportional homing on the basis of semi-active RHH signals with AO capture on the path.

Subsequent efforts of the developers were aimed at creating GWS AO with active RHH. In active RHHs irradiation and target illumination were carried out by a transmitting device included into RHH composition. This allows to consider it as a special-purpose onboard radar.

The action range of such RHHs is less than that of semi-active ones, therefore, at the first stage of GWS guidance, an inertial mode with radio correction was used, and at the second stage – active homing. In this case the "launch and forget" principle was carried out but only at the last stage of GWS guidance. Active RHHs allowed to guide simultaneously several GWSs launched from one carrier to different air objects.

To increase the launching range, RHHs were also developed, in which three modes of their operation, implemented sequentially, were provided: inertial guidance with radio correction, semi-active guidance and active homing. There are also known RHHs in which there is no inertial guidance mode with radio correction, but semi-active homing and active homing are implemented sequentially. For GWS guiding at radio emitting objects passive RHHs were developed.

Subsequently RHHs appeared, with the help of which inertial guidance with radio correction, passive homing and active homing were consistently carried out. Such RHHs provide a possibility to destroy radio-emitting objects over long distances.

Currently, there is a need for an analytical generalization of information about RHHs, published in various open scientific and technical sources of information, which will allow us to get a general idea of the current state and development prospects of the RHH GWS AO.

The purpose of the paper is to analyze the stages of creation, the current state, prospects and trends in the development of RHH from the composition of controlled weapons for destroying air objects.

2. ANALYSIS OF THE DEVELOPMENT DIRECTIONS AND CURRENT STATE OF THE RHHS FROM THE COMPOSITION OF THE GUIDED MEANS OF AIR OBJECT DESTRUCTION

2.1. Analysis of the stages of development, design features and characteristics of existing radar homing heads

Let us consider the features and characteristics of RHHs, installed on different GWS AO, taking into account the chronology of their development, realization and practical application, as it is briefly indicated in the introduction.

Note, that in the general case the perfection of RHHs used in GWS AO, is characterized by the following indicators:

– a list of targets to be destroyed (aircraft, helicopters, missiles, etc.) with an indication of their features (maneuvering, non-manuevering, high-speed, low-speed, etc);

– working area, determined by the distance ranges (D_{pmax}, …, D_{pmin}), velocities (V_{max}, …, V_{min}), altitudes (H_{max}, …, H_{min}), interception aspects in which the GWS realizes its purpose;

– the homing method used (stationary, non-stationary, with anticipation, with re-aiming, etc.);

– type of information subsystem and its operating modes (pulsed, continuous, coherent, incoherent, active, passive, semi-active, etc.);

– the possibility of implementing the "launch-and-forget" principle;

– missing the possibility to destroy the target.

In the early 60-s of the last century GWSs AO with semi-active pulsed RHH P 8M (1962), P 4, P 98 (1965), P 3P (1966) were developed. To implement the target tracking procedure a conical scanning of the antenna was used in RHHs of these GWS AO, and the monopulse method of target direction finding was used in RHHs of GWS P 40 (1970) (**Fig. 1**).

The disadvantage of semi-active pulsed RHHs was impossibility of auto-tracking AO, flying at low altitude, since simultaneously with the pulsed signals from the AO, jamming signals were received, which were formed as a result of reflections from the earth's surface of radio signals, emitted by the onboard radar of GWS carrier.

Fig. 1. *RHH GWS P-40.*

The first domestic GWS, capable of destroying an AO against the background of reflections from the ground, was created in 1973 (P-23P). The GWS launch range was 35 km, the flight speed was 3M. The AO capture in a semi-active Doppler RHH was made during the flight. Before launching, a target designation was introduced into the RHH from the onboard radar, equipped with a channel of continuous illumination signal , used for operation of a semi-active RHH after launching GWS. 3 seconds after the launch, the RHH started searching for the signal reflected from the AO and capturing it. The phase mono-pulse method of direction finding was used in RHH, which provided a higher noise immunity as compared to the amplitude mono-pulse method of AO direction finding. Note, that GWS with semi-active RHHs were used mainly for non-maneuvering AOs, thus, the range of coverage of such RHHs was comparatively low.

Subsequently, in order to increase the GWS launch range at the initial stage of the flight an inertial guidance mode was introduced, in the implementation of which the so-called pseudo-kinematic link was used, using the current parameters of GWS movement and parameters of AO movement, that entered the RHH at the moment of GWS launch. The pseudo-kinematic link provided the formation of predicted values of the GWS and AO relative motion parameters based on the known kinematic equations. This resulted in 30% increase of GWS launch range.

A distinctive feature of GWS P 27P and P 27E (1984-1985) is a combined guidance method, when various guidance methods are used at different parts of the flight trajectory: inertial-corrected guidance and proportional homing based on signals of semi-active RHH with AO capture in the path. The introduction of inertial control with correction from the onboard radar of the GWS carrier allowed to increase the GWS launch range significantly. These GWSs provide the effective AO destroying at any aspect angle. The detailed description of the construction principles of RHH GWS (**Fig. 2**) P 27P is given in [11].

It should be noted that the work on creating GWS AO with RHH was actively carried out abroad, primarily in the USA. Beginning from 1975 the development of the whole family of GWS "Sparrow" was completed.

The first version was GWS "Sparrow" AIM-7C with a semi-active pulsed RHH, which had a coverage range of 12 km. The next version was GWS "Sparrow" AIM 7D, in RHH of which a continuous illumination signal was used. The RHH GWS AIM 7F worked both with AO continuous illumination signal and with a signal of a pulsed-Doppler onboard radar of the carrier, which allowed to use GWSs from carriers equipped with various onboard radars. GWS "Sparrow" AIM 7F was the main means for destroying AOs until in early 90-s of the last century a new GWS AIM 120 with an active RHH appeared. In 1987 GWS "Sparrow" AIM 7P, having a communication line with the aircraft-carrier, appeared.

Fig. 2. *RHH GWS P-27P.*

The disadvantage of semi-active RHHs was impossibility of destroying AO by the "launch-and-forget" principle, since the AO had to be illuminated before the AO was destroyed or the GWS missed.

Hence, the development of GWS with active RHHs started.

GWS Foenix AIM 54A was developed abroad in 1973. The guidance system of this GWS is combined and consists of a semi-active radar pulsed-Doppler system working from onboard radar signals of GWS carrier at the initial and middle sections of the trajectories, and an active pulsed-Doppler RHH, switching on at GWS distance from AO of about 16 km. From the GWS carrier it is possible to carry out simultaneous guidance of 6 GWSs at 6 AOs. With further modernization the AIM–54C became completely autonomous. Most of the time GWS flies to the predicted point and at the end of the flight phase it is guided with the help of an active RHH (ARHH). This approach is most effective when aiming at rectilinearly flying AOs.

Domestic GWS PBB-AE (1994) with an active RHH (**Fig. 3**) ensures the defeat of aircraft, helicopters and cruise missiles as well as GWSs of air and ground objects. The RHH includes a monopulse direction finder and an onboard computer system. To increase noise immunity and ensure high guidance accuracy, space – time signal processing, Kalman filtering, continuous solution of kinematic equations were implemented in RHH with the ability to maintain the guiding process in case of temporary disruptions. A no-platform inertial system is installed on the GWS. A

Fig. 3. *RHH GWS PBB-AE.*

modified proportional guidance method is used for control. In conditions of organized interference, in which the onboard radar of the carrier cannot provide the RHH with information about the range and speed of the approach to the AO, guidance is carried out along a special trajectory.

Later on, GWS with combined and passive guidance methods were developed.

Medium range GWS P 27П with passive RHH is designed to destroy radio-emitting airborne objects, including those which install jamming to cover their objects. At the same time the "launch-and-forget" principle is implemented. The range of application is 70 km, the minimum altitude of the airborne object to be destroyed is 20 m.

GWS AIM 120A (USA, 1991) has the range of application -180 km and 3 guidance modes: inertial-corrected, autonomous inertial and active radar. The GWS implements the "launch-and-forget" principle in case of the sequential use of the autonomous mode and the active mode. To destroy an AO, several GWSs can be used simultaneously. A control system with an active radar guidance and sufficiently long inertial section with radio-correction can significantly increase the effectiveness of AO destruction. At the same time a feature of the implementation of the combined guiding method is the dependence of the GWS combat use efficiency on the quality of radio correction channel functioning.

When the carrier is suppressed by the onboard radar interference after the GWS launch, information about the AO coordinates and parameters is not received via the radio correction channel. In this case the GWS guidance system can perform first inertial guidance without radio correction, and then homing using the RHH active operating mode. With a large difference between the coordinates and AO moving parameters, predicted on board of GWS, and their real values by the beginning of active homing, it is not possible to guarantee the possibility of successful interception.

GWS P 37M (RF) is designed to destroy AOs at the range of up to 300 km. The GWS guiding system is an inertial guidance with radio correction and active radar homing at the final section of GWS flight. The RHH includes a digital signal processor with a large memory content and increased processing speed [14].

Monopulse Doppler active RHH 9Б 1103M ensures the destruction of AOs, such as aircraft, helicopters (including hovering helicopters), cruise missiles and antiradar missiles. Modes of operation: completely autonomous according to preliminary target designation from the carrier, but without radar support in flight; inertial guidance mode with radio correction with the subsequent transition to active homing.

ARHH measures the AO angular coordinates and the angular velocities of the line of sight rotation, as well as the speed of approach to AO and provides:

– AO reception, capture and tracking;

– reception and decryption (decoding) of radio correction signals;

– generating GWS control signals and transmitting them to the GWS control system via a digital communication line.

The RHH consists of: a controlled coordinator with an antenna, a transmitting channel, a receiving channel a reprogrammable onboard computer system. The capture range of AO with an effective reflection surface (ERS) of 5 m^2 is not less than 20 km. The range of the radio correction channel is up to 50 km.

The GWS 9Б 1103M 150 («Kolibri») provides the capture of AO with ERS of 5 m^2, moving at speeds of 0.1-5 M, at a minimum altitude of 30 m at the range of not less than 13 km. The RHH operating band is Ku (10.7-12.75 GHz, 1.67-2.5 cm). ARHH is almost completely digital, the transition to digital processing (signal digitization) is carried out at the first intermediate frequency. The antenna has a diameter of 150 mm.

The active-semi-active RHH 9B 1103M 200PA is designed for information support

Fig. 4. *RHH 9B 1103M 200PS*.

for solving the problem of destroying aircraft, helicopters (including hovering helicopters), cruise missiles and antiradar missiles. The antenna of this RHH is combined: in the active mode the RHH operates in Ku band, using a waveguide-slot antenna, in the semi-active mode an array of 12-16 dipoles is used, installed on the front of the antenna surface, it is designed to ensure the RHH operation in a semi-active mode at lower frequencies. The RHH provides the capture range of AO with ERS of 3 m^2: in inertial – semi-active mode – 80-100 km, in active mode – 20 km. The operation band in the active mode is Ku.

The active-passive RHH 9B 1103M 200PS (**Fig. 4**) ensures destroying aircraft, helicopters, cruise missiles and antiradar missiles. The passive mode makes it possible to direct RHH to the source of interference and radio-emitting onboard radar of the AO. The capture range of AO with ERS of 3 m^2 in inertial-passive mode – 200 km, in active mode – 15 km. The operation band in the active mode is Ku.

2.2. Features of RHH functioning when solving problems of trajectory control and tracking

Evaluation of characteristics of known RHH GWS AO shows, that the principles of building RHH are largely determined by characteristics of intercepted AOs and conditions of their use.

This feature predetermines the need to solve two problems: the formation of a homing law (method) and algorithms for its information support. In this case, the GWS homing method is usually understood as the law of the formation of the required trajectory, the flight along which will allow it to hit the target.

In general, the guidance method (GM) should provide: minimum guidance time; maximum launch range; minimal instantaneous overloads; minimum energy consumption of control signals; practical feasibility and invariance of the radio control system for the conditions of use.

To meet the first four requirements, the guidance trajectory should be as straight as possible. Practical feasibility implies the possibility of forming estimates for all necessary coordinates of the relative and absolute movement of the target and GWS with existing information sensors (meters), real memory volumes, speed and bit capacity of onboard computers and real energy consumption for control. Invariance provides guidance in the entire range of ranges, speeds and altitudes regardless of the presence and speed of the wind and the direction (angle) of interception.

To characterize the homing method the following is usually used:

– the type of tracings that can be realized (with anticipation, without anticipation, restrictions on the angles of interception, etc.);

– a set of coordinates of the relative and absolute movement of the target and GWS, to be measured (evaluated), and requirements for their accuracy;

– restrictions on permissible GWS transverse overloads.

If in the process of interception control error transmission coefficients do not change, this method is considered to be stationary, if they change – then it is non-stationary.

As a rule, in tracing control by existing GWS AO, the proportional guiding method or its modification is used. To implement them it is necessary to know the angular velocity of the line of sight and the velocity of the approach to AO, the estimation of which is provided by appropriate meters and tracking systems. The effectiveness of their functioning largely depends on the type of RHH used (active, semi-active and passive), as well as on the type of AO and dynamics of approaching GWS to AO. Measurement of the approach speed to AO in semi-active RHHs is associated with certain difficulties, since the source of radio emission is located onboard the GWS carrier, while the reception of the signals, reflected from AO, is performed on the GWS. In passive goniometric GWSs direct measurement of the velocity of approaching the AO is impossible.

It should be noted, that modern RHHs have significant drawbacks, due to imperfection of homing methods and AO auto-tracking algorithms which can lead to decrease of the AO destruction effectiveness, as well as to disruption of GWS guidance process, especially in the situation of intercepting new types of highly maneuverable and high-speed AOs. As the analysis showed the known homing methods:

– do not ensure interception of AOs moving with the change of signs of derived angles and ranges;

– do not ensure interception of priority AOs in the conditions of their protection (low survivability);

– do not ensure interception of AO as part of a dense group;

– do not ensure redistribution of management functions in the process of guidance (first angular errors, then linear misses, first resolution in angles, then guidance, etc.);

– do not ensure retargeting in the tracing.

The information subsystems have the following disadvantages:

– lead angle constraints, defined by antenna angle sector;

– the need to stabilize the GWS lateral axes in space with semi-active guidance;

– low order of the astaticism of the tracking systems which predetermines the tracking disruption of intensively maneuvering AOs;

– do not ensure interception at 4/4 angles when using Doppler RHH;

– large dead zones because of angle noise;

– radome errors leading to appearance of significant synchronous errors in angular velocity and requiring the formation of purely individual matrices of direction finding errors;

– the influence of an "antipode" when intercepting low-flying targets against the earth background;

– tracking disruptions due to narrow linear sections of discriminatory characteristics of tracking meters.

Thus, in connection with the emergence of new types of AOs and the change in the conditions of using GWS, the solution of the interception problem has become significantly more complicated which requires further improvement of GWS guidance methods and AO tracking.

It should be noted that RHH provides the formation of GWS control signals, necessary for the implementation of the process of its guidance to the AO, as well as for creating conditions, required when performing the procedures for evaluating coordinates and parameters of the target movement in case of missing information from the GWS carrier onboard radar and if only AO angular coordinates can be measured. In the latter case the GWS trajectory control is also necessary to create favorable conditions for the functioning of AO tracking systems, therefore, it is often referred to as the trajectory observation control (TOC).

Moreover, the TOC is used to implement the RHH protection from intentional interferences. A version of the flight trajectory corresponding to one of heuristic or optimal TOC methods is given in [27].

Another promising direction for the use of TOC is its use when GWS is pointed at the object in a dense group composition [28].

The TOC signals can also be formed at simultaneous guidance of two GWSs. A method of destroying the target – a coherent jammer GWS with an active RHH described in [16] can be indicated as an example.

It is known that coherent interference causes distortion of the phase front of the electromagnetic radio wave reflected from the target. The impact of such interference on the RHH leads to unacceptable misses and a decrease in the probability of hitting the target. However, the possibilities of setting up coherent interference have fundamental physical limitations. Effective interference can only be created in a specific angular direction. The area of space, in which it is possible to create effective coherent interference, is limited and amounts to almost 0.001 radians. For this reason, coherent interference is not effective against multi-positional radars - bistatic radars, in particular. This property of resistance to coherent interference with spaced-apart points of transmission and reception of radio signals can be implemented in GWS due to a special operation of the process of simultaneous guidance of two GWSs and their interaction with each other. The essence of the method is that the radiation of the probe signal and the reception of the signal reflected from the AO are redistributed between the GWSs alternately. In this case the interval of signal emission by one GWS should correspond to the interval of reception of the reflected signal by the other GWS. In addition, GWS guidance is carried out along maximally diverging trajectories of the "pincers" type.

The GWS guidance along the most divergent parts in the initial and middle sections of the trajectory of the "pincers" type is aimed at ensuring that on most part of the flight trajectories the GWSs are maximally distant from each other and do not enter the area of space, in which the effect of coherent interference on the RHH is effective.

In conclusion, note, that the TOC methods behind radio emitting objects in two-position goniometric radar systems are considered in detail in [21].

2.3. Features of RHH functioning in the conduct of group actions and in the conditions of radio electronic countermeasures

A specific feature of the modern interaction of attack and defense means is their group use [24]. In a sufficiently long information and control chain of group confrontation, including the detection of targets and their tracking, the use of GWS, one of the most important and complicated tasks is the target distribution and guidance of GWS AO to the most important AO. Moreover, the practical implementation of these modes of RHH operation is significantly more complicated when the opposing side uses radio electronic countermeasures.

As the analysis has shown [25,26], the armed forces of the USA and European NATO countries have sufficiently powerful electronic warfare (EW) weapons that are capable of generating various jamming effects that pose a serious threat to RHH. In particular, to suppress the channels of detection, discrimination and recognition, as well as channels for measuring range and speed, means of radio electronic countermeasure (ECM) can generate the following types of interference: continuous noise, chaotic pulse, multiple synchronous pulse, simulating pulse and combined ones (retargeting active-passive and a combination of active-simulating and masking interference). To suppress goniometric channels ECM can create single-point interference for goniometric channels with linear scanning, single-point interference for monopulse goniometric channels, multi-point interference for goniometric channels, polarization interference. Moreover, to suppress goniometric channels it is envisaged to set up deliberate interference, acting along the side lobes of the radar antenna pattern.

Thus, the successful solution of the GWS homing problem largely depends on efficiency of the active pulse-Doppler radar operation under the conditions of EW. A serious threat to the normal functioning of the active RHH is posed by individual ECM equipment installed on the targets to be hit as well as EW equipment intended for group and collective (mutual) defense of AOs. The latter ones are capable to create multi-point (non-isotropic in space) active interference, which can be masking and imitating and act both along the main and side lobes of the antenna directional pattern. In this regard, special measures in an active radar must be taken to protect against multi-point interference in space.

In such a situation in RHH first of all it is necessary to assess the signal-interference environment. To do this, two processes must proceed in it practically in parallel: the first process is the assessment of interference environment (IE), the second is the AO radar surveillance with simultaneous compensation for various kinds of deliberate interference. AO radar surveillance should begin with IE assessment operations. Various algorithms have been developed to determine the number and angular coordinates of radiation sources which include interference providers (IP) as well. These algorithms together with the algorithms for synthesizing the directional patterns of the multichannel antenna system, make it possible to form a given number of reception channels, equal to the number of IPs and conduct IP radar surveillance in them. When implementing space-time processing of signals in radar systems, this procedure is usually divided into space and time procedures which implies separate construction of spatial (beams directed to IP) and temporal channels. In the formed reception channels, which number is determined by the number of IPs, algorithms are implemented that perform such operations as detecting interfering signals, measuring the angular coordinates of IPs with subsequent correction of beams position in space and recognizing the type of acting interference.

The output signals of the time channels, IP angular coordinates, the type of interference are fed to the device for analyzing the signal-interference situation, where the type of interference situation is assessed (recognized). The results of IP assessment serve as a basis for making a decision to start a space survey with a version of the noise protection scheme that meets the current situation. Each IE class corresponds to its own version of arranging jamming protection in the radar system and, thereby, its own scenario of its operation which ensures the maximum degree of GWS protection from the effects of deliberate interference.

In addition to the above, in order to ensure GWS guidance in such a situation, it is advisable and necessary to introduce into the RHH an additional mode of passive homing for radio emitting sources, creating interference signals in the operating range of the GWS carrier onboard radar. In this case the GWS guidance can be carried out either within the framework of a passive one-position goniometric guidance system, or a passive two-position goniometric system. The most preferable is the option of using two-position guidance system which includes the guided GWS and its carrier [21].

From the above it follows that in order to successfully solve the problem of AO interception when conducting group actions in the conditions of using EW means it is necessary to supplement the GWS control system with a two-position passive guidance mode. In this mode sufficiently reliable information about the AO coordinates and motion parameters is obtained which is necessary for GWS targeting, as it makes possible to sufficiently neutralize the effect of electronic suppression on the formation of estimates of coordinates and motion parameters in RHH.

In addition, it is advisable to use an active phase antenna array (APHAR) in an active RHH, as a multichannel antenna system, which makes it possible to optimize and implement the space-time processing of useful and interference signals and provide a given level of RHH noise immunity.

2.4 RHH operation features when implementing the passive guidance mode to a radio emitting air object

As it is indicated above, when implementing passive GWS guidance methods, it is advisable to use a two-position goniometric guidance system (GTPS), as part of, for example, GWS and its carrier from which it was launched, or as part of two GWSs which form receiving positions (RP). As it is known [21], in passive two-position goniometric systems on RP the bearings of a radio emitting AO (REAO), as well as their own coordinates and motion parameters are measured with the subsequent transition of the measurement results to interacting positions. Subsequently, the trajectory parameters of REAO movement are estimated in the selected coordinate system (rectangular, spherical, etc.).

Joint processing of information in GTPS which makes it possible to significantly improve the quality of radio-emitting target (RET) observation, is divided into three stages.

At the first stage single measurements coming from different positions are converted into a single coordinate system, e.g., a Cartesian one, the origin of which is tied to a certain geographic point (a conditional GTPS center). At the second stage the measured results are identified with each other and with the previously constructed trajectories. Since the data generated in GTPS are statistical estimates of AO parameters, the problem of their identification is also statistical in nature. At the third stage the actual construction of REAO trajectories is carried out, i.e., the assessment of their coordinates and parameters of their movement. Previously at the third stage in the process of intra-base processing on the basis of the measured values of REAO bearings in each mobile position and the coordinates of these positions, the so-called generalized single measurements (indirect measurements) of the radio emitting objects coordinates are calculated: rectangular REAO coordinates or distance to them. In other words, the primary assessment of the REAO location is carried out. The trajectory of each REAO in the GTPS is formed as a result of the secondary processing of direct and indirect single measurements of coordinates.

To create effectively functioning trajectory tracking systems it is necessary to have high-quality algorithms to estimate coordinates and parameters of the REAO movement, corresponding to the specific conditions of GTPS use. Currently estimation algorithms based on methods of linear and nonlinear filtering are widely used, in particular, methods and algorithms of estimating coordinates and parameters of RET motion based on using linear and expanded Kalman filters, as well as adaptive α, β-filter and linearized α, β-filter.

The effectiveness of GTPS application largely depends on the accuracy of determining the relative and absolute REAO coordinates and the parameters of their movement. A distinctive feature of the GTPS operation is the dependence of the errors in the location of radio emission sources on the spatial system configuration («geometry»), i.e., on the size of the base and REAO position relative to the base. This circumstance makes it possible to minimize the errors in estimating the REAO phase coordinates at the expense of intentional change of the receiving positions location, and thereby to increase the efficiency of using the GTPS.

In the general case, when using the GTPS it is necessary to solve two tasks, namely, the task of guiding one GWS to the REAO and the task of trajectory control of the second GWS to create the most favorable conditions

for observing the REAO in which the errors of measuring its location are minimized. In this case one of the positions, for example, the one, closest to the REAO, solves the homing problem using one method or another, and the second one deliberately changes its position in space ensuring the highest possible accuracy in determining the radio emitting object location in both positions. The first position is usually called the leading position and the second one – the position of information support.

Currently orthogonal and gradient methods of trajectory observation control (TOC) in GTPS have been developed. When using the orthogonal TOC methods, the reduction of errors in estimating the REAO location is achieved by maintaining the angle of intersection of the lines of sight (bearings) of the REAO close to 90°. A common disadvantage of orthogonal guidance methods is the fact that prior to the GWS information support exit to an arbitrary point lying on the perpendicular to REAO line – the leading GWS, or to a given point of this perpendicular, essentially no requirements are imposed on the current values of the errors in determining the positions of the REAO. At the same time the process of guiding the leading GWS can end even before the GWS information support reaches the specified perpendicular, when the errors in determining the REAO position become minimal.

Since ensuring simultaneous exit of the leading GWS to the end point of guidance, and the GWS information support to a given line (or a given point) is a rather difficult task, the GWS information support control can be organized in such a way that the error in determining the REAO location at any time is as minimal as possible. To fulfill this condition the GWS information support must move along a special trajectory the parameters of which, for example, can be calculated using an algorithm obtained on the basis of the TOC gradient method.

3. THE MAIN DIRECTIONS AND TRENDS IN THE DEVELOPMENT OF RHHS WHICH REFER TO CONTROLLED MEANS FOR DESTRUCTING THE AIR TARGETS

When modernizing and developing new GWSs it is necessary to take into account a number of factors due to the current stage of aviation development as well as the state and prospects of avionics development in general.

These factors primarily include the following [9]:

– taking into account the state and development trends of aviation and air targets to be hit, including their means of protection (tactical factors);

– economy, determined by the total costs for the RHH development, application and maintenance;

– manufacturability, determined by the level of information technologies used, element base, depth and accessibility of technical condition monitoring, complexity of repair, as well as the ability to improve the efficiency indicators without changing the RHH constructing principles;

– a set of organizational measures for the development and implementation of the new RHH image.

Taking into account the above factors allows us to single out a number of aspects that directly affect the information and control side of the functioning of guidance systems.

These areas primarily include:

– qualitative complication of the laws of the aircraft mutual spatial movement;

– group use of both means of attack and defense;

– high dynamics and speed of air collisions;

– widespread use of control modes and information support on the verge of the loss of stability, typical for super-maneuverable AOs and tracking systems.

It is impossible to meet these requirements within the framework of traditional stationary

guidance methods. In this regard the task of developing and applying non-stationary guiding methods becomes very urgent, taking into account the higher derivatives of linear and angular coordinates, the parameters of which change depending on the initial conditions of application and during the guidance process, providing higher indicators of the method perfection as a whole.

By now, four directions of synthesis of non-stationary homing methods can be distinguished based on the use of the mathematical apparatus of the statistical theory of optimal control [35,36] and the methods of dynamics inverse problems [37].

These areas include the synthesis of the following control laws:

– with parameters depending on the initial conditions of use;

– with redistribution of priorities in the process of control;

– taking into account the discrepancy between the AO dynamic properties and the guided GWS;

– with non-linear dependence on control errors.

It should be noted, that in each direction based on different approaches different variants of non-stationary guidance methods can be obtained.

In turn, these directions for improving homing methods predetermine the following main directions for improving the information subsystems of GWS AO:

3.1. Expansion of information support capabilities

Awareness of the state of the current tactical situation and the stability of information support are a prerequisite for solving the problem of AO interception. Modern RHH GWS AO operate in a complex signal and jamming environment. This is due to the fact that collisions can be of a group nature which significantly complicates the procedure for obtaining information about AOs, especially when they are flying in a group. The expansion of information capabilities implies an increase in the amount of information, extracted from radio signals, an improvement in the detection rates, resolution and accuracy of estimating the coordinates of the AO absolute and relative motion [9].

Within the framework of this direction the most important is to provide high-precision and uninterrupted tracking of intensively maneuvering objects including those moving with a change in signs of the derivatives of range and angular coordinates. Possible variants of the synthesis of such algorithms are considered in [38,39].

APHAR plays a significant role in improving the quality of the assessment in the current signal and interference situation in promising RHHs, since they allow the formation of the required number of spatial channels, in which it is possible to conduct radar observation of the AOs and sources of interference.

When creating RHHs more and more attention is paid to the issues of increasing their resolution, which contributes to the solution of VO recognition problem. For reliable AO recognition in the RHH it is recommended to use modulation features that allow to construct a Doppler AO picture based on the analysis of the spectrum of the received signal. A feature, characterizing individual belonging to a certain type of AO is the presence of relatively well-distinguished components in the Doppler spectrum due to the rotation of turbine blades or propeller blades of aircraft [9]. To recognize helicopters it is advisable to use the secondary modulation effect from its lifting propeller [8]. It is also advisable to use modulation signs when recognizing imitation noise, including when recognizing towed false targets. A promising direction for improving the resolution is the use of TOC [28].

3.2. Providing multi-range

First of all, the multi-range requirement refers to active-passive RHHs. Along with the active homing mode, a mode of passive homing on

air objects on which radio emission sources operating in different frequency ranges are located, is implemented in these RHHs. In particular, onboard radars installed on aircraft of the USA tactical aviation, emit radio signals in the frequency range of 8-20 GHz [9], and onboard radars of aircraft for long-range radar surveillance and guidance - in the range of 3.175-3.425 GHz [19]. This circumstance complicates significantly the development of an antenna system for RHH.

Note, that abroad one of the main directions for improving RHH is the use of flat or conformal antenna arrays [8]. The main advantages of RHH with flat and conformal antenna arrays in comparison with modern reflector and slot antennas are: more efficient tuning out from natural and organized interference; electronic beam control of the antenna with a complete rejection of the use of moving parts with a significant reduction in weight and dimensions characteristics and power consumption; more efficient use of polarimetric mode and Doppler beam narrowing; increase in carrier frequencies (up to 35 GHz) and resolution, aperture and field of view; reducing the influence of the properties of radar conductivity and thermal conductivity of the radome causing its aberration and distortion. In such RHHs it is also possible to use modes of adaptive tuning of the equal-signal zone with automatic stabilization of antenna directional pattern characteristics.

In addition, the use of multiple ranges of emitted signals is an effective means for reducing the influence of angular noise on pointing accuracy [40].

3.3. Using methods of trajectory control of observation

In practice situations are possible when the measurement of the range and speed of approach to the AO in RHH active channel will be impossible when it is suppressed by the interference, and only the passive channel tracking the angular position of the interference source will be operational. In this case, in the absence of a priori information about coordinates and parameters of radio-emitting target movement it is necessary to organize the trajectory observation control to solve the guidance problem. A similar problem arises when monitoring radio-emission sources, located on air objects, in the absence of a priori information about the target coordinates in the GWS carrier onboard radar, which is necessary for transmission to the RHH in the process of target designation and radio correction. The trajectory control of observation can be carried out both in single-position and two-position systems of guiding to AO.

A specific area of TOC is the creation of negative algorithmic impacts on the enemy information systems [41].

3.4. Joint GWS guidance to a group air object

Currently, GWS AO carriers, as a rule, carry several GWSs which can be simultaneously guided to a group air object (GAO). In this case different objects for using GWS are provided. Situations are possible when either GWSs will independently choose their AOs for guidance or this process will be carried out centrally, but without the participation of the carrier. Therefore, when developing the GWS, it is necessary to provide for the need of AO resolution in a dense group [28] and organization of radio exchange of information between the GWSs as well as a two-way radio communication line with the GWS carrier.

3.5. Improving the RHH intelligent qualities

Intelligent RHHs are a new scientific and technical direction in radar systems engineering. To the greatest extent, the property of RHH intelligence is manifested when solving the problem of RHH adapting to rapidly changing external environment in order to ensure the optimal distribution of limited time, frequency, spatial and energy resources over a number of processed location objects. Besides, the level of intelligence acquires a fundamental importance

at RHH action under the EW conditions when it is exposed to unpredictable in advance complex effect of various interferences with their equally unknown space-time dynamics. The RHH intelligence abilities are especially important when conducting a GWS group actions against an AO group in conditions of electronic countermeasures from the enemy.

Hence, it follows that at the present stage of RHH development the most important are the tasks of RHH organizing and algorithmic functioning as a whole (including in the conditions of interference), the tasks of optimal RHH resource management, the tasks of organizing and optimizing its functional modes.

The RHH functioning can be arranged using artificial intelligence methods. Thus, the intelligent RHH must provide an assessment of the signal – interference environment, determination of the interference type and method of protection against it, determination of the number and importance of targets, the choice of the homing method and information sources. This makes it possible to take effective decisions on methods of protection against interference, as well as to solve the problems of target allocation and GWS guidance.

3.6. Strengthening the role of digital information processing

The decisive role in ensuring RHH high information content and giving it intellectual qualities belongs to the system of digital processing of radar signals and data. Digital methods of information processing and control are used in RHH when solving the following tasks: beamforming and antenna array directivity control; adaptive spatial filtering of radio signals received by the antenna array, including in conditions of difficult interference environment; digital time-frequency coherent and incoherent processing of radar signals; detection and tracking of trajectories based on radar measurement data; AO recognition; provision of situational awareness; control of RHH operating modes and blocks, including the arrays. Moreover, there has also been a steady trend towards the introduction of digital methods for the formation of probing and reference signals.

Achievements in digital technologies of recent years significantly expand the information capabilities of promising RHHs, allowing by forming a set of probing signals with the required properties, to provide the flexibility of the system for processing radar signals and data, adjusting it to the specified conditions of radar observation using a programmable digital signal generator, broadband digital multichannel receiver and universal processor. Thus, digital technologies make it possible to solve the problem of RHH development, relying on new approaches and making the most of the advantages of digital representation of signals.

3.7. Improvement of antenna systems

Antenna systems largely determine the appearance of the new generation RHHs. One of the promising directions of RHH development is the use of active and passive phased antenna arrays in them. The space-time signal processing used in this case allows to expand significantly the RHH information capabilities and greatly increase their noise immunity. That is why the development of highly efficient APHAR samples is of paramount importance. The latter make it possible to provide flexibility in controlling the RHH operating modes, good adaptability under the influence of various kinds of interference and changing electromagnetic environments which is due to their ability to carry out the following: almost instantaneous beam overthrow; formation of the required antenna pattern (AP) and its rapid change; simultaneous RHH operation in several modes; creation of multi-beam AP; adaptive and flexible forming of the required number of APHAR beams with low side lobe levels; simultaneous emission of multi-beam AP signals at different carrier frequencies and repetition frequencies; reduction of

radio reflection by the antenna array due to its rational, including conformal placement and control of the direction of scattering the signals incident on it by the antenna system; the use of one antenna array in the interests of several modes of RHH operation. However, note that in order to obtain all the advantages of using APHAR, a significant complication of its algorithmic support is required.

The implementation of the considered promising directions of the development in RHH design will contribute to increasing the potential and efficiency of GWS AO application.

4. CONCLUSION

The foregoing allows us to draw the following conclusions:

1. In the process of GWS AO development, several generations of these products were developed, equipped with radar homing heads. Nowadays RHHs are widespread providing inertial guidance with radio correction from the onboard radar of their carrier in the initial and middle sections of GWS flight and active homing in the final section. When using these RHHs, simultaneous guidance of several GWSs is possible. RHHs are very promising, in which the sequential implementation of three guidance modes is provided: inertial guidance with radio correction, passive guidance and active guidance. Using such RHHs radio-emitting targets can be intercepted.
2. In modern RHH the existing homing methods and algorithms for automatic target tracking and GWS trajectory control do not ensure successful GWS guidance with a given efficiency on new types of air objects. A similar disadvantage also occurs when it is necessary to intercept simultaneously a group of air objects by several RHHs. Therefore, the development of promising RHHs requires the introduction of new homing methods and tracking algorithms for AO.
3. The main directions for improving GWS AO are: the development of new, more flexible non-stationary homing methods and expansion of the possibilities for their information support. This predetermines the need to improve situational awareness, ensure multiband operation, achieve a high level of RHH protection from natural and intentional interference, using the trajectory control of observation when aiming at radio emitting objects, joint GWS guidance to GAO, intellectualization and digitalization of RHHs, improvement of antenna systems.

REFERENCES

1. Egorov K. Osnovnye napravleniya sovershenstvovaniya zarubeghnykh upravlaemykh raket klassa «vozdukh-vosdukh» [The main directions of improvement of foreign guided missiles of the "air-to-air" class]. *Zarubeghnoe voennoe obozrenie*, 2001, 8:32-38, (in Russ).
2. Davydov AN, Chernykh LG, Pankratov ON, Chabanov VA. *Sostoyanie i perspektivy razvitiya orugiya klassa «vozdukh-vosdukh» dlya samoletov pyatogo pokolenya Analiticheski obzor po materialam zarubeghnykh informacionykh istochnikov* [State and development prospects of air-to-air weapons for 5th generation aircraft (Analytical review based on materials from foreign information sources)]. Under the general editorship of Academician Fedosov E.A. Moscow, GosNIIAS Publ., 2004, 92 p.
3. Markovsky V, Perov K. *Sovetskie aviacionnye rakety «vozdukh-vozdukh»* [Soviet air-to-air missiles]. Moscow, Publishing House "Exprint", 2005, 48 p.
4. Veksin SI. *Obrabotka radiolokacionnykh signalov v doplerovskikh golovkakh samonavedeniya* [Processing of radar signals in Doppler homing heads]. Moscow, Publishing house MAI, 2005.
5. Akopyan IG, Veksin SI, Medvedev GP, Sukhov AM. Osobennosti postroeniya i

razvitiya tekhniki radiolokacionnykh golovok samonavedeniya v sistemakh raketnogo voorugheniya VVS i ZRK [Features of the construction and development of technology of radar homing heads in the systems of missile weapons of the Air Force and SAM]. *Radiotekhnika*, 2005, 2:7-12 (in Russ).

6. Akopyan IG. Osobennosti postroeniya i tendencii razvitiya golovok samonavedeniya dlya raket «poverkhnost-vozdukh» i «vozdukh-vosdukh» [Features of the construction and development trends of seeker heads for surface-to-air and air-to-air missiles]. *Vestnik koncerna VKO «Almaz-Antei». Vozdushno-kosmicheskaya oborona*, 2006, 3(28) (in Russ).
7. Bogdanov AV, Filonov AA, Kuchin AA. *Algoritmy obrabotki signalov v mnogophunkcionalnoi RGS upravlyaemykh raket klassa «vozdukh-vosdukh» dlya obespecheniya navedeniya na element gruppovoi vozdushnoi celi po zadannomu celeraspredeleniyu* [Algorithms for signal processing in a multifunctional RGS of guided missiles of the "air-to-air" class to ensure its guidance to an element of a group air target for a given target distribution]. Tver, VA VKO Publ., 2008.
8. Shcherbinin R. Golovki samonavedeniya perspectivnykh zarubeghnykh upravlyamykh raket i bomb [Homing heads of promising foreign guided missiles and bombs]. *Zarubeghnoe voennoe obozrenie*, 2009, 4:64-68 (in Russ).
9. Antipov VN, Merkulov VI, Samarin OF, Chernov VS. Osnovnye napravleniya razvitiya aviacionnykh bortovykh RLS [The main directions of development of airborne radar stations]. *Uspekhi sovremennoi radioelektroniki*, 2009, 10:7-29 (in Russ).
10. Merkulov VI, Chernov VS, Drogalin VV. *Zashchita radiolokatsionnykh system ot pomekh. Sostoyanie i tendencii razvitiya* [Protection of radar systems from interference. State and development trends]. Ed. A.I. Kanashenkov and V.I. Merkulov. Moscow, Radiotekhnika Publ., 2003, 416 p.
11. Abaturov VA Zabelin IV, Zakharov MS, Saveliev AN, Chernov VS. *Aviacionnye sistemy radioupravleniya. Radiolokatsionnye golovki samonavedeniya raket «vozduh-vozduh» i «vozduh-poverhnost': uchebnoe posobie* [Aircraft radio control systems. Radar homing heads for air-to-air and air-to-surface missiles: tutorial]. Ed. V.S. Chernov. Moscow, VUNTS VVS "VVA im. prof. N.E. Zhukovsky and Yu.A. Gagarin" Publ., 2010, 48 p.
12. Verba VS, Merkulov VI, Drogalin VV. *Otsenivanie dal'nosti i skorosti v radiolokatsionnyh sistemah. CH. 3* [Estimation of range and speed in radar systems. Part 3]. Ed. V.S. Verba, V.I. Merkulov. Moscow, Radiotekhnika Publ., 2010, 472 p.
13. Samarin OF, Tatarsky BG, Chernov VS. Razvitie cifrovyh tekhnologij i arhitektura radiolokacionnyh sistem.[Development of digital technologies and architecture of radar systems]. *Informacionno-izmeritel'nye i upravlyayushchie sistemy*, 2010, 8(1):48-57 (in Russ).
14. Akopyan IG, Veksin SI, Sukhov AI, Chernov VS. Tendencii razvitiya radiolokacionnyh golovok samonavedeniya zenitnyh raket i raket klassa «vozdukh-vozdukh» [Trends in the development of radar homing heads for anti-aircraft missiles and air-to-air missiles]. *Radioelektronnye sistemy*, 2010, 1(17), (in Russ).
15. Akopyan IG, Veksin SI, Evseev DD, Sukhov AI. O sostoyanii i perspektivah razvitiya radiolokatsionnyh golovok samonavedeniya dlya raket «poverhnost'-vozdukh» i «vozdukh-vozdukh» [On the state and prospects of development of radar homing heads for surface-to-air and air-to-air missiles]. *Vestnik Koncerna VKO «Almaz-Antej». Vozdushno-kosmicheskaya oborona,* 2011, 1(5):17-30 (in Russ).
16. Bogatskiy VG, Mordvinov IG, Danilova TV. Sposob porazheniya tseli-postanovshchika kogerentnyh pomekh raketoj s aktivnoj RGS

[The method of hitting the target-producer of coherent jamming by a missile with an active RGS]. *Patent RU 2 468 381 C1*, Starting date 18.05.2011. Publ. 11/27/2012 (in Russ).
17. Chernykh LG. Sostoyaniya i perspektivy razvitiya upravlyaemyh raket klassa «vozduh-vozduh» [State and prospects for the development of air-to-air guided missiles]. *Aviatsionnye sistemy,* 2012, 1:21-36 (in Russ).
18. Shcherbakov BF. *Aviatsionnye raketnye kompleksy: uchebnoe posobie* [Aviation missile systems: a tutorial]. Baltic State Technical University Publ., 2012, 65 p.
19. Verba VS, Vasiliev AV, Merkulov VI, Chernov VS. Radiolokatsionnye sistemy aviatsionnyh kompleksov radiolokatsionnogo dozora i navedeniya [Radar systems of aviation complexes of radar surveillance and guidance]. *Uspekhi sovremennoj radioelektroniki,* 2013, 4:3-22 (in Russ).
20. Sinikov A. Evolyutsiya i perspektivy raket klassa "vozdukh-vozdukh" [Evolution and prospects of air-to-air missiles]. *Vozdushno-kosmicheskaya oborona,* 2014, no. 14 (in Russ).
21. Belik BV, Belov SG, Verba VS. *Aviatsionnye sistemy radioupravleniya* [Aviation radio control systems]. Ed. V.S. Verba and V.I. Merkulov. Moscow, Radiotekhnika Publ., 2014, 376 p.
22. Bogdanov AV, Filonov AA, Kovalev AA. *Metody samonavedeniya istrebitelej i raket klassa «vozdukh-vozdukh» na gruppovuyu vozdushnuyu tsel'* [Homing methods of fighters and air-to-air missiles at a group air target]. Ed. A.A. Kuchina. Krasnoyarsk, Sib. feder. un-t Publ., 2018, 168 p.
23. Byzov AN, Petrov YuV, Rogozhin VA. Primenenie nejronnyh setej dlya opredeleniya dal'nosti do istochnika radioizlucheniya [Application of neural networks to determine the distance to the source of radio emission]. *Voprosy radioelektroniki*, 2019, 8:13-17 (in Russ).
24. Verba VS (ed.). *Informacionno-izmeritel'nye i upravlyayushchie radioelektronnye sistemy i kompleksy* [Information-measuring and control radio-electronic systems and complexes]. Moscow, Radiotekhnika Publ., 2020, 490 p.
25. Zaporozhets GV, Merkulov VI, Chernov VS. Aviatsionnye sredstva radioelektronnogo porazheniya radiolokatsionnyh sistem SSHA. Ch. 2. Individual'nye sredstva REP. SVCH-sredstva funkcional'nogo porazheniya. Sredstva REB bespilotnyh letatel'nyh apparatov [Aircraft means of electronic destruction of US radar systems. Part 2. Individual means of REP. Microwave devices for functional damage. Electronic warfare equipment of unmanned aerial vehicles]. *Uspekhi sovremennoj radioelektroniki*, 2020, 4-5:5-18 (in Russ).
26. Belik BV, Merkulov VI, Chernov VS. Sposoby traektornogo upravleniya nablyudeniem v aviatsionnyh odnopozitsionnyh sistemah radiomonitoringa [Trajectory control methods for observation in aviation]. *Uspekhi sovremennoj radioelektroniki*, 2020, 10:5-29 (in Russ).
27. Verba VS, Zagrebelny IR, Merkulov VI. Metod navedeniya na vozdushnuyu tsel' v sostave plotnoj gruppy [The method of aiming at an air target as part of a dense group]. *Radiotekhnika i elektronika*, 2020, 65(11):1091-1100 (in Russ).
28. Shneydor NA. *Missile Guidance And Pursuit: Kinematics, Dynamics and Control.* Woodgate, Horwood Publishing Limited, 1998, 286 p.
29. Paul Zarchan. *Tactical and Strategic Missile Guidance.* American Institute of Aeronautics and Astronautics Publ., 2012, vol. 239, 1026 p.
30. Sioris George M. *Missile Guidance and Control Systems*. Springer, 2004.
31. Rafael Yanushevsky. *Modern Missile Guidance*. CRC Press, 2008.
32. Popov IM, Khamzatov MI. *Vojna budushchego. Konceptual'nye osnovy i prakticheskie vyvody.* [War of the future. Conceptual framework and practical conclusions]. Moscow, Kuchkovo pole Publ., 2017, 832 p.

33. Fedosov EA. Realizaciya setetsentricheskoj tekhnologii vedeniya boevykh dejstvij potrebuet sozdaniya BRLS novogo pokoleniya [Implementation of the network-centric technology of warfare will require the creation of a new generation radar]. *Fazotron*, 2007, №1-2(10):11-44. (in Russ).
34. Sage EP, White CS. III. *Optimal'noe upravlenie sistemami* [Optimal systems management]. Moscow, Radio i svyaz' Publ., 1982.
35. Chernousko FA, Kolmanovsky VB. *Optimal'noe upravlenie pri sluchajnyh vozmushcheniyah* [Optimal control under random disturbances]. Moscow, Nauka Publ., 1978.
36. Krutko PD. *Obratnye zadachi dinamiki v teorii avtomaticheskogo upravleniya:* Uchebnoe posobie dlya VUZov [Inverse problems of dynamics in the theory of automatic control: Textbook for universities]. Moscow, Mashinostroenie Publ., 2004, 576 p.
37. Merkulov VI, Verba VS, Ilchuk AR, Koltyshev EE. *Avtomaticheskoe soprovozhdenie tselej RLS integrirovannyh aviatsionnyh kompleksov. T. 2.* Soprovozhdenie odinochnyh tselej. Monografiya. V 3 kh tomakh [Automatic tracking of targets of radar stations of integrated aviation complexes. V. 2. Accompanying single targets. Monograph. In 3 volumes]. Ed. V.S. Verba. Moscow, Radiotekhnika Publ., 2018, 486 p.
38. Merkulov VI, Verba VS, Ilchuk AR, Kirsanov AP. *Avtomaticheskoe soprovozhdenie tselej v RLS integrirovannyh aviatsionnyh kompleksov. Mnogotselevoe soprovozhdenie. T. 3.* V 3-kh tomakh [Automatic tracking of targets in radar stations of integrated aviation complexes. Multipurpose support. V. 3. Monograph. In 3 volumes]. Ed. V.S. Verba. Moscow, Radiotekhnika Publ., 2018, 392 p.
39. Kanashenkov AI, Merkulov VI (eds.) *Aviatsionnye sistemy radioupravleniya. T.1. Principy postroeniya sistem radioupravleniya. Osnovy sinteza i analiz* [Aircraft radio control systems. Vol. 1. Principles of building radio control systems. Fundamentals of synthesis and analysis]. Moscow, Radiotekhnika Publ., 2003, 192 p.
40. Merkulov VI, Zabelin IV. Traektornoe upravlenie nablyudeniem kak sposob sozdaniya prednamerennykh algoritmicheskikh vozdejstvij na radiolokatsionnye sistemy [Trajectory control of observation as a way of creating deliberate algorithmic influences on radar systems]. *Radiotekhnika*, 2010, 7 (in Russ).

DOI: 10.17725/rensit.2021.13.245

Mathematical Foundations of the Fractal Scaling Method in Statistical Radiophysics and Applications

Alexander A. Potapov

Kotelnikov Institute of Radioengineering and Electronics of Russian Academy of Sciences, http://cplire.ru/
Moscow 125009, Russian Federation

Jinan University, Sino-Russian Laboratory of Information Technologies and fractal signal processing, https://english.jnu.edu.cn/
Guangzhou 510632, China

E-mail: potapov@cplire.ru

Received May 04, 2921, peer-reviewed May 24, 2021, accepted May 31, 2021

Abstract: **The system of basic mathematical concepts and constructions underlying the modern global fractal-scaling method developed by the author is presented. An overview of the main results on the creation of new information technologies based on textures, fractals (multifractals), fractional operators, scaling effects and nonlinear dynamics methods obtained by the author and his students for more than 40 years (from 1979 to the present) at the V.A. Kotelnikov Institute of Radioengineering and Electronics of RAS. It is shown that, for the first time in the world, new dimensional and topological (and not energy!) Features or invariants were proposed and then effectively applied for problems in radio physics and radio electronics, which are combined under the generalized concept of "sample topology" ~ "fractal signature". The author discovered, proposed and substantiated a new type and new method of modern radar, namely, fractal-scaling or scale-invariant radar. It should be noted that fractal radars are, in fact, a necessary intermediate stage on the path of transition to cognitive radar and quantum radar.**

Keywords: **fractal, scaling, fractional operator, texture, non-Markov random process, signature, nonlinear dynamics, radiophysics, radar**

UDC 510.22: 517.2: 519.24: 537.86 + 621.396.96

For citation: Alexander A. Potapov. Mathematical Foundations of the Fractal Scaling Method in Statistical Radiophysics and Applications. *RENSIT*, 2021, 13(3):245-296. DOI: 10.17725/rensit.2021.13.245.

Contents

1. INTRODUCTION

The term "fractal" at the end of the last century was perceived as exotic. Somewhat exaggerating, we can say that fractals formed a thin amalgam on the powerful skeleton of science at the end of the 20th century. The situation has radically changed with the use of fractal structures in technical applications to the processing of stochastic signals and images, artificial intelligence, propagation and scattering of radio waves, electrodynamics, the design of antenna devices, other electrodynamic and radio engineering structures, radioelements with fractal impedance, etc. [17,42,45,57,58,62,73,79, 82,83].

Currently, we can confidently talk about the design of fully fractal radio systems. At the same time, physicists included in their arsenal a new mathematical apparatus, and mathematicians were enriched with new heuristic considerations and joint problem statements.

The purpose of this work is to give, as much as possible, a closed presentation of the basic concepts and mathematical theory for problems and applications of statistical radiophysics, using various approaches to the synthesis of the global fractal-scaling method developed by the author.

The problem presented in the title of the work began to be studied for the first time in the world by the author more than 40 years ago at the Institute of Radioengineering and Electronics (IRE) of the Academy of Sciences of the USSR in connection with the implementation of a cycle of fundamental research devoted to the creation of new breakthrough radiophysical technologies for radar. The main one is detection by a one-dimensional (probabilistic statistical signal) and multidimensional (stochastic optical and radar images) sample of various low-contrast objects against a background of intense interference from the Earth's surface. The research is carried out within the framework of the fundamental scientific direction "Fractal radiophysics and fractal radio electronics: design of fractal radio systems", initiated and developed by the author at the V.A. Kotelnikov IRE of Russian Academy of Sciences (RAS) from 1979 to the present [82,83].

The relevance of these studies is associated with the need for a more accurate description of real processes occurring in radiophysical and

radio engineering systems. This is, first of all, taking into account heredity, non-Gaussianity and scaling (self-similarity, self-similarity) of physical signals and fields. All these concepts are included in the description of fractal sets or fractals, first proposed in 1975 by B. Mandelbrot [115].

Naturally, the text does not claim to be complete; detailed evidence is lacking. All the concepts used are introduced along the way. The main purpose of this work is to acquaint the reader with the created texture and fractal (multifractal) methods, as well as their application in general. The reader will find more detailed information and necessary proofs in the author's books and original works on this topic, indicated at the end of this work. Although the choice of material for the review could not but be influenced by the author's mathematical tastes and interests, he hopes that the most fundamental concepts of a fundamental nature are reflected here in sufficient detail.

2. THEORETICAL ASPECTS OF THE METHOD

2.1. Fundamentals of fractional measure and noninteger dimension theory

The main property of fractals is the non-integer value of their dimension. The development of dimension theory began with the work of Poincaré, Lebesgue, Brouwer, Uryson, and Menger. In various areas of mathematics, sets arise in one sense or another that are negligible and indistinguishable in the sense of the Lebesgue measure. To distinguish such sets with a pathologically complex topological structure, it is necessary to use unconventional characteristics of smallness, for example, capacity, potential, Hausdorff measures and dimension, etc. The most fruitful was the use of the Hausdorff fractional dimension, closely related to the concepts of entropy, fractals and strange attractors in the theory of dynamical systems [2,3,8,18,21,24,33,62,77,90 ,94,95,134].

Fractional Hausdorff dimension is determined by a *p*-dimensional measure with an arbitrary real positive number *p*, which was introduced by Hausdorff in 1919. In the general case, the concept of a measure is not related either to a metric or to a topology. However, the Hausdorff measure can be constructed in an arbitrary metric space on the basis of its metric, and the Hausdorff dimension itself is related to the topological dimension. The concepts introduced by Hausdorff are based on the construction of Carathéodory (1914) [77,105]. Let be (M,ρ) a metric space, F a family of subsets of the space M, and f a function on F such that $0 \le f(G) \le \infty$ for $C \in F$ and $f(\varnothing) = 0$. We construct auxiliary measures m_f^z and then the main measure Λ_f as follows. For $E \subset M$ and $\varepsilon > 0$, the value m_f^z is defined as the exact lower bound of the set of numbers

$$m_f^z = \inf \sum_i f(\mathrm{G}) \tag{1}$$

over all countable ε-coverings $\{G_i\}$, $G_i \in F$.

The inequality $m_f^{z_1}(E) \ge m_f^{z_2}(E)$ for $\varepsilon_2 > \varepsilon_1$ implies the existence of the limit

$$\Lambda(E) = \lim_{\varepsilon \to 0+} m_f^{\varepsilon}(E) = \sup m_f^{\varepsilon}(E). \tag{2}$$

It is clear that m_f^z and $\Lambda(E)$ are also *outer measures* on M. Let $\rho(a,B) > \varepsilon > 0$. Consider an arbitrary ε-covering $\{G_i\}$ of the set $A \bigcup B$, consisting of a certain number of sets. Then the family $\{A \bigcap G_i\}$ and $\{B \bigcap G_i\}$ do not intersect and cover the sets A and B, respectively, therefore

$$m_f^z(A \bigcup B) \ge \mathrm{m}_f^z(A) + \mathrm{m}_f^z(B) \tag{3}$$

or

$$\Lambda_f(A \bigcup B) = \Lambda_f(A) + \Lambda_f(B). \tag{4}$$

The class of Λ_f-measurable sets of the space M form a σ-ring on which the outer measure Λ_f is regular. The measure Λ_f is also called the result of applying the Carathéodory construction to the function f, and the outer measure m_f^z is called the approximating measure of order ε. The measure Λ_f rather subtly reflects the properties of the function f and the family F, although it is usually not an extension of f.

We indicate two simple statements that describe the behavior of approximating measures on a decreasing sequence $C_1 \supset C_2 \supset$ ... of compact subsets of the space M. If the elements of the family F are open subsets of M, then

$$\lim_{i\to\infty} m_f^{\varepsilon}(\mathrm{G}_i) = m_f^{\varepsilon}(\bigcap_{i=1}^{\infty} C_i). \quad (5)$$

If $0 < \varepsilon_0 < \varepsilon$ and $f(S) = \inf\{f(T)\}$: $T \in F$, $S \subset \mathrm{Int}T$, $d(T) \le \varepsilon$ for all $S \in F$ such that $d(S) \le \varepsilon$

$$\lim_{i\to\infty} m_f^{\varepsilon}(\mathrm{G}_i) \le m_f^{\varepsilon}(\bigcap_{i=1}^{\infty} C_i), \quad (6)$$

where d is the diameter of the sets, Int is the set of all interior points of the set T.

Let X be a bounded compact metric space, F be the family of all nonempty compact sets from X, a function f: $F \to [0, +\infty]$ continuous with respect to the Hausdorff metric, and $f(C) > 0$ for all $C \in F$ such that $d(\mathrm{C}) > 0$. If $A_1 \subset A_2 \subset A_3 \subset$ ... form an increasing sequence of subsets of the space X, then

$$\lim_{k\to\infty} m_f^{\varepsilon}(A_k) \le m_f^{\varepsilon}(\bigcap_{k=1}^{\infty} A_k). \quad (7)$$

Let us define the h-Hausdorff measure. Let $h(r)$ be a continuous monotonically increasing function of r ($r \ge 0$) for which $h(0) = 0$. The class of such functions is denoted by H_0. Applying the Carathéodory construction to the function $f(E) = h[d(E)]$ for $E \ne \varnothing$ and $f(\varnothing) = 0$ (here $d(E)$ is the diameter of the set E), we obtain the Λ_h-Carathéodory measure, which is called h-Hausdorff measure. If, in addition, $h(r) = \gamma(\alpha) r^{\alpha}$, where α is a fixed positive, not necessarily an integer, and $\gamma(\alpha)$ is a positive constant depending only on α, then the h-Hausdorff measure is called an α-dimensional measure or an α-the Hausdorff *measure* H_{α}, which is a Borel regular measure.

The construction of the Hausdorff h-measure can be imagined as follows. Cover α with an arbitrary sequence of disks C_{v} of radius $\mathrm{r_v} \le \varepsilon$ ($\varepsilon > 0$; $\mathrm{v} = 1,2, ...$) and denote by $m_h^{\varepsilon}(a,h) \ge 0$ the lower bound of the corresponding sums $\sum_{v=1}^{\infty} h(r_v)$. This number increases with decreasing ε. A-priory

$$\Lambda_h(E) = \lim_{\varepsilon\to 0} m_h^{\varepsilon}(a,h), \quad (8)$$

hence

$$0 \le \Lambda_h(E) \le +\infty. \quad (9)$$

Limit (8) is the *outer* h-Hausdorff measure, which is a Borel regular measure on the σ-ring Λ_{h} of measurable sets of the space M. Choosing different functions for $h(r)$, we get: a linear measure $h(r) = 2\pi r$, a flat measure $h(r) = \pi r$, and a logarithmic measure $h(r) = 1/\ln r$.

Condition $E_1 \subset E_2$ implies $\Lambda_{\mathrm{h}}(E_1) \le \Lambda_{\mathrm{h}}(E_2)$, that is, the Hausdorff h-measure is a monotonically increasing set function. Using the h-measure, the dimension of the set is defined as follows. If $0 < \Lambda_{\mathrm{h}}(A) < \infty$, then $\langle h \rangle$ is called the metric dimension (Hausdorff dimension) of the set A. If $h(r) = cr^{\alpha}$ and $0 = \Lambda_{\mathrm{h}}(A) < \infty$, then the dimension of the set A is denoted by $\langle \alpha \rangle$, here c is a constant. A set of a certain dimension has an h-measure equal to 0 for each external dimension and ∞ for each lowest h-measure.

A further generalization of the notion of dimension is the *Hausdorff-Besicovitch dimension,* which is introduced through the nonnegative numbers $\alpha_0 = \alpha_0(E)$ in the form of the equality

$$\alpha_0(E) = \sup\{\alpha : H_{\alpha}(E) \ne 0\} = \inf\{\alpha : H_{\alpha}(E) = 0\} \quad (10)$$

for the set E. The dimension of the Hausdorff-Besicovitch set is determined by the behavior of $H_{\alpha}(E)$ not as a function of E, but as a function of α.

The correctness of definition (10) confirms the following property of the H_{α}-measure. If $H_{\alpha}(E) < \infty$, then $H_{\alpha}(E) = 0$ for any $\alpha_2 > \alpha_1$. If the measure $H\alpha_2(E)$ is nonzero, then $H\alpha_1(E) = \infty$ for any positive $\alpha_1 < \alpha_2$. This implies that for the set $E \subset M$ or $H_{\alpha}(E) = 0$ for any $\alpha > 0$, then $\alpha_0(E) = 0$ by definition, or there is a "jump" point α_0 such that $H_{\alpha}(E) = \infty$ for $\alpha < \alpha_0$ and $H_{\alpha}(E) = 0$ for $\alpha > \alpha_0$. This number α_0 is the Hausdorff-Besicovitch dimension.

If, when determining the H_α-Hausdorff measure, the coverings are carried out by balls of the same diameter, then such a measure is called entropy. Then the dimension (10) is called the entropy or Kolmogorov dimension.

For sets of positive k-dimensional Lebesgue measure, both dimensions coincide and are equal to K. The Hausdorff-Besicovitch dimension characterizes an external property of the set. Therefore, it is advisable to introduce the concept of the Hausdorff-Besicovitch set at a point that would characterize its internal structure.

In this case, the number

$$\alpha_E(x_0) = \lim_{n\to\infty} \alpha_0(E \bigcap O_n(x_0)) \quad (11)$$

is called the local Hausdorff-Besicovitch dimension of the set E at the point x_0. Here $\{O_n(x_0)\}$ is an arbitrary sequence of contracting neighborhoods of the point $x_0 \in M$.

Each bounded closed set E of an m-dimensional Euclidean space contains a point $x_0 \in E$ such that

$$\alpha_E(x_0) = \alpha_0(E). \quad (12)$$

A function $\alpha_E(x)$ is called a function of local Hausdorff-Besicovitch dimension if

$$\begin{aligned} &0 \le \alpha_E(x) \le \alpha_0(E) \text{ for any } x \in M, \\ &\alpha_E(x) = 0 \text{ if the set } E \text{ is closed and } x \notin E, \\ &\alpha_E(x) = 0 \text{ for all isolated points of the set } E. \end{aligned} \quad (13)$$

The Hausdorff-Besicovitch dimension is a metric concept, but there is a fundamental connection with the topological dimension dim$E$, which was established by L.S. Pontryagin and L.G. Shnirelman [18, p. 210], introducing in 1932 the notion of metric order, namely: the infimum of the Hausdorff-Besicovitch dimension for all metrics of the compact set E is equal to its topological dimension: dim$E \le \alpha(E)$. One of the widely used methods for estimating the Hausdorff dimension of sets, known as the principle of mass distribution, was proposed by Frostman in 1935 [58,80].

Sets, the Hausdorff-Besicovitch dimension of which is a fractional number, are called *fractal sets* or *fractals*. More strictly, a set E is called a fractal (fractal) in a broad sense (in the sense of B. Mandelbrot) if its topological dimension does not coincide with the Hausdorff-Besicovitch dimension, namely, $\alpha_0(E) >$ dim$E$. For example, the set E of all irrational points [0; 1] is fractal in the broad sense, since $\alpha_0(E) = 1$, dim$E = 0$. The set E is called fractal (fractal) in the narrow sense if $\alpha_0(E)$ is not integer. A fractal set in a narrow sense is the same and in a wide sense.

As was first shown by A.S. Besicovitch in 1929, there are profound differences between Lebesgue sets and fractals. First of all, these features relate to densities. The geometric properties of the fractal set E are determined by the behavior of the function

$$D(\mathrm{x}, \varepsilon) = \frac{H_\alpha(E \bigcap O(x, \varepsilon))}{\varepsilon^\alpha} \quad (14)$$

for small ε, where x is an arbitrary point of the set E. The upper α-density of a set E at a point x is called

$$\overline{D}_\alpha(E, x) = \overline{\lim_{\varepsilon \le 0}} D(E, x), \quad (15)$$

respectively, the lower α-density of the set E at the point x is written in the form

$$\underline{D}_\alpha(E, x) = \underline{\lim_{\varepsilon \le 0}}\, D(x, \varepsilon). \quad (16)$$

When $\overline{D}_\alpha(E, x) = \underline{D}_\alpha(E, x)$, that common value is called the α-density of the set E at the point x and is denoted by $D_\alpha(E, x)$. If ε → 0+, then $\overline{D}_\alpha(E, x)$ and $\underline{D}_\alpha(E, x)$ it is called right-sided, for ε → 0 – left-sided, and for ε → 0, two-sided upper and lower α-density, respectively.

It can be noted that for almost all (in the sense of H_α-Hausdorff) points α of the set on the line, the one-sided upper (right and left) α-density is equal to one, and the one-sided lower α-density is equal to 0 ($0 < \alpha < 1$). For two-sided densities, at almost all points of the α-set on the line, there is no two-sided α-density, that is, the upper α-density is different from the lower one.

2.2. Homogeneous functions and scaling

The last four decades have been a period of significant progress in the physics of fractals and their applied aspects. Experimenters and theorists have successfully used the concept of fractality in the study of numerous physical phenomena. At the same time, the theory of large-scale transformations (the theory of self-similarity, scaling theory) has also received great development. This is most fully reflected in the problem of phase transitions (see, for example, [96,97]).

In fact, in all natural and artificial dynamical systems, it is necessary to take into account the effects of scaling, i.e. the presence of many different spatial and/or temporal scales and all kinds of interactions between them. It is useful to approach the discussion of scaling ideas from the point of view of homogeneous functions.

As follows from [13], a function of one or several variables satisfying the condition that when all arguments of the function $f(x, y, ..., u)$ are simultaneously multiplied by the same arbitrary factor λ, the value of the function is multiplied by some power α of this factor is called homogeneous:

$$f(\lambda x, \lambda y, ..., \lambda u) = \lambda^{\alpha} f(x, y, ..., u), \quad (17)$$

where α is the order of homogeneity, or the measurement of a homogeneous function.

For example, the power function $f(t) = bt^{\alpha}$ satisfies the homogeneity relation (17) or *scaling*:

$$f(t) = \lambda^{\alpha} f(t) \quad (18)$$

for all positive values of the scale factor λ. Naturally, the power function, like many other functions that satisfy the scaling relation (18), are not fractal curves. However, many types of fractals (scale-invariant fractals) have scaling symmetry. Homogeneous functions have many properties that make them very attractive for an approximate description of real processes and objects.

There are: (1) – positively homogeneous functions for which equality (17) holds only for positive $\lambda(\lambda > 0)$, and (2) – absolutely homogeneous functions for which the equality holds:

$$f(\lambda x) = |\lambda|^{\alpha} f(x) \quad (19)$$

From the differential properties of homogeneous functions, we note *Euler's lemma*: "Homogeneous functions are proportional to the scalar product of their gradient by the vector of their variables with a coefficient equal to the order of homogeneity:

$$\vec{x} \cdot \nabla f(\vec{x}) = \alpha f(\vec{x})." \quad (20)$$

In [13], a specially normalized power function was introduced

$$f_{\lambda}(t) = \frac{1}{\Gamma(\lambda+1)} t^{\lambda}, \ t > 0, \quad (21)$$

which is called the *standard power function*.

These functions are self-similar (they have no characteristic scale, which naturally leads to the concept of *fractals*); they have the semigroup property; at the zeros of the gamma function $\Gamma(\lambda + 1)$ they are defined as generalized functions expressed in terms of the δ-function and its derivatives $\delta^{(\lambda)}(t)$; their Laplace transforms also belong to the family of power functions up to a constant factor; in contrast to exponential functions, which have the property of invariance up to a constant factor, power functions do not have this property (hence, the memory property); Tauberian theorems are applicable to them, which allow one to uniquely determine the asymptotic behavior of such functions as $t \to \infty$ from the behavior of the Laplace transform in the region of zero (these theorems are also true under the condition that zero and infinity are interchanged).

Homogeneous functions play a very important role in describing the thermodynamics of phase transitions, in describing the statistical properties of percolation [58,89], in turbulence [56,93], in the modern renormalization group theory of critical phenomena, etc.

Very often, far-reaching conclusions can be drawn from the only premise of the universality of fluctuating systems using *scaling estimates*.

2.3. Probability Power Laws and Non-Gaussian Statistics

Among the objects of the material world, self-similarity, as mentioned above, is very widely represented [6,49,57,58,73,77,89,92,96,100,115]. Power laws are the mathematical expression for self-similarity. These laws obey both objects that grow in size, for example, cities, and objects that break up into separate fragments, for example, stones. The only indispensable condition for the fulfillment of a power-law self-similar law is that *this type of objects does not have an internal scale*. Indeed, there are no real cities with the number of inhabitants less than 1 or more than 10^9. Similarly, the size of a stone cannot be less than a molecule, or more than a continent. Thus, if self-similarity is unlimited, then only in limited areas. The fact that homogeneous power laws do not have natural internal scales leads to another phenomenon – scaling or scale invariance.

We can say that power laws with integer or fractional exponents are *self-similarity generators*. As noted in [96, p. 165]: "Self-similarity, in the end, does not care whether we have an integer exponent or not. Often times, a fractional exponent holds an important clue to solving a convoluted puzzle".

In mathematics, on the basis of power functions, as we have just considered, a fractional calculus is constructed, the concept of poles is introduced and a theory of residues is created, a theory of asymptotic expansions is constructed, and stable distributions are introduced. The penetration of fractional calculus into physics accelerated sharply after the establishment of its close connection with stable distributions of the theory of probability.

The cognitive value of probability theory is revealed only by limit theorems [14]. The interest of classical research was reduced to clarifying the conditions for the convergence of distribution functions of sums of independent random variables to a Gaussian law. Therefore, the classical theory of probability studied only one limiting distribution law – the Gaussian one. In the theory of probability, in parallel with the completion of the classical problematics, the question arose of which laws, in addition to Gaussian, can be limiting for sums of independent random variables. It turned out that the class of limit laws is far from being exhausted by the Gaussian law [14,20,88,91].

The modern theory of probability is based on limit theorems on the convergence of distributions of sums of independent random variables to the so-called stable distributions: Gaussian or non-Gaussian. The former are based on the central limit theorem, and the latter (non-Gaussian) - on the limit theorem proved by B.V. Gnedenko (1939) and V. Doblin (1940) [6,14,20,91].

In this case, the limit theorem imposes restrictions on the form of non-Gaussian distributions. Namely: for the distribution law $F(x)$ to belong to the region of attraction of a stable law with a characteristic exponent α ($0 < \alpha < 2$) different from the Gaussian, it is necessary and sufficient that

$$\frac{F(-x)}{1-F(x)} \to \frac{c_1}{c_2} \text{ as } x \to \infty, \tag{22}$$

for every constant $k > 0$

$$\frac{1-F(x)+F(-x)}{1-F(kx)+F(-kx)} \to k^{\alpha} \text{ as } x \to \infty, \tag{23}$$

where $c_1 \geq 0$, $c_2 \geq 0$, $c_1 + c_2 > 0$, $0 < \alpha < 2$.

To prove (22) and (23) it is necessary and sufficient that for some selection of constants B_n, the following conditions are satisfied [14, p. 189]:

$$\begin{aligned} &nF(B_n x) \to \frac{c_1}{|x|^{\alpha}}, \ (x<0), \\ &n[1-F(B_n x)] \to \frac{c_2}{x^{\alpha}}, \ (x>0), \\ &\lim_{\varepsilon \to 0} \overline{\lim_{n \to \infty}} n \left\{ \int_{|x|<\varepsilon} x^2 dF(B_n x) - \left[\int_{|x|<\varepsilon} x dF(B_n x) \right]^2 \right\} = 0. \end{aligned} \tag{24}$$

The smaller the value of α, the longer the tail of the distribution and the more it differs from the Gaussian one. For $1 < \alpha < 2$, stable laws have a mathematical expectation; for $0 < \alpha \leq 1$, stable laws have neither variances nor mathematical expectations. Conditions (22)-(24) define the so-called non-Gaussian statistics.

The general theory of stable distributions is comparatively little known to applied specialists due to its complexity and, as was thought earlier, its purely mathematical nature. By definition, a distribution is considered stable if the composition of two such distributions leads to a distribution of the same type. This property can be viewed as a kind of self-similarity. The complexity of their use also lies in the fact that they, as a rule, are not expressed explicitly, but only through characteristic functions.

The mechanism for the formation of non-Gaussian laws does not yet have an unambiguous solution. The most common hypotheses are the following [58,73]: "the principle of least effort" – for Zipf's law, "compromise" structures – for Bradford's law, the interaction of two opposing processes (growth and limitation) and the "thermodynamic" or variational approach - for Zipf-Pareto law. (Note that the first works on the connection of the Zipf-Pareto law in linguistics and economics with stable non-Gaussian distributions belongs to B. Mandelbrot).

Stable laws play the same role in the summation of independent random variables with infinite variances as the usual Gaussian law for finite variances. The system-wide universal character of such non-Gaussian laws was established, first of all, in social and information complex systems and is associated with human behavior. Since complex systems possess structure, the analysis of such systems should take into account both aspects: the randomness of the scatter of variables and the determinism of the structures of the corresponding formations.

2.4. Fractional integroderivatives

Fractional mathematical analysis has a long history and extremely rich content [40,86]. The idea of generalizing the notion of differentiation $d^n f(x)/dx^n$ to noninteger values of n arose from the very inception of differential calculus. At the present time, in fact, there is not a single area of classical analysis that has not been touched on by fractional analysis. The mathematical language of operators of fractional integrodifferentiation is indispensable for describing and studying physical fractal systems, stochastic transfer processes (various relaxation and diffusion processes). Active attempts are being made to explain power-law dependences with fractional exponents (i.e., fractal form) by solutions of equations in fractional derivatives. Works in this direction are, apparently, restrained only by exoticism and the absence of a clear physical interpretation of fractional derivatives and fractional integrals. The apparatus of fractional derivatives and integrals is used in physics, mechanics, chemistry, hydrology, the theory of gravity, etc. (see for example [4,9,10,19,30,31,35,38,40,57,58,79,80,83,86,88,100-103,111,114,117-122,135,136]). This numerous reference was made by the author specifically to show that the applications of this mathematical apparatus are too numerous to list them all.

The time has come to apply the apparatus of fractional derivatives and integrals to the problems of fractal radiophysics and fractal radar [52,57,58,62,82,83]. To do this, first consider some of the fundamental questions of fractional calculus, which are necessary for further use.

Brief historical information. Interest in fractional mathematical analysis arose almost simultaneously with the appearance of classical analysis (even G. Leibniz mentioned this in letters to G. Lopital in 1695 when considering differentials and derivatives of order ½). Probably the earliest more or less systematic study of this issue dates back to the 19th century. and belongs to N. Abel (1823), J. Liouville (1832), B. Riemann (1847) and H. Holmgren

(1864), although earlier contributions were made by L. Euler (1730) and J. Lagrange (1772).

It was in his cycle of works that J. Liouville (1832-35), using the expansion of functions in power series, determined the "*q*"-th derivative by term-by-term differentiation. He, in particular, gave the first practical applications of the theory he created to the solution of problems in mathematical physics. Then B. Riemann (1847) proposed a different solution based on a definite integral, suitable for power series with noninteger exponents. This work, performed by Riemann in his student years, was published only in 1876 (10 years after his death). The Liouville and Riemann constructions are the main forms of fractional integration. Developing Liouville's idea, A. Grunwald (1867) introduced the concept of a fractional derivative as the limit of difference relations.

In parallel with theoretical beginnings, applications of fractional analysis to the solution of various problems were developed. One of the first such applications was the discovery of N. Abel (1823), who showed that the solution of the tautochron problem can be obtained by an integral transformation, which is written as a derivative of a half-integer order. There is a historical misconception that Abel solved the problem only with an index value of ½. In fact, as noted in [86,136], Abel considered the solution in the general case, and his work played a huge role in the development of the ideas of fractional integrodifferentiation. Holmgren's merit is the consideration of fractional differentiation as an operation inverse to integration and the application of these concepts to the solution of ordinary differential equations.

Special mention should be made of the cycle of works by Corr. Memb. Petersburg Academy of Sciences (1884) A.V. Letnikov (1837-88), who, during his 20-year scientific activity, developed a complete theory of differentiation with an arbitrary pointer (at present, his works are almost completely forgotten) [25]. The works of A.V. Letnikov remained almost unknown abroad. During the period under review in Russia, for the works of A.V. Letnikov's work was followed by N.Ya. Sonin and P.A. Nekrasov. The names of these Russian scientists are also associated with the extension of the Cauchy formula for analytic functions in the complex plane to non-integer values of the integrodifferentiation index.

While recognizing the importance of the works of the above-mentioned scientists, it is necessary, however, to note that fractional calculus became a rigorous mathematical theory only starting with the works of A.V. Letnikov [80].

At the end of the XIX century. A substantial work by J. Hadamard (1892) was published, in which, on the basis of the expansion in a Taylor series, the fractional differentiation of a function analytic in a circle with respect to the radius was considered, which is called the Hadamard approach.

In the first half of the XX century. G. Hardy, G. Weil, M. Riess, P. Montel, A. Marshaud, D. Littlewood, Ya. Tamarkin, E. Post, S.L. Sobolev, A. Sigmund, B. Nagy, A. Erdelyi, H. Kober, J. Cossard, and a number of other scientists. In 1915 G. Hardy and M. Riess used fractional integration to sum up divergent series. In 1917, G. Weil defined fractional integration for periodic functions in the form of a convolution with some special function. An analogue of S.N. Bernstein for fractional derivatives of algebraic polynomials on a finite segment was given in 1918 by P. Montaigne. A. Marshaud (1927) introduced a new form of fractional differentiation, which is applicable in the case of functions with "bad" behavior at infinity. Fractional derivatives of Marshaud were introduced into use. In the works of M. Riess (1936, 1938, 1949), operators of the type of potential (Riess potentials) were obtained, which made it possible to determine the fractional

integration of functions of several variables. For some integral operators and integral equations, fractional integrals of Erdelyi and Kober (1940), etc., turned out to be very useful.

Especially for radio physicists and radio engineers, we note the fact that the operational calculus developed by O. Heaviside (1892, 1893, 1920) turned out to be an important stage in the application of generalized derivatives. It was O. Heaviside (1920) who applied fractional differentiation in the theory of transmission lines. After that, other theorists recognized the advantages of this approach and began to develop it in accordance with the accepted mathematical concepts (N. Wiener, J. Carson (1926)).

Abel's equation. The notion of fractional integration is closely related to the Abel integral equation

$$\frac{1}{\Gamma(\alpha)}\int_a^x \frac{\phi(t)}{(x-t)^{1-\alpha}}dt = f(x),\ x > a, \tag{25}$$

where $0 < \alpha < 1$; $\Gamma(\alpha)$ is a gamma function. The solution to equation (25) has the form

$$\varphi(x) = \frac{1}{\Gamma(1-\alpha)}\frac{d}{dx}\int_a^x \frac{f(t)}{(x-t)^{\alpha}}dt. \tag{26}$$

For the Abel equation of the form

$$\frac{1}{\Gamma(\alpha)}\int_x^b \frac{\varphi(t)}{(x-t)^{1-\alpha}}dt = f(x),\ x < b, \tag{27}$$

there is a treatment formula

$$\varphi(x) = \frac{1}{\Gamma(1-\alpha)}\frac{d}{dx}\int_x^b \frac{f(t)}{(x-t)^{\alpha}}dt. \tag{28}$$

Using the method of mathematical induction, we prove a formula for an *n*-fold integral of the form

$$\int_a^x dx\int_a^x dx ... \int_a^x \varphi(x)dx = \frac{1}{(n-1)!}\int_a^x (x-t)^{n-1}\varphi(t)dt. \tag{29}$$

Noticing that $(n-1)! = \Gamma(n)$, the right-hand side of (29) can be given a meaning even for noninteger values of *n*.

Fractional Riemann-Liouville and Marshaud operators. Fractional Riemann-Liouville integrals of fractional order ($\alpha > 0$) are

$$(I_{a+}^{\alpha}\varphi)(x) = \frac{1}{\Gamma(\alpha)}\int_a^x \frac{\varphi(t)}{(x-t)^{1-\alpha}}dt,\ x > a, \tag{30}$$

$$\int_a^b \varphi(x)(I_{a+}^{\alpha}\psi)(x) = \int_a^b \psi(x)(I_{b-}^{\alpha}\varphi)(x)dx,\ x < b, \tag{31}$$

The first of them is sometimes called left-sided, and the second – right-sided. Most often they deal with left-hand fractional integration. The operator I_{a+}^{α} in the English-language literature is denoted in the form ${}_aD_x^{\alpha}$ when the sign of α is replaced in (30) by the opposite one, i.e. for $\alpha < 0$.

The fractional integration by parts formula has the form

$$\int_a^b \varphi(x)(I_{a+}^{\alpha}\psi)(x) = \int_a^b \psi(x)(I_{b-}^{\alpha}\varphi)(x)dx. \tag{32}$$

Fractional integration has the semigroup property:

$$I_{a+}^{\alpha}I_{a+}^{\beta}\varphi = I_{a+}^{\alpha+\beta}\varphi,\quad I_{b+}^{\alpha}I_{b+}^{\beta}\varphi = I_{b+}^{\alpha+\beta}\varphi,\ \alpha > 0, \beta > 0. \tag{33}$$

Fractional differentiation is naturally introduced as an operation inverse to fractional integration. Therefore, the fractional derivative is established using fractional integration and further – ordinary differentiation. Therefore, the fractional Riemann-Liouville derivatives of order α for $0 < \alpha < 1$ have the form

$$(D_{a+}^{\alpha}f)(x) = \frac{1}{\Gamma(1-\alpha)}\frac{d}{dx}\int_a^x \frac{f(t)dt}{(x-t)^{\alpha}}, \tag{34}$$

$$(D_{b-}^{\alpha}f)(x) = -\frac{1}{\Gamma(1-\alpha)}\frac{d}{dx}\int_x^b \frac{f(t)dt}{(t-x)^{\alpha}}. \tag{35}$$

This definition shows that fractional differentiation is non-local. If fractional integrals are defined for any order ($\alpha > 0$), then fractional derivatives are so far only for order ($0 < \alpha < 1$). For large orders ($\alpha \geq 1$) with their integer – $[\alpha]$ and fractional – $\{\alpha\}$ ($0 \leq \{\alpha\} < 1$) parts of the number $\alpha = [\alpha] + \{\alpha\}$ we have

$$D_{a+}^{\alpha}f = \frac{1}{\Gamma(n-\alpha)}\left(\frac{d}{dx}\right)^n \int_a^x \frac{f(t)dt}{(x-t)^{\alpha-n+1}},\ n = [\alpha]+1, \tag{36}$$

$$D^{\alpha}_{b-}f=-\frac{(-1)^n}{\Gamma(n-\alpha)}\left(\frac{d}{dx}\right)^n\int_x^b\frac{f(t)dt}{(t-x)^{\alpha-n+1}},\ n=[\alpha]+1. \quad (37)$$

If α is an integer, then the fractional derivative of order α is understood as the usual differentiation

$$D^{\alpha}_{a+}=\left(\frac{d}{dx}\right)^{\alpha},\ D^{\alpha}_{b-}=\left(-\frac{d}{dx}\right)^{\alpha},\ \alpha=1,2,3,... \quad (38)$$

Sometimes they also use notation $D^{\alpha}_{a+}f=I^{-\alpha}_{a+}f=(I^{\alpha}_{a+})^{-1}f,\ \alpha>0,$ meaning by each of them the derivative (34) and (36). Symbols $D^{\alpha}_{b-}f=I^{-\alpha}_{b-}f$ are understood in a similar way.

As an example, consider the power functions $\varphi(x)=(x-a)^{\beta-1}$ and $\varphi(x)=(b-x)^{\beta-1}$, Reβ > 0. For them, the fractional integrals are, respectively,

$$I^{\alpha}_{a+}\varphi=\frac{\Gamma(\beta)}{\Gamma(\alpha+\beta)}(x-a)^{\alpha+\beta-1};\ I^{\alpha}_{b-}\varphi=\frac{\Gamma(\beta)}{\Gamma(\alpha+\beta)}(b-x)^{\alpha+\beta-1}. \quad (39)$$

Fractional integrals (30) and (31) easily extend from the finite segment [*a, b*] to the semiaxis (*a*, ∞) or (–∞, *b*). For the general case, when $-\infty<x<\infty$, the fractional integrals along the whole line have the form

$$(I^{\alpha}_{+}\varphi)(x)=\frac{1}{\Gamma(\alpha)}\int_{-\infty}^{x}\frac{\varphi(t)}{(x-t)^{1-\alpha}}dt;\ (I^{\alpha}_{-}\phi)(x)=\frac{1}{\Gamma(\alpha)}\int_{x}^{\infty}\frac{\varphi(t)}{(t-x)^{1-\alpha}}dt. \quad (40)$$

Similarly to (34) and (35), the Liouville derivatives are introduced

$$(D^{\alpha}_{+}f)(x)=\frac{1}{\Gamma(1-\alpha)}\frac{d}{dx}\int_{-\infty}^{x}\frac{f(t)dt}{(x-t)^{\alpha}}, \quad (41)$$

$$(D^{\alpha}_{-}f)(x)=-\frac{1}{\Gamma(1-\alpha)}\frac{d}{dx}\int_{x}^{\infty}\frac{f(t)dt}{(x-t)^{\alpha}}, \quad (42)$$

where $0<\alpha<1$ and $-\infty<x<\infty$. For $\alpha\geq 1$ with $n=[\alpha]+1$ we have

$$(D^{\alpha}_{\pm}f)(x)=\frac{(\pm1)}{\Gamma(n-\alpha)}\frac{d^n}{dx^n}\int_0^{\infty}t^{n-\alpha-1}f(x\mp t)dt. \quad (43)$$

Fractional Liouville derivatives on the axis can be reduced to a more convenient form than (41) and (42). The resulting constructions are called fractional derivatives of Marshaud:

$$(D^{\alpha}_{+}f)(x)=\frac{\alpha}{\Gamma(1-\alpha)}\int_0^{\infty}\frac{f(x)-f(x-t)}{t^{1+\alpha}}dt=$$
$$=\frac{\alpha}{\Gamma(1-\alpha)}\int_{-\infty}^{x}\frac{f(x)-f(t)}{(x-t)^{1+\alpha}}dt, \quad (44)$$

$$(D^{\alpha}_{-}f)(x)=\frac{\alpha}{\Gamma(1-\alpha)}\int_0^{\infty}\frac{f(x)-f(x+t)}{t^{1+\alpha}}dt, \quad (45)$$

where $0<\alpha<1$ and $-\infty<x<\infty$.

In the theory of fractional integrodifferentiation of functions of several variables, which is a fractional power $(-\Delta)^{\alpha/2}$ of the Laplace operator, fractional Riess integrodifferentiation is widely used. In Fourier images $\hat{F}$, this operation is written in the form

$$(-\Delta)^{\alpha/2}f=\hat{F}^{-1}|x|^{-\alpha}\hat{F}f=\begin{cases}I^{\alpha}f,\ \mathrm{Re}\,\alpha>0,\\ D^{-\alpha}f,\ \mathrm{Re}\,\alpha<0.\end{cases} \quad (46)$$

A detailed exposition of the theory of Riess differentiation is given in [131]. As follows from the convolution theorem for functions, the fractional-order integral $(I^{\alpha}_{0+}f)(x)$, $\mathrm{Re}\ \alpha>0$ is a Laplace convolution of the form

$$(I^{\alpha}_{0+}f)(x)=\left[f(x)\frac{x_+^{\alpha-1}}{\Gamma(\alpha)}\right],\ \mathrm{Re}\ \alpha>0, \quad (47)$$

as a consequence of which the property of the joint action of the Laplace transform and the operator of fractional integration takes place

$$(LI^{\alpha}_{0+})(p)=p^{-\alpha}(Lf)(p). \quad (48)$$

Generalized Leibniz rule. Let us formulate the generalized Leibniz rule:

$$D^{\alpha}_{a+}(fg)=\sum_{k=0}^{\infty}\binom{\alpha}{k}(D^{\alpha-k}_{a+}f)g^{(k)},\alpha\in R^1, \quad (49)$$

$$D^{\alpha}_{a+}(fg)=\sum_{k=-\infty}^{\infty}\binom{\alpha}{k+\beta}(D^{\alpha-\beta-k}_{a+}f)(D^{\beta+k}_{a+}g), \quad (50)$$

where

$$\binom{\alpha}{\beta}=\frac{\Gamma(\alpha+1)}{\Gamma(\beta+1)\Gamma(\alpha-\beta+1)}=\frac{\sin[(\beta-\alpha)\pi]}{\pi}\frac{\Gamma(\alpha+1)\Gamma(\beta-\alpha)}{\Gamma(\beta+1)}$$

is the generalized binomial coefficient;

$\alpha,\beta\in R^1,\ R^1=(-\infty,\infty)$; with non-integer β.

Along with the last formulas, we have the Leibniz formula with remainder

$$D^{\alpha}_{a+}(uv)=\sum_{k=0}^{n-1}\binom{\alpha}{k}D^{\alpha-k}_{a+}uv^{(k)}+R_n, \quad (51)$$

$$R_n=\frac{(-1)^n}{\Gamma(-\alpha)(n-1)!}\int_a^x(x-t)^{-\alpha-1}u(t)dt\int_t^x(x-\xi)^{n-1}v^{(n)}(\xi)d\xi, \quad (52)$$

which does not require the function v(*x*) to be infinitely differentiable.

Results. The operator of integro-differentiation in the sense of the Riemann-Liouville fractional order $\alpha \in R$ with origin at the point α is defined as follows [83]:

$$ {}_{RL}D_{at}^{\alpha} f(t) = \frac{sign(t-a)}{\tilde{A}(-\alpha)} \int_a^t \frac{f(\tau)}{|t-\tau|^{\alpha+1}} d\tau, \ \alpha<0, \quad (53) $$

$$ {}_{RL}D_{at}^{\alpha} = f(t) = f(t), \ \alpha = 0, \quad (54) $$

$$ {}_{RL}D_{at}^{\alpha} = sign^n(t-a) \frac{d^n}{dt^n} D_{at}^{\alpha-n} f(t) = $$

$$ = \frac{1}{\tilde{A}(n-\alpha)} \frac{d^n}{dt^n} \int_a^t (t-\tau)^{n-\alpha-1} f(\tau) d\tau, \quad (55) $$

$$ n-1 < \alpha \le n, \ n \in N. $$

For functions differentiable on the interval [*a, b*], the definition of fractional derivatives in the sense of Riemann-Liouville and A.V. Letnikov are equivalent [86,136].

Currently, *Caputo's formulation* is widely used [12,103,104]:

$$ {}_{C}D_{at}^{\alpha} f(t) = sign^n(t-a) \, {}_{RL}D_{at}^{\alpha-n} f^{(n)}(t), \quad (56) $$

$$ n-1 < \alpha \le n, \ n \in N. $$

The Riemann-Liouville and Caputo derivatives are related by the ratio:

$$ {}_{C}D_{at}^{\alpha} f(t) = {}_{RL}D_{at}^{\alpha} f(t) - \sum_{k=0}^{n-1} \frac{f^{(k)}(\tau)}{\tilde{A}(k-\alpha+1)} |\tau - t|^{k-\alpha}, \quad (57) $$

$$ n-1 < \alpha \le n, \quad n \in N. $$

In the case $\alpha = n$ we get:

$$ {}_{RL}D_{at}^{n} f(t) = {}_{C}D_{at}^{n} f(t) = sign^n(t-a) \frac{d^n}{dt^n} f(t), \ n \in N. \quad (58) $$

The Caputo derivative has the same physical interpretation as the Riemann-Liouville derivative. In particular, for $f(0) = 0$ and $0 < \alpha < 1$, we have the exact equality:

$$ {}_{C}D_{0t}^{\alpha} f(t) = {}_{RL}D_{0t}^{\alpha} f(t). \quad (59) $$

When comparing these derivatives, it is necessary to pay attention to the fact that to calculate the Riemann-Liouville derivative it is necessary to know the values of the function, and for the Caputo derivative – its derivatives, which is much more complicated. Some advantage of the Caputo derivative is that it is equal to zero for a constant function, which is more familiar to a researcher.

Note that in [32] a biography is presented and the surviving works of the Soviet mechanic Alexei Nikiforovich Gerasimov (03.24.1897–03.14.1968) are presented, 20 years earlier than Caputo, who proposed the use of the fractional derivative for viscoelasticity problems (i.e., the Gerasimov-Caputo derivative).

In [112], a new fractional operator is introduced that defines the *local fractional Kolvankar derivative* using the following limit:

$$ D^q f(y) = \lim_{x \to y} \frac{d^q (f(x) - f(y))}{d(x-y)^q}, \quad (60) $$

if this limit exists.

The use of this operator allows the derivative to return the locality property, which is lost when passing from integers to fractional values of the orders of differentiation. Thus, a direct connection is established between the properties of local fractional differentiability and the fractal dimension of nondifferentiable functions, which is illustrated in [112] using the example of the classical nondifferentiable Weierstrass function and Levy flights/motions.

2.5. Fox function

For integral transformations in diffusion processes in fractal space and using fractional operators, the Fox *H*-function H_{pq}^{mn} is widely used, where $0 \le m \le q$, $0 \le n \le p$ [116]. The importance of the Fox function is that it includes almost all the special functions that go into applied mathematics and statistics as its special cases. Even functions such as the Wright generalization of the Bessel function, the Meyer *G*-function, or the generalized Maitland hypergeometric function are covered by the Fox class of functions. In addition, a connection has been established between stable laws and Fox functions: the analytical form of a stable law is given through the Fox function [118].

The Fox function is defined as

$$H_{pq}^{mn}\left(z\left|\begin{matrix}(a_1,\alpha_1),...,(a_p,\alpha_p)\\(b_1,\beta_1),...,(b_q,\beta_q)\end{matrix}\right.\right)=\frac{1}{2\pi i}\int_C h(s)z^s ds, \quad (61)$$

$$h(s)=\frac{\prod_{j=1}^{m}\Gamma(b_j-\beta_j s)\prod_{i=1}^{n}(1-a_i+\alpha_i s)}{\prod_{j=m+1}^{q}\Gamma(1-b_j+\beta_j s)\prod_{i=n+1}^{p}\Gamma(a_i-\alpha_i s)}, \quad (62)$$

where $\Gamma(s)$ is the gamma function; parameters α_i (i = 0, 1,…, p) and β_j (j = 0, 1,…, q) are positive numbers; a_j and b_j are complex numbers satisfying the condition $\alpha_i(b_h + \delta) \neq \beta_h(a_i - 1 - \lambda)$; δ and λ = 0, 1,…; h = 1, ..., m; i = 1,…, n.

The contour of integration C in the complex s-plane passes so that the poles of $\Gamma(b_j - \beta_{jS})$ (j = 0, 1, ..., m) are on the right, and the poles $(1 - a_i + a_{iS})$ (i = 1, ... , n) – to the left of the contour.

The Laplace transform of the Fox function is also a Fox function, but with different indices:

$$\tilde{H}(p)=\frac{1}{p}H_{q,p+1}^{n+1,m}\left(p\left|\begin{matrix}(1-b_j,\beta_j)\\(1,1),(1-a_i,\alpha_i)\end{matrix}\right.\right),\ 0\le\mu\le 1, \quad (63)$$

$$\tilde{H}(p)=\frac{1}{p}H_{p+1,q}^{m,n+1}\left(\frac{1}{p}\left|\begin{matrix}(0,1),(a_i,\alpha_i)\\(b_j,\beta_j)\end{matrix}\right.\right),\ \mu\ge 1. \quad (64)$$

For the inverse Laplace transform, we have

$$\tilde{H}(t)=\frac{1}{t}H_{q,p+1}^{n,m}\left(t\left|\begin{matrix}(1-b_j,\beta_j)\\(1-a_i,\alpha_i)(1,1)\end{matrix}\right.\right),\ 0\le\mu\le 1, \quad (65)$$

$$\tilde{H}(t)=\frac{1}{t}H_{p+1,q}^{m,n}\left(\frac{1}{t}\left|\begin{matrix}(a_i,\alpha_i)(1,1)\\(b_j,\beta_j)\end{matrix}\right.\right),\ \mu\ge 1. \quad (66)$$

The function $H(z)$ is an analytic function of z under the following conditions: $z \neq 0$ for $\mu > 0$ and $|z| < \beta^{-1}$ for $\mu = 0$, where

$$\mu=\sum_{j=1}^{q}\beta_j-\sum_{i=1}^{p}\alpha_i,\ \beta=\prod_{i=1}^{p}\alpha_i^{\alpha_i}\prod_{j=1}^{q}\beta_j^{\beta_j}. \quad (67)$$

The asymptotic expansion of the Fox functions is given by the expression

$$H_{p,q}^{m,n}(z)-\sum res[h(s)z^s], \quad (68)$$

valid for $\mu > 0$ and $n \neq 0$ for $|z| \to \infty$ on each closed sector $|\arg z| \le \pi\lambda/2$. In this case, the residues must be determined at the points $s = (a_i - 1 - v)/\alpha_i$; i = 1, ..., n; v = 0, 1, ...

2.6. Historical overview of undifferentiated functions

In his letter dated January 15, 1898 to F. Klein, L. Boltzmann specially noted that "*in Nature there are such physical problems (statistical mechanics), for the solution of which nondifferentiable functions are absolutely necessary, and if K. Weierstrass had not invented such functions , then physicists simply would have had no choice but to invent them themselves* ". At present, such undifferentiable curves are usually called *fractal* or simply *fractals*. Here is a brief historical overview of such mathematical objects, based on the sources [26,27,58,106,110].

It is also noteworthy that the *concept of self-similarity* entered mathematics from two independent directions (through Cantor sets and Weierstrass functions) at approximately the same time for the basic concepts of mathematics: numbers and functions. Recall that G.V. Leibniz in his treatise "Monadology", written in 1714, used the concept of *self-similarity* ("worlds within worlds"), and also applied it in the definition of the straight line.

After the discovery of differential calculus, it was intuitively formed that each function can be differentiated any number of times. In 1806, Ampere made an attempt to theoretically justify this belief on a purely analytical basis within the framework of the mathematical concepts of Lagrange. Later, some mathematicians automatically transferred Ampere's statements to functions that are continuous in the present sense, while others, considering it the foundation of the whole differential calculus, presented their proofs of this statement and used it to establish other results. Among them are Lacroix (1810), Galois (1831), Raabe (1839), Duhamel (1847), Lamarlet (1855), Freycinet (1860), Bertrand (1864) , Serre and Rubini (1868).

However, the time of the faith of mathematicians about the inextricable connection between the continuity of functions and its differentiability was running out. In 1830, B. Bolzano, in his manuscript

"The Doctrine of Function", constructs the first example of a continuous, nowhere, undifferentiable function. This Bolzano manuscript was discovered only after the First World War around 1920 in the Vienna State Library. Only a hundred years later, his work appeared in print. In 1834-35 the concepts of differentiability and continuity are clearly distinguished by N.I. Lobachevsky. In 1854 Dirichlet notes that in the general case it is impossible to prove the existence of a derivative for an arbitrary continuous function, and expresses his conviction in the existence of a continuous function without a derivative.

In 1861 Riemann gave an example of the function

$$f(x)=\sum_{n=1}^{\infty}\frac{\sin n^2x}{n^2}, \qquad (69)$$

which Dubois Reymond claimed to be nondifferentiable on an everywhere dense set.

How difficult the analysis of example (69) turned out to be is evidenced not only by Weierstrass' refusal to carry it out, but also by the fact that before 1916 there was no proof or refutation of the Riemann example. Only in 1916, Hardy, relying on some subtle results of Diophantine analysis, was able to show that (69) has no finite derivative at any point ξπ, where ξ is an irrational or rational number of the form $2m/(4n + 1)$ or $(2m + 1)/2(2n + 1)$, and m and n are integers; he then generalized somewhat the example of Riemann.

Gerwer expanded this result in 1969 by showing that this function has no finite derivative at the points ξπ, where ξ is a rational number of the form $(2m + 1)/2^n$, and m, n are integers and $n \geq 1$. He established the existence of a derivative, equal to $-1/2$ at the points ξπ when ξ is a rational number with an odd denominator and numerator, so that the Riemann function is differentiable on an infinite set of points. In the next paper, Gerver showed that the Riemann function has no other points of differentiability besides those indicated above.

Until 1870, apart from the Riemann function mentioned above, not a single example of a continuous function having no derivative at an infinite set of points was published. According to Guel, who reviewed Hankel's memoir on such functions, "*today there is not a single mathematician who would believe in the existence of continuous functions without derivatives.*" In 1870, Hankel proposed a method for *condensing singularities,* which consists in constructing a function using an absolutely convergent series, each term of which has a singular point. This is how he obtained examples of continuous functions that have no derivative on an everywhere dense set of rational points. One such example is a function of the form

$$f(x)=\sum_{n=1}^{\infty}\frac{1}{n^s}\sin(\pi nx)\sin\left(\frac{1}{\sin(\pi nx)}\right), \qquad (70)$$

where n is a natural number, $s > 1$.

In 1873, Schwartz constructed another example of a monotone continuous function with no derivative on an everywhere dense set of points:

$$f(x)=\sum_{n=1}^{\infty}\frac{\varphi(2^n x)}{4^n}, \qquad (71)$$

where $\varphi(x)=[x]-\sqrt{x-[x]}$, $x>0$, $[x]$ is the integer part of x.

Schwarz considered this function to be nondifferentiable, but, as it turned out later, it has a finite derivative almost everywhere.

Later, Weierstrass built, as is commonly believed in 1861, his famous function

$$f(x)\equiv W(x)=\sum_{n=1}^{\infty}a^n\cos(b^n\pi x). \qquad (72)$$

Here $0 < a < 1$, $b > 1$ is an odd integer, $ab > 1 + 3\pi/2$. Weierstrass reported to the Berlin Academy of Sciences on July 18, 1872, and the example itself was published only in 1875 by Dubois-Reymond. Therefore, as noted in [115], "*the year 1875 is nothing more than a convenient symbolic date to indicate the beginning of the Great Crisis of Mathematics.*"

In the preface to his book, S. Sachs wrote: "*Studies dealing with non-analytical functions and functions that violate those laws that were assumed to be universal, these studies were viewed almost as the spread of chaos and anarchy where previous generations sought order and harmony.*" [85]. S. Hermite wrote to T. Stiltjes in 1893: "*With horror and disgust I turn away from this growing ulcer of functions that have no derivative.*" Even at the beginning of the XX century. G. Bussensk was not alone in the opinion that "*the whole interest of a function lies in the possession of its derivative,*" meaning the ordinary derivative.

Independently of Weierstrass, Darboux came to the same idea, who generalized the examples of Hankel and Schwarz and constructed the function

$$f(x)=\sum_{n=1}^{\infty}\frac{\sin\left[(n+1)!x\right]}{n!}, \qquad (73)$$

which has no derivative for any x. Darboux reported his results at a meeting of the French Mathematical Society on March 19, 1873 and January 28, 1874, i.e. before the publication of Dubois-Reymond's publication. Some details of the priority pick between Weierstrass and Darboux were published in 1973 (*Dugac P.* Elements d 'analyze de Karl Weierstrass // Archive for Hist. Exact. Sci. 1973. V. 10. P. 41-176).

2.7. Dini's theorem on functions without derivatives and the continuation of the survey

The above studies served as the basis for constructing classes of nondifferentiable functions and searching for general conditions for the differentiability of continuous functions. The greatest contribution to this direction was made by the Italian mathematician W. Dini, who came close to Lebesgue's theorem on the derivative of a continuous monotone function. It was he who formulated in 1877, and in 1878 proved a sufficiently general theorem on the existence of continuous functions without derivatives (the statement of Dini's theorem is given by us according to [26]).

Theorem 1. (Dini, 1877). *Let $f_n(x)$ functions be given on $0 \le x \le 1$ satisfying the following conditions:*

1) all functions $f_n(x)$ are continuous and have bounded derivatives;

2) the series $\sum_{n=1}^{\infty} f_n(x)$ converges on [0, 1] *to a continuous function f(x);*

3) each of $f_n(x)$ has a finite number of extrema, and their number increases indefinitely with n and, moreover, in such a way that for any $\varepsilon > 0$ one can find n_0 such that for $n > n_0$ the distances between the extremum points will be less than ε;

4) if δ_n is the largest distance between two successive extrema, and D_n is the largest difference in absolute value between two successive extreme values, then $\lim_{n\to\infty}(\delta_n / D_n) = 0$;

5) if we denote by h_n for each x those two increments (one of which is positive and the other negative) for which $x + h_n$ gives the first right (respectively, left) extremum, for which $|f_n(x+h_n) - f_n(x)| \ge \frac{1}{2}D_n$, it is possible to specify such positive numbers r_n that for all $x \in [0,1]$ and such h_n corresponding to each x we have $\left|R_n(x+h_n) - R_n(x)\right| \le 2r_n$, where $R_n(x)$ is the remainder of the series $\sum_{n=1}^{\infty} f_n(x)$ from item 2;

6) if c_n is a sequence of positive numbers such $|u_n'(x)| < c_n$ that for all $x \in [0,1]$, then starting from some index $\frac{4\delta_n}{D_n}\sum_{\nu=1}^{n} c_\nu + \frac{4r_n}{D_n} \le \theta, \quad 0 \le \theta < 1$;

7) the sign of the difference $f_n(x+h_n) - f_n(x)$, starting from some n_0, does not depend on h_n for all x and $n > n_0$.

Then the function f(x), defined by the series $\sum_{n=1}^{\infty} f_n(x)$ from item 2, will not have a finite derivative at any point. It can have an infinite derivative on an infinite set of points $x \in [0,1]$.

Then Dini showed that under some additional assumptions such a function $f(x)$ will not have an infinite derivative at any point. It can be noted that the class of functions satisfying Dini's theorem is infinite; in particular, it contains the Weierstrass function.

In 1879, Darboux proposed a fairly general method for constructing nondifferentiable

functions. He studied the functions $\varphi(x)$ defined by the series

$$\varphi(x)=\sum_{n=1}^{\infty}\frac{f(a_n b_n x)}{a_n}, \quad (74)$$

where a_n and b_n are some sequences of real numbers, $f(x)$ is a continuous bounded function with a bounded second derivative.

If the sequences $\{a_n\}$ and $\{b_n\}$ are chosen so that for fixing k we have

$$\lim_{n\to\infty}\frac{a_n}{a_{n+1}}=0,\ \lim_{n\to\infty}\frac{a_1 b_1^2+a_2 b_2^2+\ldots+a_{n-k}b_{n-k}^2}{a_n}=0, \quad (75)$$

then series (74) converges everywhere to some continuous function $\varphi(x)$. With further restrictions on the choice of $\{a_n\}$, $\{b_n\}$, k, and $f(x)$, one can obtain continuous functions that have no derivative at any point. So, if $b_n = 1$, $k = 1$, then on the numbers a_n it is sufficient to impose the condition $\lim_{n\to\infty}\frac{a_1+a_2+\ldots+a_{n-1}}{a_n}=0$, which is satisfied, for example, the numbers $a_n = n!$, so that one can indicate an infinite set of functions $f(x)$ for which (74) would be just such a function.

Let $f(x) = \cos x$, then $\varphi(x)$ is nowhere differentiable. Choosing $b_n = n + 1$, $k = 3$ and $f(x) = \sin x$, we obtain the function $\varphi(x)$ from Darboux's previous work. In 1918 a method for constructing continuous nondifferentiable functions was indicated by *K.* Knopp. We can say that after the above-mentioned works, a whole industry was created for the production of both individual functions and their entire classes.

Note that the example of the Weierstrass function is based on the properties of the lacunary series, i.e. such a series in which nonzero terms are "very sparse and scattered." The concept of a lacunary trigonometric series was introduced by J. Hadamard in 1892 in the study of functions that cannot be analytically extended beyond the boundary of the circle of convergence. A lacunar (in the sense of Hadamard) *trigonometric series* is a series of the form

$$\frac{a_0}{2}+\sum_{k=1}^{\infty}a_k\cos n_k x+b_k\sin n_k x, \quad (76)$$

for $\frac{n_{k+1}}{n_k}\geq q>1.$. Thus, the numbers n_k of the lacunary series (76) for all k grow no slower than a geometric progression with a denominator greater than one. In 1916, J. Hardy also proved that the Weierstrass function $W(x)$ has no finite derivative at any point, provided $a < 1$, $b > 1$ and $ab \geq 1$.

2.8. Many nondifferentiable functions

Let us briefly consider the question of the place occupied by differentiable functions in the set of all continuous functions. A set X of a topological space M is *a set of the first category* on M if it is the union of a countable family of sets that are nowhere dense on M. *Sets of the second category* are defined as sets that are not sets of the first category. These definitions were formulated in 1899 by Baer [11].

By Baire's theorem, the complement of any set of the first category on the line is dense. No interval on the set of real numbers $\mathbb{R}$ is a set of the first category. Each countable set will be a set of the first category and a set of measure zero. In the set of real numbers, rational numbers form a set of the first category. The simplest example of an uncountable set belonging to a set of the first category and a set of measure zero is the Cantor set, which has the cardinality of the continuum. It can be proved that the line can be split into two complementary sets A and B so that A is a set of the first category, and B has measure zero. In many problems of topology and theory of functions, *sets of the first category play a role analogous to the role of sets of measure zero in measure theory* (sets that can be "neglected").

At present, sets of the second category are defined according to Baire, and the complement to a set of the first category is called *a residual set*. When proving existence theorems in set theory, the *method of categories* is often used, which is based on Baire's theorem, according to which every complete metric space is a set of the second category in itself. Based on this, it is proved

Theorem 2 (Banach, S. Mazurkevich; 1931). *Let C be the space of continuous functions x with period*

1, endowed with the norm $\|x\| = \max|x(t)|,\ 0 \le t \le 1$. *Let T be the set of functions from C that do not have a finite right derivative at any point* $t \in [0,1]$. *Then T is a set of the second Baire category on C, and its complement is a set of the first category.*

Consequently, the set of functions that have a finite one-sided derivative at least at one point $t \in [0,1]$ is negligible in the sense of the Baire category in comparison with the set of all continuous functions. This is all the more true for functions with a finite ordinary derivative.

Classes of continuous functions without derivatives considered in the 19th century. and in the first two decades of the XX century, did not give an example of such a singular continuous function, in which a finite or infinite one-sided (left or right) derivative did not exist at any point (the Weierstrass function (72), for example, has a one-sided derivative everywhere dense set). The first example of such a strongly nondifferentiable function was constructed in 1922 (published in 1924) by A.S. Besicovich.

In this regard, Banach and Steinhaus raised the question of extending, using the method of categories, the result of S. Mazurkiewicz and Banach to functions of Besicovitch type: is it possible to show that the complement of the set of all continuous functions that have neither finite nor infinite derivative at any point , is the set of the first category?

In 1932 Sachs gave a negative answer to this question. He showed that the set of continuous functions on [0, 1], which either have a finite right derivative, or this derivative is equal on the set of cardinality to the continuum, is a set of the second category in the space of all continuous functions. Thus, *the class of functions that are one-sided differentiable at least at one point, in the sense of categories, is substantially broader than the class of functions that have an ordinary derivative at least at one point.*

Accordingly, the class of functions that have neither a finite nor an infinite one-sided derivative at every point of the domain is narrower in the same sense of the class of functions that nowhere have a two-sided derivative. According to Sachs, "*This may explain the difficulty in finding the first example of a function that does not have a finite or infinite one-way derivative at every point.*" At the same time, Sachs' result indicated an essential difference between the operators of one-sided and two-sided differentiation.

In order to expand the known classes of nondifferentiable functions, V. Orlicz in 1947 found sufficiently general conditions *under which continuous functions that are sums of uniformly converging series are nowhere differentiable.* However, the generality of the results obtained was achieved due to the fact that the coefficients of these series were set ineffectively, using the method of categories. Orlich himself described this approach as "in a sense intermediate" between "effective" methods of specifying nondifferentiable functions in the form of series and the "ineffective" method of S. Mazurkevich-Banach.

2.9. Stationarity and nondifferentiable functions

Thus, *the class of continuous functions that have no derivative at any point is immeasurably richer than the class of functions with derivatives.* As aptly noted in [27, p. 222], "*A curious situation arose when it turned out that those continuous functions that have been studied by mathematicians for centuries, those that have been used to describe the phenomena of the external world, - these functions belong only to a negligible class of all continuous functions.*" Gradually, mathematicians got used to the fact that nowhere differentiable functions really exist, but physicists did not agree with this for a long time and perceived such functions as ugly products of mathematical fantasy that have no relation to the real world (they proceeded from the principle "in physics all functions are differentiable").

From the standpoint of modern science, *a function without a derivative is not at all an abstract concept, but the trajectory of a Brownian particle.* As noted in the 20s. XX century. N. Wiener: "*Within the framework of this theory, I was able to confirm*

Perrin's remark by showing that, with the exception of many cases with a total probability of zero, all trajectories of Brownian motion are continuous curves that are not differentiable anywhere."

It is essential that *in the spectral theory of stationary random processes*, nondifferentiable functions arise in a completely natural way and can be avoided only if the stationarity condition, which has a clear physical meaning, is abandoned, which only makes this theory simple and clear [98]. Let us briefly explain this fact.

In the spectral expansion of a stationary process $X(t)$, the use of the Stieltjes integral turns out to be inevitable, since the random function $Z(\omega)$ is not differentiable in any sense and therefore it is impossible to pass from the Fourier-Stieltjes integral

$$X(t) = \int_{-\infty}^{\infty} e^{i\omega t} dZ(\omega) \tag{77}$$

to the usual Fourier integral. In the case of the existence of the spectral density $f(\omega)$ always

$$\left\langle \left| dZ(\omega) \right|^2 \right\rangle = f(\omega) d\omega. \tag{78}$$

By virtue of (78), in all real physical cases, when the process $X(t)$ corresponds to a positive spectral density $f(\omega)$, the mean square of the increment $\Delta Z(\omega)$ of the function $Z(\omega)$ on a small segment $\Delta\omega$ of the frequency axis will be close to $f(\omega)\Delta\omega$, that is, has the same order of smallness as $\Delta\omega$. In this case, the value of $\Delta Z(\omega)$ itself is, as a rule, of order $(\Delta\omega)^{1/2}$, which is incompatible with the assumption that the function $\Delta Z(\omega)$ is differentiable, i.e. on the existence of a limit of the ratio $\Delta Z(\omega)/\Delta\omega$ as $\Delta\omega \to 0$.

As noted in [98, p. 113], "*we are faced here with a rather rare case when in a problem that has a real physical meaning, nowhere differentiable functions appear, which until quite recently were considered by many applied scientists to be an abstruse mathematical abstraction that cannot have any applications*".

In the arsenal of mathematics, there was also an analytical apparatus for describing such objects and processes. The place of the usual dimension was taken by *the Hausdorff dimension*, and the place of derivatives was taken by *the fractional derivative* or the *Hölder exponent*.

2.10. Examples of constructing some nondifferentiable functions

Here are some examples of constructing nondifferentiable functions [57,58,106,110,115].

Graphs of Riemann, Weierstrass and Takagi functions. Returning to the historical examples of the discovery of functions without derivatives, we note that specific examples of such functions sometimes lead to interesting conclusions. In 1903, the Japanese mathematician Takagi discovered a simple example of a nowhere differentiable function

$$T(x) = \sum_{n\geq 1} 2^{-n} \varphi(2^{n-1} x). \tag{79}$$

Here $\varphi(x) = 2\left|x - \left[x + (1/2)\right]\right|$, where $[x]$ is the operation of selecting the integer part of x. The function $T(x)$ is a typical example of "condensation of singularities", since it is a superposition of the so-called *sawtooth functions*. The functions of Riemann (69), Weierstrass (72), and Takagi (79) have peaks at a countable number of points (**Fig. 1**). It should be said that the graphs of such undifferentiated functions are described by an infinite number of infinitely small convolutions ("ripple waves"), but it is almost impossible to give a visual representation of them without distorting their essential features.

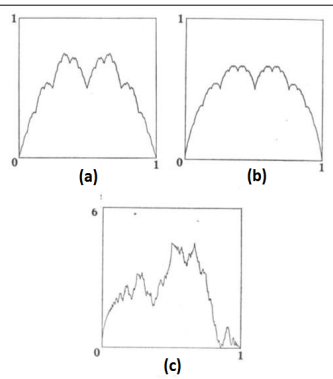

Fig. 1. *Graphs of undifferentiated functions: a - Weierstrass function (1 – W(x))/2 – for values b = a^{-1} = 2; b –Takagi function; c – Riemann function.*

E. Hobson also studied a number of

$$\sum_{n\geq 1} a^n \varphi(b^n x),\ 0<a<1, \tag{80}$$

and showed on the basis of Knopp's method that the conditions $ab > 4$ (when b is an even integer), or $ab > 1$ (when b is an odd integer) forbid the existence of a finite or infinite derivative. For $b = a^{-1} = 10$, this is an example given by Van der Waerden in 1930 (see below). De Ram also pointed out that if we take $b = a^{-1}$, considering b to be an even integer, then the series (80) will not have a finite derivative.

Construction of the Bolzano function. Now consider the construction of the Bolzano function $B(x)$. Let us define an auxiliary function $B_n(x)$. Consider the construction shown in **Fig. 2***a* and the fact that the segment AB is replaced by the broken line $ACDEB$ with the following coordinates of the points: $A[p, q]$, $C[p + (\delta/4, q - (\Delta/2)]$, $D[p + (2\delta/4), q)]$, $E[p + (3\delta/4), q + (\Delta/2)]$, $B[p + \delta, q + \Delta]$. Let the graph of the function $B_0(x)$ be the segment $A_{11}(0,0)$ and $A_{25}(1,1)$; let $A_{11}P = a$, $A_{25}P = h$ (Fig. 2*b*).

Replace $A_{11}A_{25}$ with a broken line $A_{11}A_{22}A_{23}A_{24}A_{25}$ according to the above rule. The coordinates of the characteristic points are: $A_{21} \equiv A_{11}(0,0)$, $A_{22}(1/4 - 1/2)$, $A_{23}(1/2.0)$, $A_{24}(3/4.1/2)$, $A_{25}(1.1)$, which determines the function $B_1(x)$ and its graph $A_{11}A_{22}A_{23}A_{24}A_{25}$. In Fig. 2*b* shows the graphs of the functions $B_0(x)$ and $B_1(x)$, respectively. By the function $B_1(x)$, as shown in Fig. 2*c*, we construct the function $B_2(x)$. In Fig. 2*d* shows the graphs of the functions

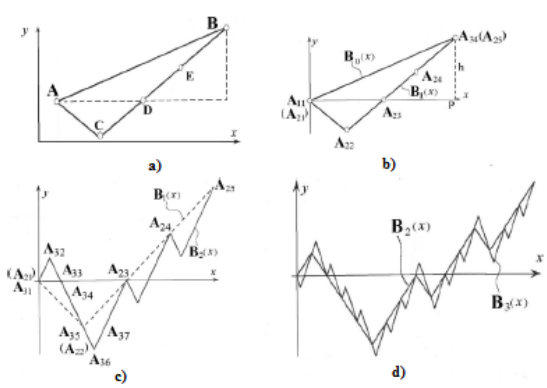

Fig. 2. *Construction of a non-differentiable Bolzano function: a) - the first construction, b) - functions $B_0(x)$ and $B_1(x)$, c) - functions $B_1(x)$ and $B_1(x)$, d) - functions $B_2(x)$ and $B_3(x)$.*

$B_2(x)$ and $B_3(x)$, respectively. Repeating this operation n times, we arrive at the function $B_n(x)$. Oscillation of the function $B_n(x)$ in each of the intervals

$$\left(\frac{s}{4^n}a,\ \frac{s+1}{4^n}a\right),\quad s = 0, 1, 2, ..., 4^n - 1,\ n = 0, 1, 2, 3, ... \tag{81}$$

will be $\omega_n\left(\frac{s}{4^n}a,\ \frac{s+1}{4^n}a\right) = \frac{h}{2^n}$. In the interval (0, a) for the oscillation $B_n(x)$, we can obtain $\omega_n(0, a) = h(2 - 2^{-n})$.

We now define the Bolzano function $B(x)$ at the points $x = ka/4^n$ for the coefficients $0 \leq k \leq 4^n$, k is an integer, $n = 0, 1, 2, 3, ...$, setting $B(x) = B_n(x)$. Then the oscillation $B(x)$ on the set of all considered points $x = ka/4^n$ belonging to one of the intervals (81) will be $\omega\left(\frac{s}{4^n}a,\ \frac{s+1}{4^n}a\right) = h/2^{n-1}$. For values of x different from $t = ka/4^n$, the Bolzano function is determined by the passage to the limit $B(x) = \lim_{t\to x} B(t)$. Oscillation in any interval of length $a/4^n$ satisfies the inequality $\omega\left(x, x + \frac{a}{4^n}\right) > h/2^n$. Thus, the Bolzano function $B(x)$ is defined on the entire interval (0, a) and is continuous on it.

Consider two more other algorithms for synthesizing the Bolzano function. Let each value

$$\frac{x}{a} = \frac{c_1}{4} + \frac{c_2}{4^2} + ... + \frac{c_k}{4^k} + ... \tag{82}$$

on the interval (0, a) corresponds to

$$\frac{B(x)}{h} = \frac{d_1}{2} + \frac{d_2}{2^2} + ... + \frac{d_k}{2^k} + ... \tag{83}$$

The numbers d_k are determined by the numbers c_k, according to the rule

$$\frac{c_k}{d_k}\ \frac{|0|}{|0|}\ \frac{1}{\mp 1}\ \frac{|2|}{|0|}\ \frac{3}{\pm 1}\ \frac{|}{|}. \tag{84}$$

Here it is necessary to take the lower signs if among the numbers c_{k-1}, c_{k-2}, ..., c_1 there is an odd number of them equal to zero, for example:

$$\begin{aligned} B\left[\left(1/4 + 2/4^2 + 1/4^4\right)a\right] &= \left(-1/2 + 1/2^4\right)h, \\ B\left[\left(1/4^2 + 1/4^4\right)a\right] &= \left(1/2^2 + 1/2^4\right)h. \end{aligned} \tag{85}$$

Relations (82)-(85) define the Bolzano function.

Consider the third algorithm for constructing the Bolzano function based on the properties of a certain series. Let us define on the segment A_1C of length a with the coordinates of the ends

0 (point A_1) and a (point C) the functions $b_0(x)$, $b_1(x)$, $b_2(x)$ by segment A_1A_5 and broken lines shown in **Fig. 3**.

Function $b_1(x)$ corresponds to a polyline with links formed by the lateral sides of a triangle with base a and height $3h/4$, function $b_2(x)$ is a polyline formed by the lateral sides of four triangles with base $a/4$ and height $3h/8$. Continuing this process, we arrive at the function

$$B_n(x) = \sum_{i=1}^{n} b_i(x). \quad (86)$$

The resulting series converges uniformly as $n \to \infty$, and its sum, equal to $B(x)$, gives us a function that is continuous on $(0, a)$ and has no derivative anywhere in this interval. The extrema of the Bolzano function $B(x)$ are observed at points with abscissas $a(s + 0.25)/4^{n-1}$ for $s = 0, 1, 2, ..., 4^{n-1} - 1$, $n = 1, 2, 3,$.. which (abscissas) form an everywhere dense set on the interval (0, a).

Construction of the Besicovitch function. Here are the stages of constructing *the Besicovitch function*. To do this, you need to build a stepped triangle. In **Fig. 4** shows the segment $AB = 2a$ and points $C(a, b)$ and $D(a, 0)$. On the segment AD we construct the segment $l_1 = a/4 = a/2^2$, placing it centrally. Then the segment AD is divided by the segment l_1 into two equal segments; on each of them we place centrally the segments $l_2 = l_3 = a/2^4$.

Segments l_1, l_2, l_3 divide segment AD into four equal segments; on each of them we place the central segments (counting from left to right) $l_4 = l_5 = l_6 = l_7 = a/2^6$, etc. Thus, on the segment AD, an infinite set of segments

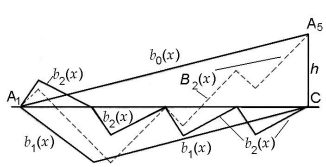

Fig. 3. *The third algorithm for constructing the Bolzano function.*

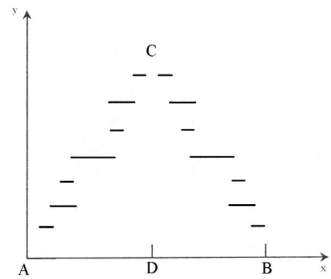

Fig. 4. *Construction of a non-differentiable Besicovitch function.*

l_1, l_2, l_3, ... will be constructed, the union of which L is an everywhere dense set with total length $a/2$. We construct a similar system of segments on the segment DB. Together we will call those and other segments the first series of segments.

We denote by $m(x)$ the Lebesgue measure of the set of points of the interval $(0, x)$ that do not belong to L, that is, measure of the set $\overline{L} \cap (0, x)$. On the segment AD, we define the function $\varphi(x)$ by setting

$$\varphi(x) = \frac{2b}{a} m(x). \quad (87)$$

It follows from (87) that the function $\varphi(x)$ has a constant value on any interval l_i. Thus, points A and C will be connected by some stepped curve; we connect points C and B with the same stepped curve. The resulting figure is called a stepped triangle with base $2a$ and height b.

On all segments of the first series, as on the bases, we construct stepped triangles with their vertices downward – equal on equal bases, choosing the heights so that the apex of the lowest of the equal triangles is on the side AB. The construction of all these triangles was named by A.S. Besicovitch operation of notching the triangle ABC inside. Having performed the same internal notching operation over the resulting infinite series of triangles (the first series), we obtain the second series of triangles. We also subject them to internal serration, etc.

Now we define the function $f(x)$ on the segment AB: **1**) at the points of the segment AB that do not belong to the first series of

segments, – the ordinates of the sides of the stepped triangle *ABC*; **2**) at the points of the segments of the first series that do not belong to the segments of the second series –by the ordinates of the sides of the triangles of the first series; **3**) at the points of the segments of the second series that do not belong to the segments of the third series – by the ordinates of the sides of the triangles of the second series, etc .; **4**) at the points belonging to the segments of all series (they constitute an ensemble of measure zero), according to the principle of continuity.

The Besicovitch function defined in this way is a singular continuous function that has neither right nor left derivative at any point.

Construction of the Van der Waerden function. Consider now the *van der Waerden function*. The idea behind this example is based on the fact that a sequence of integers converges only when all its members, starting with some one, coincide. Let $f_0(x)$ be a function equal to the distance from point x to the nearest integer point:

$$f_0(x)=\begin{cases}x, & 0\le x\le 1/2,\\ 1-x, & 1/2\le x\le 1,\end{cases} \tag{88}$$

where $f_0(x+1)=f_0(x)$ for any real x.

The function $f_0(x)$ is continuous on the entire numerical axis, periodic with a period of 1, linear on each segment $\left[\frac{s-1}{2};\frac{s}{2}\right]$, where s is an integer, and the slope of the graph $f_0(x)$ on each such segment ± 1. Next, we introduce a sequence of functions $f_n(n=0, 1, 2, ...)$:

$$f_n(x)=\frac{f_0(4^n x)}{4^n}. \tag{89}$$

For any natural n, the function $f_n(x)$ is continuous, periodic with a period of 4^{-n}, a maximum value of $4^{-n}/2$, linear on each segment $\left[\frac{s-1}{2\cdot 4^n};\frac{s}{2\cdot 4^n}\right]$, and the slope of its graph on each such segment is ± 1. Finally, we introduce the function

$$f(x)=\sum_{n=0}^{\infty} f_n(x)=\sum_{n=0}^{\infty}\frac{f_0(4^n x)}{4^n}. \tag{90}$$

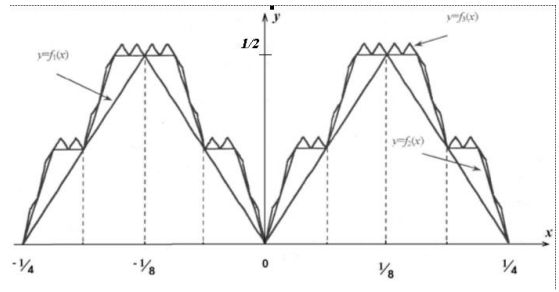

Fig. 5. *The first three partial sums in the case of constructing a non-differentiable Van der Waerden function.*

Since $0\le f_0(x)\le 4^{-n}$, then by the Weierstrass criterion the series defining $f(x)$ converges uniformly, and the continuity of all $f_n(x)$ implies the continuity of the function $f(x)$. In **Fig. 5** shows the graphs of the functions $f_1(x)$, $f_1(x)+f_2(x)$, $f_1(x)+f_2(x)+f_3(x)$. As the number of terms increases, the number of vertices at which the function $f(x)$ has no derivative increases indefinitely.

2.11. Nondifferentiable functions and functional equations

Let us briefly consider following [58,77,110] the following functional equation:

$$f(x)-af(bx)=g(x). \tag{91}$$

It was de Ram who noticed in 1957 that the Weierstrass function (72) and series (80) satisfy (91) in the case $g(x)=a\cos(b\pi x)$ and $g(x)=a\varphi(bx)$, respectively. The function $\varphi(x)$ is defined above in expression (80). If we put $g(x)=a\cos(b\pi x)$, then equation (91) will have a solution on the interval $(-\infty, +\infty)$, depending on an arbitrary function, and the only continuous solution is the Weierstrass function.

G. Faber, considering the function

$$\sum_{n\ge 1} 10^{-n}\varphi(2^{n!}x), \tag{92}$$

showed in 1907 that (92) does not correspond to the Lipschitz condition of any order. Then F. Cater in 1983 investigated the function

$$\sum_{n\ge 1} 2^{-n!}\cos(2^{(2n)!}x) \tag{93}$$

and proved that it has no cusps and has interesting extremal properties.

Consider the following functional equation:

$$\frac{1}{p}\left\{ f(\frac{x}{p})+f(\frac{x+1}{p})+...+f(\frac{x+p-1}{p})\right\}=\lambda f(\mu x). \quad (94)$$

This equation was investigated by E. Artin in 1964, characterizing its unique smooth solution by the Euler gamma function. The Japanese mathematician Hata in 1985, based on (94), solved the problem of finding the eigenvalue λ for a certain Parron-Frobenius operator and investigated various solutions (94) with respect to the eigenvalue. He also noted that if $b > 2$ is an integer, then the Weierstrass function $W(2x) + \cos(2\pi x)$ satisfies (94) for $p = b$, $\mu = 1$ and $\lambda = a$; the Takagi function $T(x) - 1/2$ also satisfies (94) for $p = 2$, $\mu = 1$, and $\lambda = 1/2$; and the Riemann function satisfies (94) for $p = 2$, $\mu = 2$, and $\lambda = 1/4$.

Using the concept of a lacunary series (see above), in 1984 (Kaplan et al.) Studied the series

$$f(x)=\sum_{n\geq 1} a^n r(b^n x),\ 0<a<1, \quad (95)$$

where $ab > 1$ and $r(x)$ is a quasiperiodic function.

Under certain restrictions on $r(x)$, series (95) is either continuously differentiable or, moreover, not differentiable anywhere. In the latter case, the dimension of the graph of function (95) satisfies the equality

$$D=2+\left[(\log a)/(\log b)\right]. \quad (96)$$

The graph of the function g will have a fractal dimension D greater than one when g is singular. In 1937 A.S. Besicovich showed that if $g(x)$ belongs to the class Lip(δ), $0 < \delta < 1$, then the function has a finite k-dimensional measure $k = 2 - \delta$; a function g was also constructed for which the k-dimensional measure is indeed positive for $1 \le k \le 2 - \delta$. At the same time, it was shown more generally that if $x(t)$ belongs to the class Lip(δ) and $y(t)$ belongs to the class Lip(δ'), where $\delta + \delta' > 1$, $0 < \delta' \le \delta \le 1$, then the curve $(x(t), y(t))$ has a finite k-dimensional measure $k = 2 - (\delta + \delta' - 1)/\delta$. In 1945, Klein constructed a curve $(x(t), y(t))$ for which the dimension $k = 2 - (\delta + \delta' - 1)/\delta$ is really attained.

If

$$g(x)=\sum_{n\geq 1}\lambda_n^{-s}\varphi(\lambda_n x), \quad (97)$$

where $0 < s < 1$ and $\{\lambda_n\}$ is a sequence of positive numbers satisfying the conditions $\lambda_{n+1}/\lambda_n \to \infty$ and $\log(\lambda_{n+1})/\log(\lambda_n) \to 1$ as $n \to \infty$, then $D = 2 - s$.

However, it is difficult to accurately determine the value of D for the Weierstrass function (72) and sequence (80). It is believed that in both cases

$$D=2+\frac{\log a}{\log b}. \quad (98)$$

This value seems to be quite reasonable, since Hardy showed in 1916 that if $\xi = -(\log a)/(\log b) < 1$, then $W(x + h) - W(x) = O(|x|^{\xi})$ and $W(x + h) - W(x) \ne o(|x|^{\xi})$, for any value of x.

2.12. Nondifferentiable functions and chaotic mappings

Based on [58,77,110], we present some information about chaotic mappings. Consider a one-dimensional dynamical system described by a one-dimensional logistic map (Verhulst map):

$$y(x)=4x(1-x) \quad (99)$$

on the unit interval **I**. It is well known that the n-fold iteration y^n can be expressed as

$$y^n(x)=\sin^2\left(2^n \arcsin\sqrt{x}\right). \quad (100)$$

Here $y^n(x)$ means the nth iteration of the function $y(x)$, not the nth power of $y(x)$. In 1983, Japanese mathematicians (Yamaguchi and Hata) first proposed to combine y^n with the Weierstrass function (72). In this case, the final dependence is obtained

$$F(a,x)=\sum_{n\geq 1} a^n y^n(x)= \\ =\frac{1}{2(1-a)}-\frac{1}{2}\sum_{n\geq 0} a^n \cos\left(2^{n+1}\arcsin\sqrt{x}\right), \quad (101)$$

and the generating function $F(a,x)$ is nowhere differentiable for $1/2 \le a < 1$.

Similarly, we find

$$F(a,x)=\sum_{n\geq 0} a^n\varphi^n(x)=\sum_{n\geq 0} a^n\varphi^n(2^{-1}x) \text{ for } x\in \mathbf{I}. \quad (102)$$

When considering (101) and (102), the question arises as to what types of functions

ω: $\mathbf{I} \to \mathbf{I}$ cause the nondifferentiability of their generating function

$$F(a,x)=\sum_{n\geq 0} a^n \omega^n(x) \tag{103}$$

given x. The answer to this question is given by the theorems given in [110].

Weierstrass function (72) for $b = 2$ can also be represented as

$$\sum_{n\geq 0} a^n \cos(2^n \pi x)=\sum_{n\geq 0} a^n \cos(\pi \varphi^n(x)). \tag{104}$$

Consequently, the Weierstrass function and series (80) for $b = 2$ are special cases of the series

$$F(a,x)=\sum_{n\geq 0} a^n g(\varphi^n(x)), \tag{105}$$

where $F(0, x) = g(x)$ is a smooth function on the unit interval **I**.

Series (105) is the only continuous solution to the functional equation

$$F(a,x)-aF(a,\varphi(x))=g(x). \tag{106}$$

For series of type (105), *a replacement operator* S_ω was introduced in the form

$$S_\omega(f)(x)=f(\omega(x)), \tag{107}$$

for $x \in \mathbf{I}$. In this case, series (105) is written as

$$F(a,x)=\sum_{n\geq 0} a^n S_\varphi^n(g)=(Id-aS_\varphi)^{-1}(g), \tag{108}$$

where the operator $(Id - aS_\varphi)^{-1}$ is known as the resolvent of the operator S_φ.

Therefore, the operator $(Id - aS_\varphi)^{-1}$ maps $g_0(x) = \cos\pi x$ to the Weierstrass function, and $g_1(x) = x$ to series (80) for $b = 2$, i.e. it maps some smooth function onto a function that is not differentiable anywhere. Further mathematical formalism of the replacement operator is beyond the scope of our description and is presented in detail in [110].

Takagi function (79) and series (102) are special cases of a function of the form

$$f(x)=\sum_{n\geq 0} c^n \varphi^n(x). \tag{109}$$

Although there are no simple functional equations that the series (109) as a whole must satisfy, it is possible to obtain a family of differentiable equations whose only solutions are this series. It is appropriate to denote the set of lattice sites $\{(n, m); 0 \leq n \leq 2^{m-1} - 1, m \geq 1\}$ as Ω. Then the sought equations are

$$f\left(\frac{2n+1}{2^m}\right)-\frac{1}{2}\left\{f\left(\frac{n}{2^{m-1}}\right)+f\left(\frac{n+1}{2^{m-1}}\right)\right\}=c_m \tag{110}$$

for all $(n, m) \in \Omega$ and boundary conditions $f(0) = 0$ and $f(1) = c_0$.

Note that the left-hand side of (110) is essentially a central difference scheme for f. We can consider the modified equation (110) in the form

$$f\left(\frac{2n+1}{2^m}\right)=(1-\alpha)f\left(\frac{n}{2^{m-1}}\right)+\alpha f\left(\frac{n+1}{2^{m-1}}\right) \tag{111}$$

with the boundary conditions $f(0) = 0$ and $f(1) = 1$, where $0 < \alpha < 1$ is a constant. Then the only continuous solution (111) satisfies the following functional equation:

$$f(x)=\begin{cases}\alpha f(2x), & 0\leq x\leq \dfrac{1}{2},\\ (1-\alpha)f(2x-1)+\alpha, & \dfrac{1}{2}\leq x\leq 1.\end{cases} \tag{112}$$

Expression (112) is a special case of *the functional de Rham equation*, which proved the following

Theorem 6 (de Rum, 1957). *Suppose that* F_0 *and* F_1 *are contraction maps to* R_n. *Then the functional equation*

$$f(x)=\begin{cases}F_0(f(2x)), & 0\leq x\leq \dfrac{1}{2}\\ F_1(f(2x-1)), & \dfrac{1}{2}\leq x\leq 1\end{cases} \tag{113}$$

has a unique continuous solution if and only if $F_0(p_1) = F_1(p_0)$, *where* p_0 *and* p_1 *are the only fixed points for* F_0 *and* F_1, *respectively.*

Moreover, de Rham showed that a solution $L(\alpha, x)$ of the form (112) is strictly monotonically increasing, and its derivative vanishes almost everywhere if $\alpha \neq 1/2$.

Functions of this kind are known as *the Lebesgue singular functions* $f_a(x)$. From (112) for the values $\alpha = \beta = a$ and $g(x) = \cos\pi x$, the Weierstrass function is obtained; for $\alpha = \beta = 1/2$ and $g(x) = |x - [x + 1/2]|$ – Takagi function; for $\beta = 1$

– α, $g(x) = \alpha\theta(x - 1/2)$ is the singular Lebesgue function $f_\alpha(x)$, when θ is a step function.

For the solution of $L(\alpha, x)$, the following expression was also obtained:

$$L(\alpha,x)=x+\left(\alpha-\frac{1}{2}\right)\sum_{n\geq 0}\sum_{p=0}^{2^n-1}\alpha^{n-m(p)}(1-\alpha)^{m(p)}S_{p,n}(x), \quad (114)$$

where $m(p)=p-\sum_{n\geq 1}[p/2^n]$ and

$$S_{p,n}(x)=2^n\left\{\left|x-\frac{p}{2^n}\right|+\left|x-\frac{p+1}{2^n}\right|-\left|2x-\frac{2p+1}{2^n}\right|\right\}. \quad (115)$$

From formula (114), one can obtain the exact interdependence between the Takagi function (79) and the solution to equation (112) in the form:

$$\frac{\partial}{\partial\alpha}L\left(\frac{1}{2},x\right)=2T(x). \quad (116)$$

Expression (114) is also applicable for the complex parameter $\alpha\in\{z;|z|<1,|1-z|<1\}$ and gives a continuous solution for (112). In particular

$$L\left(\frac{1}{2}+\frac{i}{2},x\right)=x+ \\ +\sum_{n\geq 0}2^{-(n/2)-1}\sum_{p=0}^{2^n-1}S_{p,n}(x)\exp\left[\frac{\pi i}{4}(n+2-2m(p))\right] \quad (117)$$

defines the fractal curve, which was investigated by P. Levy in 1938.

De Ram showed in 1957 that the solution of the conjugate equation (112), i.e.

$$f(x)=\begin{cases}\alpha\overline{f(2x)} \\ (1-\alpha)\overline{f(2x-1)}+\alpha \quad 1/2\leq x\leq 1.\end{cases} \quad (118)$$

is the Koch curve if $\alpha=1/2+(\sqrt{3}/6)i$ and the close-packed Polya curve if $\alpha = 1/2 + i/2$. The corresponding difference equations for (118) are a special case of the system written in the form:

$$\begin{cases}R\left(\frac{4n+1}{2^{m+1}}\right)=(1-\lambda_m)R\left(\frac{n}{2^{m-1}}\right)+\lambda_m R\left(\frac{n+1}{2^{m-1}}\right) \\ R\left(\frac{4n+3}{2^{m+1}}\right)=\mu_m R\left(\frac{n}{2^{m-1}}\right)+(1-\mu_m)R\left(\frac{n+1}{2^{m-1}}\right)\end{cases}, \quad (119)$$

for all $(n,m)\in\Omega$ and boundary conditions $R(0) = 0$ and $R(1) = 1$, $R(1/2) = \alpha$, where $0 < \lambda_m \leq \mu_m < 1$ and $m \geq 1$ are constants. Indeed, under the condition $\lambda_m = |\alpha|^2$ and $\mu_m = 1 - |1 - \alpha|^2$, the continuous solution (119) also satisfies (118). Equations (119) have a unique continuous solution if $0<\inf_{n\geq 1}\lambda_n\leq\sup_{n\geq 1}\mu_n<1$.

It is clear that the curve $R(I)$ lies in a triangle with vertices 0, 1 and α. In the case $\lambda_n < \mu_n$ for $n \geq 1$ the curve $R(I)$ becomes the Jordan curve, and for $\lambda_n = \mu_n$ and $n \geq 1$ it becomes the Peano curve. The two-dimensional Lebesgue dimension of the curve $R(I)$ is given by the expression

$$\left[\left|\operatorname{Im}\alpha\right|\prod_{n\geq 1}(1-\lambda_n-\mu_n)\right]/2. \quad (120)$$

Thus, with an appropriate choice of $\{\lambda_n\}$ and $\{\mu_n\}$, the positive domain of the Jordan curve can be regarded as the only solution to (119).

2.13. Theorems on the construction of fractal sets

Two methods are widely used to construct self-similar fractal sets in the space R^p [58,77,110]. The first, adopted by Decking in 1982, uses endomorphisms of symbols in free groups, and the second, Hutchinson's method, is based on the use of a system of iterative functions, i.e. on the set of contraction maps. It should be borne in mind that the result of using iterative functions (attractor) is not always a fractal. In general, it can be any compact.

As noted above, the mapping $F: R^p \to R^p$ will be *contracting* if there is a constant $\lambda \in (0, 1)$ for which $\|F(x)-F(y)\| \leq \lambda\|x-y\|$ for all $x, y \in R^p$. The smallest λ is *the Lipschitz constant* F and is denoted by $\mathrm{Lip}(F)$. The only *fixed point* F is denoted here by the symbol $\mathrm{Fix}(F)$.

Then the following is true

Definition 1.1 (Hutchinson). *A non-empty subset X from $\mathbf{R}^p$ is invariant under the set m contracting mappings $F_1, F_2, ..., F_m$ if X satisfies the equality*

$$X=F_1(X)\cup F_2(X)\cup\ldots\cup F_m(X). \quad (121)$$

For the set of contracting mappings $F_1, ..., F_m$, one can define the mapping

$$\Phi(X)=F_1(X)\cup F_2(X)\cup\ldots\cup F_m(X) \quad (122)$$

for an arbitrary subset X from $\mathbf{R}^p$. Obviously, the sequence (122) converges to the fixed point Φ. It

is also necessary to pay attention to the following result.

Theorem 7 (Williams, Hutchinson). *For the set of contracting images F_1, ..., F_m, there is a unique nonempty compact invariant set K. For an arbitrary nonempty compact subset X from* $\mathbf{R}^p$*, the system $\Phi^n(X)$ converges in the Hausdorff metric to K as $n \to \infty$.*

Also studied was the modification (121) of the inhomogeneous form

$$X = \Phi(X) \cup V = F_1(X) \cup ... \cup F_m(X) \cup V, \quad (123)$$

where V is a given compact subset of $\mathbf{R}^p$. Moreover, it was shown that there is a unique non-empty compact solution X satisfying (123). The following result is obtained.

Theorem 8 (Hata). *Suppose that F_1, ..., F_m are continuous mappings such that the set $\cup_{n\geq 0}\Phi^n(X)$ is a precompactum for any compact set X. Then the following statements (a) and (b) are equivalent:*
(a) - there is a unique solution (123) for any compact set V;
(b) - Φ has a unique fixed point.

From the definition of the Hausdorff dimension of an invariant set, we have the following theorem.

Theorem 9 (Marion, Hutchinson). *Suppose that each contracting map F_j, $1 \leq j \leq m$, is a composition of stretch, rotate, translate, and flip operations. Suppose further that there is an open set U satisfying $\Phi(U) \subset U$ and $F_i(U) \cap F_j(U) = \varnothing$, for $i \neq j$. Then s, the dimensional Hausdorff measure of the invariant set K, is finite and positive, that is, $dim_H(K) = s$, where s is defined by $Lip(F_1)^s + \ldots + Lip(F_m)^s = 1$.*

For connected invariant sets, we have the following theorems.

Theorem 10 (Williams). *Let $Lip(F_1) + \ldots + Lip(F_m) < 1$, and each F_j is injective. Then K is completely disconnected and perfect.*

Recall that an *injective mapping* (*injection*) of a set A into a set B is a one-to-one mapping $f: A \to B$.

To study the connectedness of invariant sets, we can introduce the *structure matrix* $M_K = (m_{ij})$ of the set K in the form:

$$m_{ij} = \begin{cases} 1 & \text{if } F_I(K) \bigcap F_J(K) = \varnothing \\ 0 & \text{in all other cases.} \end{cases} \quad (124)$$

Then there is

Theorem 11 (Hata). *An invariant set K is connected if and only if its structure matrix M_K is irreducible. Moreover, if K is connected, it is also a locally connected continuum and path-connected.*

If two contracting mappings F_1 and F_2 satisfy the equality $F_1(\mathrm{Fix}(F_2)) = F_2(\mathrm{Fix}(F_1))$, then we can introduce a parametrization of the invariant set K using Theorem 6. Indeed, let $f(x)$ be a continuous solution to (113). Then

$$f(I) = f\left(\left[0, \frac{1}{2}\right]\right) \cup f\left(\left[\frac{1}{2}, 1\right]\right) = \\ = F_1(f(I)) \cup F_2(f(I)). \quad (125)$$

Therefore, $f(I)$ is a compact invariant set for F_1 and F_2, so $K = f(I)$, as required. Taking this into account, we have proved the following statement.

Theorem 12 (Hata). *Let f(x) be a continuous solution to (113). Then,*

(a) – if $\mathrm{Lip}(F_1) \cdot \mathrm{Lip}(F_2) < 1/4$*, then the Frechet derivative f vanishes almost everywhere;*

(b) – if each F_j is a homeomorphism and $\mathrm{Lip}(F_1^{-1}) \cdot \mathrm{Lip}(F_2^{-1}) < 4$*, then f is not Frechet differentiable almost anywhere; moreover, if* $\mathrm{Lip}(F_j^{-1}) < 2$*, for j = 1,2, then f is nowhere differentiable.*

Note that the above results generalize Lax's theorem [110]. With such a parametrization, it is easy to obtain the well-known classical Peano curve, constructed by him in 1890, by Hilbert in 1891, and by Polya in 1913, using certain affine transformations in the space $\mathbf{R}^2$.

In conclusion, we note that, despite a significant number of works on nondifferentiable (fractal) functions and corresponding sets and mappings, it is too early to talk about the creation of their modern integral theory. Moreover, interest in them is currently growing significantly.

2.14. Classic fractal curves and sets

We begin our consideration with the *Cantor set* ("*Cantor dust*"), named after G. Cantor, who discovered it in 1883. The construction of the classical Cantor dust (**Fig. 6**) begins with the removal of the middle part of the segment, i.e.

open interval (1/3, 2/3). This is the first step in the iterative procedure. In the next and all other steps, we delete the middle third of all segments of the current level. The limit set C, which represents the intersection of all sets C_i, $I = 0, 1, 2, ...$, is called the classical Cantor dust.

Cantor dust is a fractal of dimension $D = \ln 2/\ln 3 \approx 0.6309$. The sum of all the lengths of the intervals removed when constructing the set C is exactly 1. The total "length", or measure, of the remaining set is equal to zero. However, the remaining "dust" still contains innumerable dots. Formally, a Cantor set is defined as completely discontinuous, closed, and perfect. It can be used to construct a continuous fractal function by integrating a suitable distribution function given on a Cantor set. Then we get a fractal function called "devil's ladder". In particular, such functions play a very noticeable role in the theory of oscillations in describing frequency synchronization, when the so-called "Arnold tongues" arise.

Another completely non-intuitive consequence of Cantor sets is *the equivalence of two-dimensional domains and one-dimensional lines*. Two sets are equivalent if there is a one-to-one correspondence between them. For example, the unit square and the unit line segment are equivalent: each point of the unit square corresponds to one point of the unit line and vice versa. In this regard, Kantor wrote: "*I see, but I do not believe.*"

Who would have thought that such contradicting common sense mathematical constructions, invented only to convince skeptics of the possibility of the existence of uncountable sets of zero measure, would become one of the central concepts and find practical application? Meanwhile, Cantor sets later turned into almost ideal models for many branches of modern natural science - from strange attractors to the distribution of galaxies in the Universe. It is appropriate in this connection to quote the statement of W. Hilbert: "*No one can expel us from the paradise that Cantor created for us.*"

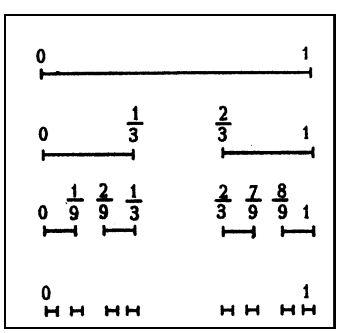

Fig. 6. *Construction of the Cantor set.*

Fractal functions are *non-differentiable functions*. They originated over a hundred years ago. The scientific community of the past called them "monsters" (often adding the epithet "pathological"), of interest only to those specialists who are characterized by mathematical quirks, but not to professional scientists. This was perceived as the destruction of mathematics: S. Hermite wrote to T. Stieltjes in 1893: "*I turn away with horror and disgust from this growing ulcer of functions that have no derivatives*".

However, the time of mathematicians' faith in the inseparability of the connection between continuous functions and their differentiability has expired (see paragraphs 6-10). From the standpoint of modern science, *a function without a derivative is not at all an abstract concept,* but the trajectory of a Brownian particle. In the arsenal of mathematics, there was also an analytical apparatus for describing such objects. The place of the usual dimension was taken by *the Hausdorff dimension*, and the place of derivatives was taken by *the fractional derivative* (see item 4). In 1906, J. Perrin stated that "*curves without tangents are a general rule, and smooth curves, such as a circle, are an interesting but very special case.*"

The curve in **Fig. 7** was originally described by Helge von Koch in 1904. Every third of the curve is constructed iteratively, starting with a line segment (initiator). Let's remove the middle third and add two new line segments. The result of this construction is called a generator. The length of the generator is 4/3 of the length of the initiator. We repeat this procedure many

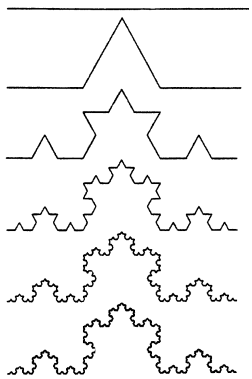

Fig. 7. *Construction of the Koch curve.*

times, at each step replacing the middle third with two new segments. In the limiting case, the nowhere nondifferentiable Koch curve is a line of infinite length with fractal dimension $D = \ln4/\ln3 \approx 1.2618$.

Applying the von Koch generator to an equilateral triangle, through an infinite number of iterations, we arrive at the von Koch snowflake (**Fig. 8**). In the limit, this curve also has infinite length, limiting an area equal to 8/5 of the area of the original triangle. The von Koch snowflake does not cross itself anywhere. If the triangles are built inward, and not outward, then a curve is obtained - an anti-snowflake, its perimeter is infinite, and it limits an infinite set of disconnected regions, with a total area of 2/5 of the area of the original triangle.

Deterministic fractals, called the Sierpinski napkin and carpet or Sierpinski curves (1915), are obtained by sequentially cutting out triangles (**Fig. 9***a*) or squares (Fig. 9*b*).

In the limit, at the Sierpinski napkin, the black areas disappear, and the full perimeter of the holes tends to infinity. Thus, in the process of constructing the napkin, an area exactly equal to the area of the original triangle will be excluded. The fractal dimension of the Sierpinski napkin is $D = \ln3/\ln2 \approx 1.5849$. One more property of the

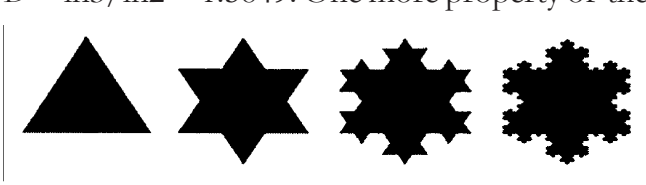

Fig. 8. *Construction of the Koch snowflake.*

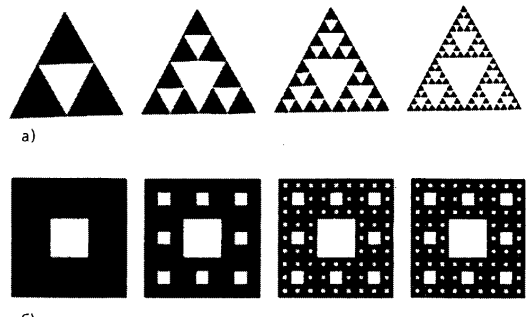

Fig. 9. *Construction of napkins (a) and carpet (b) Sierpinski.*

Sierpinski napkin can be noted. For Euclidean bodies in *n*-dimensional space, the volume V is proportional to R^n, where R is a certain characteristic size of the body. The surface area S changes in proportion to R^{n-1}, therefore $S \propto V^{(n-1)/n}$. However, for a Sierpinski napkin, the area and length of the edges are proportional to each other: $S \propto V$!

The Sierpinski napkin combines self-similarity with rotation symmetry. The shape of the Sierpinski napkin does not change when it is rotated through an angle multiple of 120°. Symmetry data (infinite scaling and rotation through a finite angle) are observed in well-known paintings by Maurice Escher. Two-dimensional and three-dimensional analogs of the Sierpinski napkin model many natural and man-made structures (for example, the Eiffel Tower in Paris). For the Sierpinski carpet, $D = \ln8/\ln3 \approx 1.8928$, i.e. it is, in a sense, less leaky. The Sierpinski carpet is an analogue of a Cantor set on a square. The Sierpinski curve consists entirely of branch points alone.

The Koch snowflake and other fractal curves on the plane are united by the fact that their dimension lies in the range $1 < D < 2$. The question arises, is there a curve of dimension 2? This question was resolved by *D*. Peano in 1890. The Piano curve in the limit fills the square so densely that its $D = 2$. At the same time, the Peano curve is a graph of a continuous function. Nevertheless, at no point can a tangent be drawn to it, since at any moment in time we do not know the direction in which the point is moving. The

concept of the Peano curve is not intuitive, but originally arose from purely analytical reasoning.

W. Hilbert in 1891 proposed a simple method for constructing a Peano curve with two endpoints. In **Fig. 10** shows the first four steps of his recursive procedure. At the limit, the curve starts and ends at the top vertices of the square.

A variant of constructing a closed Peano curve belongs to Sierpinsky and is shown in **Fig. 11**. In each of the options, the limit curve has an infinite length and completely fills the square. The approximate curves limit the areas, which tend to 5/12 in the limit, but for the graph of the limiting function, the difference between the inner and outer parts of the square loses its meaning.

Peano curves easily generalize to higher topological dimensions and can fill cubes and hypercubes. Hilbert's constructions have found interesting applications in information theory in Gray codes. Several ways to scan an image in television use the Hilbert algorithm. The point is that points adjacent in time along the "Hilbert sweep" are adjacent in space and on the scanned image, which simplifies its processing.

The Sierpinski carpet satisfies Uryson's definition of a line. Therefore, any Cantor curve, being homeomorphic to a subset of the Sierpinski carpet, is also one-dimensional and is a line in the sense of P.S. Uryson. Conversely, if a flat continuum is one-dimensional, then it will be a Cantor curve.

There are lines that are not homeomorphic to any subset of the plane. At the same time, by Menger's *theorem*, any line is homeomorphic

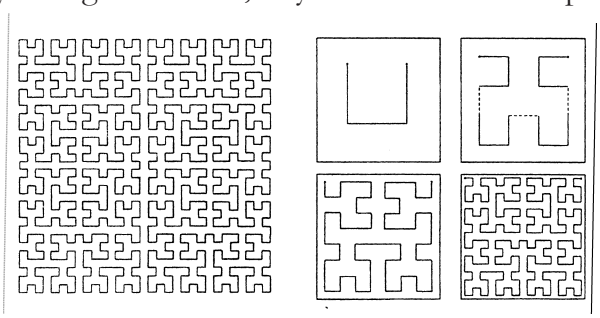

Fig. 10. *Peano's curve constructed by the Hilbert algorithm (left) and the first four iterations (right*).

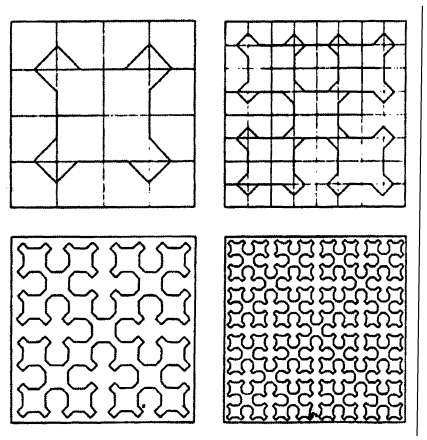

Fig. 11. *The closed Peano curve constructed by Sierpinsky.*

to some subset of three-dimensional Euclidean space. More general is the Nöbeling-Pontryagin *theorem*. In 1926, Menger constructed in $\mathfrak{R}^3$ a one-dimensional continuum M_1^3, which topologically contains any line. This continuum is called the universal Menger curve.

The construction of the universal Menger curve M_1^3 is as follows. A cube I^3 with a single edge is divided by planes parallel to its edges into 27 equal cubes with an edge 1/3. Then the inner cube and 6 adjacent cubes (cubes of the first rank) are removed. The remaining set K_1 consists of 20 cubes of the first rank. Proceeding also with each of the cubes of the first rank, we obtain the continuum K_2, consisting of 400 cubes of the second rank. In the process of infinite construction, we have a decreasing sequence of continua $I^3 = K_0 \supset K_1 \supset K_2 ...$, the intersection of which is a one-dimensional continuum I_1^3. The first steps in constructing the Menger curve are shown in **Fig. 12.**

We can say that the abstract constructions of Cantor and Peano have provided us with models *of reality much more realistic* than the entire Euclidean geometry of integer exponents and smooth forms.

There are curves in which, in contrast to Peano's original construction, there are no self-contact points. One example of this kind is the Gosper curve. The initiator for it is a segment of unit length, and the generator is shown in the upper right in **Fig. 13**. It consists of 7 sections,

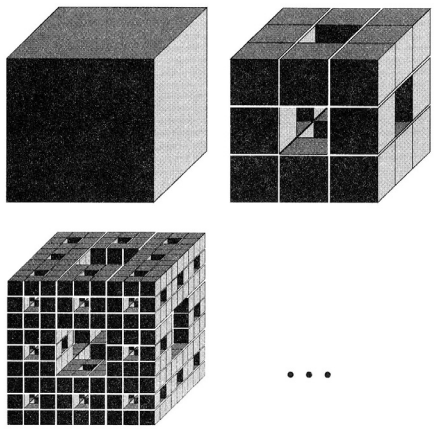

Fig. 12. *Construction of the universal Menger curve.*

each $1/\sqrt{7}$ long The dotted line denotes a triangular lattice, which serves as a kind of generatrix for this generator. The next three steps in the build process are shown in Fig. 13 below.

The dimension of the Gosper curve is $D = 2$. A distinctive feature of this curve is that the boundary of the region called the "Gosper island", which it fills in the limit, is itself fractal with $D \approx 1.1291$. These islands can be used for continuous plane coverage as they fit perfectly together. Moreover, seven such islands, docked so that one is in the center and six around it, again form the island of Gosper, three times larger. Of regular polygons, only a square has this property.

Let's give another example of the Peano curve – a fractal called "Harter-Hatway's dragon". The first four steps of its construction are shown at the top of **Fig. 14**. Each of the segments in the next step is bent at right angles. The fold direction is alternating. After each step, the number of segments is doubled, and the length of each

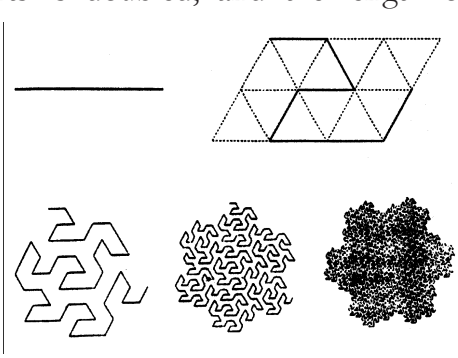

Fig. 13. *Generator of the Gosper curve and its iterations.*

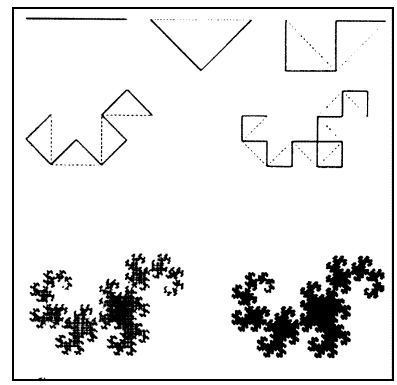

Fig. 14. *The first four stages of the construction of the "Harter-Hatway dragon" (a) and its subsequent outlines.*

segment decreases in $\sqrt{2}$. Therefore, in the limit $D = 2$. The shape of the resulting unusual figure is shown at the bottom of Fig. 14 for 12th and 16th dragon generations. The dragon curve is self-similar.

Consecutive central folds precisely fit a logarithmic spiral, which itself is one of the main smooth self-similar objects, and has practical application in the design of broadband antennas for a variety of radio systems [57,58,62,65]. Nature also uses the self-similarity of the logarithmic spiral, for example, the self-similar shell of the multichamber mollusk Nautilus.

It is amazing that a fairly simple algorithm leads to such an unusual figure as a dragon. The biological subtext inherent in the name of the curve makes one wonder: is it not encoded in genes in a similar way information about the shapes and sizes of existing living organisms?

2.15. Methods for the synthesis of fractals and fractal sets on the complex plane

When modeling deterministic fractals, special methods are used, such as systems of *L*-functions and systems of iterated functions (IFS) [28, 29, 57, 58, 62, 115].

The concept of *L*-systems appeared in 1968 thanks to A. Lindenmayer. *L*-systems were first introduced in the study of formal languages and were also used in biological breeding models. For the graphical implementation of *L*-systems, *turtle-graphics* are used as an inference subsystem. A deterministic *L*-system formally consists

of an alphabet, an initialization word called an axiom or initiator, and a set of generating rules (generator).

One of the deepest and most remarkable advances in the construction of fractals is the *system of iterated functions*. The mathematical foundations were developed by J. Hutchins (1981), and the method itself became widely known thanks to M. Barkley (1988). A system of iterated functions is a collection of *affine transformations*. As you know, affine transformations include scaling, rotation, and parallel translation. There are two approaches to implementing IFS: deterministic and randomized. *The deterministic algorithm* produces attractive images, but requires processing large arrays of zeros and ones. In *a randomized algorithm*, the initial set contains only one point. At each step, only one affine transformation is used from the entire set of transformations that define the IFS. This transformation is chosen at random.

Nonlinear algorithms for constructing fractals use iterations on a complex plane of the form $z_{n+1} = z_n^2 + c$, where c is some complex constant that is a control parameter. The apparent simplicity of this process is in no way comparable to the stunning beauty and variety of those fractal structures that arise in this process. In 1879 Sir Arthur Cayley posed the problem of iterating complex functions. The theory of iterations on the complex plane was described in 1918 by G. Julia (1893-1978), who was then in the hospital after being wounded at the front during the First World War. Both his work and the work (1919) of his contemporary and rival P. Fatou (1878-1929), were soon consigned to oblivion. As noted in [28], the most significant and impressive contribution was made by Fatou himself, but Julia made him strong competition and had some advantages associated with his status as a wounded war hero. In 1918, Julia received the "Grand Prix of Mathematical Sciences" from the Paris Academy of Sciences for his work.

The studies of P. Montel, D. Sullivan, B. Mandelbrot, J. Milnor and others have again drawn attention to their theory. The intellectual achievements of G. Julia and P. Fatou are also notable for the fact that they had to rely entirely on the imagination. Computers have made visible what could not be depicted during the years of the creation of this theory. Visual computer results exceeded all expectations.

Julia sets are fractal boundaries arising in the process of iterating a quadratic complex transformation that preserves angles, i.e. *conformal transformation*. The variety of border shapes depends only on the control parameter *c*. For some values of *c*, the Julia sets are connected (**Fig. 15**), and for other values, they are completely disconnected and represent dusty Cantor sets (*Fatou dust* - **Fig. 16**).

It turned out that absolutely all values of the parameter *c* for which the Julia set is connected belong to *the Mandelbrot set* (*M-set*), discovered in 1980. The Mandelbrot set is shown in **Fig. 17** as the blacked-out portion of the complex *C*-plane.

From an arbitrary point of the set *M* one can get to any other point without leaving the set *M*, i.e. the Mandelbrot set is connected (Douady and Hubbard 1982). This is not just a bizarre form that seems beautiful to someone, but ugly to someone; it embodies, more general than Feigenbaum's universality, *the principle of the transition from order to chaos*. The subtle mathematical web of the Mandelbrot set continues to awe even seasoned professionals. The complexity of the *M*-set is a reminder that *complexity in many natural phenomena can be a consequence of simple laws*.

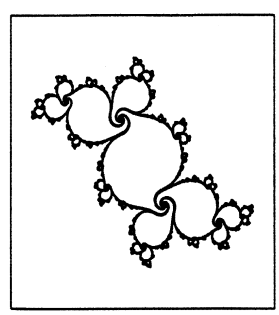

Fig. 15. *Julia set.*

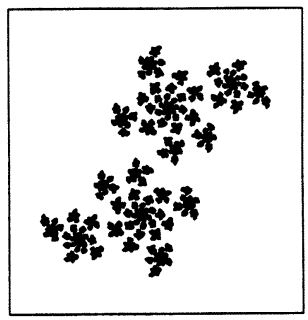

Fig. 16. *Fatou set.*

If we take the values of the constant *c* outside *M*, then the only attractor will be infinity, i.e. the point representing the iteration process goes to infinity. Then Julia's multitude disintegrates into Fatou dust. This dust becomes finer and finer with distance *c* from *M*. If point *c* is near the boundary of *M*, then the dust forms fascinating figures, examples of which are shown in Fig. 17 and **Fig. 18**. These figures are *always fractal, self-similar and carry chaotic dynamics.*

The most remarkable feature of the Mandelbrot set is that it serves as an infinitely efficient storage of images (Tang Lei, 1984). With an increase in the Mandelbrot set, in the vicinity of its boundary point *c*, forms appear that are Julia sets.

All fractals discussed above were *deterministic.* The construction of *random* fractals is not reduced to random perturbations of deterministic fractals. On the contrary, a random nature is inherent in them initially, which is associated with random processes. The main model for constructing random fractals is *fractal Brownian motion.* The existence of a fractal Brownian motion was proved by B. Mandelbrot and Van Ness in 1968.

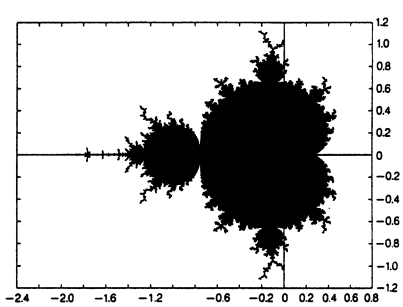

Fig. 17. Mandelbrot set.

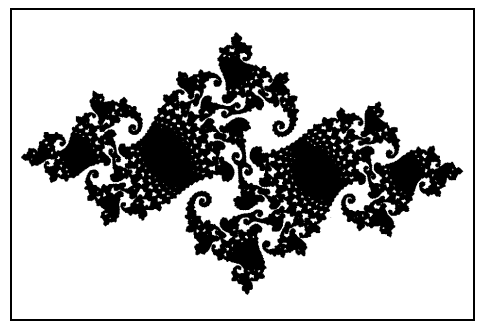

Fig. 18. *Fatou set.*

This process was implicitly considered by A.N. Kolmogorov in 1940.

The *method of random perturbations* is sometimes used. For a *randomized Koch snowflake*, equilateral triangles are added, randomly facing both inward and outward. In *a randomized Sierpinski napkin*, any of the triangles are randomly removed during construction. Sometimes, randomization of the lengths of the intervals removed when constructing the Cantor set is used. Summarizing what has been said, it can be noted that *random fractals are combinations of generative rules chosen at random on different scales*. In this case, in the iterative procedure, you can randomly change its parameters.

2.16. Hurst exponent of random processes

In fractal processing of samples $\xi(t)$ of a random process and time series, *the normalized range method* or *the Hurst method* [57,58,62,89,115] is currently often used. In this case, such processes are characterized by *the Hurst exponent* or *the codimension H*. To calculate the Hurst exponent *H* of a one-dimensional sample, it is necessary to calculate its normalized range *R*/*S*. For all kinds of random processes, this value obeys the following empirical relationship:

$$R / S = (\tau / 2)^H. \tag{126}$$

In formula (126), the expression

$$R(\tau) = \max_{1\le t\le\tau} X(t,\tau) - \min_{1\le t\le\tau} X(t,\tau), \tag{127}$$

the maximum range of amplitudes of a random process in the sample under consideration,

$$X(t,\tau) = \sum_{u=1}^{t} \{\xi(\mathrm{u}) - \langle\xi\rangle_\tau\} \tag{128}$$

deviation of $\xi(u)$ from the mean,

$$\langle \xi \rangle_\tau = \frac{1}{\tau}\sum_{t=1}^{\tau} \xi(t) \quad (129)$$

average value over the interval τ,

$$S = \left\{ \frac{1}{\tau}\sum_{t=1}^{\tau} \left[\xi(t) - \langle \xi \rangle_\tau \right]^2 \right\}^{1/2} \quad (130)$$

root-mean-square deviation, t – discrete time with integer values, τ – duration of the considered time interval.

It should be noted that the Hirst method is an extremely robust method. It does not have an initial assumption of *Gaussian distributions*.

From relation (126), the value of the Hurst exponent H is determined by logarithm. For a one-dimensional reflected signal, the fractal dimension D, which *characterizes its structural properties*, under the condition $0 \le H \le 1$, is related to the Hurst exponent as follows:

$$D = 2 - H. \quad (131)$$

In the case of a two-dimensional process (image) with parameter H, relation (131), which determines the fractal dimension D, must be written in the form:

$$D = 3 - H. \quad (132)$$

It is well known [57,58,62,89,115] that the case

$$1/2 < H < 1 \quad (133)$$

corresponds to *a persistent process* (a process that preserves the observed tendency of an increase or decrease in instantaneous amplitudes in a sample, i.e., a process with memory). At the same time, trends in the process under study are obvious. This is true on average and for arbitrarily large time intervals t, when the time series becomes less noisy.

Happening

$$0 < H < 1/2 \quad (134)$$

corresponds to *an antipersistent process* (in this case, an increase in the amplitudes of the signal envelope in the "past" means a decrease in the "future", and vice versa). The antipersistent H value characterizes a system that is more susceptible to change. This type of system is often referred to as "Return to Mean".

The value H = ½ corresponds to *the classical Brownian motion*, which is a Markov process. The structural functions of a random process are also used to estimate the Hurst parameter. In practice, it is believed that the Hurst exponent can be estimated fairly accurately using a sample of about 2500 measurements [57,58].

In the case of fractal analysis of signals, in the general case, it is necessary to construct graphs of the dependence of the variance of the signal or its structure function on a double logarithmic scale. If the obtained dependence is sufficiently well approximated by some "straight line" on a large number of time scales, then the tangent of its slope can be used to find the value $2H$ (when analyzing the time course of the signal dispersion) or the value H (when the structure function is analyzed). The linear section of the obtained experimental "straight line" will determine the scaling region of the process under study.

For fractal processes describing one-dimensional *generalized Brownian motion* with codimension $0 < H < 1$, the spectral power density $G(f)$ has a fractal form [57,58]:

$$G(f) = \frac{1}{f^{\alpha}},\ \alpha = 2H + 1. \quad (135)$$

The use of the H exponent in radiophysical problems is briefly presented in Section 2. These issues are related to the circle of general issues of the evolution of open radiophysical systems with a change in external parameters and the appearance of a chaos regime and bifurcation points, i.e., to solving urgent problems of an adaptive scheme of a fractal detector radar signals, which is also shown in clause 2.

2.17. Fox functions and processes in fractal environments

The application of the apparatus of Fox functions [116] when considering the processes of relaxation and diffusion in media with fractal dimension, characterized by an equation

of diffusion type with fractional derivatives with respect to coordinates and time, will be demonstrated on the basis of the results obtained in [22]. Because of fractality – in contrast to the standard diffusion equation, when the particle flux and $j \sim \partial\rho/\partial t$, $j \sim \partial^2\rho/\partial x^2$ – is violated due to self-similarity, the locality of such connections. The flow value begins to depend on the prehistory of the process – the concentration values at earlier points in time:

$$j(t) \approx \frac{\partial}{\partial t}\int_0^t \rho(\tau)K(t,\tau)d\tau, \quad (136)$$

those. diffusion and relaxation processes become non-Debye.

In formula (136), the kernel $K(t, \tau)$ includes the fractal dimension D of the medium and in the stationary mode depends on the difference of the arguments. At the same time, $K(t, \tau)$, when replacing a fractal medium with an ordinary one, must satisfy the standard diffusion equation. The simplest such kernel is the power function $K(t - \tau) = (t - \tau)^{-\nu(D)}$ with the exponent depending on the fractal dimension of the diffusion space D. In this case, the right-hand side of (136) coincides in structure with the definition of the fractional derivative Riemann-Liouville (36) of order $0 < \nu < 1$, i.e. $j(x,t) \sim \partial^\nu\rho(x,t)/\partial t^\nu$. At the same time, due to the complexity and entanglement of the particle trajectories, the derivative with respect to the coordinate (gradient) becomes fractal and $j \sim \partial^{2\nu}\rho/\partial t^{2\nu}$. The equations of non-Debye diffusion and relaxation take the following form, respectively:

$$\frac{\partial^\nu}{\partial t^\nu}\rho = \tilde{D}\frac{\partial^{2\gamma}}{\partial x^{2\gamma}}\rho, \quad \frac{\partial^\nu}{\partial t^{2\gamma}}\rho = -\frac{1}{\tau^\nu}\rho, \quad (137)$$

where $0 < \nu < 1$, $1 < 2\gamma \le 2$ [57,58].

Diffusion-relaxation processes investigated in [22] are described in the one-dimensional case by the equation

$$\frac{\partial^\nu}{\partial t^\nu}\rho = \tilde{D}\frac{\partial^{2\gamma}}{\partial x^{2\gamma}}\rho - \frac{1}{\tau^\nu}\rho, \quad (138)$$

and for their solution the above mathematical apparatus of Fox functions is used.

Acting on the right and left sides of Eq. (138) by the fractional integral operator (30) in the form

$${}_0D_t^{-\nu}g = \frac{1}{\Gamma(\nu)}\int_0^t dt'\frac{g(t')}{(t-t')^{1-\nu}}, \quad (139)$$

we get

$$\rho(x,t) - \rho_0(x) = {}_0D_t^{-\nu}\left\{\left[\frac{\partial^{2\gamma}}{\partial x^{2\gamma}}\tilde{D} - \frac{1}{\tau^\nu}\right]\rho(x,t)\right\} \quad (140)$$

under the initial conditions $\rho(x,t)|_{t=0} = \rho_0(x)$. Fractional differentiation (140) using the operator ${}_0D_t^\nu$ under the condition ${}_0D_t^\nu\,{}_0D_t^\nu = 1$ gives

$${}_0D_t^\nu\left\{\rho(x,t) - \rho_0(x)\right\} = \left[\frac{\partial^{2\gamma}}{\partial x^{2\gamma}}\tilde{D} - \frac{1}{\tau^\nu}\right]\rho(x,t). \quad (141)$$

Next, you need to use the Fourier transform in relation to the spatial coordinate and the Laplace transform $\tilde{\rho}(k,p) = \int_0^\infty \rho(k,t)\exp(-pt)dt$ in time. The Fourier amplitude $\tilde{\rho}(k,p)$ satisfies the equation

$$\begin{aligned}&{}_0D_t^\nu\left\{\hat{\rho}(k,t) - \rho_0(x)\right\} = \\ &= \left[\tilde{D}(ik)^{2\gamma} - \frac{1}{\tau^\nu}\right]\hat{\rho}(k,t) = -\frac{1}{T^\nu}\hat{\rho}(k,t).\end{aligned} \quad (142)$$

The action of the fractional time derivative on a time-independent function $\rho_0(x)$ is not equal to zero: ${}_0D_t^\nu\rho_0 = \rho_0 t^{-\nu}/\Gamma(1-\nu)$.. For the image $\tilde{\rho}(k,p)$, we obtain the equation

$$\tilde{\rho}(k,p) = \frac{p^{-1}}{1+(Tp)^{-\nu}}\hat{\rho}_0(k). \quad (143)$$

Next, we represent $\tilde{\rho}(k,t)$ through the Fox function:

$$\tilde{\rho}(k,p) = \frac{T(k)\hat{\rho}_0(k)}{\nu}H_{1,1}^{1,1}\left(T(k)p\left|\begin{matrix}1-1/\nu,1/\nu\\1-1/\nu,1/\nu\end{matrix}\right.\right), \quad (144)$$

and carry out the inverse Laplace transform

$$\hat{\rho}(k,t) = \frac{\rho_0(k)}{\nu}H_{1,2}^{1,1}\left(\frac{t}{T}\left|\begin{matrix}(0,1/\nu)\\(0,1/\nu),(0,1)\end{matrix}\right.\right). \quad (145)$$

The solution to equation (140) has the form

$$\begin{aligned}&\rho(x,t) = \frac{1}{2\pi}\int_{-\infty}^{\infty}dk\exp(ikx)\hat{\rho}_0(k)\times\\ &\times H_{1,2}^{1,1}\left(-t^\nu\left[(ik)^{2\gamma}\tilde{D} - \frac{1}{\tau^\nu}\right]\left|\begin{matrix}(0,1)\\(0,1),(0,\nu)\end{matrix}\right.\right).\end{aligned} \quad (146)$$

We represent the function $H_{1,2}^{1,1}$ in the form of a series and obtain the solution of equation (140) in the form

$$\rho(x,t)=\frac{1}{2\pi}\int_{-\infty}^{\infty}dk\exp(ikx)\times \\ \times\hat{\rho}_0(k)\sum_{n=0}^{\infty}\frac{\left[\tilde{D}(ik)^{2\gamma}t^{v}-t^{v}\tau^{-v}\right]^{n}}{\Gamma(1+vn)}. \quad (147)$$

Integral (146) is calculated explicitly in a number of cases. For $1/\tau = 0$, formula (146) is reduced to the form

$$\rho(x,t)=\frac{1}{2\pi}\int_{-\infty}^{\infty}dk\exp(ikx_1)\hat{\rho}_0(k)\times \\ \times H_{1,2}^{1,1}\left(-(ik)^{2\gamma}\left|\begin{matrix}(0,1)\\(0,1),(0,v)\end{matrix}\right.\right)(\tilde{D}t^{v})^{-1/2\gamma}. \quad (148)$$

For Fox functions, it is more convenient to use the sine (F_s) and cosine (F_c) of the Fourier transform. Consider a particular case $\hat{\rho}_0(k)=\rho_0=const,\ \rho_0(x)=\rho_0\delta(x)$, and let $\gamma = 1 - \varepsilon$, $0 \le \varepsilon \le 0.5$. After a series of transformations [22], we obtain an exact solution of equation (140) with $1/\tau = 0$ and the initial condition $\rho_0(x,t)|_{t=0}=\rho_0\delta(x)$, at $0.5 < \gamma < 1$:

$$\rho(x,t)=\frac{\rho_0}{4\gamma(\tilde{D}t^{v})^{1/2\gamma}}\times \\ \times\left[\begin{array}{l}\frac{(-1)^{\varepsilon/2\gamma}}{x_1}H_{3,3}^{2,1}\left((-1)^{\varepsilon/2\gamma}x_1\left|\begin{matrix}(1,1/2\gamma),(1,v/2\gamma),(1,1/2)\\(1,1),(1,1/2\gamma),(1,1/2)\end{matrix}\right.\right)+\\ +\frac{(-1)^{\varepsilon/2\gamma}}{x_1}H_{3,3}^{2,1}\left((-1)^{-\varepsilon/2\gamma}x_1\left|\begin{matrix}(1,1/2\gamma),(1,v/2\gamma),(1,1/2)\\(1,1),(1,1/2\gamma),(1,1/2)\end{matrix}\right.\right)+\\ +\frac{(-1)^{-\varepsilon/2\gamma+1/2}}{x_1}H_{3,3}^{2,1}\left((-1)^{\varepsilon/2\gamma}x_1\left|\begin{matrix}(1,1/2\gamma),(1,v/2\gamma),(1/2,1/2)\\(1,1),(1,1/2\gamma),(1/2,1/2)\end{matrix}\right.\right)-\\ -\frac{(-1)^{\varepsilon/2\gamma+1/2}}{x_1}H_{3,3}^{2,1}\left((-1)^{-\varepsilon/2\gamma}x_1\left|\begin{matrix}(1,1/2\gamma),(1,v/2\gamma),(1/2,1/2)\\(1,1),(1,1/2\gamma),(1/2,1/2)\end{matrix}\right.\right)\end{array}\right]. \quad (149)$$

For $\gamma = v = 1$, after a series of transformations, the solution to Eq. (149) coincides with the well-known solution to the ordinary diffusion equation.

The asymptotic expansion for the function $\rho(x,t)$ as $t \to \infty$ allows us to write:

$$\rho(x,t)\approx\frac{1}{2\pi}\sum_{n=0}^{\infty}\frac{t}{\Gamma\left[1-v(n+1)\right]}\times \\ \times\int_{-\infty}^{\infty}\frac{\hat{\rho}_0(k)\exp(ikx)}{\left[\tilde{D}(ik)^{2\gamma}-1/\tau^{v}\right]^{n+1}},t\to\infty, \quad (150)$$

For specific ones $\hat{\rho}_0(k)$, explicit expressions can be obtained (150). Let $\hat{\rho}_0(k)=\rho_0\delta(k),\ \tilde{D}=0$. Then

$$\rho(x,t)=\rho(t)= \\ =\frac{1}{2\pi}\rho_0\sum_{n=0}^{\infty}\frac{(-1)^{n+1}}{\Gamma\left[1-v(n+1)\right]}\left(\frac{t}{\tau}\right)^{-v(n+1)},\quad t\to\infty, \quad (151)$$

and $\rho(t)\sim 1/t^{v}$.

For $\rho_0(k)=\rho_0=const$ and $1/\tau^{v}$, we are dealing with pure diffusion. The solution is given by expression (149) and the diffusion displacement of the particle with time $x \sim t^{v/2\gamma}$. For $v = \gamma = 1$, we obtain the well-known relation $x^2 \sim t$. Approximate summation of the series in n in (147) for large t, which is carried out by preserving a small number of terms in the series in n and replacing the function $\Gamma(1 + vn)$ by the function $(1 + n)$ as $v \to 1$, allows one to obtain the asymptotics in t and for $\gamma \ne 1$.

2.18. Wave equation and fractal media

The results of studying a nonlinear equation of the generalized wave equation type in fractal space, a particular case of which are both the wave equation for a nonlinear medium and the nonlinear diffusion equation, are given in [23]. This equation describes the processes with the preservation of temporal and spatial memory in the form

$$D_{+,t}^{v}\rho(x,t)= \\ =\tilde{D}_0D_{+,x}^{\gamma}\left[\rho^{\sigma}(x,t)D_{+,x}^{\gamma}\rho(x,t)\right],v\ge0,\gamma\ge0, \quad (152)$$

where $D_{+,t}^{v}$ and $D_{+,x}^{\gamma}$ are the fractional Riemann-Liouville derivatives with respect to time and coordinate, $x > 0$; $\tilde{D}_0$ = const.

This equation differs from the nonlinear diffusion equation [57,58] of the form

$$\frac{\partial}{\partial t}\rho(t,x)=\frac{\partial}{\partial x}\left[\tilde{D}_0\rho^{\sigma}(t,x)\frac{\partial}{\partial x}\rho(t,x)\right] \quad (153)$$

with autowave solution

$$\rho=\rho_0\left[v^{-1}(vt-x)\right]^{1/\sigma},\quad 0\le x\le vt \quad (154)$$

by replacing time and space derivatives with fractional derivatives, considered as generalized functions. In this case, the boundary and initial

conditions of Eq. (153) are preserved for (152), and $\rho(x,t)$ is considered as a generalized function.

Equation (152) describes the propagation of electromagnetic waves in nonlinear fractal or weakly fractal (v ≈ 2, γ ≈ 1) media with an appropriate choice of values of v, γ, σ. With the addition of nonlinear terms in terms $\rho(x,t)$, Eqn (152) will describe both nonlinear diffusion and self-organization processes [57, 58].

3. APPLIED ASPECTS OF THE METHOD

3.1. Modern physical concept based on the theory of fractals and fractional operators

At present, there has been a noticeable increase in interest in understanding concepts such as *simplicity* and *complexity*, awareness of the various unique features of complex systems of animate and inanimate nature, including dissipativity, self-organization, fractality, scaling, heredity (non-Markovness), non-Gaussianity, linear and nonlinear responses to external disturbances. One of the main problems in analyzing signals produced by complex systems is the adequate parameterization of the contributions that characterize the components of the signals under study. Typically, the features of complex systems are manifested at different spatio-temporal scales. As is well known, stationary regimes and periodic motions have long been considered the only possible states. However, the discoveries of the second half of the 20th century radically changed our understanding of the nature of dynamic processes. Now we realize that our world is not only *nonlinear*, but also *fractal*. At present, the lack of traditional physical models is clearly felt.

Note that the main problems of radiophysics include the issues of radar detection of high-speed, stealthy and small-sized objects near the surface of the earth and the sea, as well as in meteorological precipitation, which is an extremely difficult task for high-speed targets and unpredictable trajectories [1,17,39,65]. In addition, interference from the sea surface and vegetation is of a non-stationary and multi-scale nature, especially at low grazing angles ϑ. Recently, more and more different types of unmanned aerial vehicles (UAVs) have appeared. Due to their small dimensions, as well as the use of plastics, fiberglass, polystyrene, even cardboard and other weakly reflecting electromagnetic waves in their designs, UAVs have a small effective reflectivity. The signal-to-noise ratio q_0^2 for the tasks listed above almost always fills the range of negative (in decibels) values, i.e. $q_0^2 < 0$ ... 1 dB.

As is well known, in experiments on the scattering of meter, decimeter, centimeter and millimeter waves, researchers faced questions of the legitimacy and applicability of Gaussian models. Soon, numerous artificial attempts began to create scattering models in order to increase the level of the "tails" of the probability distributions of the amplitudes of the reflected signals.

All this makes classical radar methods and detection algorithms difficult to apply, i.e. the use of energy detectors (when the likelihood ratio is determined exclusively and only by the energy of the received signal) becomes fundamentally impossible. The detection of low-contrast objects against the background of the above natural intense interference inevitably requires the introduction and calculation of some fundamentally new characteristic, which differs from the classical functionals associated with the energy of interference and signal, and is *determined solely by the topology and dimension of the received signal mixture with interference and noise.*

The application of the ideas of scale invariance - "scaling" - together with set theory, fractional dimension theory, fractional calculus, general topology, geometric measure theory, and dynamical systems theory opens up great potential and new perspectives in multidimensional signal processing and related scientific and technical fields. In other words, a complete description of the processes of modern signal and field processing is impossible using the approaches and formulas of only classical mathematics.

With the fractal-scaling approach, proposed and consistently developed by the author for more than 40 years at the V.A. Kotelnikov Institute of Radioengineering and Electronics (IRE) of RAS, the description and processing of signals and fields is carried out exclusively in the space of a fractional measure using scaling hypotheses, non-Gaussian stable distributions with heavy tails and, if possible, using the apparatus of fractional integroderivatives [1,5,7,16,17,34-84 , 99,100,107-109,113,123-133].

The evolution of the author's views and development at the moment in the IRE "fractal ideology" research is shown in **Fig. 19** and **Fig. 20**, which also provides information about the moment of their intensive deployment and open publications. All research is carried out by the author exclusively within the framework of a new fundamental interdisciplinary scientific direction, briefly designated as "Fractal radiophysics and fractal radio electronics: Design of fractal radio systems". In Fig. 19 introduced abbreviations: FNORS-fractal nonparametric detector of radar signals, FOS - fractal detector of signals.

Conventionally, three stages can be traced in these studies. At the *first stage,* the emphasis was placed on the experimental verification of the fractality of various natural and artificial formations, which made it possible to apply the concepts of fractional dimension and scale invariance to them, and to start developing methods for fractal filtering of objects in various intense noises. The *second stage* was entirely devoted to the improvement of the created original algorithms for fractal digital processing of signals and images, fractal methods of detection, recognition, enhancement of contrast, i.e. fractal

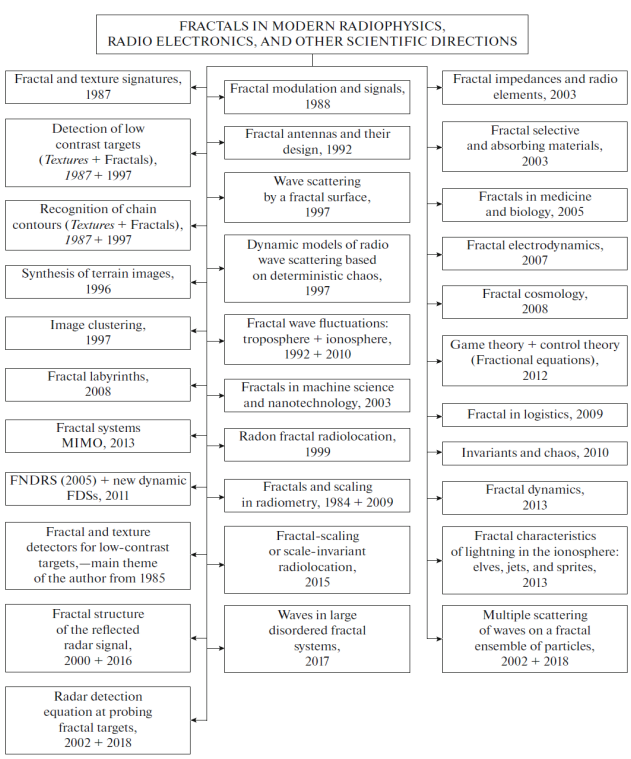

Fig. 19. *Sketch for the development of breakthrough technologies based on fractals, fractional operators and scaling effects for nonlinear physics and electronics.*

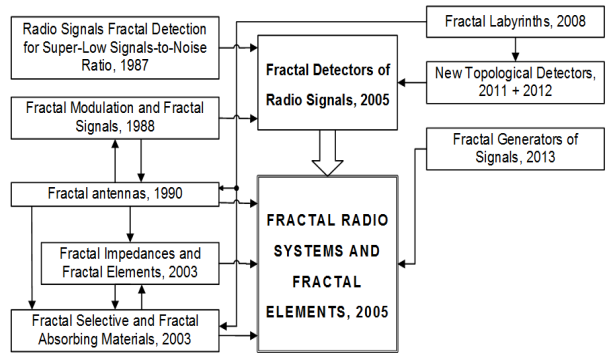

Fig. 20. *The author's concept of fractal radio systems, sensors, devices and radioelements.*

generalized filtering. The *third stage* is characterized by a transition to the design of a fractal element base and some fractal nodes, and in the future, fractal radio systems as a whole.

The analogy between the modern problems of radiophysics and radio electronics and the theory of phase transitions and critical phenomena is acquiring great importance. As is known, the modern renormalization group theory of phase transitions is based on an approach based on the scaling hypothesis, or scale invariance. On the basis of a deep study of this scientific direction, it was possible to form a similar approach for solving a large class of radiophysical and radio engineering problems.

Note that the presence of a fractional time derivative in the equations is interpreted as the presence of memory or, in the case of a stochastic process, non-Markovity.

3.2. Fractal measures and signatures

Fractals belong to sets with an extremely irregular branched or indented structure. The theory of fractals considers fractional measures instead of integer measures and is based on new quantitative indicators in the form of fractional dimensions D and corresponding fractal signatures. Fractal fractional dimensions D characterize not only the topology of objects, but also reflect the processes of evolution of dynamical systems and are related to their properties.

The classification of fractals developed by the author was approved in the USA in December 2005 and adopted by B. Mandelbrot [43,58,62]; it is shown in **Fig. 21**, where the properties of fractals are described, provided that D_0 is the topological dimension of the space in which a fractal with fractional dimension D is considered.

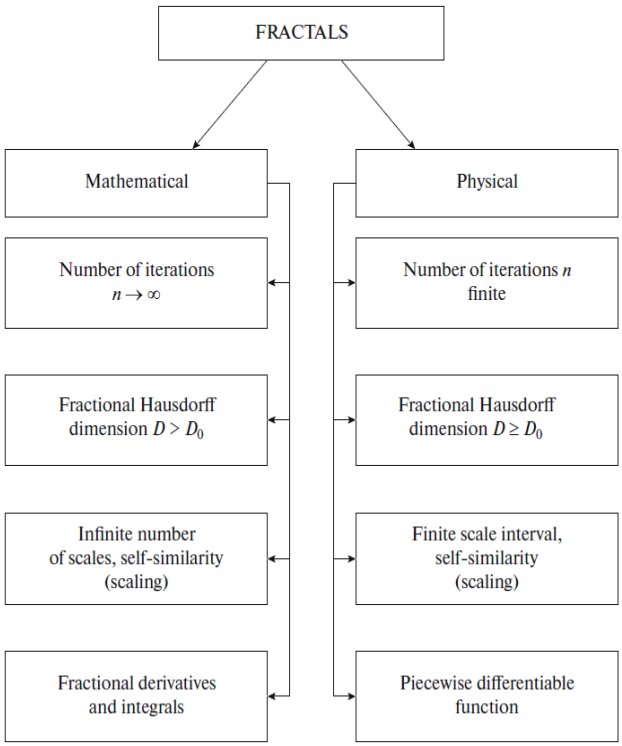

Fig. 21. *The author's classification of fractal sets and signatures, approved by B. Mandelbrot.*

Based on the data in Fig. 21, one can give a *mathematical definition* of a fractal.

A fractal is a functional mapping or set obtained by an infinite recursive process and having the following properties: 1) self-similarity or scale invariance (infinite scaling), that is, fractals on small scales look on average the same as on large ones; 2) fractional dimension (called Hausdorff dimension) strictly greater than topological dimension; 3) nondifferentiability and operation of fractional derivatives and integrals ".

The *physical* definition of a fractal is as follows:

"*Fractals* are geometrical objects (lines, surfaces, bodies) with a highly irregular structure and possessing the property of self-similarity on a limited scale."

The introduction by the author into the practice of measurements of the concepts of *fractal signatures* and *fractal cepstras* proved to be very fruitful [44,45,48,49,52-64,66-79,82,84,124-133]. The concept of "cepstrum" historically comes from the permutation of letters in the word "spectrum". The concept of "fractal cepstrum" is determined by the fact that when calculating the fractal dimension D of the received multidimensional signal, it is necessary to take the logarithm of the amplitudes averaged on different scales of the received time/space samples. Fractal signatures and fractal cepstras reflect the property of self-similarity of real signals and electromagnetic fields. Thus, in fractal processing methods it is always necessary to take into account the *scaling effects of real radio signals and electromagnetic fields*.

3.3. Texture and fractal processing of low-contrast images and ultra-weak signals in intense non-Gaussian interference and noise

In **Fig. 22** shows the complete structure of the author's research at the IRE of Russian Academy of Sciences of *texture* and *fractal* methods for processing low-contrast images and ultra-weak signals in intense non-Gaussian noise. The textural and fractal digital methods developed by the author make it possible to partially overcome the a priori uncertainty in radiophysical and radar problems using the *geometry* or *topology of the sample* - one-dimensional or multidimensional [17,57,58,62,82,84].

In this case, the topological features of the sample are of great importance, rather than the averaged realizations, which often have a different character. In order to focus on taking these features

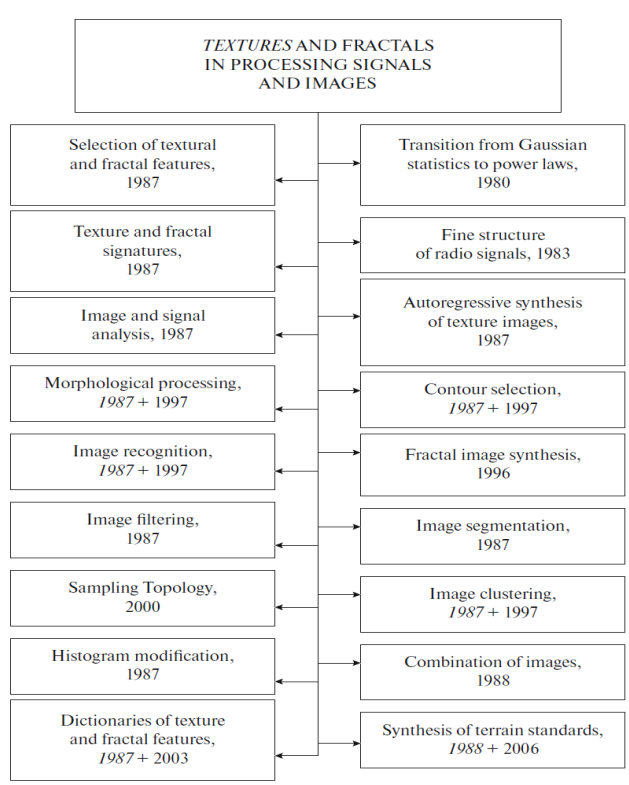

Fig. 22. *Classification of texture and fractal methods for processing low-contrast images and ultra-weak signals.*

into account, the term *dimensional sclerosis* of physical signals, fields and their fractal signatures was specially introduced [57,58,82]. When describing non-Markov processes, as is known [88], the term *asymptotic sclerosis* is widely used to reveal the physical meaning of fractional derivatives.

Texture is a matrix or fragment of spatial properties of image areas with homogeneous statistical characteristics [57,58]. Textural features (TP) are based on the statistical characteristics of the intensity levels of image elements and refer to probabilistic features, the random values of which are distributed over all classes of natural objects. The decision on whether a texture belongs to a particular class can be made only on the basis of specific values of the features of a given texture. In this case, it is customary to talk about t*he signature of the texture.*

Classic radar signatures include temporal, spectral and polarization features (features) of the reflected signal. The term "signature" describes the distribution of the general set of measurements for a given texture in scenes of the same type as this one [53]. In our experiments, we also optimized estimates of the effect of window size on the accuracy of determining texture features for images of various types of land cover. For a long time, the first works of the author in the field of research of joint radar (RI) and optical images (including synthetic aperture radars - SAR) of the earth covers using texture and fractal information, were actually the only ones in the USSR and Russia, and today they are also not lost relevance.

On the basis of the results obtained by the author, the following unconventional and rather effective methods of signal detection at small signal-to-background ratios were first proposed and implemented: q_0^2*-the dispersion method, the detection method using linearly modeled standards, and the method with direct use of the ensemble of texture features* [44].

We especially note that the developed fractal (topological) methods constitute an independent area of research and are not directly related either to classical probability distributions of mathematical statistics, or to the classical theory of outliers, or to questions of statistical topography of random processes and fields.

If, in syntactic or structural recognition, the structure of objects, its hierarchy and connections between them are investigated, then in *fractal recognition,* the topology of the object and the background, displayed in one-dimensional and multidimensional received radar signals, is investigated. With the fractal approach, it is necessary to search, implement and use the rules that obey the fractional (complex) topology of the images under consideration. Then the procedure of *fractal recognition* is a comparison with the dictionary of fractal features [57,58,62,77,82].

In this case, we will highlight the "*fractal primitives*" - the elements of the "*fractal language*". The question inevitably arises about the composition of fractal primitives - *fractal symbols*, which are the smallest elements of a fractal language. We will call the set of fractal symbols used "*fractal alphabet*" or "*fractal dictionary*", denoted by the symbol Φ. On the basis of the latter, one can compose "*fractal strings*" - finite sequences of symbols included in the alphabet. The string can be any length. All possible strings of the fractal alphabet form a universal set of strings or a closure Φ. If we introduce a set of empty lines, then a finite or countable infinite subset of the closure of the fractal alphabet Φ is a more precise definition of the concept of "*fractal language*". Separate fractal lines, composed of its fractal symbols, we will call "*fractal words*".

Further, performing some logical operations on a fractal language, you can create a new language. The rules for creating, transforming and interacting fractal words will be determined by the "*fractal grammar*". For its construction, it is possible to use the ideas of formal grammar developed in mathematical linguistics.

3.4. Formal fractal grammars

Formal grammar methods are characterized by two features [15]. First, they describe only a set of possible results and do not give direct instructions on how to get the result for a particular task. Secondly, in them all statements are formulated exclusively in terms of a small number of well-defined and elementary symbols and operations. Therefore, formal grammars are simple from the point of view of their logical construction.

A formal grammar can be defined by a generative grammar - the system

$$G = \langle C_t, C_n, P, A \rangle, \tag{155}$$

consisting of four parts: terminal (main) dictionary C_t, nonterminal (auxiliary) dictionary C_n, set of substitution rules P, initial symbol or initial axiom $A(A \in C_n)$.

Terminal (main) dictionary C_t is a set of non-derivative terminal elements or features from which the chains generated by the grammar are built. The choice of non-derivative elements refers to the problem of determining informative and stable features for recognition. Nonterminal (auxiliary) vocabulary C_n - a set of symbols that denote classes of source elements or chains of source elements, as well as some special nonterminal or auxiliary elements. The initial symbol A is a distinguished nonterminal symbol denoting a collection or class of all those linguistic objects for which this grammar is intended to describe (for example, in a grammar that generates sentences, the initial symbol is a symbol meaning a sentence, etc.). The set of substitution rules P is a finite set of rules of the form $\varphi \to \psi$, where φ and are words in the dictionary (alphabet) $C_n \cup C_t$ and "→" is a symbol that does not belong $C_n \cup C_t$. Generative grammar is not an algorithm because substitution rules are a collection of solutions, not a sequence of prescriptions.

Formal grammar is characterized by the following ratios:

$$C = C_n \cup C_t,\ C_n \cap C_t = 0, \quad (156)$$

where C is a dictionary.

The process of creating a language begins with Axiom A, to which the substitution rules are applied one by one. Conjunction, disjunction, negation are used as operations on statements.

Let's consider an example of the formation of some *fractal primitives*. In practice, to obtain a fractal grammar, it is necessary to derive it from a given ensemble of learning objects. This procedure is similar to the learning problem in various recognition methods. Algorithms for fractal pattern recognition are based on the use of the "t*arget topology - its fractal dimension*" paradigm. The a priori space of deterministic or probabilistic features is determined using a dynamic test.

The selection and preparation of test material for experimental verification of fractal recognition methods and verification of the principles of constructing algorithms significantly affect the reliability of the research results. In the vast majority of problems arising in practice, the classical methods of the theory of statistical decisions are of little use for recognizing radar targets. This is due to the fact that there are: severe restrictions on the analysis time, bandwidth of information transmission channels; high level of a priori uncertainty; the impact of various kinds of interference, a wide variety of characteristics of targets combined into one class, unknown target orientation; the simultaneous presence of several targets, differing in orientation and size.

The formalization of the problem under consideration classically presupposes the following stages: (**i**) - the initial a priori classification of goals or their classes, i.e. compilation of an alphabet of classes of goals; (**ii**) - determination of the required list of features that characterize the goals (in this case, we are talking only about fractal features); (**iii**) - development of a reference dictionary of fractal attributes of goals or classes of goals; (iv) - description of the alphabet of target classes in the language of the ensemble of fractal features of the reference dictionary or their combinations; (v) - partition of the space of fractal features into regions corresponding to the original classes of the alphabet; (**vi**) - the choice of a metric (decision rule) or recognition algorithms that ensure the assignment of a recognized target to one or another class of targets. When developing the first reference dictionary of fractal features, the latter were selected: 1) - the value of the fractal (fractional) dimension D; 2) - the type of fractal signatures or fractal cepstras; 3) - the type of the spatial spectrum and the values of spatial frequencies that characterize the texture of the images [57,58,62,77,82].

It is proved that fractal cepstrum is, on the one hand, a convenient topological invariant - it does not require preliminary orientation/scaling, and on the other hand, it is insensitive to image contrast. Thus, the positions of the characteristic points on fractal cepstras make it possible to determine the class of the target (according to some rule), its size, as well as the number of targets. The relative change in the position of the characteristic points makes it possible to solve the problem of detecting a deterministic target even with very low contrast.

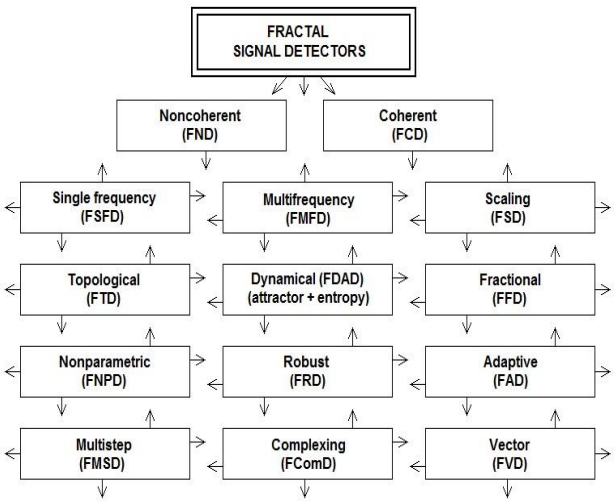

Fig. 23. *The main types of the proposed fractal-scaling or topological signal detectors.*

3.5. Fractal radar signal detectors

Creation of the first reference dictionary of fractal features of target classes and constant improvement of algorithmic support were the main stages in the development and prototyping of the first fractal nonparametric radar signal detector (FNORS) in the form of a special processor [16,17,47,57,58,62,77,82-84]. The main types of the proposed topological signal detectors are shown in **Fig. 23**.

3.6. Adaptation of fractal detectors

The creation of adaptive methods as applied to fractal information processing is of great interest. As is known [87], an adaptive problem is characterized by a change in the parameters and / or structure of the system in accordance with external conditions. Some ways of obtaining theoretical and technical solutions to the problem of synthesis of adaptive fractal detectors are shown below [42,46,57,58].

Working with signal sampling against the background of noise and noise in the space of fractional measure, we inevitably come to algorithms (criteria) of adaptive fractal filtering. The adaptation of such nonlinear fractal filtering under conditions of a priori uncertainty is provided, in particular, by the current estimate of the Hurst exponent N. As noted above, the Hurst exponent, depending on its value relative to the value H = ½, characterizes either persistence (½) or antipersistence ($0 < H <$ ½) sampling.

In the first case, when $1/2 < H < 1$, we observe a process that maintains the tendency of an increase or decrease in instantaneous amplitudes in the sample, i.e. process with memory. In the second case, when $0 < H < 1/2$, an increase in the amplitudes of the signal envelope in the "past" means a decrease in the "future", and vice versa, i.e. a process that is more subject to change, often referred to as "return to the mean".

Fixing the value of H in terms of [87] is a *counter hypothesis* that improves the quality of adaptation to real conditions. In the general case, the device is a tracking system that adapts the values of the Hurst exponent N to the interference situation or, conversely, to the useful signal. An example of an adaptive procedure is the automatic control of the receiver gain depending on the current estimate $H = f(t)$. In another adaptive procedure, the detection threshold P is automatically adjusted according to the values $H = f(t)$. This ensures the stabilization of the false alarm probability.

3.7. Fractal scaling or scale invariant radar

The detection of low-contrast objects against the background of natural intense interference inevitably requires the calculation of a fundamentally new characteristic, which differs from the functionals associated with interference and signal energy, and is determined only by the topology and dimension of the received signal. The introduction of the concepts of "deterministic chaos", "texture", "fractal" and "fractal dimension D" into the scientific use of radar [17,36,57,58,62,77,82-84] allowed us for the first time in the world to propose, and then and apply new dimensional and topological (not energy!) features or invariants (**Fig. 24**), which are combined under the generalized concept of "sample topology" ~ "fractal signature".

Fractal-scaling or scale-invariant radar [17,47,52,54,55,61,66-68,82-84,125,127,130,131] is based on three *postulates:* 1 – intelligent signal/ image processing based on fractional measure theory and scaling effects, for calculating the field of fractal dimensions; 2 – the sample of the received signal in noise belongs to the class of stable non-Gaussian probability distributions D of the signal; 3 – maximum topology with minimum energy of the input random signal. These postulates open up fundamentally new possibilities for ensuring stable operation at short q_0^2 or increased ranges of radars. Algorithms for detecting extended objects and targets on optical and radar images using texture

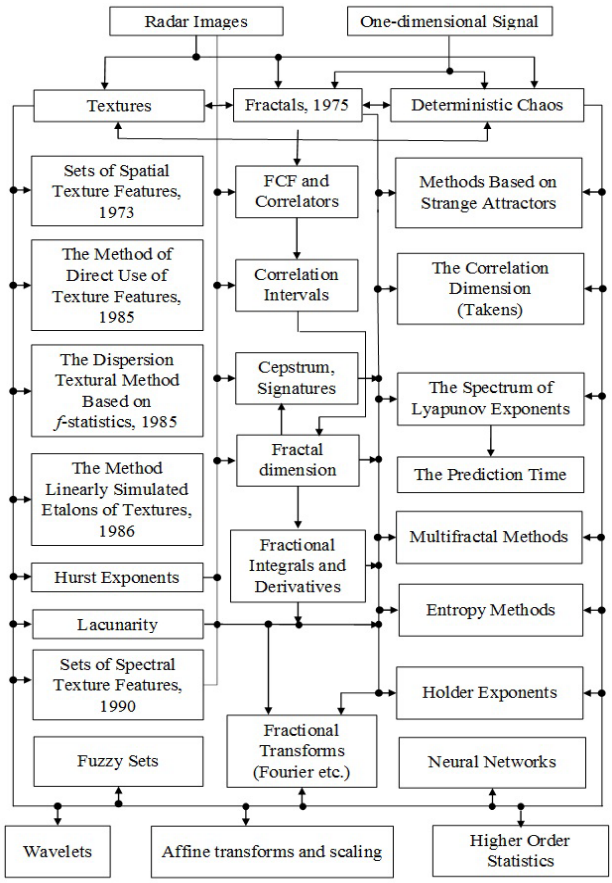

Fig. 24. *New topological features and methods for detecting low-contrast objects against the background of interference (TP - texture features, PFC - frequency coherence function).*

processing were created by us back in the 80s of the XX century (see the left column in Fig. 24).

3.8. Main results

As a result of joint long-term field experiments with leading industry research institutes and design bureaus of the USSR and Russia, a statistical analysis of large arrays of new data on the spatial and temporal characteristics of earth cover scattering in the IIM and CMB ranges was carried out, taking into account their seasonal and angular variations in various meteorological conditions in order to assess boundaries of radar contrasts, distribution laws of specific RCS, spectrum width, time and correlation interval of intensity fluctuations of reflected simple and complex phase-shift keyed signals in the IIM range and the structure of reflected pulse signals, which makes it possible to take into account terrain features when designing various imaging systems.

A theory of scattering of millimeter radio waves by chaotic covers has been developed, using the first introduced functionals of backscattering stochastic fields and frequency coherence functions (PFCs) taking into account the antenna directional pattern and correlation of the slopes of irregularities. The results of this theory make it possible to determine the coherence bands of space-time radio channels with variable parameters for the optimal choice of the width of the sounding signal spectrum, frequency spacing in multifrequency systems and the base value of complex sounding signals, characteristics of reflected signals, generalized uncertainty functions, potential accuracy of estimates of the flight altitude, and the characteristic dimensions of the irregularities. Theoretical and experimental results were used in the synthesis of reference digital radar maps of the area.

For the first time, a new class of informative features has been proposed, based on the fine structure of reflected millimeter-wave radar signals, and allowing to improve the identification of earth covers.

For the first time, complete ensembles of texture and spatial correlation-spectral features of optical and radar images of real earth covers were investigated, followed by the selection of clusters and the determination of the most informative features for certain classes of textures. It is proved that the area of existence of texture features of radar images is completely determined by the corresponding areas of features of optical images. The experiments carried out have demonstrated the efficiency and generality of the proposed approach in the problems of classification of the earth's covers when integrating images at optical and millimeter waves. Image integration increases the efficiency of detection, recognition and classification based on an extended vector of informative and stable features. Image processing results in detailed digital radar maps of the area. Such maps make it possible to present radar information in a form convenient for further use in radio navigation of aircraft and recognition of various types of ground objects. [Note that these studies had no analogues, both in the USSR and in Russia, and have not lost their relevance at the present time].

For the first time, a number of texture methods have been developed (Fig. 22, Fig. 24) for detecting various objects and their contours on real optical and radar images of the earth's surface at low signal /background ratios. A relationship is established between the size of the object and the analyzed

fragment of optical and radar images of a wide class of earth covers in the case of optimal detection. The possibility of stochastic autoregressive synthesis of optical and radar images of earth covers with the operation of converting brightness histograms has been theoretically substantiated and experimentally confirmed. The optimal sizes of the brightness space and the order of autoregressive series involved in forecasting for adequate synthesis of images have been determined. With an increase in the order of correlation, the areas for determining the textural features of synthesized images are narrowed. When comparing sections of the original optical or radar image with the synthesized standard, it is shown that the final two-dimensional binary field of cross-correlation coefficients directly fixes the location of the object in the original image. This allows you to form a motion map and the dynamics of the detected object. It was established using various matching algorithms (classical correlation, pair function method, absolute difference method) that the physical reliability of stochastic autoregressive synthesis reaches 90%.

A system approach to the formation of an information-axiomatic model of radar maps of heterogeneous terrain has been developed and implemented on the basis of the above radiophysical studies. A generalized radiophysical model for the formation of radar maps of heterogeneous terrain has been created, which includes both methods of stochastic autoregressive synthesis of images, and information about the field of specific EPR of the earth's covers. The characteristic number of gradations of the specific EPR of the earth's surface has been established. Based on the analysis of the system architecture to obtain a standard, an algorithm for the synthesis in the radio range of contour and grayscale radar maps of inhomogeneous terrain is implemented. It is shown that the destruction of the correlation maximum occurs for a contour radar map of the area at a wavelength of 8.6 mm at an angle of mutual rotation of 5°… 7°, and for a half-tone radar map - at an angle within 14°… 17°. Then, fractal parameters were first introduced into the generalized radiophysical model of the formation of radar maps of heterogeneous terrain, which increased the information content of the synthesis.

The presence of a strange attractor is predicted to control radar scatter from vegetation. Subsequently, the effect was discovered experimentally at a wavelength of 2.2 mm (2002). The results obtained confirmed the theoretical concepts of the existence of a chaos regime in a dynamical system that describes the nature of the scattering of electromagnetic waves by vegetation [81].

Reconstruction of the attractor made it possible to determine its fractal dimension *D*, the maximum Lyapunov exponent, the dimension of the embedding, and the prediction interval (time). The experimental characteristics of the strange attractor formed the basis for a fundamentally new non-Gaussian model of radar scattering of the IMV by vegetation covers based on the theory of dynamical systems and stable distributions. It is shown that the interval (time) for predicting the intensity of the reflected radar signal exceeds the classical correlation time by about an order of magnitude. This made it possible to introduce into the theory of radar a new essential characteristic, namely, the prediction interval (time), which expands the methods and circuitry of radars.

A reliable physical substantiation of the practical application of fractal methods (Fig. 19 - Fig. 24) in modern fields of radiophysics, radio electronics and information control systems is given.

In the mid 80s. XX century. A working model of a coherent compact digital solid-state radar (TsTR) based on parametrons with a probing wavelength of 8.6 mm with a complex signal base> 106 and with processing of an input subnoise signal at a carrier frequency was created jointly with the Almaz Central Design Bureau. With optimal processing, the energy potential of the CTR increased by 50 dB. Then, a DTC was created at two sounding frequencies in the MMV and CMB bands with a fractal slot antenna (the first in the USSR); for the synthesis of images, the Radon transform is used. In 1997, the first developed methods of fractal modulation and fractal signals, including the first introduced by the author H-signals.

Together with representatives of the Central Design Bureau "Almaz" A.A. Potapov was one of the co-leaders of the international project No. 0847.2 through the ISTC (2000-2005) to create a multifunctional automated radio measuring system

with a complex signal at centimeter and millimeter waves, using fundamentally new patented circuitry and digital information processing technologies based on fractal and Radon algorithms in real time. Giving lectures on fractal and texture technologies developed by him at IRE RAS and reports on the ISTC project in 2000 and 2005 in the USA (Washington, New York, Huntsville, Atlanta, Franklin), in China (2011 to the present) time) and at numerous International conferences (England, USA, Canada, Holland, Austria, Germany, France, Spain, Italy, Hungary, Greece, Turkey, Scotland, Switzerland, Sweden, Mexico, China, Serbia, Montenegro, Bulgaria, Kazakhstan, Belarus, Ukraine) brought him wide fame in the circles of the international scientific community.

In December 2005, American specialists (from the University of Alabama and the Center for Space Plasma and Aerial Research of the United States) in an official letter addressed to the Director of the IRE RAS Academician Yu.V. Gulyaev, it was noted that "... *The seminars were extremely interesting and confirmed the high scientific qualifications of Dr. A. Potapov. Radar technologies presented by Dr. A. Potapov are based on the theory of fractals and are new. The importance of these studies for the international community of specialists and scientists is undeniable*" – (**Fig. 25**).

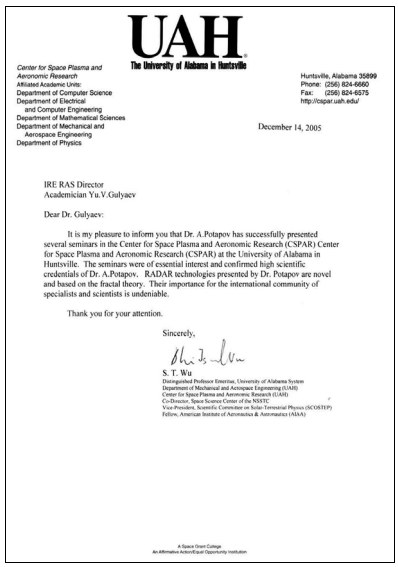

UAH
The University of Alabama in Huntsville

Center for Space Plasma and Aeronomic Research
Affiliated Academic Units:
Department of Computer Science
Department of Electrical and Computer Engineering
Department of Mathematical Sciences
Department of Mechanical and Aerospace Engineering
Department of Physics

Huntsville, Alabama 35899
Phone: (256) 824-6680
Fax: (256) 824-6575
http://cspar.uah.edu/

December 14, 2005

IRE RAS Director
Academician Yu.V.Gulyaev

Dear Dr. Gulyaev:

It is my pleasure to inform you that Dr. A.Potapov has successfully presented several seminars in the Center for Space Plasma and Aeronomic Research (CSPAR) Center for Space Plasma and Aeronomic Research (CSPAR) at the University of Alabama in Huntsville. The seminars were of essential interest and confirmed high scientific credentials of Dr. A.Potapov. RADAR technologies presented by Dr. Potapov are novel and based on the fractal theory. Their importance for the international community of specialists and scientists is undeniable.

Thank you for your attention.

Sincerely,

S. T. Wu
Distinguished Professor Emeritus, University of Alabama System
Department of Mechanical and Aerospace Engineering (UAH)
Center for Space Plasma and Aeronomic Research (UAH)
Co-Director, Space Science Center of the NSSTC
Vice-President, Scientific Committee on Solar-Terrestrial Physics (SCOSTEP)
Fellow, American Institute of Aeronautics & Astronautics (AIAA)

A Space Grant College
An Affirmative Action/Equal Opportunity Institution

Fig. 25. *Letter from the US Space Plasma Center.*

At the same time, a significant and long-term scientific meeting of A.A. Potapov with the founder of fractal geometry B. Mandelbrot at his home in the USA, when he accepted and approved the definition of fractals introduced by A.A. Potapov in his books and articles, and his work (**Fig. 26**).

For the first time, the effectiveness and prospects of applying the theory of fractional measures and scaling relations (for textures and fractals) in the case of detection and recognition (generalized filtering) of one-dimensional and multidimensional radar signals from low-contrast targets against the background of intense non-Gaussian interference of various kinds was discovered and proved. Thus, this is a *fundamentally new* radioengineering.

It has been proved that when collecting, transforming and storing information in modern complex systems for monitoring remote and mobile objects in conditions of intense interference, the newest methods of processing information flows and multidimensional signals, proposed by the author, are of great importance. Typically, the features of such complex systems are manifested at different spatio-temporal scales. The most adequate assessments of the states of the system under study and the dynamics of changes in the state of its subsystems are realized using the theory of fractals and processing multidimensional signals in a space of fractional dimension with the indispensable consideration of the effects of scaling, which was first proposed and developed by the author at the IRE RAS.

A new method of measuring fractal dimension and corresponding fractal signatures of signals, images and wave fields is proposed and substantiated. This method, as well as its effectiveness, has been confirmed in practice by numerous examples of appropriate digital processing of optical and radar natural and synthesized images, including those

Fig. 26. *B.B. Mandelbrot and A.A. Potapov. New York, USA, 2005*

with low-contrast objects. Texture and fractal digital methods (Fig. 19 and Fig. 22) make it possible to partially overcome the a priori uncertainty in radar problems using the *geometry* or *topology of the sample* - one-dimensional or multidimensional. In this case, the topological features of the sample are of great importance, rather than the averaged realizations, which often have a different character.

Methods of fractal classification, clustering and recognition of many types of natural and artificial objects have been studied for the first time on large arrays of experimental data in the form of optical and radar images of real earth covers with surface and subsurface objects. The number of areas around which the fractal dimension values are grouped depends on the parameters of the algorithm and the measurement method. For example, with a small size of the measuring window, we have a large number of groups; increasing the size, we get a fixed number of groups or clusters; and finally, with a very large window size, 2 - 3 groups remain (fractal objects - non-fractal objects - exclusion objects).

The study of the type or topology of sampling a one-dimensional (multidimensional) signal for tasks, for example, artificial intelligence, for the first time made it possible to create dictionaries of fractal features based on fractal primitives, which are elements of a fractal language with fractal grammar. The data obtained were incorporated into the synthesis of reference and current radar maps of heterogeneous terrain, as well as into non-energy radar detectors.

The results (UAV, SAR, medicine, etc.) show that fractal processing methods increase the quality and detail of objects and targets in passive and active modes by several times. These methods can be successfully applied to process information from space, aviation complexes, low-signature high-altitude pseudo-satellites (HAPS) or the detection of HAPS and UAV clusters, synthesized clusters of space antennas and space debris.

The fractal characteristics of elves, jets and sprites - the most interesting types of recently discovered high-altitude discharges in the ionosphere - are investigated.

Algorithms for detecting a moving distant object of unknown shape (fractal or non-fractal) on a low-contrast image formed in optoelectronic systems have been synthesized with co-authors. Experimental results on images obtained in field conditions confirm the effectiveness of the proposed processing methods.

For the first time, the fundamental possibility of synthesizing new fractal functions and fractal functionals on the basis of the theory of fuzzy sets has been proved. Formalized the construction of new classes of fractal and multifractal subsets on fuzzy sets. Any classic non-differentiable functions can be used as trial functions.

It is shown for the first time that the physical content of the theory of diffraction, containing multiscale surfaces, becomes clearer with the fractal approach and the separation of the fractal dimension D or the fractal signature as a parameter. Taking into account fractality significantly brings the theoretical and experimental characteristics of the scattering indicatrices of the earth's covers closer together, which is important for the problems of radar and remote sensing. For the first time in the world, an extensive catalog of characteristic types of more than 70 fractal surfaces based on Weierstrass functions, as well as more than 70 three-dimensional scattering indicatrices and their cross sections calculated for wavelengths $\lambda = 2.2$ mm, $\lambda = 8.6$ mm and $\lambda = 3$ cm at different values of fractal dimension D and varying scattering geometry.

Analogs of Maxwell's equations with fractional Caputo derivatives are obtained. Gauge invariance is considered and a diffusion-wave equation for scalar and vector potentials is derived. A particular solution of the diffusion-wave equation is found and analyzed [9,10].

A rigorous electrodynamic calculation of numerous types of fractal antennas was carried out, the design principles of which underlie fractal frequency-selective surfaces and volumes (fractal "sandwiches").

A family of broadband miniature fractal antennas is synthesized based on the topology of fractal labyrinths. The author proposed to synthesize large stochastic robust antenna arrays using the properties of fractal labyrinths. Combining several fractal labyrinth clusters with different fractal dimensions makes it possible to create adaptive broadband fractal antennas. For the first time, a model of a "fractal"

capacitor as a fractal impedance is proposed and implemented.

Created, substantiated and applied fractal-scaling methods for radar problems and the formation of the foundations of a fractal element base, fractal sensors and fractal radio systems. A physical approach to modeling a fractal capacitor and fractal impedances has been developed. Promising elements of fractal radio electronics are functional elements, the fractal impedances of which are realized on the basis of the fractal geometry of conductors on the surface (fractal nanostructures) and in space (fractal antennas), fractal geometry of the surface microrelief of materials, etc. The developed approaches can be extended to a wide class of electrodynamic problems in the study of fractal magnonic crystals, fractal resonators, fractal screens and barriers, as well as other fractal frequency-selective surfaces and volumes.

A new type and new method of modern radar, namely, fractal-scaling or scale-invariant radar, has been discovered, proposed and substantiated. The efficiency of functionals, which are determined by the topology, fractional dimension and texture of the received multidimensional signal, for the synthesis of fundamentally new non-energy detectors of low-contrast objects against the background of noise has been proved (Fig. 19, Fig. 20, Fig. 23). An increase in the sensitivity of the radio system (which is equivalent to an increase in the range) was confirmed when using fractal and texture features in topological detectors. This entails fundamental changes in the very structure of theoretical radar, as well as in its mathematical apparatus.

Fractal radar is capable of adequately describing and explaining a much broader class of radar phenomena. The scientific direction created for the first time in Russia and in the world is based on the concept of fractal radio systems and fractal radioelements, sampling topology and the global fractal-scaling method, proposed and created by the author at the V.A. Kotelnikov IRE of RAS. The research carried out in the field of theoretical radar makes it possible to effectively solve the problems of signal detection in conditions of intense interference and create new fractal multifrequency MIMO systems

The postulates of fractal scaling radar have been developed: 1 – intelligent signal/image processing based on the theory of fractional measures and scaling effects for calculating the fractal dimension field; 2 – the sample of the received signal in noise belongs to the class of stable non-Gaussian probability distributions D of the signal; 3 – maximum topology with minimum energy of the input random signal (ie, maximum "deviation" from the energy of the received signal).

These postulates open up new possibilities for ensuring stable operation at low signal / (noise + interference) ratios or increasing the range of radars.

Theoretical issues of fractal non-inertial relativistic radar and quantum cosmology in curved space-time of negative fractal dimension have been significantly developed together with colleagues from Russia (Moscow, VNIIOFI) and Israel (Haifa, Technion). *Example:* on the basis of the Schrödinger equation with the operator of fractional calculus in spatial coordinates, the Feynman integral over trajectories is calculated for the generalized Lagrangian with the operator of fractional differentiation in time. Note that at present in the United States this fundamental scientific direction has received the bright name "*Fractal Cosmology*" [34,35,82,99,108,123].

4. CONCLUSION

The results of experimental and theoretical research obtained by the author and his students were introduced by the leading industry research institutes and design bureaus of the USSR and Russia and were used in the design of radio systems for various purposes, in the interpretation of data from remote radiophysical studies of the environment and in other applied problems in which optical and radar systems serve as information materials. images of the earth's surface.

On the basis of many years of research, new theoretical directions in the theory of statistical decisions, statistical radio engineering and statistical radiophysics have been formulated and developed, for example, "Fractal analysis and its application in the theory of statistical decisions and statistical radio engineering", "Statistical theory of fractal radar", "Statistical fractal radio engineering", "Theoretical foundations of fractal radar", etc.

The above results formed the basis of the fractal paradigm and a single global idea of fractal natural science [73, 82].

The performed studies are a priority in the world and serve as a basis for further development and substantiation of the practical application of the fractal-scaling and texture methods created by the author in modern radiophysics and radar, as well as in the creation of fundamentally new and more accurate topological fractal-texture methods for detecting and measuring parameters of radio signals in spatio-temporal radar channel of propagation of electromagnetic waves with scattering.

The radio engineering "fractal geometry" of the transceiver or any information radio engineering, optoelectronic and acoustoelectronic systems, along with fractal modulation/demodulation and cryptographic resistance methods (fractal ultra-wideband signals, fractal information compression [57,58]) are extremely promising measures for solving urgent problems of traditional radio electronics, which since its inception is completely based on an integer measure.

These issues are relevant in solving the problems of constructing and optimizing the characteristics of modern and promising radio-physical intelligent sensing systems for detecting and recognizing various objects in difficult conditions using topological fractal and texture methods based on the previously proposed general principles of fractal-scaling or scale-invariant radar [57, 58.82.84.125-132.137.138]. It should be noted that *fractal radars* are, in fact, a necessary intermediate stage on the path of transition to *cognitive radar* and *quantum radar*. Note that our recent results with our Chinese colleagues on the effects of microscale optoelectronics and photonics [107,139-145] will help open the way for controlling light scattering using magnetoelectric couplings and previously unknown wave phenomena in order to design new devices for processing multidimensional signals in such intelligent systems.

Based on the author's monographs, courses of lectures on fractals in radiophysics and radio electronics have been delivered at various universities in Russia and neighboring countries, as well as in China. The author's priority in the above scientific areas is secured in the world by more than 1150 scientific works, including 45 domestic and foreign monographs and individual chapters in them in Russian and English, and 2 patents (see, for example, [82,83,139]).

REFERENCES

1. Akinshin RN, Potapov AA, Rumyantsev VL and others. *Physical foundations of the device of missile and artillery weapons. Algorithms and devices for the functioning of airborne radio-technical means of air reconnaissance of artillery.* Penza: Branch of VA MTO, Penz. art. Ing. Institute, 2018, 400 p.
2. Alexandrov PS. *An introduction to set theory and general topology.* Moscow, Nauka Publ., 1977, 368 p.
3. Alexandrov PS, Pasynkov VA. *An introduction to dimension theory*. Moscow, Nauka Publ., 1973, 576 p.
4. Babenko YI. *Fractional Differentiation Method in Applied Problems of Heat and Mass Transfer Theory.* SPb, NPO "Professional" Publ., 2009, 584 p.
5. Bagmanov VH, Potapov AA, Sultanov AH, Wei Zhang. Fractal filters for signal detection in remote sensing data processing. *Radioengineering and electronics,* 2018, 63(10):1062–1068.
6. Bardou F, Buscho J-F, Aspe A, Cohen-Tannoudji K. *Levy statistics and laser cooling. How rare events stop atoms.* Moscow, Fizmatlit Publ., 2006, 216 p.
7. Bekmachev YES, Potapov AA, Ushakov PA. Designing fractal proportional-integral-differential fractional order controllers. *Uspekhi sovrem. radioelectr.*, 2011, 5:13-20.
8. Bogachev VI. *Foundations of measure theory.* Moscow-Izhevsk, Research Center Regular and Chaotic Dynamics Publ., 2006, vol. -544 p.; vol. 2-576 p.
9. Bogolyubov AN, Potapov AA, Rekhviashvili SS. Interpretation of the solution of the diffusion-wave equation using fractional integro-differentiation. *Vestn. Moscow univ. Ser. 3. Physics. Astronomy,* 2010, 3:54-55 (in Russ.).
10. Bogolyubov AN, Potapov AA, Rekhviashvili SS. Method of introducing fractional integro-differentiation in classical electrodynamics. *Vestn. Moscow univ. Ser. 3. Physics. Astronomy,* 2009, 4:9-12.
11. Baer R. *Theory of discontinuous functions.* Moscow-Leningrad, ONTI Pudl., 1932, 136 p.
12. Voroshilov AA, Kilbas AA. Cauchy problem for diffusion-wave equation with partial derivatives of Caputo. *Differentsialnye uravneniya*, 2006, 42(5):595-609 (in Russ.).
13. Gelfand IM, Shilov GE. *Obobshchennye funktsii i deystviya nad nimi* [Generalized functions and actions on them]. Moscow, Fizmatlit Publ., 1958, 440 p.
14. Gnedenko BV, Kolmogorov AN. *Predel'nye raspredeleniya dlya summ nezavisimykh sluchainykh velichin* [Limit distributions for sums of independent random variables]. Moscow-Leningrad, GITTL Publ., 1949, 264 p.

15. Gorelik AP, Skripkin VA. *Metody raspoznavaniya* [Recognition methods]. Moscow, Vysshaya shkola Publ., 1989, 232 p.
16. Gulyaev YuV, Nikitov SA, Potapov AA, German VA. Scaling and fractional dimension ideas in a fractal radio signal detector. *Radio engineering and electronics,* 2006, 51(8):968-975.
17. Gulyaev YuV, Potapov AA. Application of the theory of fractals, fractional operators, textures, scaling effects and methods of nonlinear dynamics in the synthesis of new information technologies for problems of radio electronics (in particular, radar). *Radio engineering and electronics*, 2019, 64(9):839-854.
18. Gurevich V, Volman G. *Dimension theory*. Ed. and with a foreword. PS. Alexandrova. Moscow, IL Publ., 1948, 232 p.
19. Erofeev VI, Potapov AA. International scientific colloquium "Mechanics of generalized continua: one hundred years after Cosserat". *Nelineinyi mir,* 2009, 7(8):652-654 (in Russ.).
20. Zolotarev VM. *One-dimensional stable distributions*. Moscow, Nauka Publ., 1983, 304 p.
21. Kantor G. *Trudy on set theory*. Eds. AN Kolmogorov and AP Yushkevich. Moscow, Nauka Publ, 1985, 432 p.
22. Kobelev VL, Romanov EP, Kobelev YL, Kobelev LYa. Non-Debye relaxation and diffusion in fractal space. *DAN,* 1998, 361(6):755-758.
23. Kobelev YL, Kobelev L Ya, Romanov EP. Autowave processes in nonlinear fractal diffusion. *Dokl. RAS*, 1999, 369(3):332-333.
24. Kolmogorov AN, Fomin SV. *Elements of the theory of functions and functional analysis*. Moscow, Vysshaya shkola Publ., 1989, 624 p.
25. Letnikov AV. The theory of differentiation with an arbitrary pointer. *Mat. collection*, 1868, no. 3:1-68.
26. Medvedev FA. *Essays on the history of the theory of functions of a real variable*. Moscow, Nauka Publ., 1975, 248 p.
27. Medvedev FA. *The development of set theory in the 19th century*. Moscow, Nauka Publ., 1965, 232 p.
28. Milnor J. *Holomorphic Dynamics*. Per. from English. Izhevsk, Research Center "Regular and Chaotic Dynamics" Publ., 2000, 320 p.
29. Morozov AD, Dragunov TN. *Visualization and analysis of invariant sets of dynamical systems*. Izhevsk, Institute of Computer Research Publ., 2003, 304 p.
30. Nakhushev AM. *Fractional calculus and its application*. Moscow, Fizmatlit Publ., 2003, 272 p.
31. Nakhushev AM. *Elements of fractional calculus and their application*. Nalchik, Ed. KBNTs RAN Publ., 2000, 299 p.
32. Novozhenova OG. *Biography and scientific works of Alexei Nikiforovich Gerasimov. On linear operators, elastic viscosity, eleutherosis and fractional derivatives*. Moscow, Perot Publ., 2018, 234 p.
33. Stepson BA, Fedorchuk VV, Filippov VV. *Dimension theory. Results of Science and Technology. Series: Algebra. Topology. Geometry*. Moscow, VINITI Publ., 1979, 17:229-306.
34. Podosenov SA, Potapov AA, Sokolov AA. *Pulse electrodynamics of broadband radio systems and fields of coupled structures*. Ed. AA Potapov. Moscow, Radiotekhnika Publ., 2003, 720 p.
35. Podosenov SA, Potapov AA, Foukzon J, Menkova EP. *Nonholonomic, fractal and coupled structures in relativistic continuous media, electrodynamics, quantum mechanics and cosmology*. Ed. AA. Potapov. Moscow, LENAND, URSS Publ., 2015, in 3 vols., 1128 p.
36. Potapov AA. Waves in disordered large fractal systems: radar, nanosystems, clusters of unmanned aerial vehicles and small spacecraft. *Radio Engineering and Electronics*, 2018, 63(9):915-934.
37. Potapov AA. Diffractals at a frequency of 36 GHz observed during radar scattering of an electromagnetic wave by a fractal surface, and wave catastrophes in fractal randomly inhomogeneous media. *Proc. XIII Int. conf. "Zababakhin Scientific Readings", dedicated. 100th anniversary of the birth of EI Zababakhin* (Snezhinsk, March 20-24, 2017). Snezhinsk, RFNC-VNIITF Publ., 2017, p. 137-138.
38. Potapov AA. Fractional and integer topological dimensions as the main components in the topology of multidimensional signal sampling and their processing. *Proc. Int. conf. "Differential equations and topology", dedicated. 100th anniversary of the birth. acad. LS Pontryagin* (Moscow, June 17-22, 2008). Moscow, Steklov Mat. inst. of RAS and Lomonosov Moscow State University (MAKS Press), 2008, pp. 478-479.
39. Potapov AA. On the theory of functionals of backscattering stochastic fields. *Radio Engineering and Electronics,* 2007, 52(3):261-310.
40. Potapov AA. A short historical essay on the origin and formation of the theory of fractional integrodifferentiation. *Nelineinyi mir*, 2003, 1(1-2):69-81.
41. Potapov AA. Multiple scattering of waves by a fractal ensemble of particles and in large disordered fractal systems. In the book: "*Turbulence,*

dynamics of the atmosphere and climate" (Collection of proceedings of the International conference "Turbulence, dynamics of the atmosphere and climate", dedicated to the centenary of the birth of Academician AM Obukhov (Moscow, 16-18.05.2018) Ed. By GS Golitsyn et al. Moscow, Fizmatkniga Publ., 2018, pp. 564-573.

42. Potapov AA. Is it possible to build a fractal radio system? *Review of Applied and Industrial Mathematics*, 2007, 14(4):742-744.
43. Potapov AA. My meeting with B. Mandelbrot. *Nelineinyi mir,* 2007, 5(6):402-404.
44. Potapov AA. New information technologies based on probabilistic texture and fractal features in radar detection of low-contrast targets. *Radio engineering and electronics,* 2003, 48(9):1101-1119.
45. Potapov AA. On the concept of fractal radio systems and fractal devices. *Nelineinyi mir*, 2007, 5(7-8):415-444.
46. Potapov AA. On the application of the Hurst exponent H in adaptive fractal information processing and the synthesis of new classes of fractal "H-signals". *Review of Applied and Industrial Mathematics*, 2008, 15(6):1121-1123.
47. Potapov AA. On strategic directions in the synthesis of new types of radar texture-fractal detectors of low-contrast objects with the allocation of their contours and localization of coordinates against the background of intense interference from the surface of the earth, sea and precipitation. *Proceedings of the IV All-Russian STC "RTI Systems VKO-2016", dedicated. To the 100th anniversary of NIIDAR and the 70th anniversary of the RTI named after V.I. acad. AL Mints* (Moscow, JSC "RTI named after Academician AL Mints", 02-03.06.2016). Moscow, Bauman MSTU Publ., 2017, p. 438-448.
48. Potapov AA. On fractal radiophysics and fractal radio electronics. *Sat. report anniversary. scientific and technical conf. "Innovations in radio information and telecommunication technologies", dedicated to the 60th anniversary of JSC "Radiotekhn. inst.im. acad. AL Mints "and the Faculty of Radio Electronics of Aircraft MAI* (Moscow, 24-26.10.2006). Moscow, Extra Print, 2006, Part 1, p. 66-84.
49. Potapov AA. About fractal radio systems, fractional operators, scaling, and more ... Chapter in the book: *Fractals and fractional operators*. With a preface acad. YuV Gulyaev and Corresponding Member RAS SA Nikitov. Kazan, "Fan" Acad. sciences RT Publ., 2010, p. 417-472.
50. Potapov AA. Fractal fluctuations of microwave radio waves in an absorbing medium and negative fractal dimension. *Review of Applied and Industrial Mathematics,* 2008, 15(6): 123-1124.
51. Potapov AA. Scattering of waves on a stochastic fractal surface. *Sat. scientific works for the 65th anniversary of the creation of the Kotelnikov IRE of RAS and the 110th anniversary of the birth. acad. VA Kotelnikov.* Ed. Corresponding Member RAS SA Nikitov. Moscow, Kotelnikov IRE of RAS Publ., 2018, p. 155-159.
52. Potapov AA Modern fractal radio systems and technologies (40 years of scientific development): the basics of fractal-scaling or scale-invariant radar. *Proc. of the V Int. scientific. conf. "Nonlocal boundary value problems and related problems of mathematical biology, computer science and physics", dedicated. 80th anniversary of AM Nakhushev* (Nalchik, KBR, Russia, 4-7.12.2018). Nalchik, IPMA KBSC RAS Publ., 2018, p. 165-166.
53. Potapov AA. Statistical approach to the description of images of textures of the earth's surface in the optical and radio bands. *Abstracts. report V ses. conf. "Mathematical Methods for Pattern Recognition* (MMRO-IV)" (Riga, 24-26.10.1989). Riga, MI-PKRRiS Publ., 1989, 4:150-151.
54. Potapov AA. Texture and fractal scaling methods for detecting, processing and recognizing weak radar signals and low-contrast images against a background of intense interference. *Aerospace Defense Bulletin*, 2018, 2(18):15-26.
55. Potapov AA. Textures, fractals, fractional operators and nonlinear dynamics methods in radiophysics and radar: 40 years of scientific research. *Sat. works XXV Int. STC "Radar, navigation, communication", dedicated. 160th anniversary of the birth. AS Popov* (Voronezh, 16-18.04.2019). Voronezh, Voronezh State University Publ., 2019, 4:214-242.
56. Potapov AA. Turbulence, fractals and waves. *Sat. thesis. report Int. conf. "Turbulence, dynamics of the atmosphere and climate", dedicated. centenary from the date of birth. acad. A.M. Obukhov* (05.05.1918-03.12.1989) (Moscow, 16-18.05.2018). Moscow, Fizmatkniga Publ., 2018, p. 211.
57. Potapov AA. *Fractals in radio physics and radar.* Moscow, Logos Publ., 2002, 664 p.
58. Potapov AA. *Fractals in Radiophysics and Radar: Sample Topology.* Ed. 2nd, rev. and add. Moscow, University book Publ., 2005, 848 p.
59. Potapov AA. Fractals and fractional operators in radio engineering, radar and multidimensional

signal processing. *Abstracts. report Int. NTK to the 100th anniversary of the birth. VA Kotelnikov* (Moscow, 21-23.10.2008). Moscow, MPEI Publ., 2008, p. 29-33.

60. Potapov AA. Fractals and negative capacitor. *News from int. Chinese-Russian Symposium "New Materials and Technologies"* (Hainan, China, 28.11-1.12.2017). Sat. tr. XXIV int. STC "Radar, navigation, communication" (Voronezh, 17-19.04.2018). Voronezh, Ed. "Scientific research. publications "(WELBORN LLC), 2018, 3:372-388.
61. Potapov AA. Fractals and Textures in Radiophysics and Radio Electronics: 40 Years of Scientific Research. *Sat. mater. XIV int. conf. "Zababakhin Scientific Readings"* (Snezhinsk, 18-22.03.2019). Snezhinsk, RFNC-VNIITF Publ., 2019, p. 105-107.
62. Potapov AA. Fractals and chaos as the basis of new breakthrough technologies in modern radio systems. Add. book: Kronover R. *Fractals and chaos in dynamical systems*. Per. from English; ed. TE Krenkel. Moscow, Technosphere Publ., 2006, p. 374-479.
63. Potapov AA. Fractals, scaling and fractional operators in modern physics and radio engineering. *Sat. annotations Int. conf. XIV Kharitonov thematic scientific readings "Powerful Pulsed Electrophysics", dedicated. 110th anniversary of the birth. acad. YB Khariton* (Sarov, 21-25.04.2014). Sarov, RFNC-VNIIEF Publ., 2014, p. 80-81.
64. Potapov AA. Fractal radio electronics: state and development trends. *Sat. scientific. Art. by mater. III All-Russia. scientific-practical conf. Avionics* (15-16.03.2018). Voronezh, VUNC VVS "VVA im. prof. NOT Zhukovsky and YA Gagarin" Publ., 2018, p. 267-272.
65. Potapov AA. Fractal electrodynamics. Numerical modeling of small fractal antenna devices and fractal 3D microstrip resonators for modern ultra-wideband or multiband radio engineering systems. *Radio Engineering and Electronics,* 2019, 64(7):629-665.
66. Potapov AA. Fractal-scaling or scale-invariant radar: discovery, justification and development paths. *Sat. scientific. Art. by mater. II All-Russia. scientific-practical conf. Avionics* (Voronezh, March 16-17, 2017). Voronezh, VUNTS VVS "VVA im. prof. NOT Zhukovsky and YA Gagarin" Publ., 2017, p. 143-152.
67. Potapov AA. Fractal scaling or scale invariant radar and fractal signal and image processing. *Sat. scientific. works for the 65th anniversary of the creation. Kotelnikov IRE of RAS and the 110th anniversary of the birth. acad. VA Kotelnikov.* Ed. Corresponding Member RAS SA Nikitov. Moscow, IRE RAS Publ., 2018, p. 99-104.
68. Potapov AA. Fractal and texture detectors of weak radar signals against a background of intense interference. Part I. Introduction to the principles of topological detectors. *Radio engineering,* 2019, 1:80-92.
69. Potapov AA. Fractal methods for studying fluctuations of signals and dynamical systems in a space of fractional dimension. Chapter in the book: "*Fluctuations and noises in complex systems of animate and inanimate nature.*" Ed. RM Yulmetyeva et al. Kazan, Min. Education and Science Rep. Tatarstan Publ., 2008, p. 257-310.
70. Potapov AA. Fractal models and methods in problems of nonlinear physics. *Abstracts. report int. Congr. "Nonlinear dynamic analysis-2007", dedicated. 150th anniversary of the birth. acad. AM Lyapunov* (St. Petersburg, June 4-8, 2007). SPb., SPGU Publ., 2007, p. 301.
71. Potapov AA. Fractal models and methods based on fractional operators and scaling in fundamental and applied problems of physics. *Proc. 2 int. "Mathematical physics and its applications"* (Samara, 29.08-04.09.2010). Ed. Corresponding Member RAS IV Volovich and Doctor of Physical and Mathematical Sciences, prof. YUN Radaeva. Samara, Book Publ., 2010, p. 266-268.
72. Potapov AA. Fractal models and methods based on scaling in fundamental and applied problems of modern physics. *Sat. scientific. tr. "Irreversible processes in nature and technology."* Ed. VS Gorelik and AN Morozov. Moscow, Bauman MSTU Publ., 2008, II:5-107.
73. Potapov AA. *Fractal method and fractal paradigm in modern natural science*. Voronezh, Scientific book Publ., 2012, 109 p.
74. Potapov AA, Bulavkin VV, German VA, Vyacheslavova OF. Investigation of the microrelief of the processed surfaces using the methods of fractal signatures. *ZhTF*, 2005, 75(5):28-45.
75. Potapov AA, German VA. Application of fractal methods for processing optical and radar images of the earth's surface. *Radio Engineering and Electronics*, 2000, 45(8):946-953.
76. Potapov AA, German VA. Fractal nonparametric radio signal detector. *Radio engineering,* 2006, 5:30-36.
77. Potapov AA, Gulyaev YuV, Nikitov SA, Pakhomov AA, German VA. The latest methods of image

processing. Ed. AA Potapova. Moscow, Fizmatlit Publ., 2008, 496 p. (RFBR grant No. 07-07-07005).
78. Potapov AA, Laktyunkin AV. The theory of wave scattering by a fractal anisotropic surface. *Nelineinyi mir*, 2008, 6(1):3-36.
79. Potapov AA, Potapov AA (Jr.), Potapov VA. Fractal capacitor, fractional operators and fractal impedances. *Nelineinyi mir,* 2006, 4(4-5):172-187.
80. Potapov AA, Chernykh VA. *Fractional calculus AV Letnikov in the physics of fractals*. Saarbrücken, LAMBERT Academic Publishing, 2012, 688 pp.
81. Potapov AA, German VA. The effects of deterministic chaos and a strange attractor in the radar of a dynamic system such as vegetation. *ZhTF Letters*, 2002, 28(14):19-25.
82. Professor Alexander Alekseevich Potapov. Biobibliographic Index. Ed. Academician Yu.V. Gulyaev. Moscow, CPU "Raduga" Publ., 2019, 256 p. (Approved by the Academic Council of the Kotelnikov IRE of RAS on December 26, 2018).
83. Potapov AA. Brief scientific biography. In the book: "*International Forum for Industrial Development of New Materials*" (Jining, China, 11-13.12.2019). Jining: Jining National High-tech Industrial Development Zone, 2019, p. 8 (Chinese, Japanese, Russian).
84. Potapov AA. Application of the principles of fractal-scaling or scale-invariant radar in SAR, UAV and MIMO systems. In the book: *Radar. Results of theoretical and experimental research. In 2 books. Book. 2. Ed. AB Blyakhmana*. Moscow, Radiotekhnika Publ., 2019, p. 15-39.
85. Saks S. *Teoriya integrala*. Moscow, IL Publ., 1949, 496 p.
86. Samko SG, Kilbas AA, Marichev OI. *Integrals and derivatives of fractional order and some of their applications*. Minsk, Sci. and techn. Publ., 1987, 688 p.
87. Stratonovich RL. *The principles of adaptive reception*. Moscow, Sov. radio Publ., 1973, 144 p.
88. Uchaikin VV. *Fractional Derivatives Method*. Ulyanovsk, Artichoke Publ., 2008, 512 p.
89. Feder E. *Fractals*. Moscow, Mir Publ., 1991, 262 p.
90. Fedorchuk. BB. *Foundations of dimension theory. Results of Science and Technology. Modern probl. mat. Fund. directions. General topology–1*. Moscow, VINITI Publ., 1988, 17:111-124.
91. Feller V. *Introduction to the theory of probability and its applications*. Moscow, Mir Publ., 1967, vols. 1,2.
92. Fractals in physics. Per. from English ed. YAG Sinai and IM Khalatnikov. Moscow, Mir Publ., 1988, 672 p.
93. Frisch W. *Turbulence*. Legacy of AN Kolmogorov. ML Blank (ed.). Moscow, Fazis Publ., 1998, 346 p.
94. Halmos P. *Measure theory*. Moscow, IL Publ., 1953, 292 p.
95. Hausdorff F. *Set theory*. Per. with it.; ed. and with add. PS Aleksandrov and AN Kolmogorov. Moscow-Leningrad, ONTI Publ., 1937, 304 p.
96. Schroeder M. *Fractals, chaos, power laws*. Moscow-Izhevsk, Research Center "Regular and Chaotic Dynamics" Publ., 2001, 528 p.
97. Shuster G. *Deterministic chaos: an introduction*. Per. from English ed. AV Gaponov-Grekhov and MI Rabinovich. Moscow, Mir Publ., 1988, 240 p.
98. Yaglom AM. *Correlation theory of stationary random functions*. Leningrad, Gidrometeoizdat Publ., 1981, 280 p.
99. Agalarov AM, Gadzhimuradov TA, Potapov AA, Rassadin AE. Edge States and Chiral Solitons in Topological Hall and Chern-Simons Fields. *Modeling and Analysis of Information Systems,* 2018, 25(1):133-139.
100. Alisultanov ZZ, Agalarov AM, Potapov AA, Ragimkhanov GB. Some Applications of Fractional Derivatives in Many-Particle Disordered Large Systems. Ch. 7 in: *Fractional Dynamics, Anomalous Transport and Plasma Science*. Ed. C. Skiadas. Switzerland, Springer Int. Publ., 2018, p. 125-154.
101. Anastassiou GA. *Fractional Differentiation Inequalities*. N.Y., Springer, 2009, 686 p.
102. Applications of Fraction Calculus in Physics. Ed. by R. Hilfer. Singapore, World Scientific Publishing Co., 2000, 472 p.
103. Caputo M. *Elasticita e Dissipacione*. Bologna, Zanichelli Publ., 1969.
104. Caputo M. Linear models of dissipation whose Q is almost frequency independent. II. *Geophys. J.R. Astr. Soc.*, 1967, 13:529-539.
105. Caratheodory C. *Variationsrechnung und partielle Differentialgleichungen erster Ordnung*. Leipzig-Berlin, Teubner, 1935, 407 s. (English transl.: *Calculus of Variations and Partial Differential Equations of the First Order*. N.Y., Chelsea Publishing Company, 1965, 654 p.
106. Edgar GA. (ed.) *Classics on Fractal*. N.Y., Addison-Wesley, 1993, 366 p.
107. Danping Pan, Tianhua Feng, Wei Zhang, and Alexander A. Potapov. Unidirectional light scattering by electric dipoles induced in plasmonic nanoparticles. *Opt. Lett.,* 2019, 44(11):2943-2946.
108. Foukzon J, Potapov AA, Podosenov SA. Hausdorff-Colombeau measure and axiomatic quantum field theory in spacetime with negative B. Mandelbrot dimensions. http://arxiv.org/abs/1004.0451, 5 Feb. 2011, 206 c.

109. German VA, Potapov AA, Sykhonin EV. Fractal Characteristics of Radio Thermal Radiation of a Different Layer of Atmosphere in a Range of Millimeter Waves. *Proc. PIERS 2009 "Progress in Electromagnetics Research Symp"* (18-21.08.2009, Moscow, Russia). Cambridge, MA, Electromagnetics Academy, 2009, pp. 1813-1817.
110. Hata M. Fractals in Mathematics. Pattern and Waves: Qualitative Analysis of Nonlinear Differential Equations. *Studies in Mathematics and its Applications, V. 18.*/Ed. by T. Nishida, M. Mimura, H. Fujii. Tokyo, Kinokuniya Comp. Ltd., 1986, pp. 259-278.
111. Kiryakova V. *Generalized Fractional Calculus and Applications*. N.Y., Wiley & Sons, 1994, 360 p.
112. Kolwankar KM, Gangal AD. Fractional Differentiability of Nowhere Differentiable Functions and Dimensions. *Chaos*, 1996, 6(1):505-513.
113. Laktyunkin Alexander, Potapov Alexander A. The Hurst Exponent Application in the Fractal Analysis of the Russian Stock Market. In: *Advances in Artificial Systems for Medicine and Education II*. Ed: Z. Hu, S. Petoukhov, M. He (Part of the *Advances in Intelligent Systems and Computing book series – AISC, V. 902*). Cham, Switzerland, Springer Int. Publ., 2018, pp. 459-471.
114. Mainardi F. *Fractional Calculus and Waves in Linear Viscoelasticity: An Introduction to Mathematical Models*. London, Imperial College Press, 2010, 368 p.
115. Mandelbrot B. *The Fractals Geometry of Nature*. N.Y., Freeman, 1982, 468 p.
116. Mathai AM, Saxena RK. *The H-Function with Applications in Statistics and Other Disciplines*. New Delhi, Wiley Eastern Limited, 1978, 192 p.
117. McBride AC. *Fractional Calculus and Integral Transforms of Generalized Functions*. San Francisco, Pitman Press, 1979, 179 p.
118. Metzler R, Klafter J. The random walk's guide to anomalous di!usion: a fractional dynamics approach. *Physics Reports,* 2000, 339:1-77.
119. Miller KS, Ross B. *Introduction to the Fractional Calculus and Fractional Differential Equations*. N.Y., Wiley, 1993, 384 p.
120. Nishimoto K. *Fractional Calculus. V. 1-5*. Koriyama (Japan), Descartes Press Co., 1984, v.1.-195 p.; 1987, v.2 – 189 p.; 1989, v.3 – 202 p.; 1991, v.4 – 158 p.; 1996, v.5 – 193 p.
121. Oldham KB, Spanier J. *The Fractional Calculus*. N.Y., Academic Press, 1974, 234 c.
122. Podlubny I. *Fractional Differential Equations*. N.Y., Academic Press, 1999, 368 p.
123. Podosenov SA, Foukzon J, Potapov AA. A Study of the Motion of a Relativistic Continuous Medium. *Gravitation and Cosmology,* 2010, 16(4):307-312.
124. Potapov AA, German VA. Detection of Artificial Objects with Fractal Signatures. *Pattern Recognition and Image Analysis,* 1998, 8(2):226-229.
125. Potapov AA. Fractal and topological sustainable methods of overcoming expected uncertainty in the radiolocation of low-contrast targets and in the processing of weak multi-dimensional signals on the background of high-intensity noise: A new direction in the statistical decision theory. *IOP Conf. Ser.: Journal of Physics*, 2017, 918(012015):19.
126. Potapov AA. The Textures, Fractal, Scaling Effects and Fractional Operators as a Basis of New Methods of Information Processing and Fractal Radio Systems Designing. *Proc. SPIE*, 2009, 7374:73740E-1–14.
127. Potapov AA. On the Issues of Fractal Radio Electronics: Part 1. Processing of Multi-dimensional Signals, Radiolocation, Nanotechnology, Radio Engineering Elements and Sensors. *Eurasian Physical Technical Journal,* 2018, 15(2(30)):5-15.
128. Potapov AA, Potapov Alexey A, Potapov VA. Fractal Radioelement's, Devices and Fractal Systems for Radar and Telecommunications. *Proc. 14th Sino-Russia Symposium on Advanced Materials and Technologies* (Sanya, Hainan Province, China, 28.11-01.12.2017). Ed. Mingxing Jia. Beijing, Metallurgical Industry Press (China), 2017, pp. 499-506.
129. Potapov AA. On the Issues of Fractal Radio Electronics: Part 2. Distribution and Scat-tering of Radio Waves, Radio Heat Effects, New Models, Large Fractal Systems. *Eurasian Physical Technical Journal*, 2018, 15(2(30)):16-23.
130. Potapov Alexander A. Postulate "The Topology Maximum at the Energy Minimum" for Textural and Fractal-and-Scaling Processing of Multidimensional Super Weak Signals against a Background of Noises. Глава 3 в кн.: *Nonlinearity: Problems, Solutions and Applications*. Ed. LA Uvarova, AB Nadykto, and AV Latyshev. N.Y., Nova Science Publ., 2017, 2:35-94.
131. Potapov Alexander A. Chaos Theory, Fractals and Scaling in the Radar: A Look from 2015. Глава 12 в кн.: *The Foundations of Chaos Revisited: From Poincaré to Recent Advancements*. Ed. C. Skiadas. Switzerland, Basel, Springer Int. Publ., 2016, pp. 195-218.

132. Potapov Alexander A. On the Indicatrixes of Waves Scattering from the Random Fractal Anisotropic Surface. Глава 9 в кн.: *Fractal Analysis - Applications in Physics, Engineering and Technology*. Ed. Fernando Brambila. Rijeka, InTech, 2017, pp. 187-248.
133. Potapov Alexander A, Pakhomov Andrey A, Grachev Vladimir I. Development of Methods for Solving Ill-Posed Inverse Problems in Processing Multidimensional Signals in Problems of Artificial Intelligence, Radiolocation and Medical Diagnostics. In: *Advances in Artificial Systems for Medicine and Education II*. Ed: Z. Hu, S. Petoukhov, M. He (Part of the Advances in Intelligent Systems and Computing book series–AISC, V. 902). Cham, Switzerland, Springer Int. Publ., 2018, pp. 57-67.
134. Rogers CA. *Hausdorff Measures*. London, Cambridge University Press, 1970, 179 p.
135. Rubin B. *Fractional Integrals and Potentials*. Harlow, Longman, 1996, 409 p.
136. Samko SG, Kilbas AA, Marichev OI. *Fractional Integrals and Derivatives: Theory and Applications*. N.Y., Gordon and Breach, 1993, 688 p.
137. Potapov Alexander A, Wu Hao, Xiong Shan. *Fractality of Wave Fields and Processes in Radar and Control*. Guangzhou, South China University of Technology Press (First edition: November 2020), 2020, 280 p. – ISBN 978-7-5623-6276-0.
138. Potapov AA, Kuznetsov VA, Pototsky AN. A new class of topological texture-multifractal features and their application for the processing of radar and optical low-contrast images. Radio Engineering and Electronics, 2021, 66 (5); 457-467. DOI: 10.31857 / S0033849421050107.
139. Kuznetsov VA, Potapov AA, Alikulov EA. Method of fractal complexing of multifrequency radar images. Patent 2746038 RF. MPK8 N 01 G 19/18 (2006.01). (The priority of the invention is 09/05/2020, the date of state registration is 04/06/2021).
140. Pan Danping, Wan Lei, Potapov Alexander A, and Feng Tianhua. Performing Spatial Differentiation and Edge Detection with Dielectric metasurfaces. *QELS_Fundamental Science "OSA Technical Digest Conf. on Lasers and Electro-Optics* (CLEO) (San Jose, California, USA, 10-15 May 2020)". Washington: Optical Society of America, 2020. Paper FW4B.2.pdf.- 2 p. (From the session "Inverse Design and Computation (FW4B)").
141. Lei Wan, Danping Pan, Shuaifeng Yang, Wei Zhang, Potapov Alexander A, Xia Wu, Weiping Liu, Tianhua Feng, and Zhaohui Li. Optical analog computing of spatial differentiation and edge detection with dielectric metasurfaces. *Opt. Lett.*, 2020,45(7):2070-2073.https://www.osapublishing.org/ol/abstract.cfm?URI=ol-45-7-2070.
142. Tianhua Feng, Potapov Alexander A., Zixian Liang, and Yi Xu. Huygens Metasurfaces Based on Congener Dipole Excitations. *Physical Review Applied,* 2020, 13(021002):1-6. DOI: 10.1103/PhysRevApplied.13.021002.
143. Tianhua Feng, Shuaifeng Yang, Ning Lai, Weilian Chen, Danping Pan, Wei Zhang, Potapov Alexander A, Zixian Liang, and Yi Xu. Manipulating light scattering by nanoparticles with magnetoelectric coupling. *Phys. Rev. B.*, 2020, 102(205428): 7 p. – (Published 30 November 2020). DOI: 10.1103/PhysRevB.102.205428.
144. Lei Wan, Danping Pan, Tianhua Feng, Weiping Liu, Potapov A.A. A review of dielectric optical metasurfaces for spatial differentiation and edge detection. *Frontiers of Optoelectronics*, 2021, 14 p. DOI: 10.1007/s12200-021-1124-5.
145. Danping Pan, Lei Wan, Min Ouyang, Wei Zhang, Potapov Alexander, Weiping Liu, Zixian Liang, Tianhua Feng, Zhaohui Li. Laplace metasurfaces for optical analog computing based on quasi-bound states in the continuum. *ACS Photonics,* 2021, 8(3)

DOI: 10.17725/rensit.2021.13.291

Microwave cyclotron protective devices for radar receivers

Sergey V. Bykovskiy
RPC "Istok" named after Shokin", http://www.istokmw.ru/
Fryazino 141190, Moscow region, Russian Federation
E-mail: serbyko@mail.ru

Received April 04, 2021, peer-reviewed April 19, 2021, accepted April 26, 2021

Abstract: **Brief overview of the latest developments of microwave cyclotron protective devices, their functioning and parameters is given. It is noted that these devices have a number of important advantages over other types of protective devices: they are autonomous, provide no peak of microwave power leaking to the output, frequency filtering and low noise figure (0.7-1.2 dB). The upper limit of the linearity of cyclotron protective devices in the signal transmission mode when the transmission coefficient is compressed by 1 dB is ~ 1 mW. The devices can operate with an input pulse power of up to 10 kW or more, while the attenuation of the input power in the protection mode is more than 60-80 dB. The recovery time of parameters after the end of a powerful input pulse is 10-20 ns. For devices of the 3-cm wavelength range, experimental data are given on the recovery time, the upper limit of linearity, attenuation of the input power in the protection mode, and filtration characteristics.**

Keywords: **cyclotron protection device, tape electron beam, fast cyclotron wave, peak leakage power, recovery time, noise figure**

UDC 621.385.69

For citation: Sergey V. Bykovskiy. Microwave cyclotron protective devices for radar receivers. *RENSIT*, 2021, 13(3):297-302. DOI: 10.17725/rensit.2021.13.297.

Contents

1. INTRODUCTION

The parameters of modern radar systems are determined by the design features and characteristics of antennas and devices for generating emitted signals and their element base [1]. Of no less importance for the operation of the radar is the processing of the received signals reflected by the target. A very important role in this process belongs to the protective device for the radar receiver. The task of the device is to protect the sensitive input stages of the receiver from the impact of a powerful pulse of transmitter (usually up to 10% of the power of the emitted pulse is reflected from the antenna and enters the input of the receiver), as well as from the targeted electromagnetic influence of extraneous electronic suppression means [2].

Over the past 20 years, cyclotron protective devices (CPD) have become quite widespread in new Russian developments of microwave radars, as well as cyclotron-protected complexed amplifiers (CPCA), which are a combination of a CPD with a low-noise transistor amplifier (LNA) and additional service devices. Radars with active phased antenna arrays are not considered in this case.

The main properties of the CPD and their advantages over other types of protective devices (gas-discharge, semiconductor and others) are as follows:

- CPD is an autonomous protector, i.e. passes from the signal transmission mode to the protection mode and back without a control signal;

- there is no peak of the microwave power leaking to the output in the CPD, which usually occurs in other types of protectors at the moment of the leading edge action of a powerful input pulse;
- due to the specifics of the interaction of the CPD resonators and the electron beam the device performs the functions of a frequency filter;
- CPDs are capable to operate with an input pulse power up to 10 kW and more, while the attenuation of the input power in the protection mode is 60-80 dB and more;
- CPD recovery time after the end of a powerful pulse at the input is 10-20 ns;
- CPDs have low noise figure (0.7-1.2 dB) in signal transmission mode;
- the upper limit of the CPD linearity in the signal transmission mode with compression of the transmission coefficient by 1 dB is 0.5-3 mW, when the input power increases by 3-5 dB more the device goes into protection mode.

Let us consider the basic principles of the CPD operation.

2. DESIGN AND PRINCIPLES OF WORK

CPD is a vacuum electron beam low noise microwave device of the O-type with transverse interaction, the operation of one based on the excitation of a fast cyclotron wave (FCW) in an electron beam [3-6]. CPD continues the line of low noise electron beam parametric amplifiers (EPA) and electrostatic amplifiers (ESA), developed in the 60-80s of the 20th century. EPA also known as Adler tube. Relativistic effects during the operation of the devices are negligible.

In **Fig. 1** shows the functional diagram of the CPD in the transmission mode. The electron gun (1) forms a tape electron beam (2), which sequentially passes through the input resonator (4), the dividing section (5), the output resonator

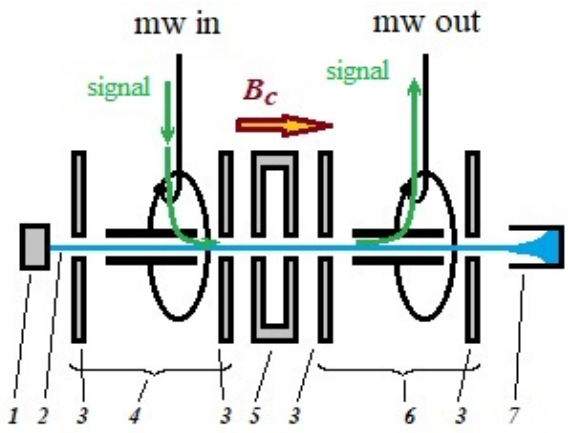

Fig. 1. *Functional schema of the CPD in the transmission mode.*

(6) and settles in the collector (7). The input and output resonators in the plane perpendicular to the beam axis are closed on both sides by disks (3). The input resonator, the dividing section, and the output resonator form the electrodynamic system of the CPD is located in a longitudinal uniform magnetic field Bc, which provides cyclotron resonance of electrons at the operating frequency.

The input and output resonators of the CPD are resonators with an extended capacitive gap, the so called Cuccia resonators (Cuccia couplers) [7,8]. The transverse dimension of the electronic gap is from 0.1 mm to 0.25 mm for the CPD of various frequency ranges. The gap length is such that the electron makes several cyclotron revolutions in the cavity. A tape electron beam is emitted by an oxide microcathode with an emission surface of 0.02 mm by 0.7 mm; the beam current is from 150 μA to 250 μA. The CPD uses a shielded-type magnet system with a samarium-cobalt permanent magnets and thermal stabilization based on thermomagnetic shunts.

CPD in the transmission mode works as follows: FCW is excited in the beam in the input resonator due to the signal energy (transverse oscillations of electrons with added energy at the cyclotron frequency) and transferred by the beam to the output resonator, where it is removed from the beam and transmits to

the output of the CPD. When a signal wave is excited, electron bunches do not appear in the beam; for this reason, the signal transmission is linear up to the input power level (~1 mW), at which the deposition of electrons begins on the walls of the electron gap due to an increase in the amplitude of transverse oscillations.

Since the operation of the device is based on interaction with a fast wave of an electron beam, this makes it possible to remove thermal noise from the signal wave in a passive coupler (input resonator) simultaneously with the introduction of the signal power into the FCW. This mechanism allows you to achieve a fairly low intrinsic noise figure (0.7 ... 1.2 dB). The working frequency band of the CPD is determined by the band in which the conditions of complex-conjugate matching of the conductivities of the electron beam, the resonator itself, and the external load are fulfilled at an acceptable level.

When the input microwave power increases to a level above several mW, the electron beam destroys in the input cavity. The input and output resonators will be separated from each other by a dividing section, while the power from the input resonator to the output one can only be transmitted through the electron beam opening in the dividing section with significant attenuation.

As is known, classic autonomous protective device is a high frequency line connecting the input and output, which includes gas discharge, semiconductor (pin-diode) or other devices, the impedance of which decreases sharply and significantly with an increase in the transmitted power to a certain level (see **Fig. 2**).

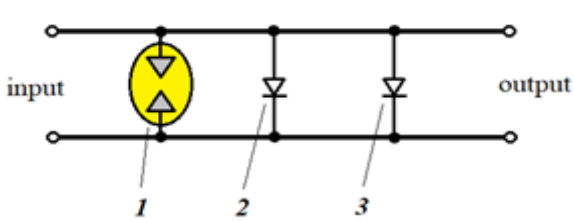

Fig. 2. *Functional schema of a classic microwave hybrid protector.*

In Fig. 2, numbers indicate: 1 – gas discharge protection element, 2 and 3 - pin-diode stages of the protector. With a sufficiently steep leading edge of a high level power pulse falling on the protector, at the initial moment of time, until the gas discharge in the element (1) ignites and the pin-diodes (2) and (3) open, the input microwave power is supplied to the output of the protector. In this case, a peak of leakage power forms at the output of the device.

There is no single high frequency line connecting the input and output in the CPD. At the moment the CPD transits from the transmission mode to the protection mode, the peak power at the output of the device corresponds to the maximum energy capacity of the electron beam on the verge of its destruction.

In the protection mode, the input resonator is not loaded with an electron beam and is mismatched with the input line (VSWR of CPD input ≈30), for this reason up to 90% of the microwave input power reflects from the CPD input. The remaining power dissipates in the input line and the input resonator as heat.

3. ELECTRICAL PARAMETERS

The working frequency band of the CPD as well as the frequency parameters of filtering the input signals (see **Fig. 3**) are determined by the active and reactive conductivities of the electron beam in the gap of the Cuccia resonator near the cyclotron frequency [4,8] and the degree of their matching with the conductivities of the resonator and external loads as above.

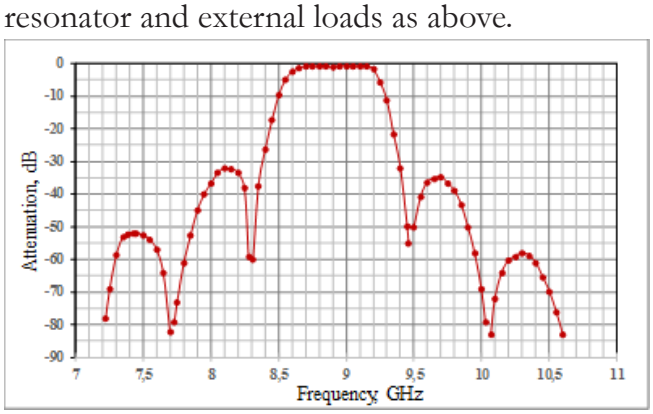

Fig. 3. *An example of the transmission coefficient of a CPD in a wide frequency band.*

Dips in the transfer coefficient (Fig. 3) correspond to the frequencies of detuning from cyclotron resonance in the angle of flight of electrons in the resonator gap by $2\pi n$, where $n = \pm1, \pm2,\ldots$ [4,8]. Physically, this is explained by the fact that the longitudinal axis of the electron beam (the axis on which the centers of mass of electrons in each cross section of the beam are located), upon excitation of the FCW at frequencies other than the cyclotron frequency, takes the form of a weakly twisted spiral. At the frequencies of the transmission coefficient dips, the indicated "spiral" of the electron beam axis along the length of the resonator has an integer number of turnovers; for this reason, the cyclotron rotation of the beam in the resonator gap does not induce a current in it (for each electron there is another electron within the resonator oscillating in antiphase with it).

The filtering properties of the CPD play an important role in suppressing side reception channels in the radar receiving devices [9].

The transition of the CPD from the transmission mode to the protection mode is associated with an increase in the input microwave power, an increase in the radius of rotation of the beam electrons and their settling on the walls of the electron gap in the input resonator. As the input power increases, the edge electrons of the beam first begin to settle, the transmission coefficient of the CPD decreases, the linearity of the transmission coefficient violates, and the beam current reaching the collector decreases [10].

The total power received from the field by all beam electrons located in the cavity gap can be obtained from the expression:

$$P = \frac{I_0}{2(e/m)}\omega_c^2 R^2, \qquad (1)$$

where I_0 is the beam current, ω_c is the circular cyclotron frequency (corresponds to the center frequency of the operating frequency band), R is the radius of the cyclotron rotation of electrons, e is the charge and m is the electron mass. Based on (1), it is possible to estimate the power at which the edge electrons of the beam begin to settle: $P_{lim} \approx -4$ dBm (frequency is 9 GHz, beam current is 200 μA, gap between the beam and the gap wall is 15 μm), which is in good agreement with the experimental data in the **Fig. 4.** The decrease in the current passing to the collector by a factor of 1.26 (corresponds to –1 dB) coincides with the input power, at which there is a compression of the CPD transmission by 1 dB: $P_{-1dB} \approx 3$ dBm. The input power attenuation in protection mode is ≈ 75 dB.

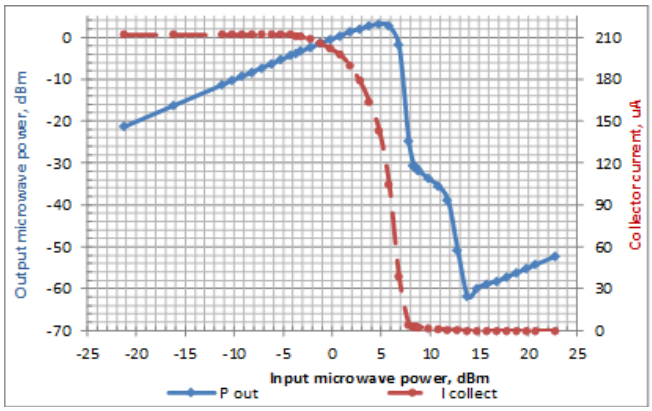

Fig. 4. *Linearity boundary and transition to the protection mode of the CPD for a wavelength range of 3 cm.*

The maximum power supplied to the output of the CPD during the transition to the protection mode does not exceed 4-5 mW, for higher frequency CPDs – 8-10 mW, for low frequency CPDs – 1 mW.

One of the main advantages of a CPD is a short recovery time. Taking into account the high mobility of electrons in vacuum, the recovery time of the CPD is determined by the time of decreasing the amplitude of electromagnetic oscillations in the low-Q input resonator caused by the action of the input power pulse, and the time of flight of the electron beam between the input and output resonators. At the initial stage (stage 1) of restoring the signal transmission, the resonator is loaded with an external load and its own losses (typical resonator Q-factor $Q_1 \approx 25$). At the next stage (stage 2), the passage of the beam in the gap restores and, accordingly, the Q factor of the resonator decreases from

the level Q_1 to the maximum loaded level $Q_3 \approx 8$ (stage 3 – the passage of the beam and the signal is restored). The figure of merit averaged over the transient stage 2 can be assumed to be $Q_2 \approx 16$.

As known, the time of decreasing the amplitude of oscillations in a circuit with a quality factor Q from the power level P_1 to the level P_2 determines by the expression:

$$t = \frac{Q}{2\pi f} \ln \frac{P_1}{P_2}, \quad (2)$$

where t is the time of decreasing the amplitude of oscillations, f is the frequency of oscillations.

For a wavelength range of 3 cm, estimates from expression (2) at typical power levels shown in Fig. 4 give the following values: the duration of stage 1 is $t_1 \approx 4$ ns for an input pulse power of 1 kW and $t_1 \approx 5$ ns for an input pulse power of 10 kW (90% of the microwave input power is reflected from the mismatched resonator). The duration of stage 2 is $t_2 = 0.6$ ns.

With a typical time of flight of electrons between the centers of the input and output cavities of 2-4 ns, the recovery time of the CPD in the 3 cm wavelength range will be $t_r \approx 10$ ns. In the wavelength range of 10 cm, the recovery time of the CPD is $t_r \approx$ 22-26 ns.

For an additional time from 3 to 10 ns (the duration of stage 3, depending on the frequency range), the maximum sensitivity in the CPD corresponding to a noise figure of 1-1.5 dB is restored.

In the present estimates of the recovery time it is assumed the ideal trailing edge with zero duration of a powerful input microwave pulse.

As noted above, most of the high level input microwave power reflects from the mismatched resonator. To ensure an extremely short recovery time of the device the reflected power should be directed into the load for prevent its re-reflection from the elements of the antenna-CPD path and the input of the CPD. **Fig. 5** shows the oscillograms of the microwave energy reduce at the CPD output

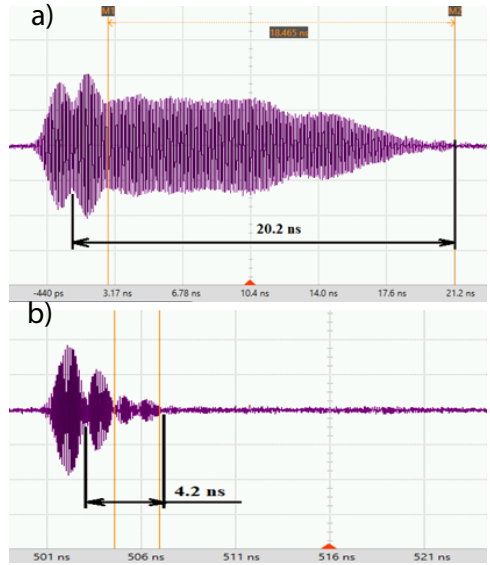

Fig. 5. *Oscillograms of the recovery time of the CPD in the wavelength range of 3 cm: a) without a ferrite valve at the input, the length of the connecting cable between the generator and the input of the CPD is 0.9 m; b) a ferrite valve is connected to the CPD input.*

at the end of an input pulse with a power of 23 dBm with a cutoff duration (trailing edge) of a pulse of 0.5 ns. Fig. 5*a* - the duration of the reduction process of 20.2 ns is due to the propagation of the power reflected from the CPD input to the generator of a powerful signal, followed by reflection of the power from the output of the generator and its re-entry to the input of the CPD with the length of the connecting cable 0.9 m. The swelling on the oscillogram to the left of the 20.2 ns time interval is due to the passage of the input pulse cutoff through the CPD (the left border of the 20.2 ns time interval on the oscillogram separates the modes of operation of the CPD: on the left – the mode of protection against the input pulse, on the right – the transmission mode in the absence of an input pulse. Figure 5b – similarly for 4.2 ns interval).

The use of a ferrite valve directly at the input of CPD (Fig. 5*b*) makes it possible to exclude the re-reflection of the microwave power in the path generator-CPD and to observe the proper recovery time of the CPD, in this case 4.2 ns.

4. CONCLUSION

CPD is a very attractive device for use in radar receivers due to the physical principles on which its work is based:

- interaction with the fast wave of the electron beam allows to remove thermal noise from the beam in the coupling resonator and achieve a low noise figure;
- interaction with a transverse (cyclotron) wave does not lead to the formation of electron charge bunches in the beam and provides a high linearity of the device;
- work with an electron beam in a vacuum – the use of charged particles with maximum mobility – allows to achieve an ultra-short recovery time of the protective device;
- connection of the input and output of the CPD in the transmission mode through an electron beam ensures the absence of a leakage peak power.

REFERENCES

1. Bystrov RP, Potapov AA. Functional devices and element base of radar systems. *RENSIT*, 2009, 1(1-2):43-58.
2. Bystrov RP, Dmitriev VG, Potapov AA, Perunov YuM, Cherepenin VA. Electromagnetic systems and tools of intentional impact on physical and biological objects. *RENSIT*, 2014, 6(2):129-169.
3. Vanke VA, Lopukhin VM, Savvin VL. Supernoiseless cyclotron-wave amplifiers. *Sov. Phys. Usp.*, 1970, 12(6):743-755; DOI: 10.1070/PU1970v012n06ABEH003970.
4. Vanke VA. Transverse electron-beam waves for microwave electronics. *Phys. Usp.*, 2005, 48(9):917-937; DOI: 10.1070/PU2005v048n09ABEH002397.
5. Budzinskiy YuA, Kantyuk SP. Electrostaticheskie usiliteli [Electrostatic amplifiers]. *Electronnaya tekhnika. Ser.1. Svch-tekhnika*, 1993, (1):21-27 (in Russ.).
6. Manheimer WM, Ewell GW. *IEEE Trans. Plasma Sci.*, 1998, 26(4):1282-1296.
7. Cuccia CL. The Electron Coupler – A Developmental Tube for Amplitude Modulation and Power Control at Ultra-High Frequencies. Part I. *RCA Review*, 1949, 10(2):270-303.
8. Dubravec V. Wellentheorie des Cuccia-Kopplers. *Archiv für Electronik und Übertragungatechnik,* 1964, 18(10):585-593.
9. Bykovskiy SV, Gradova TI, Orekhov MB. Parametry elektromagnitnoy sovmestimosti ciklotronno-zashchishchennykh kompleksirovannykh usiliteley (TsZKU) [Parameters of electromagnetic compatibility of cyclotron-protected complexed amplifiers (CPCA)]. *Vestnik vozdushno-kosmicheskoy oborony*, 2020, (1):51-54 (in Russ.).
10. Bykovskiy SV, Budzinsky UA, Kalina VG, Kotov VE, Savrukhin OA. Ciclotronnye zashchitnye ustroystva: granitsa lineynosti i perekhod v rezhim zashchity [Cyclotron protective devices: linearity limit and transition to protection mode]. *Electronnaya tekhnika. Ser.1. Svch-tekhnika*, 2018, (3):43-49 (in Russ.).
11. Bykovskiy SV, Budzinsky UA, Kalina VG, Kotov VE, Nikolaev SV, Savrukhin OA. Ciclotronnye zashchitnye ustroystva: vremya vosstanovleniya parametrov [Cyclotron protective devices: recovery time of parameters]. *Electronnaya tekhnika. Ser.1. Svch-tekhnika*, 2020, (1):12-21 (in Russ.).

DOI: 10.17725/rensit.2021.13.303

Magnetic Fields And High-Temperature Superconductivity In Excited Liquids. Unknown Particles

Gennady V. Mishinsky

Joint Institute for Nuclear Research, http://www.jinr.ru/

Dubna 141980, Moscow Region, Russian Federation

E-mail: mysh@jinr.ru

Received May 31, 2021, peer-reviewed June 14, 2021, accepted June 21, 2021

Abstract: **The article presents a number of experiments in liquid media on the transformation (transmutation) of atomic nuclei of some chemical elements into atomic nuclei of other chemical elements. In the theory of low-energy nuclear reactions, the transmutation of atomic nuclei occurs in strong magnetic fields, more than 30 T. Magnetic fields appear in ionized liquid media as a result of the unidirectional motion of an ensemble of electrons. The exchange interaction between electrons with parallel spins forms a self-consistent field in the medium, in which electrons pair into orthobosons with S = 1ħ. Orthobosons are attracted to each other and form orthoboson "solenoids" - "capsules" with strong magnetic fields inside. "Capsules" can fly out of liquid media, and then they are registered as unknown particles with strange properties. In some cases, when an electric current passes through the liquid, the electric current can be realized in the form of orthobosonic "solenoids" connected in continuous "filaments" from one electrode to another. Such "filaments" exhibit characteristics of superconductivity.**

Keywords: **low-energy nuclear reactions, exchange interaction, quantum fluids, low-temperature plasma, electron pairing, strong magnetic fields, high-temperature superconductivity, unknown particles**

PACS: 03.75.Mn; 03.75.Nt; 25.60.Pj; 25.85.-w; 52.25.Xz; 67.57.Lm; 74.20.−z; 75.50.Mm

For citation: Gennady V. Mishinsky. Magnetic Fields And High-Temperature Superconductivity In Excited Liquids. Unknown Particles. *RENSIT*, 2021, 13(3):303-318. DOI: 10.17725/rensit.2021.13.303.

Contents

1. INTRODUCTION

"Impossible" radiationless and low-energy nuclear reactions were discovered at the end of the last century, in 1989-1992: cold nuclear fusion reactions and low-energy transmutation reactions [1-3].

It turned out that nuclear reactions with the transformation of some chemical elements into other chemical elements can occur in weakly excited condensed matter with a low, only ~ 1 eV/atom, excitation energy in the reaction region. This phenomenon has received the name: low-energy transmutation of chemical elements (hereinafter- transmutation). The methods of experiments on the transmutation are extremely diverse and fundamentally different from the methods of nuclear physics. Transmutation reactions were discovered and subsequently reproduced in a glowing gas discharge [4-6]; in

industrial electronic zone melting of zirconium ingots in a vacuum furnace [7]; during explosions of metal targets irradiated by a powerful pulse of electrons [8,9]; during explosions in liquid dielectric media of metal foils, through which a powerful pulse of electric current was passed [10,11]; when exposed to a pulsed current on a melt of lead with copper [12]; during the passage of electric current in water-mineral media [3]; during ultrasonic treatment of aqueous saline solutions [13]; when irradiating condensed gases with braking gamma quanta [14-16]; in growing biological structures [17-19] and in many others [1-3]. The results of transmutation experiments, despite their variety, are qualitatively similar to each other.

Transmutation reactions are carried out for all chemical elements, starting with hydrogen, and they usually occur with the participation of a large number of atomic nuclei. Transmutation reactions include both fusion and decay of nuclei. Experiments show that practically all chemical elements can be synthesized in transmutation reactions: from hydrogen and, so far, to actinium [15]. In this case, the reaction products, which are isotopes of chemical elements are obtained as stable isotopes, i.e. non-radioactive isotopes.

The synthesis of chemical elements with a nuclear charge Z greater than that of iron nuclei ($Z = 26$) led to the conclusion that multinuclear reactions take place in transmutation reactions. Multinuclear transmutation reactions must be introduced to explain the production of heavy chemical elements in a medium consisting of light elements in many experiments. Such heavy elements cannot be obtained in paired reactions that occur between light elements of the medium.

Transmutation reactions occur only as a result of external influence on the condensed matter. In most experiments, transmutation reactions occur due to action of electrons on the medium by means of powerful pulses of electrons or powerful currents. So, for example, the book [3] "discusses the transformation of some chemical elements into others under electromagnetic influences. Five methods of exposure are shown that give qualitatively similar results. The transformation processes are accompanied by energy release. The general nature of the impact by various ways is associated with large pulse currents and pulse fields. Basically, there are two types of media that are exposed: metal melts and aqueous media".

The above considerations and numerous experiments show that transmutation reactions take place in liquids, in solutions, in melts and in gases under high pressure, i.e. on free atoms, the density of which is close to the density of a solid state, and during the passage of directed flows of electrons through these media.

The theory that explains transmutation reactions is connected, firstly, with the discovery of the fundamental resonant interference exchange interaction. RIEX-interaction occurs between nuclei that have common resonance states [20,21]. Such nuclei form nuclear molecules, including multinuclear molecules. Strong-weak, electromagnetic and inertial-gravitational interactions are realized simultaneously in RIEX-interactions between nuclei. And, secondly, the theory of transmutation is associated with the creation of the theory of pairing of atomic electrons into orthobosons with a total spin equal to one $S = 1\hbar$. This pairing of electrons occurs in strong magnetic fields > 30 T. Orthobosons form electron Bose-Einstein condensate in the atom. Such atoms are called Transatoms. Transatoms have external and internal ultra-strong magnetic fields. Internal magnetic fields that interact with the orbital and spin magnetic moments of nucleons in nuclei, transform them into Transnuclei. External magnetic fields allow transatoms to be attracted to each other. When transatoms approach each other, their electronic Bose-Einstein condensates are combined into one, common Bose-Einstein condensate and, thus, form binuclear, and then, multinuclear molecules.

Atomic electrons, in a strong magnetic field, inevitably pair into orthobosons. Atoms transform into Transatoms. Transatoms automatically enter into low-energy transmutation reactions.

The question arises, how strong magnetic fields are created in a condensed matter? This paper makes an assumption about the mechanism that creates such magnetic fields.

2. TRANSMUTATION OF CHEMICAL ELEMENTS

First, we present several experiments on low-energy transmutation of chemical elements in order the readers can get acquainted with it.

2.1. Transmutation of elements in electric discharge

Work on the transmutation of elements in an electric discharge in liquid media was carried out by A.V. Vachaev and N.I. Ivanov [3]. The installation consisted of two tubular electrodes with an inner diameter of 6 to 50 mm located opposite each other at a distance of 1–1.5 mm of their diameter. Between the electrodes, inside which the liquid moved, a specific electric discharge was created, and plasma appeared. The electrodes were inside a coil that creates a magnetic field. The plasma was ignited by a pulsed discharge of additional electrodes located across the liquid jet between the tubular electrodes. The plasma between the tubular electrodes was an electrically conductive film that formed a multidimensional figure of the type of revolution hyperboloid with a pinch 0.1–0.2 mm in diameter. The discharge proceeded almost noiselessly with a minimum release of heat and gas phase. The magnitude of the current that passed through the tubular electrodes varied within 0.1-100 A, but the current was 20-40 A in most cases.

As a result of the work of the installation, a stable process of transformation of the initial material of the medium into new elements and their compounds, in the gaseous, liquid (dissolved in the medium) and solid state, arose in it. All works were carried out in a mode with a maximum solid phase yield, up to 300 g/*L* on the average. The installation was able to work for many days. In the experiments, various liquid media were supplied to the inlet of the installation: water (distilled, drinking, river water), water-mineral mixtures, effluents from various production facilities, water-carbon, organic mixtures. **Fig. 1** shows, by way of example, the yields of "extraneous" elements for the cases of distilled water treatment (Fig. 1a) and domestic wastewater treatment (Fig. 1b).

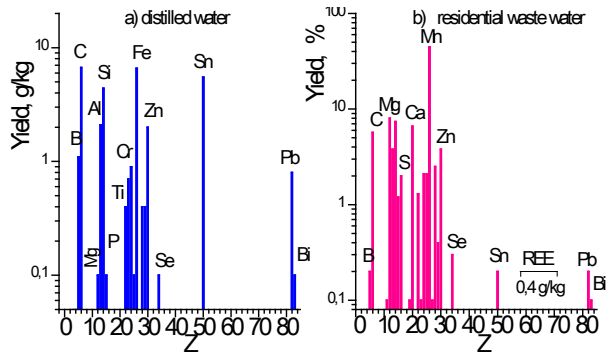

Fig. 1. *Elements yield at processing in electric discharge a) of distilled water, b) of residential waste water. REE – rare earth elements.*

2.2. Experiments on melting zirconium with an electron beam

The paper by M.I. Solin [7] describes the results of experiments on zone melting of zirconium ingots by an electron beam. The experiments were carried out in industrial vacuum furnaces with heating of the ingot by means of an electron beam. The accelerating voltage in the electron gun was maintained at a level of 30 keV. The density of the power supplied to the surface of liquid zirconium was 0.38 - 0.4 kW/cm^2.

After melting, microstructures or, as the author calls them, nugget products, were discovered in the zirconium ingot. The elemental composition of those nugget products significantly differed from the initial material. The minimum size of microstructures was 0.1–1 μm. **Fig. 2***a* shows a typical mass spectrum of zirconium blanks, and Fig. 2*b* shows mass spectrum of the nugget product formed in the ingot. As can be seen, Li, Be, B, Ba and rare earth metals - elements that

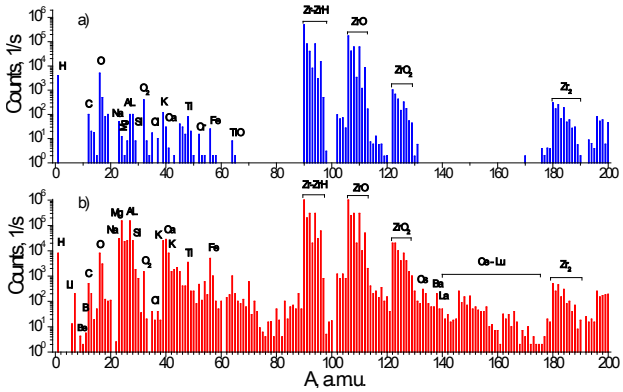

Fig. 2. *a) mass-spectrum of zirconium ingot prior to electron melting, b) mass-spectrum of nugget product.*

were absent in the original ingot - were formed in the nugget product. In addition, the content of elements such as Na, Mg, Al, Si, K, Ca, Ti, Cr, Mn, Fe was increased by 2-3 orders of magnitude in the nugget. The content of these elements in individual nuggets ranged from 2 to 45 weight percent. By means of *X*-ray microanalysis and Auger spectroscopy, a high content of carbon, nitrogen and oxygen was found in nuggets.

In the experiments, a significant increase in the melting rate of zirconium by a factor of 6-8 was noted with a constant input energy of the electron beam, and for some modes of heating the ingot, the rate of its melting would increase by a factor of 50. Thus, the melting process was accompanied by significant energy release. The author points out that the mass of the metal is a critical parameter for the onset of anomalous processes.

2.3. Ultrasound element transmutation

The works of A.F. Kladov [13] noted the transmutation of atomic nuclei of chemical compounds in the process of ultrasonic treatment of their aqueous solutions. The experimental installation was a hydrodynamic rotor-type generator of ultrasonic vibrations. The main parameters of the installation are as follows: sound intensity $>10^6$ W/m^2, frequency (fundamental tone) – $5.9 \cdot 10^3$ Hz, operating pressure in the activator – 10^6 Pa, working volume – 6.3 liters, active zone volume – 0.25 liters.

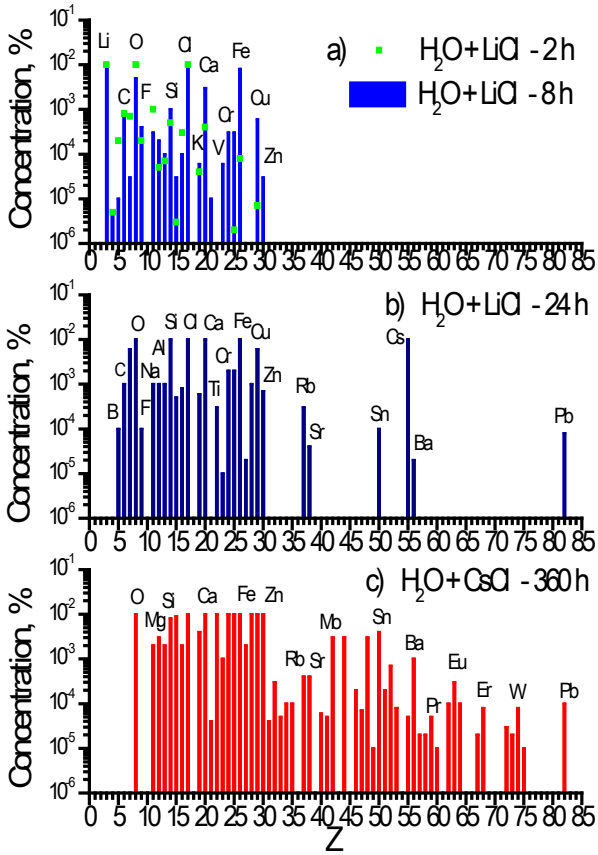

Fig. 3. *a), b) Element composition of LiCl-solution after 2-hour, 8- hour and 24-hour ultrasound activation, c) element composition of CsCl -solution after 360-hour ultrasound activation.*

The author worked with stable and radioactive isotopes. **Fig. 3** shows the spectra of the elements obtained at different times of treatment of solutions of LiCl and CsCl salts. The LiCl solution was treated for 2, 8, 24 hours, and the CsCl solution – for 360 hours. The histograms show that over time, the amount of "extraneous" elements in the solution increases - from boron to lead (Fig. 3*a-c*). Unfortunately, the author did not give, in his paper, the elemental composition of a solution of LiCl and CsCl salts before ultrasonic activation. However, an indirect assessment of the intensity of the appearance of foreign elements can be made by comparing the spectra of LiCl after 2 and 24 hours of treatment.

The paper also describes experiments with radioactive isotopes: ^{60}Co, ^{137}Cs, ^{40}K, ^{126}Sn, ^{188}Pt, ^{197}Hg. It turned out that during the operation of the installation, the number of radioactive

nuclei changes, i.e. there is a transformation of radioactive isotopes into stable isotopes. Also, A. Kladov discovered a significant, twofold, decrease in the activity of the plutonium-beryllium neutron source after the activator was in operation. The source was located at a distance of 2.4 m from the activator. The correctness of the measurements has been confirmed by repeated checks.

During the operation of the installation, the volume of the solution decreased with the guaranteed tightness of the activator. The average rate of solution decrease was 28 ml/hour. This fact means that water molecules are involved in transmutation reactions.

A. Kladov believes that the main operating factor in the presented technological process is cavitation.

2.4. Exposure of gases to braking gamma radiation

In the experiments of A.Yu. Didyk, R. Wisnievsky and others [14-16], high-pressure gases hydrogen, deuterium, helium and xenon were irradiated with braking gamma quanta with a maximum energy of 10 MeV for tens of hours. After irradiation, solid-state micro-objects in the form of crystalline and amorphous microparticles, filaments, nodules and inclusions were found on the inner surfaces of the reaction chambers. The sizes of microobjects were from 0.5 μm to 1 mm. Studies of the elemental composition of the revealed structures, carried out using X-ray microprobe analysis, showed the presence of chemical elements in them that were absent in the reaction chambers before irradiation. Chemical elements were recorded in the range from carbon to actinium (Z = 89).

The most impressive result in the experiment on the irradiation of helium at a pressure of 1.1 kbar for 28 hours was the detection of thin, cylindrical, black foils of considerable size in the inner part of the chamber (**Fig. 4**) [14]. The internal dimensions of the chamber were 15 mm long, 8 mm in diameter, and 0.75 cm^2

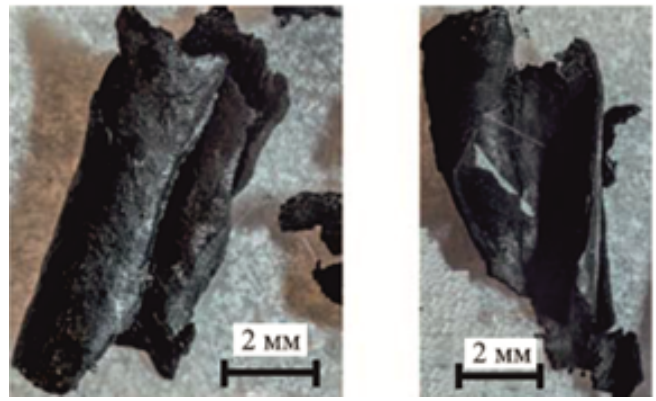

Fig. 4. *Pictures of black foils.*

in volume. The foils consisted predominantly of carbon and left oily marks on the paper. The latter indicates the presence of liquid oils on the foils in the form of hydrocarbons and synthesis of hydrogen. **Fig. 5** shows the total elemental composition of foils and other solid-state microparticles formed as a result of irradiation, averaged over 11 measurements [15].

In three experiments on braking gamma quanta irradiation of xenon $_{54}$Xe at pressures of 250, 270, and 550 bar and with a duration of 60–70 hours, reaction chambers with an inner diameter of 1 cm, a length of 5.8 cm, and a volume of 4.5 см^3 were used [15]. As a result of irradiation in all three experiments, after their completion, newly formed objects were found in the chambers: microparticles with a size of 0.5 μm to 1 mm, and anomalous solid-state structures on the walls of the reaction chambers. The resulting objects mainly contained "extraneous" elements

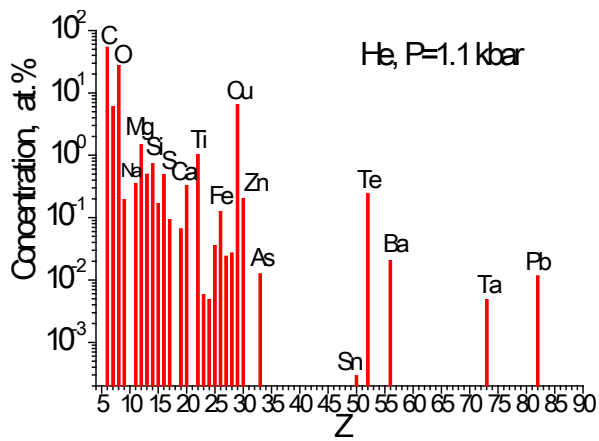

Fig. 5. *The concentrations of elements for experiment with He, P = 1.1 kbar.*

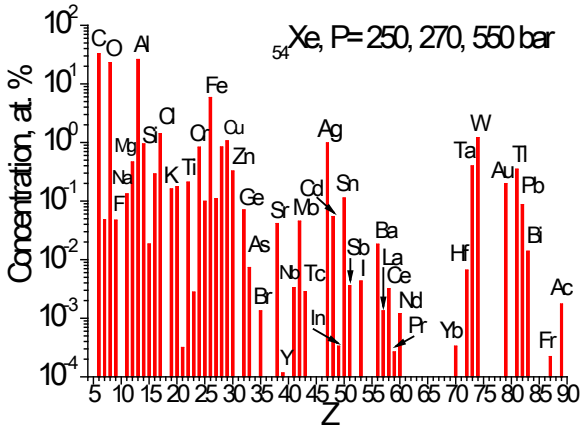

Fig. 6. *The concentrations of chemical elements for three experiments with Xe.*

ranging from carbon to bismuth. Elements were registered in the experiments that do not have stable isotopes: technetium, francium, actinium. **Fig. 6** shows the concentrations of chemical elements averaged over three experiments P = 250, 270, 550 bar. 289 measurements were used in this distribution. Based on the totality of the data of these experiments, it can be argued that "practically all elements" of the Periodic Table are synthesized in xenon as a result of prolonged exposure of condensed xenon to braking gamma quanta.

The first two experiments in the presented experiments on transmutation are associated with electronic action on liquid media: electric current and electron beam. Transmutation in the third experiment is caused by the collapse of cavitation bubbles, in which electrons in the near-surface layer move towards the centers of the bubbles. The directional movement of electrons in experiments with high-pressure gases is created by unidirectional gamma quanta that ionize the gases.

The production of graphite foils in weighed amounts in the experiment with helium **2.4** is explained by the production of orthohelium atoms. Orthohelium is obtained as a result of ionization, by gamma radiation, of gas atoms with subsequent recombination of their ions [22]. The orthohelium atom, in which electron spins and, accordingly, their magnetic moments are parallel to each other, has magnetic fields: ~ 400 T at the center of the atom, in the region of the nucleus and ~70 T at its diameter ~$1.75 \cdot 10^{-10}$ m. Therefore, orthohelium atoms are attracted to each other, combine and create multinuclear molecules, in which transmutation reactions take place.

The production, in experiment **2.1**, of a huge amount of "extraneous" chemical elements up to 300 g/L during the treatment of liquid media in an electric discharge, is associated with the creation of a continuous specific electron current, through which a liquid flow inevitably flows. It is obvious that it is in the plasma film of a specific electric discharge that low-energy transmutation reactions take place. A strong magnetic field is formed inside the discharge film, and that field creates conditions for these reactions.

In experiments: with zone melting of zirconium, with ultrasonic cavitation and with gamma quanta irradiation of xenon, no gram amounts of "extraneous" chemical elements in transmutation products were registered. This is due to the fact that transmutation processes occur in local areas of condensed matter in these experiments. An important feature of these local areas is the presence of strong magnetic fields inside them.

3. ELECTRONS IN EXCITED LIQUIDS

By liquids, we will also mean metal melts and gases at a pressure of ~1 kbar in this paper.

Since in most experiments the transmutation reactions are carried out not in the entire volume of the excited matter, it is logical to assume that some local regions –"capsules" are formed in the matter, which contain a large number of atoms and in which transmutation reactions take place. In addition, the large variety of physical experiments on transmutation requires the existence of some one-type object, characteristic of all these experiments. Such an object of the same type is a "capsule". "Capsules", according to the author, are plasma formations with a strong electromagnetic field inside. Since the diameters

of atoms are in the range (0.1-0.4) nm, and the distances between them in liquids, in melts and in gases at a pressure of ~1 kbar are ~ (0.3-0.5) nm, then, to accommodate several atoms in such "capsules", simple geometric considerations should give their minimum linear dimensions ~1-2 nm.

Numerous experiments have shown that transmutation reactions are carried out from room temperature of a condensed matter [23] to temperatures of ~2000°C. One of the characteristic temperatures favorable for triggering transmutation reactions is the temperature range of 300-400°C. Nanoclusters with a diameter of 6-7 nm are formed near metal surfaces at such temperatures [24]. Such nanocluster size makes it possible to achieve 300% of the concentration of hydrogen or deuterium atoms per cluster atom [25]. This concentration allows us to start cold fusion reactions. I.S. Filimonenko created a hydrolysis installation designed to generate energy in the reaction of "warm" nuclear fusion of helium from deuterium, which works at a temperature of 1150°C [26]. A. Smits and A. Karssen obtained mercury by passing an electric current through thoroughly purified molten lead at a temperature of T = 800°C [27]. V.A.Krivitsky also carried out transmutation reactions, when passing a pulsed current of ~ 7.5 kA through the melt of metals: Pb, Cu and Na_2O, at a temperature of T = 1100°C [12]. A. Rossi [28] and A.G. Parkhomov reactors of [29] operate at temperatures of 1200-1400°C and even at a temperature of 1800°C. Cold fusion reactions were carried out in their reactors followed by the launch of low-energy transmutation reactions.

The average electron energy at room temperature 300 K is 0.025 eV, and it is 0.2 eV at 2300 K. Correspondingly, the de Broglie wavelength $\lambda = h/p$ (p is electron momentum) for the specified temperature range varies from 7.8 nm to 2.7 nm. Correlations can arise between electrons at such distances. Correlations between electrons can also be realized along their coherence length.

The de Broglie wavelength of electrons at a temperature of T ~3 K has a value of ~80 nm, while it is known from the theory of superconductivity that the "size" of a Cooper pair or coherence length is ξ ~2000 nm, $\xi \sim \hbar p_F / m_e k T$, where $p_F = \sqrt{2 m_e \varepsilon_F}$ – the Fermi momentum, ε_F is Fermi energy, k is the Boltzmann constant, m_e is the electron mass. At a temperature T~2300 K, the coherence length for electrons will be ξ~3 nm, which is commensurate with their de Broglie wavelength. The coherence length can be increased by changing the effective Fermi energy $\varepsilon_F^* = \frac{\hbar^2}{2m_e}\left(3\pi^2 \frac{N}{V}\right)^{2/3}$. To do this, it is necessary to increase the density of free electrons by increasing the density of electron current j = $e\rho v$, where V is the volume of the metal, N is the total number of free electrons in it, e is the electron charge, ρ is the density of free electrons, v is the speed of their directed motion.

Correlation between electrons (or other objects) arises from an additional interaction. This interaction does always exist between electrons, but it can be suppressed. Additional interaction begins to manifest itself only when certain conditions are created.

The electron-phonon interaction in metals at extremely low temperatures, at several degrees Kelvin begins to manifest itself, and it transforms metals into a state of superconductivity [30]. In a pairwise electronic interaction that occurs through phonon exchange, electrons are attracted to each other. In the case when their total momentum is equal to zero $\mathbf{P}_{1e} = -\mathbf{P}_{2e}$, correlated electrons pair and form a Cooper pair with oppositely directed spins $S = 0\hbar$.

Electrons are attracted to each other in an atom that is in a strong magnetic field. This attraction is provided by an additional exchange Coulomb interaction when the electron spins are parallel [31]. Exchange interaction appears between identical particles when their wave functions overlap. The more the wave functions

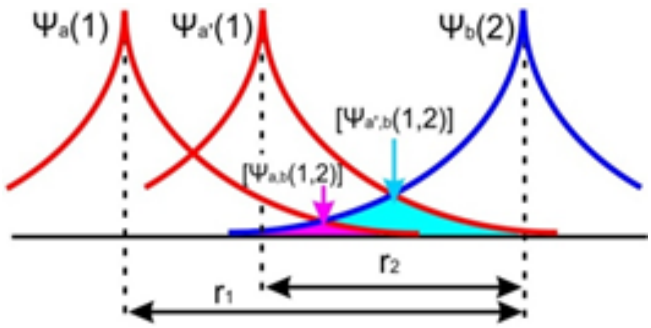

Fig. 7. *Overlap of wave functions of identical particles.*

of identical particles overlap, the greater is the exchange interaction (**Fig. 7**). Due to the exchange interaction, atomic electrons combine into orthobosons – into pairs with $S = 1\hbar$. The fulfillment of the Pauli principle and the equality to zero of the total momentum of electrons in the orthoboson are ensured by the appearance of oscillations of electrons around their orbitals. Electrons in the orthoboson oscillate in antiphase, $\mathbf{P}_{1e} = -\mathbf{P}_{2e}$ [32].

Most transmutation experiments occur, as already mentioned in the introduction, due to the electronic impact on condensed matter with a high electron density: with the help of powerful pulses of electrons or powerful currents. Condensed matter, weakly excited for transmutation reactions, are ionized liquid matter in which, to create strong magnetic fields,

- firstly, there are free electrons and ions not bound into atoms, in sufficient quantities, with a density of $\varrho \geq 10^{21}$ cm^{-3};
- secondly, all or most of the electrons move in liquid matter in the same direction. These electrons make up an ensemble of electrons of volume *W*.

It is known that the directed motion of electrons creates a magnetic field both due to the transfer of electric charges of electrons e− and due to the transfer of their magnetic moments μ_e. The magnetic moments of electrons, which move in one direction, are directed, due to the property of helicity, in one direction, in the direction of their momenta. The spins of electrons are directed against the momenta - they have a left-handed helicity. The electron magnetic moment is directed against the spin. The magnetic field $\mathbf{B}_\mu$ created by the magnetic moments is described by the Landau equation [33]:

$$\mathbf{B}_\mu = \mu_0 \sum_i \frac{3\mathbf{n}_i(\boldsymbol{\mu}_e \cdot \mathbf{n}_i) - \boldsymbol{\mu}_e}{r_i^3}, \quad (1)$$

where $\mu_0 = 1.26 \cdot 10^{-6}$ *H/m* is magnetic constant; $\mu_e = 9.29 \cdot 10^{-24}$ J/T= $5.79 \cdot 10^{-5}$ *eV/T*, *r* – is the distance from the electron to the point at which the field $\mathbf{B}_\mu$ is calculated; $\mathbf{n}_i$ is a unit vector in the direction r_i, i is the number of electrons with parallel spins. It follows from formula (1) that the magnetic moment of an electron $\boldsymbol{\mu}_e$ creates a magnetic field equal to 30 *T* at a distance of 0.092 nanometers along its direction axis (the diameter of a hydrogen atom is 0.106 nm).

Thus, a directionally moving ensemble of electrons generates a seed magnetic field $\mathbf{B}_{\mu 0}$ (1) in a condensed matter, which averaged direction coincides with the direction of electron motion. Therefore, the electrons, in addition to moving predominantly in one direction, additionally rotate around the lines of the magnetic field created by them. In this case, the rotation of all electrons in the ensemble is also unidirectional – clockwise, if you look in the direction of electron motion. In an ionized liquid, as different from a solid state, singly charged ions also move directionally towards the electrons. Therefore, electrons also revolve around ions. Moreover, due to the regular change in the distance between ions and electrons, as a result of the Coulomb interaction between them, the electrons begin to oscillate both along and across the direction of their motion. Due to the thermal motion of electrons and because of their constant collision both with each other with a frequency of $(2\text{-}7) \cdot 10^{14}$ *c*$^{-1}$ and with atoms-ions, the rotation and oscillations of an individual electron can be spoken of as of trends in motion in the general field created by the ensemble of electrons. However, the combined motion of all electrons in the ensemble forms both a local vortex motion

of matter in a liquid medium and oscillations of matter inside the vortex.

The electron spins are oriented in the seed magnetic field $\mathbf{B}_{\mu 0}$ either along the field or against it. Due to its nature, the magnetic field $\mathbf{B}_{\mu 0}$ created by the sum of magnetic moments of electrons, is spatially inhomogeneous and anisotropic. Therefore, electrons which move in a changing field $\partial \mathbf{B}_{\mu 0}/\partial t$ and which have a field-antiparallel orientation of the magnetic moments $\mathbf{B}_{\mu 0}\uparrow\downarrow\boldsymbol{\mu}_e$, will change the direction of the magnetic moments $\boldsymbol{\mu}_e$. Thus, the number of free electrons in a state with magnetic moments parallel to the field increases, up to the moment when most electrons would pass into this state. Consequently, the seed magnetic field increases up to saturation $\mathbf{B}_{\mu}$. Accordingly, the spins of these electrons will also become parallel. Spin plasma is formed.

4. PAIRING OF ELECTRONS IN LIQUIDS

4.1. Strong magnetic fields

At a temperature of molten metals T ~2300 K (0.2 eV), the density of electrons is ϱ ~(1-3)·10^{22} см$^{-3}$, which corresponds to the average distance between them ~(5-3)·10^{-8} cm. The volume of a sphere with a radius equal to the de Broglie wavelength or the coherence length $\lambda \approx \xi$ ~30·10^{-8} cm contains ~(1-3)·10^3 electrons. At a density of ϱ ~10^{21} см$^{-3}$, the volume of such a sphere contains ~ 100 electrons.

In an ensemble of unidirectionally moving electrons with the number n and volume W, both spins and magnetic moments are parallel. Parallel magnetic moments of electrons generate a collective, magnetic field $\mathbf{B}\boldsymbol{\mu}$.

Electrons with parallel spins are attracted to each other due to the exchange interaction. Each electron attracts electrons in itself, which are in the volume of the correlation sphere with a radius $\lambda \approx \xi$. The volume of the electrons ensemble W can be larger than the volume of the correlation sphere; however, all electrons that make up the ensemble are cross-attracted to each other. Therefore, the ensemble of electrons forms, due to the exchange interaction, a collective exchange field in its micro- and more than microvolume W. The energy of one electron ε_i with a wave function φ_i can be determined using the Hartree-Fock self-consistent field method from the equation:

$$\left\{-\frac{\hbar^2}{2m}\nabla^2 - \sum_A \frac{Z_A e^2}{r_{iA}}\right\}\varphi_i + \left[\sum_{j=1}^{n}\int d\vec{r}\,\varphi_j^* \frac{e^2}{r_{ij}}\varphi_j\right]\varphi_i -$$

$$-\left[\sum_{j=1}^{n}\int dr\varphi_j^* \frac{e^2}{r_{ij}}\varphi_i\right]\varphi_j = \varepsilon_i\varphi_i, \quad i = 1,2,3,...,n.$$

The curly brace gives the sum of the operators of the kinetic energy of an electron and its potential interaction energy with all ions Z_A. We can assume that Z_A =1. The first square bracket shows the operator of the energy of the usual, interelectronic Coulomb repulsion – the Hartree contribution, the operator of the interelectron exchange Coulomb attraction energy – the Fock contribution – is given in the second bracket.

The contribution of Hartree (E_H) to the self-consistent field can be neglected, since the repulsion of electrons is compensated at densities of ~10^{21} cm^{-3} by their attraction to positively charged ions, because Debye radius − the distance over which the action of the electric field of a separate charge in a quasi-neutral medium extends, has the size of an atom $r_D = \sqrt{\frac{\varepsilon_0 kT}{\rho e^2}} = 69\sqrt{\frac{T}{\rho}} = 10^{-8} cm,$ where $\varepsilon_0 = 8.8\cdot 10^{-12}\ F/m$ is electric constant.

Therefore, a self-consistent field is formed only due to the Fock contribution (E_F), which is determined by the multi-exchange Coulomb attraction between electrons with parallel spins. The Hartree-Fock equation takes the following form:

$$\left\{-\frac{\hbar^2}{2m}\nabla^2 - \sum_A \frac{e^2}{r_{iA}}\right\}\varphi_i - \left[\sum_{j=1}^{n}\int dr\varphi_j^* \frac{e^2}{r_{ij}}\varphi_i\right]\varphi_j = \varepsilon_i\varphi_i.$$

Strictly speaking, the Fock contribution to the self-consistent field potential must be larger than the Hartree contribution for electron pairing in liquids, $E_F > E_H$. The exchange attraction between electrons associated with the overlap

of their wave functions decreases exponentially with an increasing distance between electrons (Fig. 7). Therefore, since the net interelectronic repulsion is much greater than the interelectronic exchange attraction, and to satisfy the condition $E_F > E_H$, in a liquid plasma it is necessary that $\lambda >> r_D$.

$$\lambda = \frac{h}{\sqrt{3m_e kT}} \gg \sqrt{\frac{\varepsilon_0 kT}{\rho e^2}} = r_D,$$

then,

$$\rho \gg 3m_e\varepsilon_0\left(\frac{k}{he}\right)^2 T^2 = 4.1\cdot 10^{11} T^2 [cm^{-3}].$$

At temperatures of liquids of 300-2300 K, the last ratio is fulfilled at electron densities above 10^{18}-10^{20} cm^{-3} respectively. The densities of electrons in liquids with values of $\rho \geq 10^{21} cm^{-3}$ are important for the formation of seed magnetic and exchange fields in them.

Since the electrons in the ensemble W are attracted to each other, then, consequently, the first Cooper condition on their pairing is satisfied [30]. According to L. Cooper condition for pairing electrons, the attraction between them can be arbitrarily small. It is important in our case that the exchange potential is greater than the energy of the thermal motion of electrons. Then, the continuous spectrum of electronic states in the negative field potential of volume W will transform into a discrete spectrum with their n_a, ℓ, m, n_b – quantum numbers that satisfy the Pauli principle. It is noteworthy that the exchange field generated by electrons with parallel spins affects them only. Since all electrons in the exchange field have parallel spins, then practically the only way to fulfill the Pauli principle is the pairing of electrons into orthobosons $S = 1\hbar$. This pairing is carried out due to the fact that electrons in a magnetic field acquire new, oscillatory quantum numbers n_b [20]. The electrons that make up the orthoboson have oscillations, which are correlated in the pulses $\mathbf{P}_{1e} = -\mathbf{P}_{2e}$ — this is the second condition for electron pairing [30]. Due to the fulfillment of the condition $\mathbf{P}_{1e} = -\mathbf{P}_{2e}$, the oscillatory quantum numbers of paired electrons are equal to each other in absolute value, but opposite in sign $n_b^1 = -n_b^2$, n_b = 1,2,3… The Pauli principle is satisfied.

Consequently, pairing of electrons into orthobosons will be carried out automatically in local regions of weakly excited liquids, in which electrons move unidirectionally and have a density ≥ 10^{21} cm^{-3}.

The trajectories of motion of electrons in the orthoboson can be represented as closed spirals nested into each other, located on the toroid surface. An orthobosonic pair is a toroidal ring current with a radius (**Fig. 8***a*). In contrast to the atom, in which the atomic nucleus with charge Z is always in the center, the counter flux of positive ions in the orthopair in its "center" can be not only different, but it also changes in time.

According to Bohr's theory, the radius of the electron orbital in a hydrogen-like atom with a nuclear charge Z and a principal quantum number na is equal to:

$$r_Z = \frac{4\pi\varepsilon_0\hbar^2}{m_e Ze^2} n_a^2. \qquad (2)$$

The electron velocity on the orbital is equal to: $V_Z = n_a\hbar / m_e r_Z$. The ring current of the orthoboson $2e^-$ is equal to:

$$I_Z = 2eV_Z / 2\pi r_Z = en_a\hbar / m_3\pi r_Z^2. \qquad (3)$$

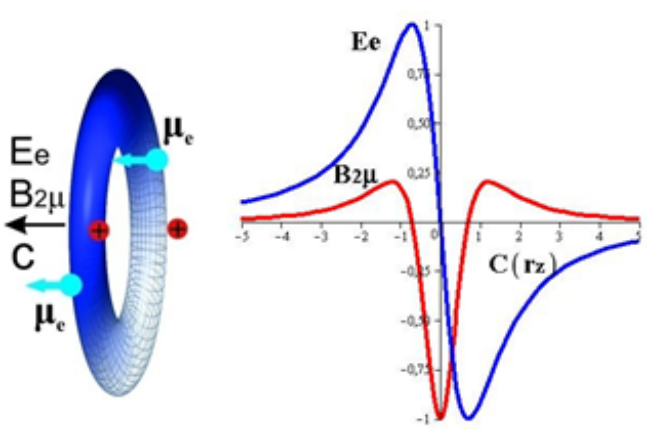

Fig. 8. *a – orthoboson; b - dependence of the electric Ee and magnetic $B_{2\mu}$ fields in relative units along the C axis.*

Let us assume that the correlation between the electrons, which make up the orthoboson arises from the minimum average distance between free electrons in metal melts to the minimum size of "capsules" 0.3–1 nm (r_Z = 0.15–0.5 nm). Then, the magnetic field formed by the parallel magnetic moments μ_e by a pair of electrons in the center between them according to (1) $\boldsymbol{B}_{2\mu} = -\mu_0 2\boldsymbol{\mu}_e / r_Z^3$: varies in the range from 7 to 0.2 *T*. The average effective ion charges for electron correlations at such distances according to formula (2) for the principal quantum number n_a = 1 are, respectively, *Z* = 0.35-0.1. The physical meaning of such values is that the ions are not constantly in the center of the orthobosonic pair, since they and electrons move towards each other. In addition, the Coulomb field of the ions is screened by the field of other, uncorrelated electrons.

It is known from [20] that the radius of the orthoboson decreases by a factor of three compared to the initial radius at which the correlation arises. This is due to the fact that electronic oscillations generate additional binding energy of electrons with ions. And since the energy of rotation of electrons around ions and the energy of oscillations depend on each other, then an additional energy connection of electrons with ions arises. In addition, the exchange Coulomb attraction between electrons in an orthobosonic pair completely compensates for their Coulomb repulsion: electrons in an orthoboson interact only with ions. Because of this, the orthoboson radii r_Z decrease threefold and become equal to ~0.05-0.15 r_Z, and the magnetic fields at the center of the orthoboson increase, respectively, up to $B_{2\mu}$ ~ (190–7) T.

The ring current of the orthoboson ($2e^-$) also forms the magnetic field B_e. In the center: $B_e = \mu_0 I_Z / 2r_Z$. We substitute the value of the ring current (3) for n_a = 1 in the formula, we obtain, $\boldsymbol{B}_e = -\mu_0 \boldsymbol{\mu}_e / \pi r_Z^3$, $(\boldsymbol{\mu}_e = e\hbar / 2m_e)$. The magnetic field at the center of the ring current is 2π times less than the field created by the magnetic moments of the electrons μ_e.

Thus, electrons move in an ionized liquid in one direction and have a density of ≥ 10^{21} cm^{-3}, a seed magnetic field $B_{\mu 0}$ is generated. The saturation magnetic field B_μ and the exchange field of electrons with parallel spins produce orthobosons *S* = 1ħ, each of which is formed from a pair of correlated electrons. Orthobosons create a strong magnetic field $B_{2\mu}$ in the liquid. A "spontaneous" magnetization of the liquid occurs [34].

4.2. "Capsules", unknown particles and high-temperature superconductivity

The ring current of radius r_Z with charge e creates electric and magnetic fields on the *C* axis, respectively: $E_e = (ec/4\pi\varepsilon_0)\cdot(r_Z^2 + c^2)^{-3/2}$ and $B_e = \mu_0(I\cdot r_Z^2/2)\cdot(r_Z^2 + c^2)^{-3/2}$, where *I* is the ring current [35]. The joint solution of these equations gives a potential well on the *C* axis at a distance $r_Z / \sqrt{2}$ from the center of the ring (Fig. 8).

The magnetic field $B_{2\mu}$ generated by the magnetic moments of the orthoboson, has a maximum value in the center. In this case, the magnetic induction vector $\mathbf{B}_{2\mu}$ is directed against the direction of the magnetic moments of the electrons μ_e. The magnetic field becomes zero on the *C* axis, at a distance $c = r_Z / \sqrt{2}$ from the center of the ring. The direction of the field changes sign at this point. Further, it coincides with the direction of the magnetic moments. The maximum of the external field is located at a distance $r_Z\sqrt{3/2}$ from the center of the orthoboson. And its value is five times less than the maximum value of the field in the center. In accordance with the values calculated in the previous chapter, the maximum values of external magnetic fields will be 40−1.5 *T*. Further, the magnetic field decreases with increasing distance c as $4\mu_0\mu_e/c^3$ (1), (Fig. 8*b*). The *C*-axis distance is given in r_z units in Fig. 8*b*.

Orthobosons are attracted to each other due to their external magnetic fields. In this case, magnetic self-focusing is carried out and

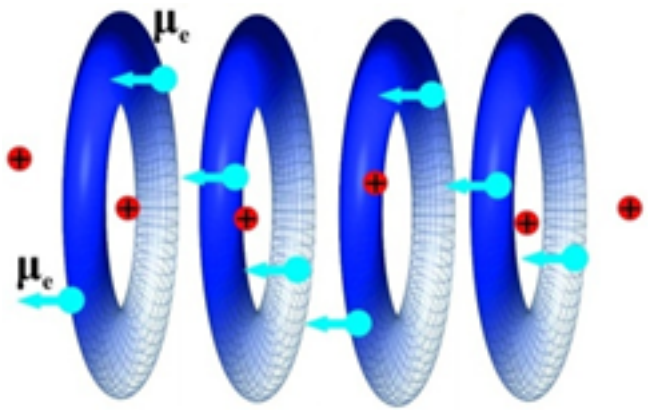

Fig. 9. *"Capsule" – orthoboson "solenoid".*

an orthoboson "solenoid" is formed with equal distances $r_z/\sqrt{2}$ between the centers of the orthobosons. Since the flux of positive ions inside the orthobosonic "solenoid" are the same for all orthobosonic pairs, their diameters will be equal to each other (**Fig. 9**). The orthobosons of the "solenoid" do not form a single Bose-Einstein condensate, since each orthoboson has no constant central positive charge. Positive ions which pass inside the orthobosons constantly change their location from one orthoboson to another, neighboring orthoboson. Therefore, there is no directional Coulomb attraction of neighboring orthobosons to neighboring ions. Unlike transatoms, which have Bose-Einstein orthobosonic condensates and have central, positively charged atomic transnuclei. Therefore, Bose-Einstein condensates of transatoms are combined into one, common condensate. With such a combination, a nuclear transmolecule is formed, in which transnuclei enter into low-energy nuclear reactions. **Fig. 10**, as an example, shows the formation of the sodium transmolecule $_{11}Na^{M}$ from the transatoms of boron $_5B^{T}$ and carbon $_6C^{T}$.

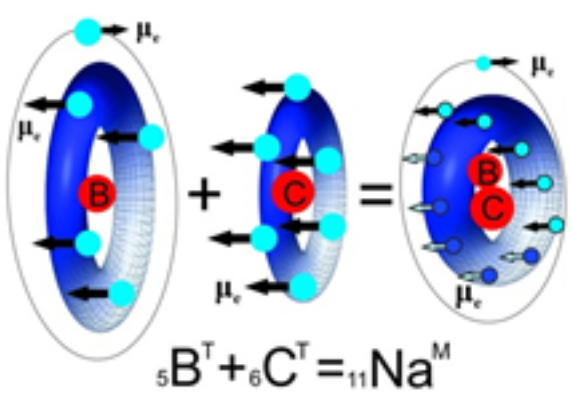

Fig. 10. *The formation of sodium transmolecule from boron and carbon transatoms.*

The orthobosonic "solenoid" is the very "capsule" that was discussed at the beginning of chapter 3. The number of orthobosons in "capsules" can be different. It depends on the state of a weakly excited liquid, on its temperature, on its chemical composition, and on the density of the electron flux.

Although the orthobosons of the "solenoid" do not create a **united** Bose-Einstein condensate, when they join into a "capsule", they nevertheless form a common condensate **distributed** in space. All electrons in the "capsule" have equal energies, and the orthobosons have additional binding energy due to the exchange interaction, but this time due to exchange interaction of bosons with each other. This relation makes the "capsule" resistant to both external and internal influences. "Capsules" will exist as long as there is a sufficient amount of free electrons in the condensed matter, which are formed as a result of external influence or due to transmutation reactions.

It is obvious that inside the orthobosonic "solenoid" magnetic fields multiply increase, thus creating conditions for the transformation of atoms into transatoms and triggering low-energy transmutation reactions. Despite the fact that nuclear transmutation reactions take place inside the "capsules", as mentioned above, "capsules" are stable objects. Low-energy nuclear transmutation reactions are non-radiation reactions. Energy is released in these reactions in the form of kinetic energy of multiply charged ions. The scattering positive multiply charged ions will pull with them a separate orthoboson or the entire orthoboson "solenoid" and can pull it out of the liquid.

It is known that the process of transmutation is accompanied by the emission of rare, unknown particles, which leave "strange" traces in photographic emulsions, on thin sections

of metals and which, when interacting with a substance, change its structure and chemical composition. It is the "capsules", which generate in a condensed matter, move inside and outside it, are that exact "strange" radiation that is recorded in many experiments [6,7,10,36,37]. "Capsules" possess strong electric and magnetic fields. If the "capsules" together with the interacting transatoms inside them move along the surface of the "detectors", then they create bizarre patterns on them, which are observed in experiments.

It was emphasized in [38] that the higher the energy density of the excited matter, the more atoms can be involved in the input channel of the transmutation reaction. This means that the size of the "capsule" changes, and the higher the density of electrons moving in one direction in the liquid, the more orthobosons are formed in it and the larger is the linear size of the orthoboson "capsule".

The "capsule" has strong, symmetrical magnetic and electric fields at its ends and it will draw in itself, along its axis, positively charged ions. The number of ions drawn in will be as much as is necessary to maintain the size of the diameters of the orthobosons in the "capsule". Moreover, these electromagnetic fields separate the energies of free electrons that surround the "capsule" and capture them in orbitals of large radii with different principal quantum numbers according to formula (2). After being captured in the orbital, electrons will carry out transitions to lower electronic levels, as happens in atoms. The transitions will be accompanied by the emission of photons. And since electrons rotate on orbitals, and additionally oscillate around them, the electrons begin to pair into orthobosons and join the "capsule". Consequently, a "capsule" in a condensed matter saturated with free electrons will stimulate the formation of orthobosons and, thus, will automatically increase its size. Formation of a "capsule" can begin with one orthoboson.

The maximum size of the orthoboson "capsule", in the case of the passage of electrons through the liquid, can be from the cathode to the anode. Orthobosons form continuous, unbreakable "filaments" from one electrode to another. It is this orthoboson current, in the form of a specific electric discharge that was observed in A.V. Vachaev and N.I. Ivanov installation (see **2.1**) [3]. The orthobosonic current has the property of superconductivity, since it is impossible to destroy it due to the energy of the thermal motion of the atoms of the medium. Consequently, high-temperature superconductivity can, under certain conditions, be realized in weakly excited liquids.

5. CONCLUSION

Numerous experiments on low-energy transmutation reactions have shown that nuclear reactions occur at low energies in weakly excited condensed matter. The properties of transmutation reactions contradict the properties of conventional nuclear reactions. This circumstance allows us to assert that, the process of paradigm change in science starts at present [21].

The analysis of the experiments on transmutation revealed the conditions under which they occur. The main condition is the presence of regions with a strong magnetic field in the excited matter, more than 30 *T*. It turned out that atoms pass into another, altered state, into transatoms in such fields. Transatoms combine into one common transatom, and their transnuclei form multinuclear molecules and enter into transmutation reactions.

It follows from the proposed model of the emergence of strong magnetic fields in excited liquids, that there must be free electrons and free ions in it with a concentration of $\geq 10^{21}$ cm^{-3}. It is also necessary that all or some of the electrons move predominantly in the same direction. Unidirectionally moving electrons have parallel spins and, accordingly, parallel magnetic moments. Parallel magnetic moments

of electrons generate a common seed magnetic field. Electrons with parallel spins, due to the exchange interaction, create a collective self-consistent field with a negative potential. Under such conditions, correlations arise between pairs of electrons, and they form orthobosons with $S = 1\hbar$. Orthobosons, in turn, are attracted to each other and create an orthoboson "solenoid" – "capsule" with a strong magnetic field. Transmutation reactions take place inside such "capsules".

To enhance pairing of electrons, the excited liquid can be placed in an external magnetic field, which direction coincides with the direction of motion of electrons [3,12]. It is also helpful to create directional vortex flows in the fluid. A natural process that increases the density of electrons and ions in orthobosonic liquids is low-energy reactions, the products of which, due to their ionization losses, generate additional free electrons and ions in the matter. The largest ionization losses correspond to high-energy ions: protons, alpha particles, fragments from uranium fission and other multicharged ions. This property of ions can be used to generate "capsules".

It should be remembered that spontaneous orthobosonic electron pairing can occur in liquid and solid-state, melted-down industrial fuel cells. Such pairing will lead to transmutation reactions, to additional uncontrolled energy release and, possibly, to explosive destruction of energy generators!

It is worth paying attention to the fact that:

- the Coulomb repulsion between electrons, in an ordinary atom, is many times greater than the interelectron exchange Coulomb attraction;

- but already in orthobosones of transatoms, the energy of exchange attraction between two electrons is exactly equal to the energy of Coulomb repulsion between them;

- and, finally, the exchange attraction between free electrons completely dominates over their electron-electron Coulomb repulsion in a spin plasma.

A well-known, useful rule follows from the above: If unequal forces act on an object under normal conditions, then there must exist such conditions, that when the object is placed into them, the ratio of the forces that act on it will not only change, but some of the forces can be significantly suppressed, i.e. the ratio of the forces that act on an object depends on the conditions in which it is located.

Due to exchange forces in weakly excited condensed matter [39], ordinary liquids turn into quantum liquids, and their theoretical and experimental studies will make it possible to control low-energy nuclear reactions, and not just that.

REFERENCES

1. *Proceedings of the 1-26th Russian Conferences on Cold Transmutation of Nuclei of Chemical Elements,* 1993-2018. (*RCCTNCE*).
2. *Proceedings of the 1-23th International Conferences on Condensed Matter Nuclear Science* (*Cold Fusion, ICCF*).
3. Balakirev VF, Krymsky VV, Bolotov BV, Vasilieva NV, Vachaev AV, Ivanov NI, Kazbanov VI, Pavlova GA, Solin MI, Trofimov VI, Urutskoev LI. *Vzaimoprevrashcheniya khimicheskikh elementov* [Mutual transformation of chemical elements]. Ekaterinburg, Urals Branch of RAS Publ., 2003, 96 p.
4. Karabut AB., Kucherov YaR., Savvatimova IB. Nuclear product ratio for glow discharge in deuterium. *Phys. Letters A*, 1992, 170:265-272.
5. Savvatimova IB, Karabut AB. The products of nuclear reactions recorded at the cathode after experiments in a glow discharge in deuterium. *Poverhnoct'* [*Surface Investigation: X-Ray, Synchrotron and Neutron Techniques*], 1996, 1:63-75-81.
6. Savvatimova IB. Transmutation Effects in the Cathode Exposed Glow Discharge. Nuclear

Phenomena Or Ion Irradiation Results? *Proc. 7th Int. Conf. on Cold Fusion* (*ICCF*), Canada, 1998: 342-350; Reproducibility of Experiments in Glow Discharge and Processes Accompanying Deuterium ions Bombardment. *Proc. 8th ICCF*, Italy, 2000:277-283.

7. Solin MI. Experimental facts of spontaneous appearance of condensate of soliton charges with the formation of nuclear fusion products in liquid zirconium. *Physical Idea in Russia*, 2001, 1:43-58 (in Russ.).
8. Controlled Nucleosynthesis Breakthroughs in Experiment and Theory. Editors Adamenko SV, Selleri F, A van der Merwe. Series: *Fundamental theories in Physics,* Springer, 2007, v. 156, p. 780. http://www.springer.com/physics/elementary/book/978-1-4020-5873-8.
9. Adamenko SV. The concept of artificially initiated collapse of matter and the main results of the first stage of its experimental implementation. *Preprint*, 2004, Kiev (in Russ.). http://proton-21.com.ua/publ/Preprint_ru.pdf.
10. Urutskoev LI, Liksonov VI, Tsinoev VG. *Annales de la Fondation Louis de Broglie* (*AFLB*), 2002, 27(4):701-726.
11. Kuznetsov VD, Mishinsky GV, Penkov FM, Arbuzov VI, Zhemenik VI. Low energy transmutation of atomic nuclei of chemical elements. *AFLB*, 2003, 28(2):173-214.
12. Krivitsky VA. *Paradoksy transmutatsii i razvitie Zemli* [Paradoxes of transmutation and the development of the Earth]. Moscow, NITs "Academica" Publ., 2016, 238 p.
13. Kladov AF. Cavitation destruction of matter (in Russ.); http://roslo.narod.ru/rao/rao1.htm.
14. Didyk AYu, Wiśniewski R and Wilczynska-Kitowska T. The carbon-based structures synthesized through nuclear reactions in helium at 1.1 kbar pressure under irradiation with braking γ-rays of 10 MeV threshold energy. *Euro. Phys. Lett.*, 2015, 109: P.22001-P.1-22001-P.6.
15. Wiśniewski R, Mishinsky GV, Gulbekian GG, Wilczyńska-Kitowska T, Semin VA. Sintez khimicheskikh elementov i tverdotelnukh struktur pri obluchenii γ-kvantami kondensirovannykh gazov [Synthesis of chemical elements and solid-state structures under irradiation by γ-quanta in condensed gases]. *International Journal of Unconventional Science* (*IJUS*), 2017, 17-18(5):6-15 (in Russ.). http://www.unconv-science.org/.
16. Wisniewski R, Mishinsky GV, Wilczynska-Kitowska T, Zukowska Z, Rostocki A. Graphite-like structures, synthesized from gaseous He under high pressure, by braking irradiation of maximum energy of 10 MeV – modeling of the process. *Acta Physica Polonica B, Proceedings Supplement*, 2020, Vol. 13, No 4.
17. Vysotskii VI, Kornilova AA. *Nuclear fusion and transmutation of isotopes in biological systems*. Moscow, Mir Publ., 2003, 304 p.
18. Vysotskii VI, Kornilova AA. Transmutation of stable isotopes and deactivation of radioactive waste in growing biological systems. *Annals of Nuclear Energy*, 2013, 62:626–633.
19. Kornilova AA, Vysotskii VI. Synthesis and transmutation of stable and radioactive isotopes in biological systems. *Radioelectronics. Nanosystems. Information Technologies* (*RENSIT*), 2017, 9(1):52-64. DOI: 10.17725/rensit.2017.09.052, http://en.rensit.ru/.
20. Mishinsky GV. Resonant interference exchange interaction. *RENSIT,* 2019, 11(3):261-278. DOI: 10.17725/rensit.2019.11.261.
21. Mishinsky GV. Towards a New Paradigm. *RENSIT*, 2020, 12(3):529-544. DOI: 10.17725/rensit.2020.12.529.
22. Mishinsky GV. Multinuclear reactions in condensed helium. *RENSIT*, 2017, 9(1):94-105. DOI: 10.17725/rensit.2017.09.094.

23. Fleishmann M, Pons S, Hawkins M. Electrochemically induced nuclear fusion of deuterium. *J. Electroanal. Chem*., 1989, 26:301-308.
24. Nesvizhevsky VV, Voronin AYu, Lambrecht A, Reynaud S, Lychagin EV, Muzychka AYu, Strelkov AV. Observation of quantum levitation of nanoparticles by the method of ultracold neutrons. *Crystallography*, 2013, 58(5):730-736 (in Russ.).
25. Arata Y, Zhang YC. Formation of Condensed Metallic Deuterium Lattice and Nuclear Fusion. *Proc. Jpn. Acad., Ser. B*, 2002, 78:57.
26. Filimonenko IS. Demonstratsionnaya termoemissionnaya ustanovka dlya yadernogo sinteza [Demonstrational therm-emission device for nuclear fusion]. Materials *3 Sci. Symp. "Perestroyka estestvoznaniya* [*Restructuring of Natural history*]"-92, Volgodonsk, Russia, 17-19 Apr. 1992 (in Russ.).
27. Smits A, Karssen A. Vorläufige Mitteilung über einen Zerfall des Bleiatoms. *Naturwissenschaft*, 1925, 13:699; Ein Zerfall des Bleiatoms, *Zeit Elektrochemie*, 1926, 32:577-586.
28. Levi G, Foschi E, Höistad B. Observation of abundant heat production from a reactor device and of isotopic changes in the fuel. – http://www.sifferkoll.se/sifferkoll/wp-content/uploads/2014/10/LuganoReportSubmit.pdf.
29. Parkhomov AG, Alabin KA, Andreev SN, Zabavin SN, Sobolev AG, Timerbulatov TR. Nickel-hydrogen reactor: heat generation, isotopic and elemental composition of fuel. *RENSIT,* 2017, 9(1):74-93. DOI: 10.17725/rensit.2017.09.074.
30. Cooper LN. Bound electron pairs in a degenerate Fermi gas. *Phys.Rev*, 1956, 104:1189.
31. Heisenberg W. Über die Spektra von Atomsystemen mit zwei Elektronen. *Z. Phys.,* 1926, 39(7):499-518.
32. Mishinsky GV. Atom in a strong magnetic field. Transformation of atoms to transatoms. *RENSIT,* 2017, 9(2):147-160. DOI: 10.17725/rensit.2017.09.147.
33. Landau LD, Lifshitz EM. *Field theory*. Moscow, Nauka Publ., 1973, 138 p.
34. Kulakov AV, Rumyantsev AA. Spontaneous magnetization of a plasma of quantum origin. *JTP*, 1988, 58(4):657-662.
35. Druzhkin LA. *Field theory problems*. Moscow, Energy Publ., 1964, 461p.
36. Nesterovich AV, Rodionov BU, Savvatimova IB. Formation of tracks during cold transmutation of atomic nuclei. *Proc. of 8th RCCTNCE*, Moscow, 2001, pp. 211-215.
37. Baranov DS, Baranova OD. Observation of the isomers 212m1Bi at the experiments with some bismuth salts aqueous solutions. *Proc. of Intern. Conf. on Isomers INIR-2011*. Ed. JINR E15, 18-2012-15, Dubna, 2012, pp. 141-159.
38. Mishinsky GV, Kuznetsov VD. Element distribution in the products of low-energy transmutation. Nucleosynthesis. *AFLB*, 2008, 33(3-4):331-356.
39. Kulakov AV, Orlenko EV, Rumyantsev AA. *Quantum exchange forces in condensed matter*. Moscow, Nauka Publ., 1990, 120 p.

DOI: 10.17725/rensit.2021.13.319

Transfer of "dark hydrogen" by atomic matter. Methods of diagnostics of "dark hydrogen"

Dmitry S. Baranov
Joint Institute for High Temperatures of Russian Academy of Sciences, https://jiht.ru/
Moscow 125412, Russian Federation
E-mail: bds07@yandex.ru

Valery N. Zatelepin
Laboratory INLIS
Moscow 127521, Russian Federation
E-mail: zvn07@yandex.ru

Viktor A. Panchelyuga
Institute of Theoretical and Experimental Biophysics of Russian Academy of Sciences, https://iteb.ru/
Pushchino 142290, Moscow region, Russian Federation
E-mail: victor.panchelyuga@gmail.com

Alexander L. Shishkin
LLC "AVK-BETA"
Dubna 141983, Moscow region, Russian Federation
E-mail: avkbeta@mail.ru

Received July 05, 2021, peer-reviewed July 19, 2021, accepted July 26, 2021

Abstract: **This work experimentally shown that traces found on track detectors during the study of low-energy nuclear reactions are also formed in the course of many widely used technical processes (combustion of hydrocarbons, operation of internal combustion engines, physicochemical processes accompanying the process of charging smartphone batteries). This coincidence of the track pattern allows us to consider low-energy nuclear reactions as a significant environmental factor, and indicates the important role of "dark hydrogen" in nature. The paper shows the convective transfer of "dark hydrogen" from the discharge zone along the path of the air-water mixture. Using the theoretical model of "dark hydrogen", fundamentally new, less laborious, in comparison with track, methods of its registration have been developed and described: 1) measurement of the charge of a copper box with its irradiation with "dark hydrogen", 2) measurement of pressure in a closed volume when irradiated with "dark hydrogen", 3) the use of a torsion balance with a nickel plate with magnets when irradiated with "dark hydrogen".**

Keywords: **low-energy nuclear reactions, "dark hydrogen", track detectors, tracks, registration methods.**

УДК 537.58:53.047

For citation: Dmitry S. Baranov, Valery N. Zatelepin, Viktor A. Panchelyuga, Alexander L. Shishkin. Transfer of "dark hydrogen" by atomic matter. Methods of diagnostics of "dark hydrogen". *RENSIT,* 2021, 13(3):319-328. DOI: 10.17725/rensit.2021.13.319.

Contents

1. INTRODUCTION

The work of the authors of the 2018 [1] led to the understanding that the reactions that are responsible for the "excess" energy release in LENR reactors go with the formation of a special form of substance, which was called "dark hydrogen". Experiments on the detection of soft and hard *X*-rays with energies of 28 keV and 260±30 keV at a 20 kV discharge in a water-air droplet medium are described in [2-3], and a model of a "dark hydrogen" particle is constructed. In [2], the sign $\hat{H}_2$ was introduced to denote "dark hydrogen".

In [3], a model of $\hat{H}_2$ is constructed that allows analyzing the unique physical and chemical properties of $\hat{H}_2$, which requires the development of special methods for its registration and research. One of the properties of "dark hydrogen", which is noted in [3], is the ability to form a compound with the atoms (nuclei) of particles of the surrounding matter. In this reaction of $\hat{H}_2$ with the surrounding matter, an energy of several hundred keV is released per single act. It is this property of "dark hydrogen" that helps the formation of tracks and craters in the substance located near its source. "Dark hydrogen" of 10-13 m in size can be the basis for constructing objects of 10-10 m or more in size. In this range of sizes lies a gigantic variety of "unknown particles" of new matter.

In many studies, the formation of craters and tracks in the surrounding matter was recorded during experiments with electric discharges [3], and with a nickel-hydrogen reactor [4].

In this paper, it is experimentally shown that tracks and craters (derivatives of "dark hydrogen") are formed in many other processes: near a gas burner, in the exhaust of a car, when charging a smartphone. These experiments, made using CD disks as detectors, suggest a more significant role for "dark hydrogen" in nature.

With the help of CD disks, the convective transfer of "dark hydrogen" from the discharge zone along the path of the water-air medium movement was registered, when CD disks were located along the path of movement.

In this paper, the registration of "dark hydrogen" was carried out by three other fundamentally new, less time-consuming methods than the analysis of tracks on CD: (1) measurement of the charge of a copper box with an electroscope when it is irradiated with "dark hydrogen", (2) measurement of the pressure in a closed volume when irradiated with "dark hydrogen", (3) use of a torsion balance with a Ni plate with magnets when irradiated with "dark hydrogen".

Experimental methods for detecting "dark hydrogen" (1)-(3) were developed on the basis of a theoretical model. The successful implementation of these methods confirms the validity of the theoretical model.

2. REGISTRATION OF UNKNOWN PARTICLES USING CD

Perhaps one of the first researchers who described the use of a CD disk for recording unknown radiation from a reactor was paper [5]. Before him, *X*-ray films were used to record traces of unknown radiation [4]. Other works describe traces of unknown radiation recorded on glass, smooth metal surfaces [6], and on ccarbon paper.

Almost all the photos presented in this paper are reduced to a uniform scale, at which the width of the photo corresponds to 2 mm of the field of observation in the microscope. The multi-colored triangle at the top of the photos is due to the side illumination, which is done to visualize the traces of unknown particles.

The CD surface, which, when registering traces of unknown radiation, turns to the source of unknown radiation, has the appearance of a smooth surface with an aluminum sheen. But this is not an aluminum surface, as can be seen from the left part of **Fig. 1***a*, but a surface of optically transparent polycarbonate with a thickness of 0.3 mm. The aluminum layer is located deeper. Thus, the unknown particles that are detected by CD leave their traces in the surface layer and in the depth of the polycarbonate deposited on the aluminum layer. It is also possible for unknown parts to adhere to the CD surface. The right side (*b*) of Fig. 1 shows the recording surface of the CD before placing it in the vicinity of the reactor. It can be seen that the recording surface is smooth and has no noticeable craters, tracks, or stuck particles.

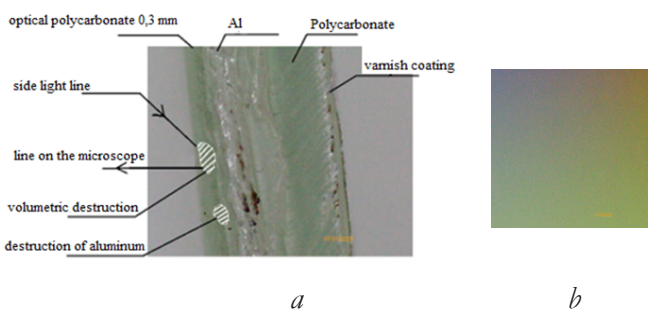

a *b*

Fig. 1. *(a) - a photo of the CD cut under a microscope, (b) a recording surface of a fresh CD under a microscope with an x40 magnification.*

3. THE UNIFIED NATURE OF UNKNOWN PARTICLES ARISING FROM THE OPERATION OF VARIOUS REACTORS

We believe that the nature of the "unknown particles" that are detected near: *a*) nickel-hydrogen heat generators, *b*) during the electric explosion of a metal foil, *c*) during a discharge in a heterogeneous water-air environment, are of a similar nature and are traces formed by the reaction of "dark hydrogen" or "dark hydrogen" compounds with the usual substance of the CD surface material. The basis for this statement is the registration of *X*-ray radiation of 28 keV and 260 keV, characteristic of "dark hydrogen", during the discharge in the water-air medium, and the coincidence of the nature of the traces on the CD in the vicinity of the nickel-hydrogen reactor and near the discharge in the water-air medium.

The two photographs in **Fig. 2** compare the traces in such experiments. Photo in Fig. 2*a* the surface of the CD located next to the nickel-hydrogen reactor from the article [5]. Photo Fig. 2*b* the surface of a CD located near a high-voltage electric discharge in a water-air environment (this work). It can be seen that the characteristic features of the traces in the two experiments coincide. There are usually different types of tracks on a CD. We specifically chose a zone with tracks similar to

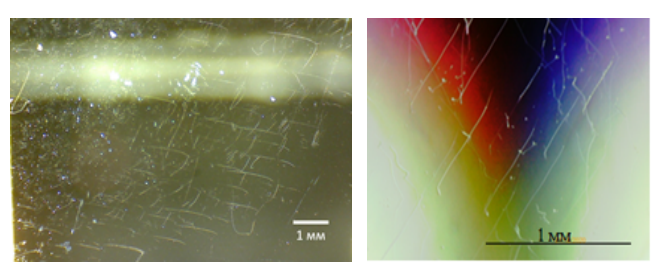

a *b*

Fig. 2. *Traces of unknown particles on the surface of the CD: (a) - nickel-hydrogen reactor* [5]*, (b) - this work, discharge in a heterogeneous water-air environment.*

the tracks registered in [5]. These are relatively short club-shaped tracks. It can be seen that not only the shape of the tracks, but also their length in photo (*a*) and (*b*), taking into account the scale, are close to each other. It can also be seen that both in photo (*a*) and photo (*b*) there are point traces scattered around the observation area.

The coincidence of the shape of the traces suggests a similar mechanism of their formation, despite the completely different types of reactors that generated unknown particles.

4. UNKNOWN PARTICLES ARE THE PRODUCT OF THE INTERACTION OF "DARK HYDROGEN" $\hat{H}_2$ WITH ATOMIC MATTER

The question arises as to how the tracks appear on the CD. Some researchers believe that the traces are the conversion of the kinetic energy of an" unknown " particle into heat, which leads to the evaporation of the polycarbonate covering the disk. But if we take into account the fact that there are three types of traces-tracks, craters and "adhered" particles, and the craters have a complex shape and are completely different from the craters from the impact, then it seems more natural to assume that the traces are the result of the transformation of the energy of the electromagnetic interaction of an unknown particle and the polycarbonate molecules of the disk. Moreover, this interaction involves not only electrostatic potential forces, but also the forces of magnetic interaction.

To answer this question, we consider it appropriate to use the ideas about" dark hydrogen " developed in [1-3]. There are a lot of questions about the interaction of "dark hydrogen" $\hat{H}_2$ with atomic matter. We are just beginning to explore this topic. In fact, we are talking about creating an independent science, which can be called "High-energy Chemistry". But we can already say something about the reaction (1)

$$\hat{H}_2 + A \rightarrow (\hat{H}_2{}^*A) + q, \quad (1)$$

where one of the atoms that make up substance A (most likely oxygen) interacts with a particle of "dark hydrogen" $\hat{H}_2$, $(\hat{H}_2{}^*A)$ is the quasimolecule formed, q is the heat released. The value of q can reach several MeV, which will lead to melting and evaporation of the substance in the vicinity of the quasimolecule $(\hat{H}_2{}^*A)$. This quasimolecule has a magnetic moment and causes polyatomic structures to form from neighboring carbonate atoms. This polyatomic structure is perceived as a "adhered" particle located in the crater.

5. REGISTRATION OF "ADHERED" UNKNOWN PARTICLES. MAGNETIC PROPERTIES OF UNKNOWN PARTICLES

As an example of particles stuck to the surface, you can give the photo in **Fig. 3**. Photos (*a*) and (*b*) show a trace of a beautiful shape in the form of a "pearl pendant". In photo (*a*), the scale is such that the width shows 2 mm of the observation area. The size of the large footprint in the center of photo (*a*) is approximately 17 microns. In the enlarged photo (*b*) Fig. 3 you can see that a bluish particle is embedded in the large trace. It is possible that this is an adherent particle formed as a result of the adhesion of the polycarbonate substance due to the magnetic properties of the atom $(\hat{H}_2{}^*A)$.

Reconstruction of the crater on the Amphora microscope in [7] **Fig. 4***b*, confirms that "adhered" spherical particles are formed in the crater.

Very often, craters form circular structures that are clearly similar to the behavior of

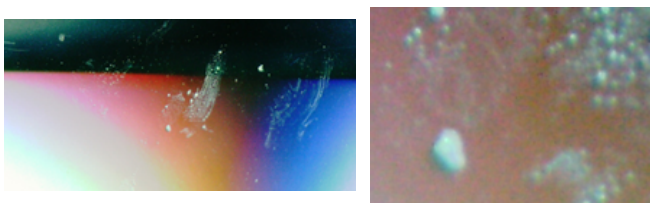

a *b*

Fig. 3. *Example of particles adhering to the CD surface.*

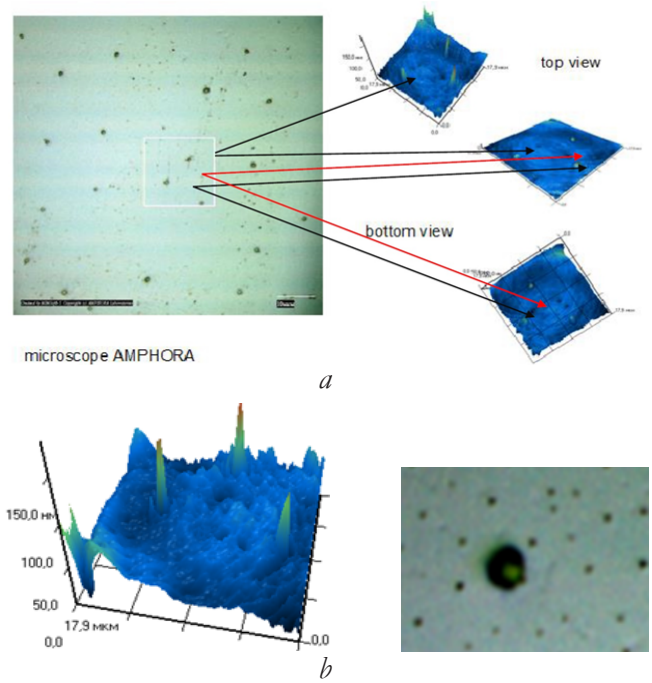

Fig. 4. *An example of "unknown particles" (balls) and pits (shown by red arrows) on a golden surface (a) from* [7]*, their three-dimensional reconstruction only for the area in the white square (b), an example of a large ball against a background of small ones (c). These measurements were carried out on an AMPHORA microscope.*

particles with magnetic properties. The presence of magnetic properties in the traces of particles of unknown radiation is easily explained if we assume that the particle is constructed with the participation of "dark hydrogen", which has a noticeable magnetic moment. In the left part of **Fig. 5**, two circular tracks are clearly visible, which are made up of spherical tracks.

Fig. 5 shows a more complex trace on the CD, around which small craters are visible, forming a circular structure, which also confirms the considerations about the magnetic property of the particles forming the craters.

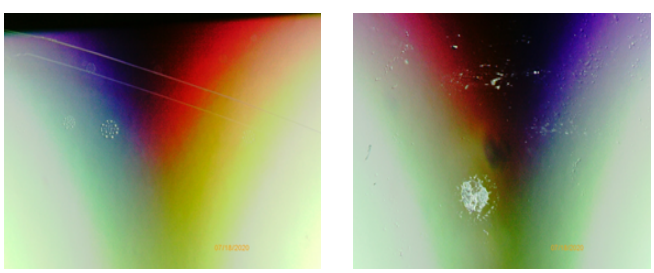

Fig. 5. *The magnetic properties of unknown particles are manifested in the formation of circular traces.*

6. TRANSFER OF "DARK HYDROGEN" BY ATOMIC MATTER

One of the sections of research on the interaction of "dark hydrogen" and atomic matter is the question of whether or not "dark hydrogen" $\hat{H}_2$ is transferred by atomic matter. In experiments on the transfer of "dark hydrogen", we used the previously approved [2-3] method of generating" dark hydrogen " in a high-voltage electric discharge in a finely dispersed water-air mixture.

Fig. 6 shows a humidifier that creates a flow of fine-dispersed water-air medium using high-frequency vibrations of a ceramic piezoelectric. From the humidifier, the flow is directed through a dielectric hose with a diameter of 12 mm and a length of 1.5 m at a speed of approximately 1m/s to the Discharge chamber I. In the I-size discharge chamber 12×12×13 cm, made of 10 mm Plexiglass, two electrodes are inserted. The pointed electrodes are made of copper, tungsten and nickel-plated steel. The distance between the electrodes is 2-3 cm. A high voltage with an amplitude of 15-20 kV is applied to the electrodes from the source. The electrodes are arranged in such a way that the electric current generated in the flow of the air-water medium of the electric discharge flows along the flow. The pressure in the discharge chamber is slightly higher than atmospheric pressure, so the water-air mixture that has passed through the discharge flows through a dielectric tube from the Discharge Chamber I to the tightly closed plastic Chamber II and Chamber III located downstream. The distance between the Discharge chamber I, Chamber II and Chamber III is about 7 cm. The

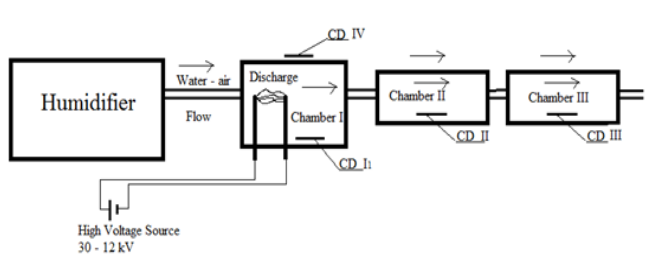

Fig. 6. *The layout of the stand for the study of the transport of "dark hydrogen".*

length of Camera II and Camera III is 14 cm. After Chamber III, the water-air mixture enters the exhaust system.

All chambers contain CD disks: in the Discharge chamber I – CDI, in the Chamber II-CDII, in the Chamber III-CDIII. In addition, a CDIV disk is located above the Bit Chamber I. CD disks are used by many researchers to record traces of unknown particles emitted from cold fusion reactors. In this work, the CD was always placed either in a plastic or paper envelope to get rid of dust sticking to the surface of the CD.

Comparison of traces on CD **Fig. 7** (in the Discharge chamber I) and **Fig. 8** (Chamber III) shows that they are very similar. This confirms the thesis that "dark hydrogen", as a source of traces of unknown radiation, is transported along the path together with the movement of the water-air medium. Interestingly, there are fewer traces registered on the disk located in Chamber II than in Chamber III, located further along the path from the Discharge Chamber I.

a *b*

Fig. 7. *Traces on two sections of CD (a) and (b) from "unknown" radiation in the Discharge chamber I.*

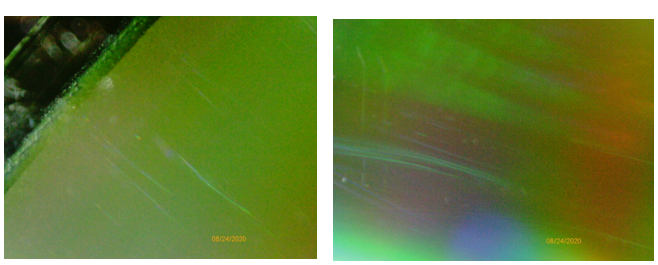

a *b*

Fig. 8. *Traces on two CD sections (a) and (b) from "unknown" radiation in Chamber III.*

7. PROCESSES IN WHICH "DARK HYDROGEN" IS GENERATED

In this work, and the works of other authors, it is shown that the source of unknown particles (according to our ideas, this is "dark hydrogen") can be metals saturated with hydrogen and an electric discharge in a medium containing hydrogen. Thanks to our experiments, the range of sources of "dark hydrogen" can be significantly expanded.

7.1. Generation of "dark hydrogen" by burning propane in a gas burner

Fig. 9 shows a layout of the experiment with a gas burner and a CD disc located behind a non-flammable screen. After 3 hours of exposure, a lot of traces appeared on a clean disk in a plastic package (**Fig. 10**).

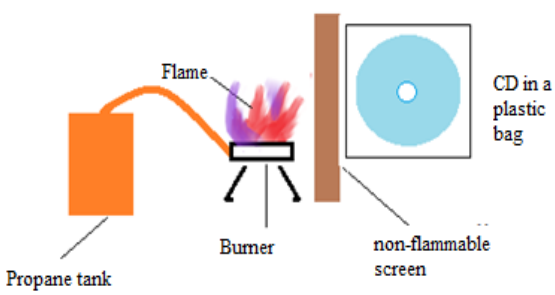

Fig. 9. *The scheme of the experiment with a gas burner.*

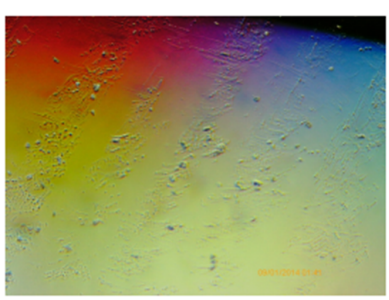

Fig. 10. *Traces on the CD after 3 hours of exposure near the gas burner.*

7.2. "Dark hydrogen" in the exhaust gases of the car

Fig. 11 shows a layout of the experiment with the exhaust pipe of a car engine working and a CD. After 20 minutes of exposure, a lot of traces appeared in the exhaust gas stream of the working car on a clean disk placed in a plastic bag, **Fig. 12**.

Fig. 11. *The layout of the experiment with the exhaust gases of a gasoline-powered engine.*

Fig. 12. *Traces on the disc after a 20-minute exposure near the exhaust pipe.*

7.3. Generation of "dark hydrogen" when charging the smartphone

Fig. 13 shows a layout of the experience of registering traces on a CD located next to smartphones during charging. After 2 hours of exposure, many traces appeared on a clean disk located in a plastic bag, **Fig. 14**.

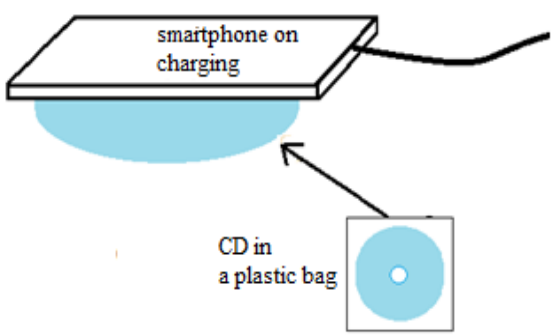

Fig. 13. *Layout of the experience with a smartphone while charging.*

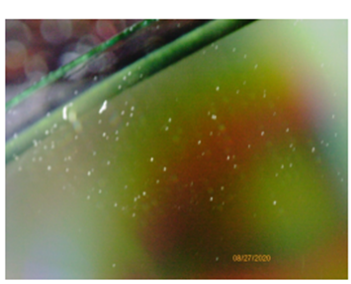

Fig. 14. *Traces on the disk after a 2-hour exposure near the smartphone.*

8. NEW METHODS FOR DETECTING "DARK HYDROGEN"

8.1. Electroscope

The question of the exit of penetrating charged particles from the discharge zone arose in connection with two circumstances. The first is the observation of traces of an unknown nature outside the discharge zone behind dielectric barriers. And the second is that a particle ("dark hydrogen" [1-3]) with two relativistic electrons, despite its quasi-neutrality, creates an electric field in the surrounding space, which is perceived by the surrounding charges as the presence of a charge in $\hat{H}_2$. This charge, or more precisely the sum of these charges, we measured using an electroscope.

It was assumed, given some experience of numerous failures of electronics, that the "dark hydrogen" particles relatively easily seep through the dielectric medium and get stuck in metals. In this case, the metal object is charged. A copper foil box was used as a charge storage device. It was separated from the discharge zone by a dielectric stand made of thick cardboard. The box was connected by a copper wire 1700 mm long with an electroscope (**Fig. 15**). The electrical capacitance of the box-wire-electroscope system was measured. It turned out to be equal to ~$3 \cdot 10^{-9}$ F. Test tests of the electroscope showed that the supply of a voltage of 1.8 kV to the copper box leads to a displacement of its dielectric lobes by 1.5 mm. This displacement of the lobes is

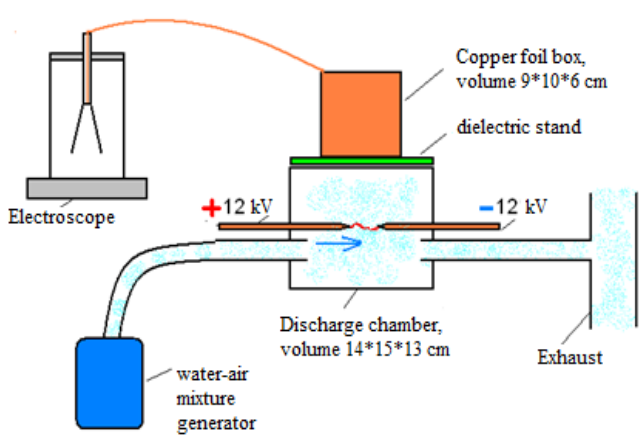

Fig. 15. *Layout of an experiment on charging a copper foil box with "dark hydrogen".*

caused by the charge $q = C \cdot U = 3 \cdot 10^{-9} \cdot 1.8 \cdot 10^{3} = 5.4 \cdot 10^{-6}$ *C*. A similar divergence of the lobes in the experiment occurs in 10 seconds of operation of the discharge chamber with the supply of a water-air mixture. This means that in 10 seconds, *N* particles of "dark hydrogen" $\hat{H}_2$ were stuck in the box, each with an electric field equivalent to ~10 units of electron charge:

$N = 5.4 \cdot 10^{-6}$ Кл/$(100 \cdot 1.6 \cdot 10^{-19}$Кл$) = 3 \cdot 10^{10}$ particles per 10 sec.

The difference in the effect of the control voltage of 1.8 kV and the charge from "dark hydrogen" on the electroscope was manifested in the discharge rate of the electroscope. The discharge rate for "dark hydrogen" is an order of magnitude slower, which is quite understandable, given the large mass of the particles of" dark hydrogen", with the substance associated with it. This observation is still a very convincing confirmation of the validity of our theoretical model. It should be noted that when the discharge is operated without the supply of a water-air mixture, the charge accumulation on the electroscope does not occur.

8.2. Measurement of pressure in a closed volume (plastic bottle)

The charge-neutral "dark hydrogen" creates a strong electric field around itself and is able to collect dipole molecules from the air, primarily oxygen molecules. A decrease in the number of particles in a closed volume at a fixed temperature leads to a drop in pressure. Thus, the penetration of" dark hydrogen "through the walls into a closed vessel and the subsequent reaction of "dark hydrogen" with air molecules should lead to a drop in pressure.

Fig. 16 shows a layout of an experiment with measuring the pressure in a closed volume in the vicinity of a source of "dark hydrogen".

The pressure in the area near the discharge is stable when the steam-air mixture supply is switched off, **Fig. 17**. When the air-water mixture is supplied, the pressure in the vessel

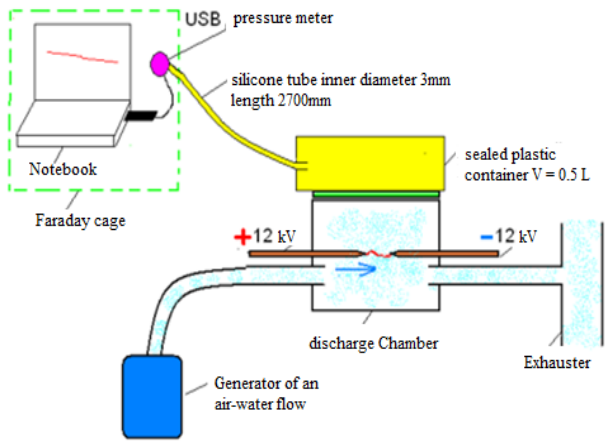

Fig. 16. *Layout of an experiment to measure the air pressure drop in a vessel irradiated with "dark hydrogen". From the discharge to the plastic container 5 cm.*

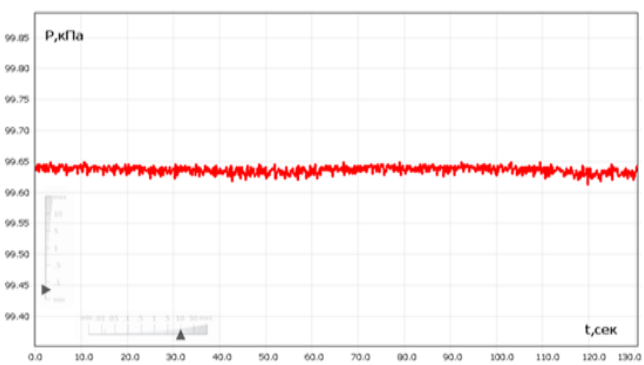

Fig. 17. *Pressure in the vessel during discharge without a water-air medium.*

begins to drop. The pressure dropped by 0.02 kPa (0.02%) in 10 seconds (**Fig. 18**). In total, there are $13.4 \cdot 10^{21}$ air molecules in the vessel, and in 10 seconds "dark hydrogen" bound 0.02% ($27 \cdot 10^{17}$) air molecules. If we assume that 10^{10} particles of "dark hydrogen" got into the vessel (the vessel is similar in size to the foil box from the

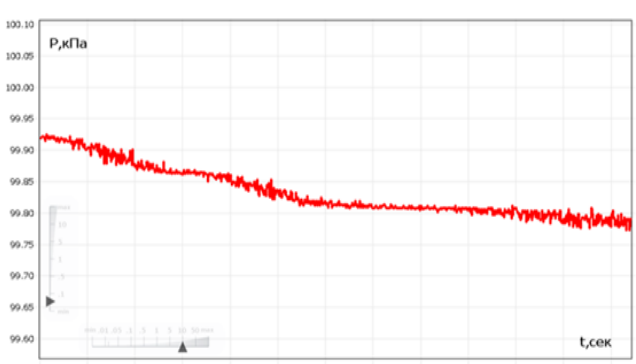

Fig. 18. *Pressure in a closed vessel located near the discharge zone when a water-air medium is supplied to the discharge zone.*

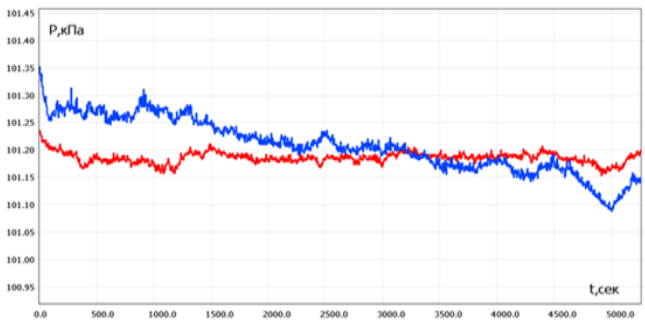

Fig. 19. *Pressure drop in closed vessels (volume = 0.5 liters) irradiated with "dark hydrogen": blue curve-5 cm from the discharge, red curve-30 cm from the discharge zone.*

previous experiment), then we can conclude that one particle of "dark hydrogen" bound about 10^8 air molecules.

The pressure drop in two vessels located at different distances from the discharge was measured, **Fig. 19**. It can be seen that at large distances (30 cm), the pressure drop in the vessel is practically not observed. This is consistent with the data of [5], where it was found that "unknown particles" are 1-2 orders of magnitude less detected by CD disks at distances greater than 20 cm from the reactor.

8.3. Torsion balance with nickel plate and magnets

A torsion scale with a nickel plate and magnets, **Fig. 20**, begins to rotate counterclockwise near a cold fusion reactor containing hydrogenated nickel (see Fig. 1). This is explained by the flow of "dark hydrogen" that escapes from the reactor, gains mass in the paraffin block (6 cm thick) and spins the torsion balance.

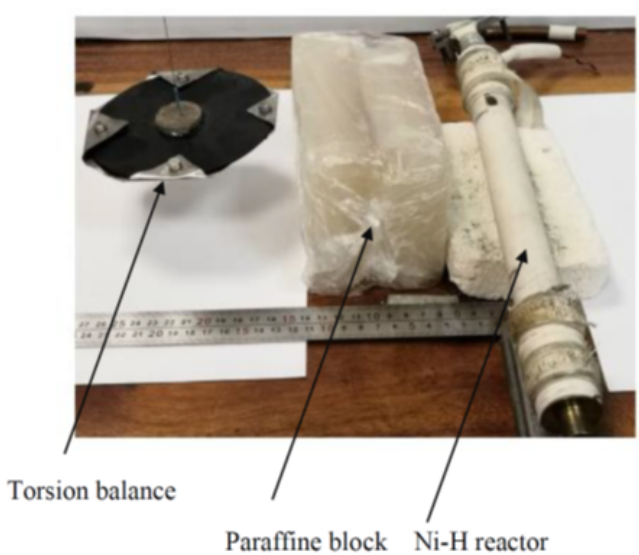

Fig. 20. *Experience on the impact of the Ni-H reactor on the torsion balance.*

9. CONCLUSION

1. It is shown that the substance that forms tracks and craters on CD disks is transported along the path with a water-air mixture.
2. It is shown that the substance that forms tracks and craters on CD disks is formed while a) burning hydrocarbon, b) into an internal combustion engine, c) charging a smartphone.
3. New objective methods for the diagnosis of "dark hydrogen" have been developed, taking into account its physical properties. The application of these methods shows that at least 10^{11} particles per second formed by "dark hydrogen" fly out of the discharge zone in the presence of a water-air mixture. Each particle can bind up to 10^8 oxygen molecules.

REFERENCES

1. Baranov DS, Zatelepin VN. Avtokolebatel'nyy nagrev nikel'-vodorodnogo reaktora [Self-oscillating heating of a nickel-hydrogen reactor]. *Materialy 25 Rossiyskoy konferentsii po Kholodnoy Transmutatsii Yader khimicheskikh elementov i Sharovoy Molnii*, Rossiya, Adler, Sochi, 1-8 October 2018, pp. 239-256. Moscow, NIC FTP "Erzion" Publ., 2018.
2. Baranov DS, Zatelepin VN. The Synthesis of Dark Hydrogen (neutron-like particles) in a Hydrogen reactor. *International conference "Scientific research of the SCO countries: Synergy and integration"*, Beijing, China, August 15, 2019, p.166-174.
3. Baranov DS, Zatelepin VN. Mekhanizm formirovaniya i fiziki-khimicheskiye svoystva «temnogo vodoroda». Teoriya i eksperiment [Mechanism of formation and physics-chemical properties of "dark hydrogen". Theory and experiment]. *Materialy 26 Rossiyskoy konferentsii po Kholodnoy Transmutatsii*

Yader khimicheskikh elementov i Sharovoy Molnii, Sept. 28-Oct. 2, Moscow, 2020. Moscow, NIC FTP "Erzion" Publ., 2020 (in Russ.).

4. Urutskoyev LI, Liksonov VI, Tsinoyev VG. Eksperimental'noye obnaruzheniye «strannogo» izlucheniya i transformatsiya khimicheskikh elementov [Experimental detection of "strange" radiation and transformation of chemical elements]. *Prikladnaya fizika*, 2000, 4:83-100 (in Russ).
5. Zhigalov VA, Zabavin SN, Parkhomov AG, Sobolev AG, Timerbulatov TR. Statistika trekov strannogo izlucheniya ot dvukh tipov reaktorov LENR [Statistics of strange radiation tracks from two types of LENR reactors]. *Materialy 25 Rossiyskoy konferentsii po Kholodnoy Transmutatsii Yader khimicheskikh elementov i Sharovoy Molnii,* pp. 51-62. Adler, Sochi, 1-8 Oct. 2018, Russia. Moscow, NIC FTP "Erzion" Publ., 2018 (in Russ).
6. Baranov DS, Baranova OD. Evidence the Formation and Decay of Giant long-lived Nuclear Molecules. *Proceedings of Intern. Symposium on Exotic Nuclei* (*EXON2012*), Vladivostok, October 2012, pp. 209-212. http://exon2012.jinr.ru.
7. Baranov DS, Baranova OD. Observation of the Structure of Charged Macroscopic Particles on the Metal Surface (analog dusty plasma). *10-th International Workshop on Magneto-Plasma Aerodynamics,* Moscow, April, 2011, pp. 349-353.

DOI: 10.17725/rensit.2021.13.329

Strange radiation and LENR: what's the relation?

Vladislav A. Zhigalov

Moscow Institute of Electronic Technology, http://miet.ru/

Zelenograd, Moscow 124498, Russian Federation

E-mail: zhigalov@gmail.com

Received July 31, 2021, peer-reviewed August 16, 2021, accepted August 30, 2021

Abstract: **A review of studies showing the phenomenon of "strange radiation" is given. The issues of relation of this phenomenon with low energy nuclear reactions (LENR) are discussed. The results of our own experiments, revealing such a relation, are presented on the example of two LENR reactors. Based on the developed technique for assessing the intensity of tracks on sensitive materials, it is shown that tracks of strange radiation with high intensity appear only in the near zone of reactors (up to 20 cm). The aftereffect is described, when the tracks appear after the reactor is turned off. The large variability of the intensity of the tracks makes it difficult to use them as a marker of LENR. The paradoxical properties of strange radiation are discussed.**

Keywords: **strange radiation, low-energy nuclear reactions, LENR**

UDK 53.043

Acknowledgments: The author thanks A.G. Parkhomov and the team of the KIT laboratory for supporting the research.

For citation: Vladislav A. Zhigalov. Strange radiation and LENR: what's the relation? *RENSIT,* 2021, 13(3):329-348. DOI: 10.17725/rensit.2021.13.329.

Contents

1. INTRODUCTION

Low-energy nuclear reactions (LENR) as the research topic have a long pre-history, 30-year "new" history (since 1989) and a promising future. Despite the rich experimental material and many theories claiming to explain this phenomenon, so far it is just a phenomenon, without a generally accepted theory that would satisfy the scientific community.

Another less known phenomenon is also without a satisfactory explanation, called "strange radiation", and which has been studied for 20 years. Twenty years for research on a certain phenomenon is a long time. For 20 years, nuclear physics was formed and the structure of the atom became clear at the beginning of the 20th century. During the same first 20 years of the last century, two scientific revolutions took place that turned our ideas about the world upside down. Why didn't this happen with LENR and strange radiation? The fact that for many years there has been no progress in finding the mechanisms of low-energy nuclear reactions could be explained by the inapplicability of traditional approaches of nuclear physics to work with this phenomenon. However, the history of physics and steady progress in experimental technology say that if a phenomenon exists and physicists are willing to investigate it, progress will sooner or later follow. Another thing is that this progress may require a new scientific revolution. Is physics ready for it? However, the social reasons for the inhibition of some areas of research are not the subject of this article.

If there is a suspicion that the price of progress is a rethinking of the scientific picture of the world, then it makes sense to pay attention to the strangest features of the studied phenomena, if, of course, they are reliably fixed. Many researchers, working in the field of LENR, are familiar with strange radiation tracks. This is definitely a rather strange phenomenon. But is there a relation between this phenomenon and LENR? What is this relation? Can we use strange radiation as reliable marker of low energy nuclear reactions like well-known nuclear radiation is an unmistakable marker of conventional nuclear reactions?

This article attempts to answer these questions. The first part of the article is a review of key publications that investigate the phenomenon of strange radiation. The second part presents the results of experiments carried out in the KIT laboratory in 2017-2019 to answer the question whether the operation of LENR reactors is associated with the appearance of tracks of strange radiation.

2. OVERVIEW

The first work in which the term "strange radiation" was introduced into scientific use was an article by L.I. Urutskoyev and colleagues [1]. In it, "strange" tracks on photographic emulsions were a concomitant factor for anomalous processes occurring during the electric explosion of titanium foil in water. The consequences of such processes were excess energy release, the appearance of new elements after an electric explosion, and a distortion of the natural isotopic composition of Ti (**Fig. 1**).

The accompanying radiation was indeed strange. It did not resemble any known type of radioactivity, it was biologically active (see below), and it generated tracks of a certain shape on the photoemulsion (**Fig. 2**).

These tracks are reminiscent of a tractor track - they have often periodic shape. In Urutskoyev's experiments, the tracks went in a plane perpendicular to the direction to the foil explosion site (in this case, apparently, they "slid" strictly in the plane of the emulsion).

Another interesting property of this radiation was its ability to accumulate in matter. During one of the experiments after the explosion of the foil,

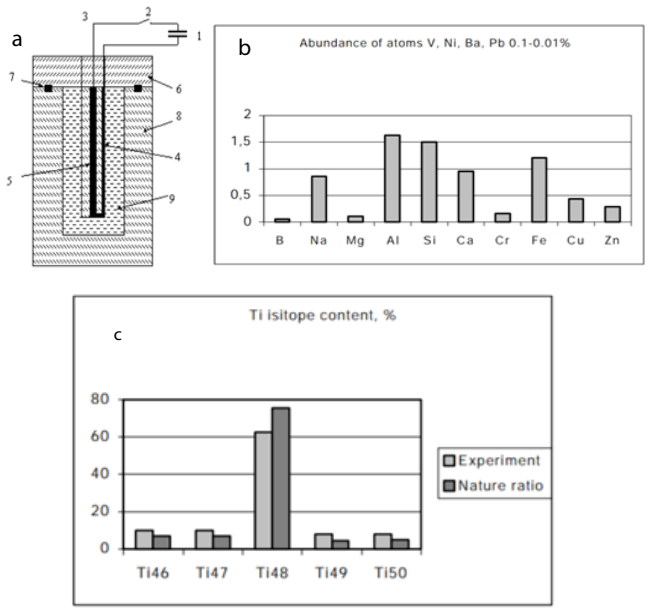

Fig. 1. *(a) Urutskoyev's explosive cell, (b) the appearance of new elements, (c) distortion of the isotopic composition* [1].

water and the remains of the foil were poured into a Petri dish and a photographic film was placed at a distance of 10 cm. After an 18-hour exposure on the film, the same tracks were observed as from the electric explosion itself (**Fig. 3**).

The magnetic field affected the tracks - a form of tracks in a magnetic field is obtained comet-shaped. This made Urutskoyev assume that these tracks belong to electrically neutral particles with a magnetic charge (magnetic monopoles). Light monopoles were predicted by the French theorist George Lochak back in the 1980s as a development of Dirac's ideas about the magnetic monopole. According to Lochak's theory, a magnetic monopole is a massless magnetically excited neutrino. To test this hypothesis, traps made of a ^{57}Fe isotope foil

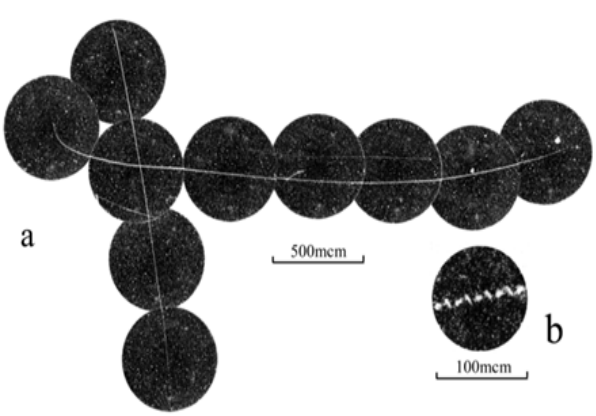

Fig. 2. *Tracks on photographic film from an electric explosion in the experiments of Urutskoyev* [1].

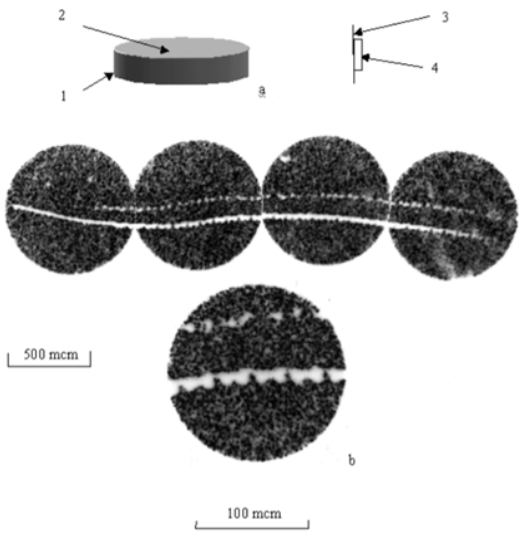

Fig. 3. *Experiment with "aftereffect": (a) - placement of photographic material; (b) - tracks on the photographic emulsion* [1].

placed at the S and N poles of a magnet were used [2]. The experiment showed that when the foils were exposed to "strange radiation", the foil at the S-pole showed a Mössbauer deviation in the spectrum in one direction, and at the N-pole in the other:

"*The results of the measurements showed that in the foils placed at the N-pole, the absolute value of the hyperfine magnetic field increased by 0.24 kG. On the other foil (S), it decreased by about the same value 0.29 kG. Measurement error 0.012 kG.*"

The authors explain this by the bound state of the Lochak's monopoles with the iron nucleus.

Urutskoev conducted many other experiments to study this phenomenon, in particular, when testing high-voltage industrial electrical equipment in an abnormal short circuit mode [3]. It was shown that, in this case, the tracks of monopoles are also recorded (**Fig. 4**). Moreover, as in the case of electric explosion of foils in water, the isotopic composition of titanium in varistors was distorted. The conditions for the experiment were as follows: "*A short circuit on the buses in a complete switchgear (KRU) is carried out by installing jumpers from a wire of any metal with a diameter of no more than 0.5 mm on the current-carrying buses, the main task of the wire being installed is to initiate an arc, which is then maintained by the power of the source for a given period of time. The value of the supplied short-circuit current has a range from 1 to 40 kA, the voltage of the no-load circuit is 8-10 kV. A characteristic feature of the traces is that they are mainly located in the surface layer of the photoemulsion of the detectors. Traces differ markedly from each other in size. Transverse dimensions 5-30 microns, length from 100 microns to several millimeters. As a result of experiments, it was found that the further from the test site is the detector, the narrower the track width. So, traces with transverse dimensions 30 microns are observed on detectors located at a distance L: 0.5 m < L <1 m, and tracks with dimensions of 5-10 microns - at a distance L > 2 m from the test site. If the tests were carried out at currents I ~ 1-2 kA, then no traces were found on the detectors. On the contrary, if the tests were carried out at a current of I ~ 40 kA, then many different traces were recorded. When testing vacuum interrupters, not a single trace of "radiation" was recorded, although 15 experiments were carried out, in which more than 20 photodetectors were installed. This confirms the results of laboratory studies, in which the tracks were observed only in an electric discharge in a medium*".

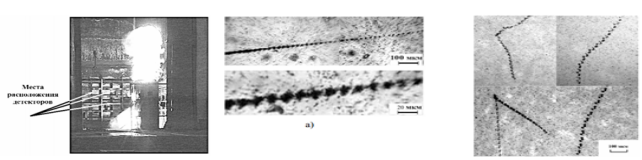

Fig. 4. *Tests of electrical equipment (current ~ 40 kA) and tracks on photodetectors* [3].

N.G. Ivoilov (Kazan University) in [2] together with L.I. Urutskoev studied the Mössbauer spectra of an iron foil exposed to "strange radiation".

Further Ivoilov's experiments were devoted to the study of the properties of particles that form "strange" tracks, and their interaction with matter [4]. Double-sided photographic films were used as detectors, and the author made "sandwiches" from photographic film and various materials, and also used an external magnetic field. The work can be roughly divided into two parts. In the first, experiments are carried out with radiation from a spark discharge in a liquid with graphite electrodes (**Fig. 5**). The

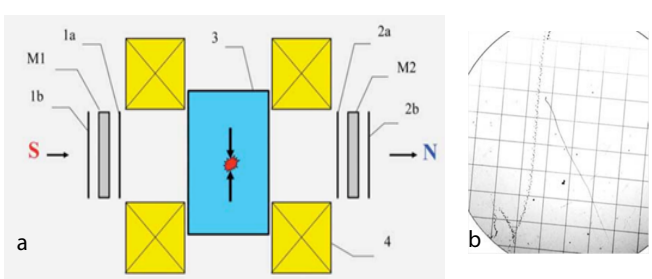

Fig. 5. *(a) - Scheme of the Ivoilov setup: 1 and 2 –X-ray photoplates, M1 and M2 –the material ivestigated. 3 –the thin wall plastic vessel, 4 – Helmholtz induction coils. S →N – direction of magnetic field; (b) - example of tracks, step is 1 mm* [4].

current did not exceed 40 A , the voltage was about 80 V. As a result, in addition to confirming the results of Urutskoyev, very interesting new results were obtained. Ivoilov was able to detect paired tracks of monopoles with mirror symmetry when the recording film was placed close to the reflecting material. Mirror tracks were obtained from different sides of the film - one from the side of the radiation source, the other from the side of the reflecting material (**Fig. 6**). Ivoilov assumes that mirror pairs are S and N monopoles.

As for the interaction with matter, it turned out that magnetic particles are completely absorbed by ferromagnets (Fe and Ni films were used), aluminum shows itself as a weakly reflecting and weakly absorbing substance, and glass and single-crystal germanium and silicon turned out to be well reflecting materials.

In passing to the second part, the author uses a beta-radioactive source in a strong magnetic field to test the new hypothesis, i.e. abandons the original method of obtaining monopoles in a spark discharge. What is this hypothesis? Ivoilov suggests that, since the Lochak monopole is a magnetically excited neutrino, then it should arise from the cosmic neutrino component, as well as from the neutrino component of beta decay of local sources in the presence of a magnetic field. The experimental results support this hypothesis. Here is what the author writes: "*When working with photographic films, as a rule, together with the irradiated films, control films were processed that passed all stages of preparation, except for irradiation. As the control films in this experiment, we used photographic films that were kept during the supposed time of the experiment (10 min) in a constant magnetic field with strength of 20 kOe. After developing in control films are detected the same characteristic tracks which occur during the combustion of the electric arc in the fluid. These tracks we called the background. In the case of the films location near the source in the absence of a magnetic field background is not detected. When a neutrino source (^{90}Sr) was introduced into the magnetic field, the number of tracks recorded during the same time almost doubled in comparison with the background, and some of the tracks had a clearly radial direction from the center where the radioactive source was located. A similar result was obtained with the ^{137}Cs source.*"

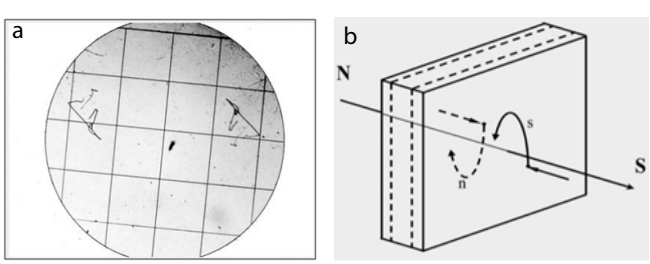

Fig. 6. (*a) - Paired tracks in Ivoilov's experiments, (b) - behaviour of particles flying in opposite directions along radial fluctuating magnetic field* [4].

The author writes in his conclusions: "*1) During an electric explosion and an electric discharge in a liquid, the flowing current, compacted by the liquid, is a source of large magnetic fields, in which magnetically excited neutrinos (magnetic monopoles) are born during the beta decay of cosmic particles. 2) The component of cosmic radiation, which has not yet been clarified, is a necessary factor in the production of magnetic monopoles in the beta decay of unstable nuclei in a magnetic field. 3) S- and N-magnetic monopoles are born in pairs.*"

As we can see, in the works of Urutskoyev and Ivoilov, the relation between the tracks of strange radiation and nuclear transformations is considered from different positions.

The LENR topic has been actively studied by the Proton-21 laboratory in Kiev. There, under the leadership of S.V. Adamenko obtained experimental evidence of the nuclear transformation of a metal under the influence of coherent electron beams [5,6]. Since 2000, thousands of experiments ("shots") have been carried out on cylindrical targets of small (about a millimeter) diameter. The inner part of the target explodes, and the explosion products contain almost the entire stable part of the periodic table in macroscopic quantities, as well as superheavy stable elements.

What is the Adamenko installation? Experimenters call it a high-current vacuum diode. The target itself is the anode - as a rule, it is a copper wire with a diameter of about half a millimeter with a rounded end. The electron beam from the cathode strikes its surface coaxially, as a result of which the central part of the anode explodes (**Fig. 7**). Explosion products are deposited on storage screens (disks about 10 mm in diameter with a hole in the center), made, as a rule, of the same material as the target. The widest range of methods available in a modern laboratory is used to study explosion products.

If we briefly describe the processes occurring with the substance in the target, then, according to the researchers from Proton-21, there is a process of

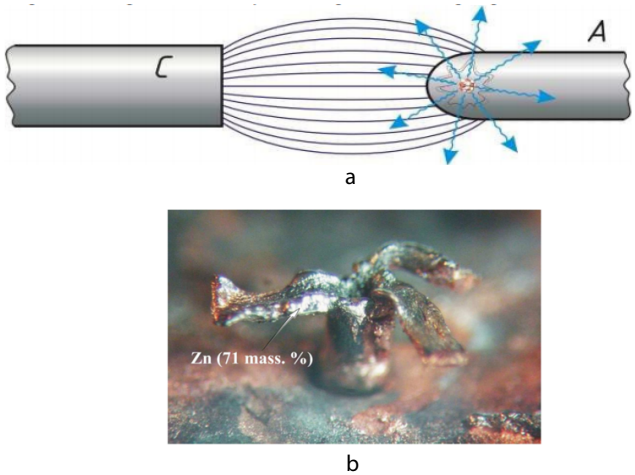

Fig. 7. *(a) - Schematic of self- focusing of an electron beam on the surface of the concentrator anode, which excites a soliton-like density pulse in its near-surface layer converging to the axis of symmetry (illustration from* [5]*). (b) - copper target after the experiment with traces of solidified silver-white "lava" on its petals, pouring out from the center of the exploded target (illustration from* [5]).

collapse of the substance, triggered by the impact of an electron beam on the surface of the metal anode, and leading to the formation of a "nucleon plasma", followed by the creation from it of the widest range of elements, as well as superheavy elements, with atomic masses of thousands of AU. This process is similar to supernova explosions, and the spectrum of X-ray radiation is very strongly correlated with the spectra of cosmic *X*-ray and gamma-ray bursts. The known elements resulting from the explosion are stable, i.e. the reaction products are non-radioactive. In addition, experiments with explosion radioactive targets (^{60}Co) show a substantial decrease of their radioactivity. About 30% of the original target material undergoes nuclear transformation. The amount of released energy is orders of magnitude greater than the amount of energy supplied.

The same team, while studying the properties of hot spot radiation at the facility of the Proton-21 laboratory, investigated some related phenomena. One of them is the tracks of magnetically charged particles in a multilayer MOS structure (metal-oxide-semiconductor). In the structure, which usually serves as the basis for the production of microcircuits, "layered cake" Al-SiO_2-Si, tracks were found that appear when such a structure is exposed under the influence of explosion [7] . Such particles behave like a needle in a sewing machine shuttle - they periodically pierce through a layer of aluminum

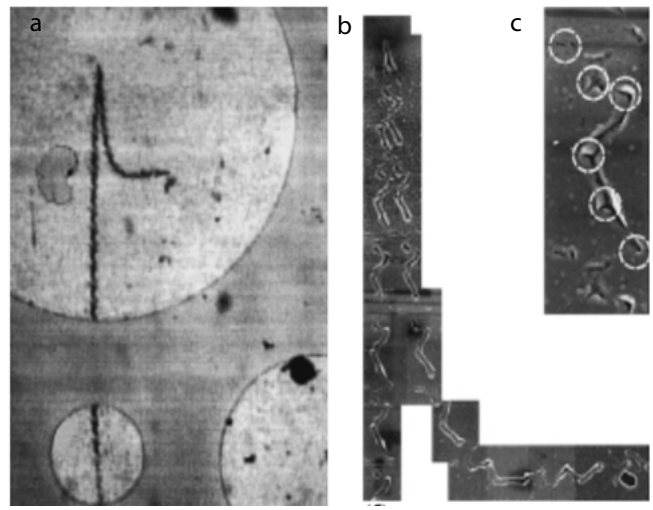

Fig. 8. *(a) - general view of the MIR-structure with a track; (b) - a fragment of the track panorama containing all types of repeating elements; (c) - highlighted zones demonstrate silicon emissions onto the aluminum surface (illustration from* [7]).

with a small constant pitch (60 μm), leaving a fused, winding hollow tunnel about one micron wide in its path (**Fig. 8**).

In the work "Experimental detection and modeling of the orientational motion of hypothetical magnetically charged particles on a multilayer surface" [7], the authors V.I. Vysotsky and S.V. Adamenko give an estimate of the energy release during the passage of such particles through a metal - it turns out to be about 10^6 GeV/cm. These tracks run perpendicular to the direction from the hot spot, parallel to the surface of the MOS structure. The authors calculated that the most plausible hypothesis explaining this behavior of the particle is the hypothesis of a magnetically charged particle, which moves through the paramagnetic layer in an external magnetic field (which is directed approximately parallel to the surface).

Further, the authors point out that simple deceleration of particles is not capable of generating such a volume of energy at a practically nondecreasing particle velocity in the track, and they assume that such particles are capable of magnetic catalysis of energetically beneficial nuclear reactions. Monopoles should stimulate nuclear reactions due to the fact that when they move, they greatly distort the electronic shells of atoms that they come across along the way, and thereby increase the likelihood of nuclear tunneling and their fusion. Getting into aluminum (paramagnet) as in a potential well, a magnetically charged particle stimulates nuclear

reactions with the release of energy. By melting the aluminum layer , the particle changes its magnetic properties (it becomes a diamagnet) and, as a result, tends to "jump" out of this layer. Coming out of the aluminum, and passing a certain distance along the surface, the particle is again attracted by the potential well of the paramagnet, and the whole process is repeated.

The authors suggest that the external magnetic field is essential for this behavior of the particle. An estimate of the velocity of the observed monopoles, which was calculated on the basis of their trajectory and experimental conditions, shows that this velocity should be more than 200 km/s - just so fast the particle should fly so that the magnetic field does not have time to change significantly during its flight. This is important for the hypothesis explaining the behavior of a magnetic particle, since the step on the tracks remains constant throughout the entire track, and, therefore, the entire track (2 mm long) should be produced in a time significantly less than 30-50 ns (this is how long the current pulse lasts).

M.I. Solin (Yekaterinburg) obtained results back in the 1980s that also indicate the joint occurrence of LENR reactions and the manifestation of strange radiation.

Reactor of M.I. Solin is a vacuum melting furnace where zirconium was melted by an electron beam with an accelerating voltage of 30 kV [8]. At a certain mass of liquid metal, reactions began, which were accompanied by anomalous electromagnetic effects, the release of energy exceeding the supplied one, and after analyzing samples of the newly solidified metal, "foreign" chemical elements and strange structural formations were found there. The author writes: "*In the melting zone, long-range propagating volumetric forces appear, which significantly affect the distribution of the pressure force vectors in the liquid phase, change the shape of its free surface and cause the transition of the substance mass from the state of stable equilibrium of the system to the state of ordered and accelerated motion. In the center of liquid mass, although the input of the energy of the magnetic field by the known methods was not performed, the formation of dynamic perturbations in the form of wave ripples on its surface occurs, and then spontaneous curvature and displacement of the interface between the liquid phase surface and the vacuum space of the melting chamber. The relatively large mass of the liquid phase in this process regularly accumulates in the area of exposure to an electron beam and accelerates upward in the form of a traveling solitary wave, acquiring the shape of a cone and a bright white glow, which is clearly distinguished by its shade from the glow of liquid zirconium* (**Fig. 9**)".

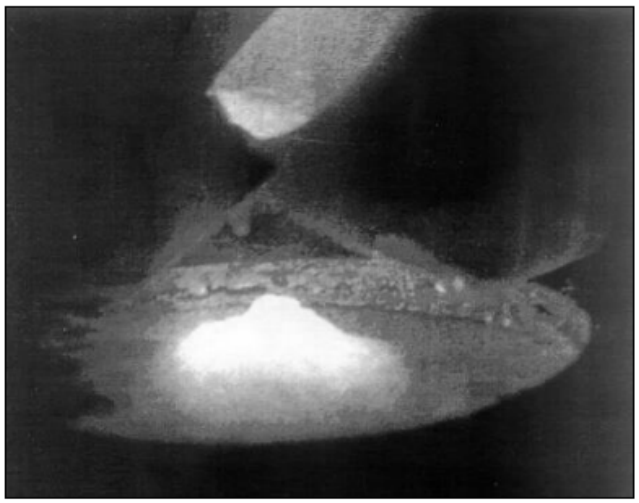

Fig. 9. *A solitary wave in zirconium during the formation of a bulge (illustration from* [8]).

As a result of some strange phenomena, the molten metal begins to behave like Lem's Solaris, periodically blowing up, forming pits, ripples and standing waves. Vortexes are formed in the liquid, as well as solitary stable waves (solitons). In some modes, these processes are accelerated, and the amount of released energy becomes so great that it is necessary to stop the process by turning off the electron beam: "*According to estimated calculations, taking into account the above-described anomalous hydrodynamic, shock-sound and explosive effects occurring in the volume of a liquid phase with a large mass, the total amount of energy released in it is 1000 or more times greater than the initial input energy of the electron beam.*"

The usual process of melting metal billets has nothing to do with such processes: usually the liquid remains calm, with a smooth horizontal surface, with a visible trace of an electron beam. This is exactly how the melt behaves at the beginning of melting, until the critical mass of liquid zirconium is reached. And the fact of excessive energy release is checked extremely simply - by a sharp increase in the melting rate of the billets. After the liquid mass set solid, anomalous formations are observed in it - hollow spheres and cylinders, winding "wormholes", nugget inclusions, and the structure of the metal itself differs significantly from the structure of ordinary zirconium. "*One group of defects is represented by extended tubular channels of various configurations. They show the*

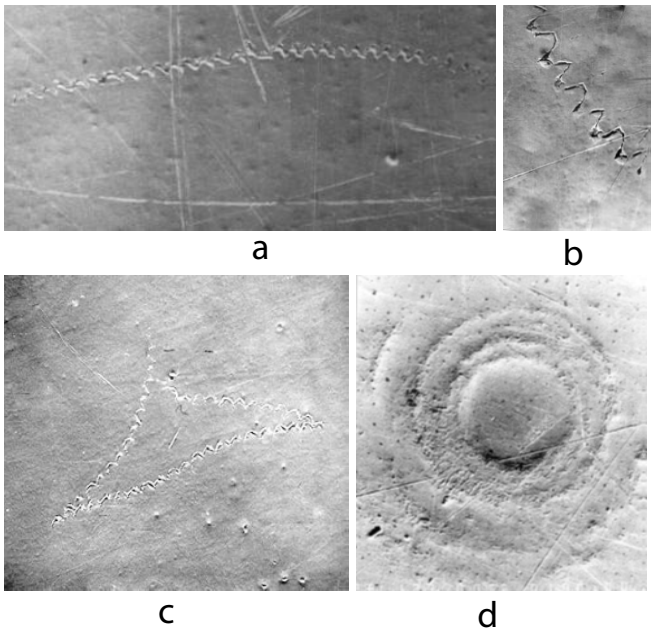

Fig. 10. *Tubular channels in a zirconium ingot: (a) and (b) - in the form of sinusoidal holes, (c) - in the form of a hollow triangular wave loop, (d) - in the form of concentric annular holes (illustration from* [8]).

appearance of cavities in the solidified metal in the form of interconnected sinusoidal wave and rectilinear holes, a hollow triangular wave loop-chain, consisting of regularly repeating semicircular links. These channels are also concentric annular holes. In addition, their configuration contains elements of a meander shape and regularly repeating symmetrical geometric shapes (**Fig. 10**)".

"*Studies by the method of secondary ion mass spectrometry showed the presence of lithium, beryllium, boron, barium and elements of a number of lanthanides in the discovered products-nuggets. These elements are not present in the starting material (in the remelted zirconium). As shown by the results of the analysis of the chemical composition, in the products found in nuggets, in contrast to the initial zirconium is significantly higher (by 2-3 orders of magnitude) of sodium, magnesium, aluminum, silicon, potassium, calcium, titanium, chromium, manganese and iron. By means of X-ray spectral microanalysis and Auger spectrometry, the enrichment of the above-named chemical elements, as well as carbon, nitrogen and oxygen, of the material of cylindrical and spherical shells and the above-mentioned products has been established.*"

Experiments with the generation of radiation leaving the same recognizable tracks and possessing biological activity were carried out by I.M. Shakhparonov (**Fig. 11**). After the action of an electromagnetic pulse generator [9] on diamagnetic materials (including graphite, polymers, glass,

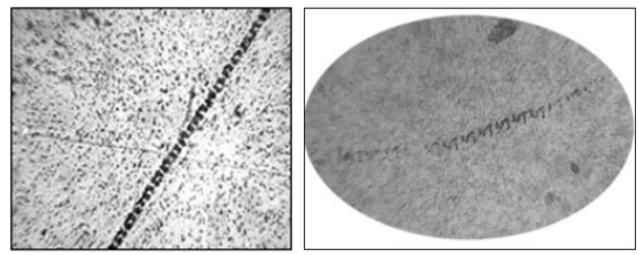

Fig. 11. *Tracks of strange radiation from the Shakhparonov's installation.*

ceramics), they acquired paramagnetic properties [10,11]. The author points out that substances with the highest oxygen content, which is a paramagnet, lend themselves to the greatest magnetization. Shakhparonov called the stream from the emitter of his design "Kozyrev-Dirac radiation". The results of the effect of this radiation on radioactive isotopes show an increase in the rate of the beta decay process (in the patent "Method for the decontamination of radioactive materials" experimental confirmation for ^{131}I is mentioned [12]). The impact of radiation on oil samples showed a complex picture of change in the content of various elements depending on the time of irradiation [13].

Biological studies of radiation (in mice) show that it is biologically active, reduces blood clotting, leads to a decrease in blood glucose, at the same time, it can increase immunity, as well as increase resistance to gamma radiation [14].

Similar results on biological effects were obtained by E.A. Pryakhin and coworkers (Chelyabinsk). They investigated the biological effects on laboratory mice of "strange radiation" from Urutskoyev's setup [15]. They showed that radiation enhances cell division in bone tissue. In experiments where mice were exposed to "strange radiation" (at a distance of 1 meter from the installation) before exposure to hard gamma radiation, an increased resistance to gamma radiation was noted. The authors suggested that this radiation can affect human health.

Recently, studies of the biological effect of strange radiation from an electric explosion were continued by E.A. Pryakhin and colleagues [16]. The influence of the factors of electric explosion of a tungsten wire in a vacuum on damage to nuclear DNA in leukocytes of human peripheral blood, the frequency of chromosomal aberrations in dividing cells of onion root, the growth rate of green unicellular algae, germination and growth rate

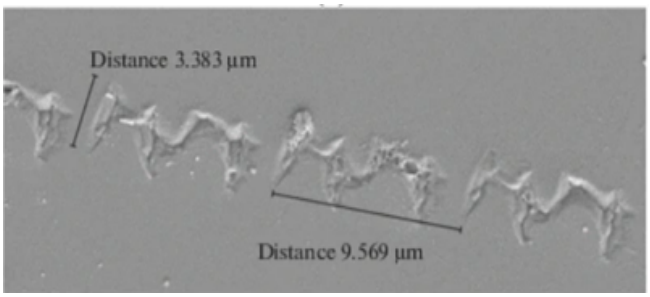

Fig. 12. *Tracks from electric explosion of a tungsten wire in vacuum in the study* [16].

of plant seeds was studied (**Fig. 12**). The authors separated the effects from various factors of electric explosion: strange radiation, light exposure, pulsed magnetic field. Among the results is a reduction in the level of DNA damage caused by strange radiation. It also turned out that the biological effect of strange radiation depends on the material through which this radiation passes: "*The level of damage to nuclear DNA increased depending on the atomic mass of the shielding material with a coefficient of 0.557 ± 0.031 per atomic mass unit.*"

A.L. Shishkin et al. investigated the radiation called "magnetotoroelectric" (in other publications, the authors call the radiation "neutrino-cluster") [17,18]. In addition to extended tracks, microcraters on the surface of an X-ray photographic film with a diameter of up to several microns were studied, and formations of the order of millimeters in size - blackening in the form of "birds" were also observed (**Fig. 13**). The effects of the following processes were studied: water treatment in a cavitation device, rotation of cones made of various materials, irradiation of materials with a gamma source, a high-voltage pulse in a flat capacitor. The study included measuring the diameters of many microcraters and finding patterns in the appearance of microcraters of different diameters. The authors argue that the diameter of the microcraters is proportional to the atomic weight of the elements through which the radiation passes. For example, a diameter of 0.9 µm corresponds to carbon (atomic weight 12), 1.1 µm to nitrogen (atomic weight 14), 1.3 µm to oxygen (atomic weight 16). Aluminum (atomic weight 27) corresponds to a crater diameter of 2.4 µm etc. [17].

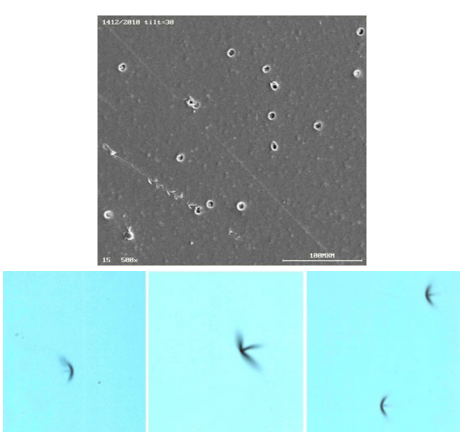

Fig. 13. *Traces of strange radiation on photographic film in Shishkin's experiments* [17].

Similar structures ("birds", spots) on photographic films were observed in the studies of V.V. Evmenenko et al [19]. The scheme for obtaining strange radiation from this group was as follows: water was placed in a magnetic field of ~ 0.5 T, then, after removing the magnetic field, this water was shone through with a low-power laser. A photographic material with protection from the optical component of the laser was placed in the path of the laser. In addition to traces on photographic films (**Fig. 14**), this method of producing strange radiation was accompanied by other phenomena: a change in the weight of ampoules with water, "reactive" effects from such ampoules, when a light raft with an ampoule of water through which a laser was shone through, began to move towards laser, magnetization of non-magnetic materials. These results are described in the review [20].

In this review, it is impossible to describe in detail all the results of studies of strange radiation. Let us briefly mention the results of B.U. Rodionov and I.B. Savvatimova (**Fig. 15**) - the appearance of tracks during a glow discharge. The tracks were formed both on the surface of the electrodes inside the chamber and on photographic films outside the discharge chamber [21]. D.S. Baranov, V.N. Zatelepin et al. investigated tracks on CD-disks from various

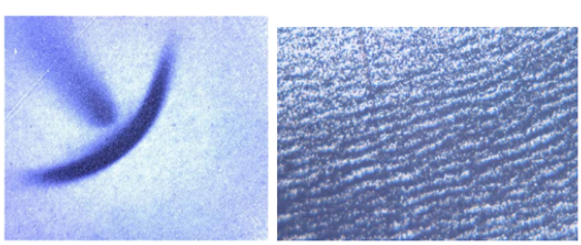

Fig. 14. *"Bird" on photographic film and its "fine structure" in the experiments of V.V. Evmenenko and others* [19].

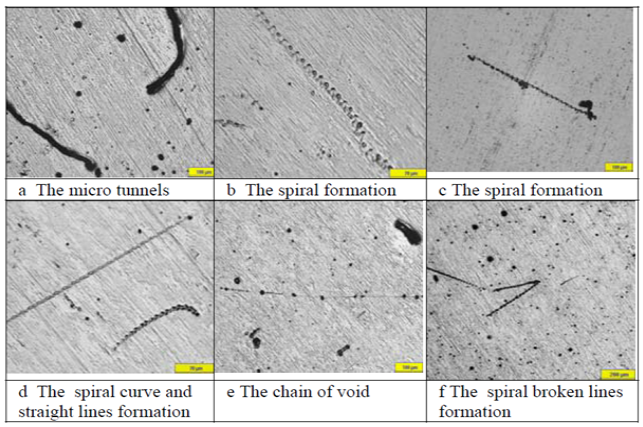

Fig. 15. *Tracks in the study of Rodionov and Savvatimova* [21].

sources (high-voltage electric discharge in an air-water mixture, combustion of propane, charging a smartphone, etc.); they observed extended tracks, craters and spherical particles [22]. Review and results of original experiments are presented in the paper of K.A. Fredericks [23]. A replication of experiments with an electric explosion in water and typical tracks of strange radiation is presented in [24] by C. Daviau et al.

Even a quick glance at the photographs of the tracks suggests that different researchers in different experimental conditions observed the same phenomenon. Some of the works were clearly related to the LENR theme, some were not. To the question posed in the title of this article, the joint consideration of many experiments does not give an unambiguous answer: perhaps LENR and strange radiation are just two phenomena that are noticed by researchers together. After all, in the presence of one anomalous effect, experimenters often pay attention to others at the same time. But does strange radiation always accompany low-energy reactions? Can strange radiation be considered as a marker of LENR? Is LENR the only reason for the strange radiation?

The next section of the article describes experiments that purposefully answered the question: is the appearance of tracks of strange radiation related to the operation of LENR reactors.

3. TRACK STATISTICS FROM OPERATING LENR REACTORS

In order to answer the question of whether there is an unambiguous connection between the operation of LENR reactors and strange radiation, it was necessary to estimate the intensity of strange radiation near and far from operating reactors. This required the creation of a technique for measuring the total track length, as well as the accumulation of statistics in the near and far zones from the reactors [25].

3.1. Materials and methods

Reactors of two types were used as devices in which LENR processes take place. The first device is a Ni - H reactor operating in the mode of continuous generation of excess heat (**Fig. 16***a*). This reactor operated nonstop for 225 days at an average excess heat release power of 200 W [26]. The second reactor is a plasma electrolysis cell in water with movable electrodes "Woodpecker" [27] (Fig. 16*b*). The upper electrode periodically comes into contact with the lower one, which leads to the appearance of plasma in the discharge gap. Used electrodes from graphite, copper, tungsten. In contrast to the Ni-H reactor, which operated in a relatively stable mode, the water reactor operated in various modes with a power consumption of 100–400 W.

To identify the tracks from the reactors, the method of sequential and parallel control was used. Previously, before the exposure at the reactors, the samples of the sensitive material were photographed using an optical microscope at low magnification (x55), then, after the exposure, photography of the entire sample was repeated. For further comparison, photographs of transparent materials were taken using a coordinate grid in the background with a positioning accuracy of 3 mm. Sequential control consisted in the fact that the analysis took into account only those tracks that were absent in the preliminary photos, but appeared in the samples after exposure near the reactors. Parallel control consisted in the fact that in parallel with the exposure at the reactors, the same samples were exposed in other places far from the reactors. The control samples were processed in the same way as the main ones.

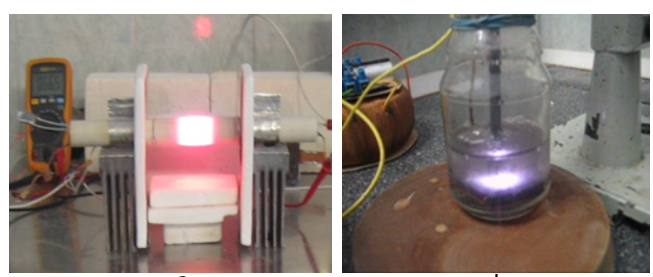

Fig. 16. *Reactor Ni-H (a) and reactor for plasma electrolysis in water (b).*

Various materials were tested to accumulate tracks. Initially, rolls of b/w photographic films and sheet *X*-ray films were used. However, photographic films turned out to be an inconvenient material for the purposes of this study, since the task was to estimate the rate of appearance of strange radiation tracks as reliably as possible, and not to study the types of tracks, which has been mainly done by researchers so far.

After it was found that tracks are formed on almost any smooth surfaces, we refused to use photographic materials that require rather complex processing, introducing artifacts that are difficult to control.

Convenient detectors for recording tracks that can be placed near a hot reactor are microscope slides.

In addition, muscovite mica with a thickness of ~15...30 μm and a size of 50×50 mm was tested. The accumulation rate of tracks on mica in preliminary studies turned out to be higher than on glass, with equal processing convenience, but this material was available only in small quantities.

The most convenient material turned out to be standard DVD-R disks made of polycarbonate. One side of the disk is very smooth and free from defects. The inner Al layer is a reflective surface. This is useful when analyzing tracks under a microscope. At the same time, DVD-R disks have a marked system of tracks, which creates a diffraction pattern, which can somewhat interfere with shooting and analyzing tracks at some surface illumination angles. The main results of a set of statistics were obtained on a DVD-R . Only the smooth side of the disks (polycarbonate) was analyzed.

The method of numerical estimation of the intensity of tracks consists in calculating the total length of the tracks and comparing the obtained values of the experimental samples with the control. For this, the photographs of the captured areas of the samples were first opened in a graphic editor and the tracks of strange radiation were outlined with a pencil tool of a fixed color and a fixed thickness. Then the total length of the lines of a given color was programmatically calculated from a group of photographs. Thus, the intensity estimation technique contains both a manual part (outlining tracks) and an automatic part (calculating the total length). The counting method does not imply the calculation of the average length of the tracks.

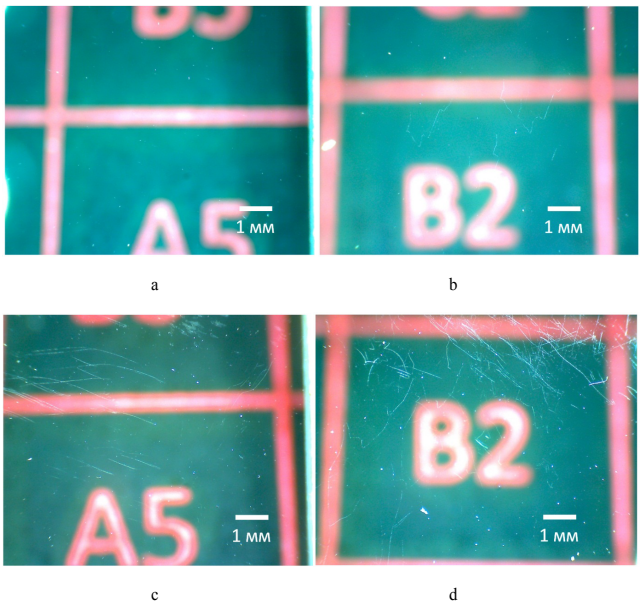

Fig 17. *Photo of mica before exposure (a, b) and after (c, d). Water reactor, distance 5 cm.*

3.2. Examples of tracks

In order to acquaint readers with the main object of this study - extended tracks of strange radiation, we will show several characteristic photos. **Fig. 17** shows a photo of the mica areas - before the exposure at the reactors (*a, b*) and after (*c, d*). It can be seen that the original mica is either clean of tracks (*a*) or has a small number of tracks (*b*), the source of which is unknown (judging by the date of manufacture on the pack, the mica was stored after manufacture for about 30 years). There are many more tracks after exposure. Groups of narrow lines, usually curved, several mm long, visible under lateral illumination appeared (these tracks are especially clearly visible under dark-field microscopy).

Tracks are usually grouped in areas of the order of 1 cm^2. A typical group of tracks on mica is shown in **Fig. 18**. Tracks within a group are often identical in shape (for example, "boomerang" in Fig. 18). Twin

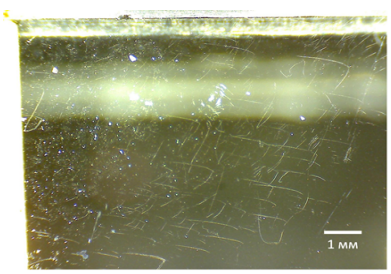

Fig. 18. *Twin tracks on mica: the "boomerang" shape is repeated many times. Ni-H reactor, distance 5 cm.*

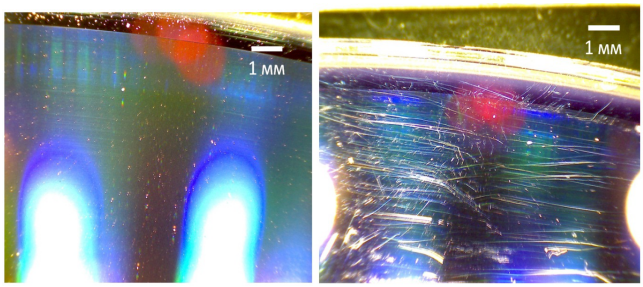

a b

Fig. 19. *Photo of the surface of DVD disks. (a) - control (fume hood 2 m from the water reactor), (b) - 10 cm from the water reactor.*

tracks are localized within one group. Tracks in other groups have a different shape.

Similar track features are found on DVDs. In **Fig. 19** for comparison shows a photo of the disks of control (*a*) and experiment (*b*). Here, too, a large number of tracks are in a group with an area of the order of 1 cm^2. They are mostly parallel tracks several mm long. A more detailed analysis of the track structure is presented in [25], but here we present just one illustration concerning the structure of periodic tracks.

Fig. 20-21 show fragments of a periodic track on DVD at different magnifications. The constancy of the step of such tracks has already been indicated by other authors, we can confirm such observations. But a surprise was the complete repetition of the track structure from period to period, with an accuracy up to the resolution of an electron microscope (tens of nanometers). Periodic traces are repeated down to the smallest detail (**Fig. 21**). It is impossible to explain such a picture by anything other than rolling on the surface of a micron-sized solid particle. The ratio of the track width and period length in **Fig. 20** roughly corresponds to 2π. Similar periodic traces were observed on glass , while on mica the nature of surface destruction was different [25].

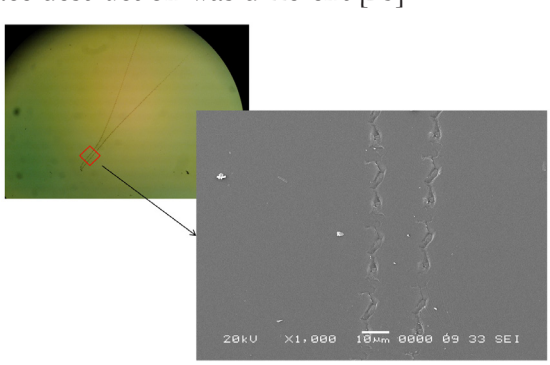

Fig. 20. *Optical and SEM image of a fragment of a track on DVD.*

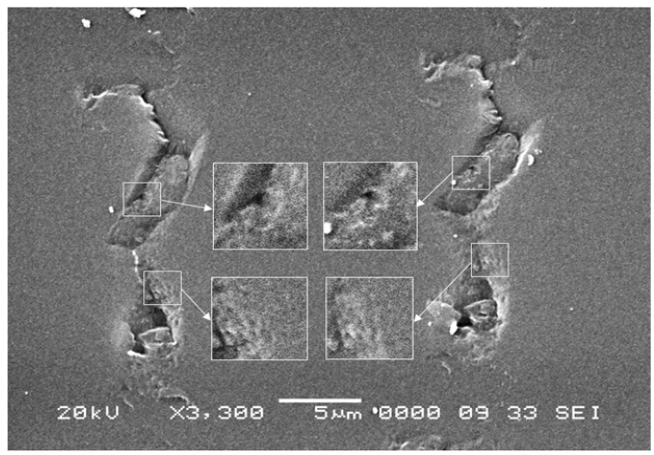

Fig. 21. *Detailed SEM image of a fragment of a track on DVD (increased contrast). Explanations in the text.*

3.3. Track statistics

This section presents the main results of analyzing the statistics of the total track length. Exposure conditions and summary results are presented in **Table I**.

Analysis of the data shows that the total track length increases significantly near the reactors.

Results for mica and DVDs obtained near and far from the reactors are shown in **Fig. 22**. Further these areas are referred to as "near zone" (up to 20 cm) and "far zone" (more than 20 cm). Control exposures with parallel control are also included in the far zone.

Sequential control showed that the total length of tracks on mica before exposures corresponds, on average, to parallel control, i.e. far zone. Analysis of the initial surface condition of DVD (before exposure) showed complete absence of tracks.

The average total length of tracks on mica for distances of 5 cm from the reactors (948 mm per sample) exceeds by more than an order of magnitude the average total length for large distances (37 mm

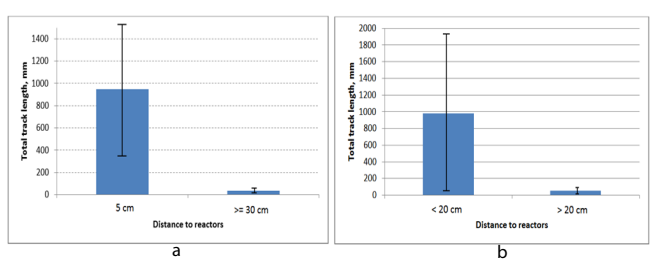

a b

Fig. 22. *Average value of total track lengths for mica and DVD, depending on proximity to the reactor. (a) - for mica at a distance of 5 cm (5 exposures) and at distances from 30 cm (10 exposures); (b) - for DVD at distances <20 cm (49 exposures) and at distances> 20 cm (30 exposures). The intervals show the average deviations.*

Table 1

Summary results of track statistics by exposure conditions.

	Number of samples, pcs.	Total track length, mm	Exposure hours	Hours of operation of the reactor	Average total length, mm	Density of tracks, mm/cm^2	Track accumulation rate per exposure, mm/cm^2/h	Track accumulation rate during reactor operation, mm/cm^2/h
Mica 50x50 mm								
5 cm to Ni- H reactor	4	4096	1344	1344	1024	41.0	0.1219	0.1219
5 cm to the water reactor	1	642	120	2	642	25.7	0.2140	12.8400
30 cm from Ni-H reactor	2	117	336	336	58.5	2.3	0.0139	0.0139
Fume hood (>2 m from reactors)	4	107	672	0	26.75	1.1	0.0064	
In an adjacent room (> 5 m from reactors)	2	109	336	0	54.5	2.2	0.0130	
Exposure in oven 200C	2	38	6	0	19	0.8	0.2533	
DVD-R								
5-13 cm from Ni- H reactor	7	3928	1440	1440	561	5.6	0.0272	0.0272
20-30 cm from Ni- H reactor	3	247	528	528	82	0.8	0.0047	0.0046
Up to 20 cm from the water reactor	42	44089	7240	194	1050	10.5	0.0609	2.2726
20-60 cm from water reactor	15	513	2520	45	34	0.3	0.0020	0.1140
1 m from water reactor	5	757	512	27	151	1.5	0.0148	0.2804
Fume hood (>2 m from reactors)	7	116	595	0	17	0.2	0.0020	

per sample). At the same time, there is a large scatter of values (the figure shows the average deviation[1]). A large scatter is also observed in the far zone, but large values of the sums of track lengths (> 500 mm per sample) are completely absent in exposures in the far zone.

The results on the DVD are similar to those obtained for mica: an average of 980 mm per sample for the near field (up to 20 cm from the reactors) and 54 mm per sample for the far field (over 20 cm). There is also a large scatter of the values obtained both in the near zone and in the far zone, and the absence of large values for the far zone.

To illustrate the large scatter of data, **Fig. 23** shows the total track lengths for various DVD images, separately for the near and far zones on the same scale.

Note that the shown in Fig. 22 data on the total track lengths for mica and for disks were obtained for different areas of the detectors. The area of the mica sheet is 25 cm^2, the working area of the disk is 100 cm^2. The average total length of tracks in the near zone turned out to be approximately the same, but the density of tracks (total length per 1 cm^2) for mica is 4 times higher. There may be several reasons for this difference. First, the susceptibility of different materials to strange radiation is possible. Second: for mica, it is possible to accumulate tracks on both sides, while for DVD, tracks were analyzed only on one side, not covered with paint. Third, the effectiveness of the track counting technique for transparent material (mica) and material with a mirror-like interior (DVD) can be different.

To assess the character of the dependence of the track intensity on the distance, an experiment was carried out, the results of which are shown

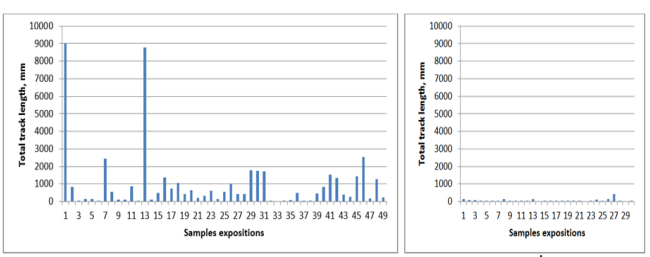

Fig. 23. *Total lengths of tracks on DVD by exposure: (a) - for the near zone, (b) - for the far zone.*

[1]Due to the large scatter of values, the intervals in the graphs show the mean of the absolute values of the deviations of the data points from the mean, rather than the standard deviations, which are about 2 times greater.

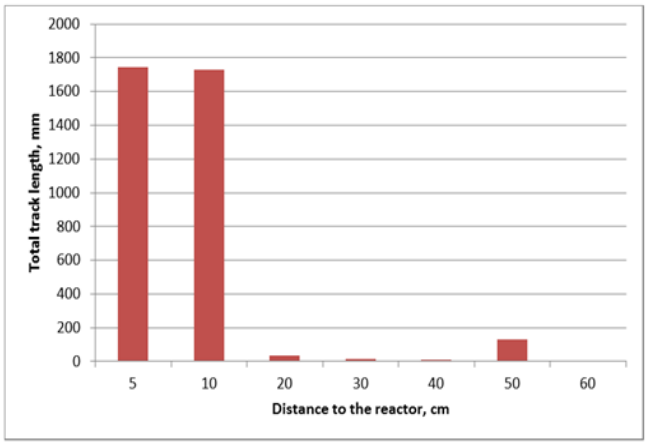

Fig. 24. *Results of the experiment with different distances of the disks from the water reactor.*

in **Fig. 24**. Seven disks were placed at different distances from the water reactor. The disks, which were at a distance of 5 and 10 cm, showed a large number of tracks; at a greater distance, the number of tracks drops by more than an order of magnitude.

Another feature of the results obtained is as follows. The exposure time of the samples in the continuously operating Ni-H reactor was, on average, one week. The exposure time at the water reactor can be calculated in different ways. The total time of its active work per one exposition usually amounted to several hours, while the samples themselves stood continuously at the reactor and during the hours when the reactor was not working (calendar time on average is also one week). Table I summarizes both continuous exposure times and reactor operation times. If we calculate separately the average track density from Ni-H and water reactors in the near zone (the sum of the track lengths, divided by the total area of the samples), we obtain similar values: 10.0 mm/cm^2 for Ni-H reactor and 10.6 mm/cm^2 for a water reactor. However, if we divide them by the time of active operation and obtain the rate of track accumulation during the active operation of the reactors, it turns out that a water reactor produces an order of magnitude more tracks per hour of operation (0.0540 mm/cm^2/h for a water reactor, 0.0036 mm/cm^2/h for Ni-H reactor). Thus, a variant is possible when strange radiation accumulates in the water during the operation of the reactor and gradually comes out of it [1]. To clarify the situation, additional studies were carried out.

3.4. Experiments with aftereffect

Separate exposures were carried out during the operation of the reactor and after shutdown, but with the preservation of the geometry of the arrangement of the disks and the reactor [28].

Test 1

The pulsed plasma electrolysis reactor described in [29] was used as a source of strange radiation. The reactor was turned on for 5 minutes. During his work, disks W1 and W2 were located next to it (10 cm). After turning it off disks were removed to a distance of > 3 m, and instead placed disks A1.1 and A1.2. They stood for one day next to the shutdown reactor. Then they were removed to a distance of > 3 m, and instead of them disks A2.1 and A2.2 were placed for two days. Then they were also removed and instead of them A3.1 and A3.2 were placed - for three days next to the shutdown reactor. In addition to these disks, at a distance from the reactors there were two control disks C1 and C2, which were placed for one day.

In **Fig. 25***a* shows the results in absolute values; Fig. 25*b* - track accumulation rate (mm/h) by disk group. It can be seen, on the one hand, that the tracks are mainly collected already with the reactor turned off, and, on the other hand, the rate of collection is maximum when the reactor is on. The rate of track accumulation after shutdown gradually decreases with time and approaches control on 4-6 days.

Test 2

The accumulation experiment was repeated one more time. In the second experiment, one disk was used during a short turn-on (5 minutes) of the same reactor (W20.02), and one disk each for aftereffect on the first day after shutdown (A20.02), on the second day after shutdown (A21.02), 3-5th days after shutdown (A22.02), as well as the sixth (A25.02) and seventh (A26.02) days after shutdown. There were also two control disks (C27.02*a*, C27.02*b*).

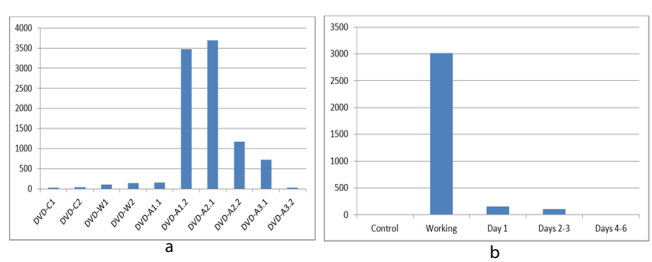

Fig. 25. *Experiment 1 with aftereffect . (a) - total track lengths by disks (mm), (b) - accumulation rate of total track lengths by disk groups (mm/h).*

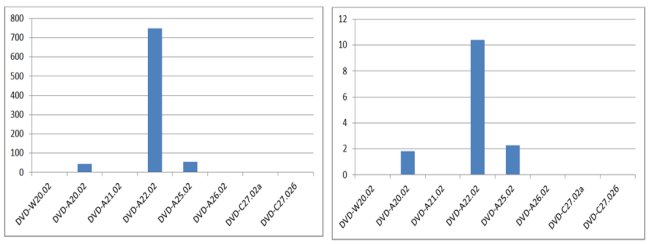

Fig. 26. *Experiment 2 with aftereffect. (a) - total lengths of tracks on disks (mm), (b) - rate of accumulation of total lengths of tracks on disks (mm/h).*

Unfortunately, the results of the experiment revealed the previously noted variability of the track intensity: the total intensity of experiment 2 was an order of magnitude less than for the first experiment with accumulation. There were one disks in each exposure, that is, two times less than in the first experiment. The results are shown in **Fig. 26**.

A noticeable number of tracks appeared only on the disk, which was exposed within three days after the operation of the reactor. The rest of the disks, including "working" showed near-zero track intensities. However, these results do not contradict those shown in the first accumulation experiment, taking into account the variability of the number of tracks from time to time.

There was also an attempt at a third experiment in order to find out what exactly in the reactor accumulates the strange radiation - the vessel or the electrolyte. But practically zero intensities were obtained in it in all disks. On this, experiments to study the aftereffect were discontinued.

At least the results of two experiments indicate that after shutting down the reactor for several days, the reactor itself and/or the environment around it operates as a source of strange radiation tracks. This must be taken into account by LENR experimenters.

3.5. Impact of disk orientation

Experiments were also carried out with different orientations of the disks against the water reactor in the near zone. A diagram of the total track lengths was plotted for three experiments with the same conditions for placing 4 disks around the reactor. The orientation of the disks and the distance from the core to the centers of the disks in each experiment are shown in **Fig. 27**. The sensitive side of the disks at a distance of 2 and 4 cm was directed towards the discharge.

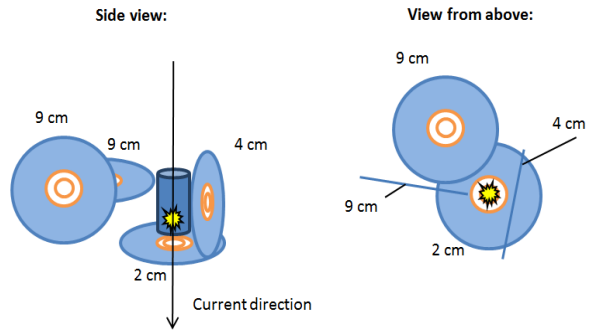

Fig. 27. *The orientation of the disks and the distance to the centers of the disks from the discharge.*

The values from the total track lengths are shown in **Fig. 28**. If we analyze the dependence on the distance, we can see that the average for the sum of the track lengths is approximately the same - about 600 mm per disk for three distances (2, 4, 9 cm) with a large scatter. Also, there is no regularity in the accumulation of tracks by disks, depending on their orientation (for a distance of 9 cm, vertical (v) and horizontal (h) orientations are shown). The operating time of the reactor in two repetitions is 3 hours, in the third - 4 hours.

3.6. Shielding issues

Initially, we believed that the penetrating power of the strange radiation was extremely high, and for some of the exposures, DVDs were wrapped in foil. Surprisingly, there were no tracks in any of the expositions where the disks were wrapped in foil. Therefore, we continued our experiments in this direction purposefully.

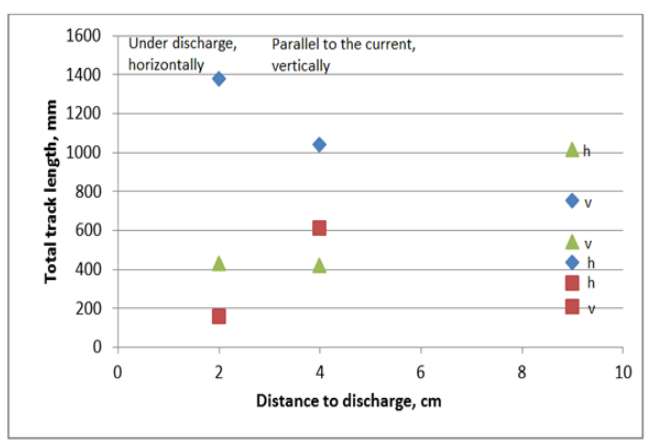

Fig. 28. *Three repetitions of experiments with different orientations of the disks. Diamonds - first repeat, squares - second repeat, triangles - third. The letters "v" and "h" show the vertical and horizontal orientations of the disks for a distance of 9 cm.*

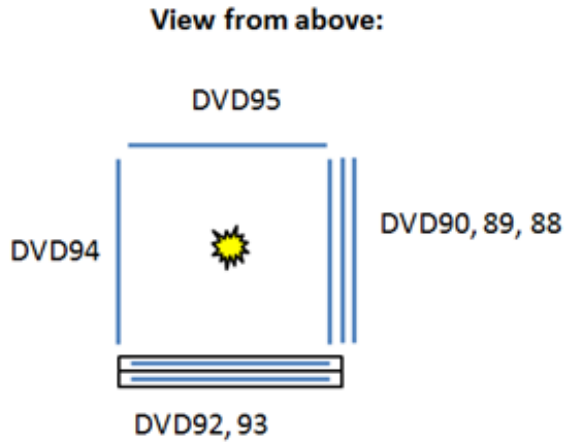

Fig. 29. *Experiment 1 with screening. The layout of the disks near the "Woodpecker" reactor.*

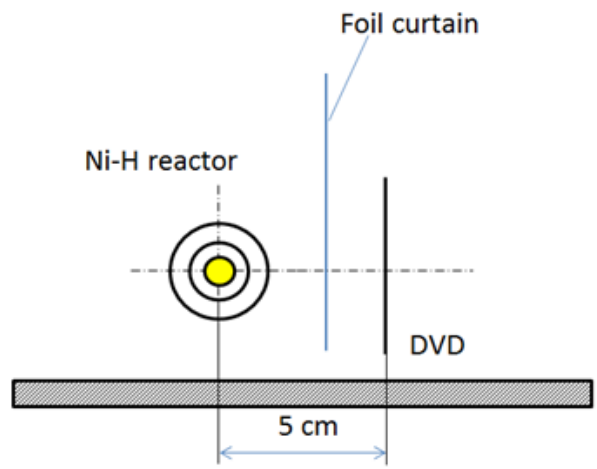

Fig. 31. *Scheme that did not interfere with the formation of tracks on DVD.*

For illustration, we present the results of one of the experiments with screening [28]. Seven disks were exposed near the "Woodpecker" plasma discharge in water reactor (**Fig. 29**) at a distance of 5...10 cm from the reactor, and 2 control disks in one meter from the reactor. The reactor was located in the fume hood. The three disks were stacked, in a row, with the sensitive side to the reactor, in the order of DVD90 - DVD89 - DVD88 from the reactor. The other two disks were each wrapped in 10 μm aluminum foil (DVD92, DVD93). Two more disks were unshielded - DVD94, DVD95, the sensitive side to the reactor. The active operation time of the reactor is 8 hours, the continuous exposure time is 6 days.

The results are shown in **Fig. 30**. It can be seen that in a stack of 3 disks, the closest one received many times more tracks than those that he obscured. Disks in foil showed a relatively small number of tracks. Unshielded disks DVD94, DVD95 show a large number of tracks for first

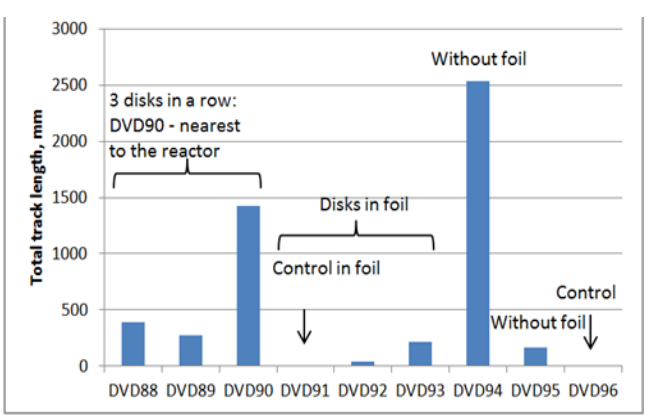

Fig. 30. *Results of experiment 1 with screening.*

one, the second had a small number, at the level of shielded disks.

The control disks showed no tracks. One of the control disks was opened (DVD96), the other was wrapped in foil (DVD91).

Other experiments confirm the results of the described experiment [28]. Disks in a stack protect each other from tracks. Disks located in a plastic box closed on all sides are also protected from tracks of strange radiation.

However, these results turn out to be paradoxical if we take into account that part of the exposures from the hot Ni-H reactor was performed in the following scheme: an aluminum foil shutter covered the DVD disks from the thermal radiation of the reactor (**Fig. 31**). This shutter did not form a continuous envelope around the disk, and was spaced from the disk at a distance of several cm. In this case, the disks gained a significant number of tracks, in contrast to the control disks located at a distance from the reactor. The track protection works, therefore, only in the case of a solid screen, or a screen covering a large solid angle around the protected object.

4. DISCUSSION

Returning to the question in the title of the article - what is the relation between strange radiation and LENR, let's try to draw conclusions from the experiments carried out. The statistics of the appearance of tracks indicates that a large number of tracks appear in the near zone of operating reactors, and continues to appear for several days

after the reactor is turned off. In addition, there is a strange background radiation - its source is unknown, and its intensity is one or two orders of magnitude less.

However, if we refine the question of whether the appearance of tracks is connected with LENR reactions inside reactors (let's call it a strong hypothesis), then the results of the experimental part of this work, although they do not contradict this hypothesis, nevertheless, do not rigorously prove it. To prove this hypothesis, it is necessary to study the possibility of the appearance of tracks from other factors involved in the operation of LENR reactors (electric current, electromagnetic fields, high temperature, sorption/desorption, phase changes, etc.), as well as to test the reactors in regimes without nuclear reactions, but with the participation of these factors.

So, the first conclusion is that strange radiation accompanies the operation of LENR reactors. However, the discovered large variability of strange radiation does not allow drawing a direct analogy with ordinary nuclear reactions and ordinary ionizing radiation (alpha, beta, gamma radiation, neutrons), which are usually considered as a marker of nuclear reactions. Strange radiation appears sporadically near a stably operating reactor: with equal geometry and exposure time, sometimes a lot of tracks appear near the reactor, sometimes there are none at all. This raises the question of both the nature of the strange radiation and the development of methods for measuring its intensity. Perhaps the movements of the particles that cause the tracks are irregular and occur in random directions, and it is necessary to collect the tracks in the entire solid angle. Perhaps we are at such an early stage in the study of the phenomenon that we see only distant and minor consequences of something that generates strange radiation. It may also turn out that the cause of the strange radiation is some elusive third factor, which is also the cause of LENR, but it is still in the shadows and has not been investigated at all. By jointly studying LENR and strange radiation, we can reach their common cause, and then these two phenomena will receive a common explanation.

One of the possible explanatory schemes is that the particles themselves, forming the tracks, directly cause low-energy nuclear reactions. In our studies, using the energy-dispersive method, there were attempts to see traces of nuclear transformations along the tracks, as a consequence of hypothetical nuclear catalysis [25]. Unfortunately, we did not find extraneous elements within the error of the method, in contrast to the studies [7,8].

Summarizing many publications, we can see that strange radiation appears as a result of quite different processes:

- Discharge in vacuum
- Discharge in water
- Glow discharge
- Arc discharge
- Pulsed electric field of a capacitor
- Heating system Ni-H
- Electrolysis
- Laser radiation
- Rotating objects

So far, it cannot be said that all these processes also lead to LENR. In addition, in biological transmutation [30], traces of strange radiation in the form of tracks have not yet been noticed. At least some of the processes may not generate strange radiation, but "release" the accumulated radiation from the substance - the aftereffect gives rise to such a hypothesis. Therefore, it is premature to conclude that LENR is necessary and sufficient for the strange radiation to occur.

The results obtained raise new questions. The structure of the tracks, studied by optical, electron, and atomic force microscopy, directly indicates that the tracks are formed by micron-sized solid particles that are harder than a sensitive surface, including mica, glass, plastic, and aluminum [25,28]. If the source of such particles are LENR reactors, how do these particles pass through a solid reactor vessel, especially multilayer ones? What forces are used to press these particles against the surface of sensitive materials over the course of millimeters and centimeters of their movement over the surface? Why are they grouped and move as a whole group as a whole, forming a kind of solid frame? What causes the abrupt changes in the direction of movement of these grouped particles? At what speed do they move and what is the very nature of these particles? All these questions must be answered not speculatively, but experimentally.

Many researchers, in an attempt to explain the observed tracks, have argued in favor of the hypothesis of magnetic monopoles. There is no

reason to believe that the periodic tracks in our study are of any other nature compared to the recognizable tracks in the publications of Urutskoyev, Ivoilov, Adamenko and Vysotsky, Shakhparonov and others. However, the mechanism of periodic motion of magnetically charged particles in the MOS-structure proposed by Adamenko and Vysotsky cannot explain the detailed picture of periodic tracks, where clearly there are traces of a micron-sized solid. Especially if we take into account the appearance of similar tracks on different homogeneous materials, and periodic tracks are only a small part of all tracks. It is in no way the movement of individual elementary particles, to which nuclear physicists are accustomed to analyzing the tracks of radioactive radiation. Track photos like Fig. 21 sharply narrow down the range of possible hypotheses.

Another note concerns possible replications. The author began his experiments with strange radiation [31, 32] with an attempt to repeat the results of the Evmenenko group [19]. Replication was rather unsuccessful - when statistics were accumulated, the number of tracks in the experiment was equal with the number of tracks in the control. The study, however, was useful - it became clear that there was a background component of the strange radiation, the first numerical method for estimating the intensity of tracks was applied, the author was faced for the first time with a large variability of the intensity. But the example of this replication clearly shows that due to a lack of understanding of the strange radiation nature, researchers often find themselves in the position of looking for a black cat in a black room. Worse, they don't even suspect that the cat itself is somewhere - they look through the microscope only the scratches from its claws. But we must eventually find a way to turn on the light in this room.

And, since the picture of the phenomenon really turns out to be unusual, it is worth taking a closer look at adjacent anomalous phenomena. For example, if particles forming tracks of strange radiation exert a force on the surface, it is necessary to pay close attention to the behavior of sensitive detectors with a moving mechanical part: experimenters have long noticed the strange behavior of torsional balance from various factors, for example, from moving water nearby [33,34,35]. If in two studies that are completely different in design, experimenters noticed that strange radiation, passing through various substances, changes its properties (the diameter of microcraters in [17] and the biological effect in [16]), then one should pay attention to publications in which such the effect is also noticed, for example, from the radiation of torsion generators, see, for example, [36,37].

Finally, the development of research on strange radiation and LENR could create a new scientific revolution that integrates many anomalous results and requires bold hypotheses to explain them, which in turn will need to be tested. This will require the mobilization of not only researchers of this narrow topic, but a significant part of the scientific community. But is the scientific community ready for such a mobilization?

5. SUMMARY

1. Many experimenters have noticed that tracks of strange radiation accompany low-energy nuclear reactions in completely different experimental design.
2. The investigated LENR reactors of two types (Ni-H and plasma electrolysis in water) are sources of strange radiation tracks.
3. The intensity of tracks in the zone closer than 20 cm from the reactors is an order of magnitude or two higher than at a greater distance.
4. Besides tracks from reactors, there are background tracks from unknown sources.
5. Tracks appear unevenly both in time and in spatial arrangement on samples. Tracks that are copies of each other are usually localized in areas of the order of 1 cm^2.
6. Tracks are formed when solid microparticles with a size of the order of microns moving along the surface. The nature of the particles and the force pressing them to the surface remain unknown.
7. Tracks of strange radiation are screened by various solid surfaces - plastic, foil. One closely spaced surface can provide good track protection for the other. The continuous screens protect well.
8. Strange radiation, although it has operating LENR reactors as one of its sources, can be accumulated in the substance and leave the substance within several days after the reactors are turned off.

9. The nature of the strange radiation, in our opinion, remains undisclosed; many of its paradoxical properties are still unexplained.

6. CONCLUSION

At this stage, strange radiation is inconvenient to use as a reliable marker of LENR: the large variability of track lengths does not yet allow practical use of tracks as reliable evidence of the occurrence of LENR reactions in reactors. Apparently, without disclosing the nature of strange radiation, we will not be able to make either its reliable detectors, or understand its relation with low-energy nuclear reactions, the nature of which is also still unclear. But progress in this area is possible only in attempts to create new methods of detection and in new experiment designs. New intensive targeted experiments are needed, and bold research programs in related fields are needed. The race is got by running.

REFERENCES

1. Urutskoev LI, Liksonov VI, Tsinoev VG. Experimental detection of 'strange' radiation and transformation of chemical elements. *Prikladnaya fizika*, 2000, (4):83-100 (in Russ.). (http://www.urleon.ru/files/article_58.pdf). See also Urutskoev LI, Liksonov VI. Observation of transformation of chemical elements during electric discharge. *Ann. Fond. Louis de Broglie*, 2002, 27(4):701-726; Urutskoev LI. Review of experimental results on low-energy transformation of nucleus. *Ann. Fond. Louis de Broglie*, 2004, 29 Hors-série 3, p. 1149-1164, p. 701-726.
2. Ivoilov NG, Urutskoev LI. The influence of "strange" radiation on the Mössbauer spectra of Fe^{57} in metal foils. *Prikladnaya fisika*, 2004, 5:20-25 (in Russ.).
3. Agapov AS, Kalensky VA, Kaitukov ChB, Malyshev AV, Ryabova RV, Steblevsky AV, Urutskoev LI, Filippov DV. Detection of "strange radiation" and isotopic distortion of titanium during testing of industrial electrical equipment. *Prikladnaya fisika*, 2007, 1:37-46 (in Russ.).
4. Ivoilov NG. Low Energy Generation of the 'Strange' Radiation. *Annales de la Fondation Louis de Broglie,* 2006, 31(1) (https://aflb.minesparis.psl.eu/AFLB-311/aflb311m484.pdf).
5. Adamenko SV. The concept of artificially initiated collapse of substance and key results of the first stage of its experimental implementation. *Preprint 2004*, Kiev, p. 36. (http://proton-21.com.ua/articles/Preprint_en.pdf).
6. Adamenko Stanislav, Selleri Franco, Merwe Alwyn van der (Eds.). *Controlled Nucleosynthesis. Breakthroughs in Experiment and Theory, Series: Fundamental Theories of Physics*, vol. 156, 780 p., Springer, 2007. (http://www.springer.com/physics/elementary/book/978-1-4020-5873-8).
7. Adamenko SV, Vysotsky VI. Experimental detection and modeling of the orientational motion of hypothetical magnetically charged particles on a multilayer surface. *Poverkhnost'*, 2006, (3):84-92 (in Russ.).
8. Solin MI. Experimental facts of spontaneous nucleation of condensate of soliton charges with the formation of nuclear fusion products in liquid zirconium. Part 1. *Fizicheskaya mysl' Rossii*, 2001, (1):43-58 (in Russ.). http://www.invur.ru/print.php?page=proj&cat=neob&doc=solin1.
9. Shakhparonov IM. Device for vacuum polarization. *Patent 1806477*, dated 05.21.1990 (in Russ.).
10. Shakhparonov IM. Method for magnetizing non-magnetic materials. *Patent 2123736* dated 20.12.1998 (in Russ.).
11. Stanzo V. Ivan and his monopoles. Tekhnica molodezhi, 1996, No. 10, (in Russ.).
12. Shakhparonov IM. Method for the disinfection of radioactive materials. *Patent 2061266* dated 05.25.1996 (in Russ.).
13. Shakhparonov IM, Kolotukhin SP, Chepenko BA, Khandurov YuN. Primenenie kholodnogo nukleosinteza v neftyanoy promyshlennosti [Application of cold nucleosynthesis in the oil industry], 2004 (in Russ.) https://textarchive.ru/c-2996740.html.
14. Shakhparonov IM. Izluchenie Kozyreva-Diraka i ego vliyanie na zhivotnykh [Kozyrev-Dirac radiation and its effect on animals] (in Russ.), https://pandia.ru/text/79/566/46687.php.
15. Pryakhin EA, Tryapitsina GA, Urutskoyev LI, Akleyev AV. Assessment of the biological effects of "strange" Radiation. *Annales de la Fondation Louis de Broglie*, 2006, vol. 31, no 4, (http://citeseerx.ist.psu.edu/viewdoc/download?doi=10.1.1.668.6555&rep=rep1&type=pdf).

16. Priakhin EA, Urutskoev LI, Stiazhkina EV, Tryapitsyna GA, Aldibekova AE, Peretykin AA, Priakhin EE, Alabin KA, Pilia ND, Chikovani NZ, Voitenko DA, Arshba RM. Biological detection of physical factors related to the high-current electric explosion of conductors in a vacuum. *Izvestiya RAN. Fizika* [Bulletin of the Russian Academy of Sciences. Physics], 2020, 84(11):1341-1348 (in Russ.).
17. Shishkin AL, Baranov VA, Vinogradov AV, Dubovik VM, Tatur VYu. Investigation of the characteristics of MagnetoToroElectric Radiation using photographic film detectors. *Academy of Trinitarianism*, Moscow, El No. 77-6567, publ. 17244, 21.01.2012 (in Russ.) (http://www.trinitas.ru/rus/doc/0231/004a/02311041.htm).
18. Shishkin AL, Tatur VYu. Assessment of the radiation effect of string-vortex solitons. *Materials of 25th Russian conference on cold transmutation of nuclei of chemical elements and ball lightning,* 2018, October 1-8, Adler, Sochi, Russia. Moscow, NIC FTP "Erzion" Publ., 2018 (in Russ.).
19. Evmenenko VV, Malakhov YuI, Perevozchikov NF, Sharikhin VF. Registration of high-energy radiation observed during the interaction of laser radiation with magnetized water. *Materials of the 18th Russian conference on cold transmutation of nuclei of chemical elements and ball lightning,* Krinitsa, Krasnodar region, Russia, Sept. 4-11, 2011, Moscow, NIC FTP "Erzion" Publ., 2012 (in Russ.).
20. Medvedeva AA, Panchelyuga VA. The Volkov effect. *Metafizika*, 2014, 11(1):151-159 (in Russ.).
21. Rodionov B, Savvatimova I. Unusual structures on the material surfaces irradiated by low-energy ions. *Condensed Matter Nuclear Science (Proc. 12th Intern. Conf. on Cold Fusion, Yokohama, Japan, 27 Nov.-2 Dec. 2005, doi: 10.1142/6190)*, 2006, pp. 421-429.
22. Baranov DS, Zatelepin VN, Panchelyuga VA, Shishkin AL. Transfer of "dark hydrogen" by atomic matter. Methods for the diagnosis of "dark hydrogen". *Proc. 26th Russian conf. on cold transmutation of nuclei of chemical elements and ball lightning*, 2020, p. 87. Moscow, NIC FTP "Erzion" Publ., 2020 (in Russ.).
23. Fredericks KA. Possible detection of tachyon monopoles in photographic emulsions. 2013, http://restframe.com/downloads/tachyon_monopoles.pdf.
24. Daviau C, Fargue D, Priem D, Racineux G. Tracks of magnetic monopoles. *Ann. Fond. Louis de Broglie*, 2013, 38:139-153.
25. Zhigalov VA, Zabavin SN, Parkhomov AG, Sobolev AG, Timerbulatov TR. Statistics and structure of strange radiation tracks from two types of LENR reactors. *Zhurnal formiruyushchikhsya napravleniy nauki* (*ZhFNN*) [Journal of Emerging Areas of Science], 2018, 21-22(6):10-25 (in Russ.).
26. Parkhomov AG, Zhigalov VA, Zabavin SN, Sobolev AG, Timerbulatov TR. Nickel-hydrogen reactor that has been in continuous operation for 7 months. *ZhFNN*, 2019, 23-24(7):57-63 (in Russ.).
27. https://e-catworld.com/2018/10/18/q-a-with-alexander-parkhomov/
28. Zhigalov VA. Experiments with screening and aftereffect of strange radiation. *ZhFNN*, 2019, 25-26(7):62-66 (in Russ.).
29. Parkhomov AG. Research of processes at the installation of pulsed plasma electrolysis. *Proc. of the 20th Russian conference on cold nuclear transmutation and ball lightning*. Sept. 29-Oct. 6, 2013, p. 65-76. Loo, Sochi, Rossia, http://www.unconv-science.org/n25/parkhomov/.
30. Vysotsky VI, Kornilova AA. *Nuclear fusion and transmutation of isotopes in biological systems*. Moscow, Mir Publ., 2003, 304 p.
31. Zhigalov VA. Tracks on photographic film from strange radiation: replication. *ZhFNN*, 2015, 9(3):55-62 (in Russ.).
32. Zhigalov VA. Background tracks of strange radiation. *ZhFNN*, 2017, 17-18(5):90-95 (in Russ.).
33. Pugach AF. Torsind is a device of new physics. Part 3. Laboratory research of torsind. *ZhFNN,* 2015, 8(3):6-14 (in Russ.).
34. Panchelyuga VA Stepanov IN, Panchelyuga RV. Influence of water circulation on the reaction of torsind. *ZhFNN*, 2019, 23-24(7):81-89 (in Russ.).
35. Tatur VYu, Negodailov AN. *The effect of shielded moving water on a torsion balance.* Moscow, Academy of Trinitarism, El No. 77-6567, publ. 26113, 16.02.2020 (in Russ.), http://www.trinitas.ru/rus/doc/0016/001g/00164268.htm.

36. Panov VF, Testov BV, Klyuev AV. The reaction of mice to torsion radiation. Scientific foundations and applied problems of energy-informational interactions in nature and society. *Proc. of the Intern. Congress "InterENIO-99"*. Moscow, Publishing house of VIU, 2000, (http://www.roerich.com/zip/mouse_t.zip)(in Russ.).
37. *Experiments with generators and detectors of a torsion field. Collection of works*. Moscow, Folium Publ., 2014, 326 p. (in Russ.).

DOI: 10.17725/rensit.2021.13.349

New polymorphic varieties of boron nitride with graphene-like structures

Dmitry S. Ryashentsev, Eugeny A. Belenkov

Chelyabinsk State University, https://www.csu.ru/

Chelyabinsk 454001, Russian Federation

E-mail: ryashentsev_dmitry@mail.ru, belenkov@csu.ru

Received March 09, 2021, peer-reviewed March 22, 2021, accepted March 29, 2021

Abstract: **First-principle calculations of the structure and electronic properties of four new polymorphic varieties of graphene-like boron nitride, the structure of which is similar to the structure of graphene polymorphs, the atoms in which are in the spirit of different structural positions, were performed by the density functional theory method in the generalized gradient approximation. As a result of the studies carried out, the possibility of stable existence of three monoatomic boron nitride layers: BN-$L_{4\text{-}6\text{-}8a}$, BN-$L_{4\text{-}6\text{-}8b}$ and BN-$L_{4\text{-}10}$ has been established. The BN-$L_{4\text{-}12}$ layer is transformed into the BN-$L_{4\text{-}6\text{-}8}$ layer during geometric optimization. The lengths of interatomic bonds in boron nitride monolayers vary in the range 1.4353 Å ÷ 1.4864 Å, and the bond angles in the range 84.05° ÷ 152.26°. The band gap of the BN layers varies from 3.16 eV to 3.90 eV. Sublimation energies are in the range from 16.67 eV/(BN) to 17.61 eV/(BN).**

Keywords: **boron nitride, crystal structure, polymorphism, ab initio calculations, electronic properties**

UDC 538.911+538.915

Acknowledgments: The research was funded by RFBR and Chelyabinsk Region, project number 20-43-740015.

For citation: Dmitry S. Ryashentsev, Eugeny A. Belenkov. New polymorphic varieties of boron nitride with graphene-like structures. *RENSIT,* 2021, 13(3):349-354. DOI: 10.17725/rensit.2021.13.349.

Contents

1. INTRODUCTION

The structure of boron nitride crystals can be different and similar to the structure of graphite or diamond [1-3]. In addition, there are boron nitride analogs of carbon nanostructures - nanotubes and graphene layers [4,5]. Crystals of hexagonal boron nitride, like graphite crystals, consist of BN monolayers, the structure of which is similar to the structure of graphene layers [6, 7]. The relevance of studying monatomic layers of graphene and boron nitride is associated with the possibility of their use in electronics for the synthesis of heterostructures with variable properties. The electronic properties of graphene monolayers can change significantly for different structural types [8-10]. It is theoretically predicted that the existence of four main polymorphic varieties of graphene such as L_6, $L_{4\text{-}8}$, $L_{3\text{-}12}$ and $L_{4\text{-}6\text{-}12}$, in which all atoms are in the same structural positions, are possible [8]. Studies of BN polymorphs with a structure similar to the structure of these graphene polymorphs have shown the possibility of their stable existence, as well as a significant change in their electronic properties [11,12]. In addition to the main polymorphic varieties of graphene, there can

be many other structural types in which carbon atoms are located in two, three, four, or more different structural positions [9,10]. The range of changes in the properties of these polymorphic graphene varieties is much larger than for the four main ones - for example, there may be structural types of graphene, the conductive properties of which are semiconducting rather than metallic. Apparently, the existence of monolayers of boron nitride with a structure similar to the structure of minor graphene polymorphs is possible. Studies of the possibility of the existence of boron nitride analogs of these compounds have not yet been carried out. Therefore, in this work, we performed model studies of structural analogs of boron nitride, similar to graphene layers, consisting of carbon atoms in two different structural positions.

2. MATERIALS AND METHODS

The graphene layers $L_{4\text{-}6\text{-}8a}$, $L_{4\text{-}6\text{-}8b}$, $L_{4\text{-}10}$, and $L_{4\text{-}12}$ described in [10] were taken as the initial structures for modeling BN layers. In these layers, carbon atoms are in two different structural states. The construction of the primary structure of boron nitride layers was carried out by replacing carbon atoms with boron and nitrogen atoms, so that each atom of one type has neighboring atoms with which it forms covalent bonds were of a different type. As a result, the number of different structural positions in boron nitride layers doubles - there are four of them - two unique structural positions for boron and nitrogen atoms. Model calculations were performed using the Quantum ESPRESSO software package [13]. Geometrically optimized structures of BN layers were found by the density functional theory (DFT) method [14]. The structure of three-dimensional crystals was calculated, consisting of graphene layers packed in stacks, so that the distance between the layers was 10 Å. In this case, the distance between the layers and the interaction between them is negligible, and it can be assumed that the layers in such crystals are identical to isolated layers. In the calculations, we used the generalized gradient approximation (GGA) [15], a 12×12×12 k-point grid, a temperature of 0.01 K, and a cutoff energy in the plane wave basis of 70 Rydberg. The lengths of the vectors of elementary translations (*a, b*), the lengths of interatomic bonds (Å), and the angles between them (°) were calculated as parameters characterizing the structure of the layers. Interatomic bonds and angles were determined for each of two unique structural states. Since boron and nitrogen atoms were in different structural positions, the number of unique states where measurements were performed was four. As an integral parameter characterizing the deformation of the layer structure in comparison with the ideal structure of the hexagonal graphene layer, we calculated the deformation parameter (Def), which is equal to the sum of the moduli of the differences between the bond angles and the angle of 120°, characteristic of hexagonal graphene. In addition, for the structural states, the values of the Wells ring parameter (Rngi) were determined, which symbolically shows the number of units in the rings from the minimum number of interatomic covalent bonds passing through the atom in the corresponding structural state. Energy characteristics of BN layers (total bond energy E_{total}, sublimation energy E_{sub}) and their electronic properties (band structure, density of electronic states, Fermi energy E_F, band gap) by the DFT-GGA method.

3. RESULTS AND DISCUSSION

As a result of DFT-GGA model calculations, geometric optimization of the structure of the original BN layers was performed. The structure of one of the studied layers, BN-$L_{4\text{-}12}$, turned out to be unstable, and as a result of optimization it was transformed into the structure of the BN-$L_{4\text{-}6\text{-}8}$ layer. The new layer obtained as a result of geometric optimization consists of atoms in six structural positions, which exceeds the number of structural positions in other layers studied. Compounds with a minimum number of structural positions should have the highest stability. In this work, we considered only boron

nitride layers with four structural positions; therefore, the new BN-$L_{4\text{-}6\text{-}8}$ layer obtained by transforming the original BN-$L_{4\text{-}12}$ layer was not considered further. The remaining three layers: BN-$L_{4\text{-}6\text{-}8a}$, BN-$L_{4\text{-}6\text{-}8b}$ and BN-$L_{4\text{-}10}$ - have a stable structure, and their images are shown in **Fig. 1**. In this figure, the unit cells of the layers are highlighted. The BN-$L_{4\text{-}6\text{-}8a}$ and BN-$L_{4\text{-}6\text{-}8b}$ layers have rectangular unit cells containing 12 and 16 atoms, respectively (**Table 1**). The lengths of the vectors of elementary translations are a = 7.67 Å, b = 4.56 Å and a = 10.19 Å, b = 4.49 Å for the boron nitride layers BN-$L_{4\text{-}6\text{-}8a}$ and BN-$L_{4\text{-}6\text{-}8b}$, respectively. The word density of new polymorphic varieties varies from a minimum value of 0.6339 g/cm^2 for the BN-$L_{4\text{-}10}$ layer to a maximum value of 0.7204 g/cm^2 for the BN-$L_{4\text{-}6\text{-}8b}$ layer (Table 1).

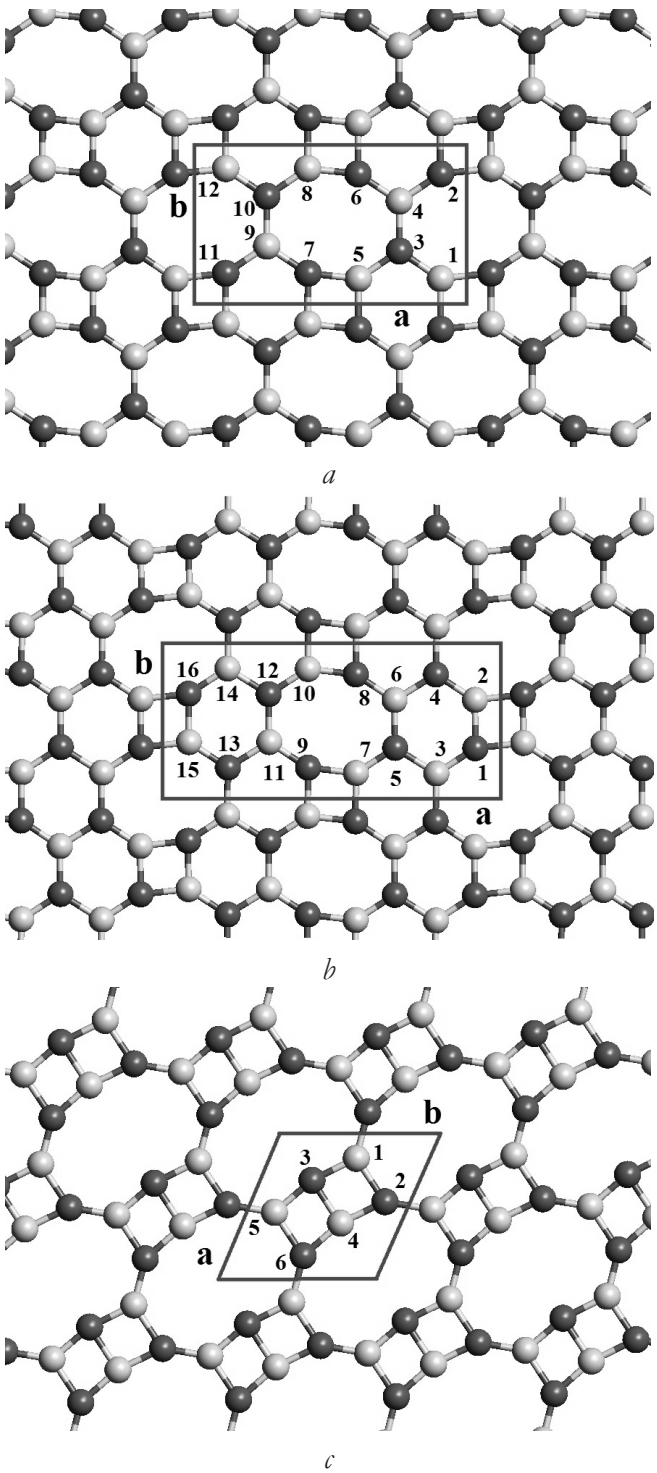

a

b

c

Fig. 1. *Layer structure and unit cells of polymorphic species of boron nitride geometrically optimized as a result of DFT-GGA calculations: (a) BN-$L_{4\text{-}6\text{-}8a}$; (b) BN-$L_{4\text{-}6\text{-}8b}$; (c) BN-$L_{4\text{-}10}$.*

Table 1

Properties and structural parameters of polymorphic varieties of boron nitride

Layer	BN-$L_{4\text{-}6\text{-}8a}$	BN-$L_{4\text{-}6\text{-}8b}$	BN-$L_{4\text{-}10}$
a, Å	7.6686	10.1945	4.6395
b, Å	4.5600	4.4891	10.000
c, Å	10.000	10.000	4.6375
β, °			115.12
Rng_I	416181	416181	41102
Rng_{II}	6182	6281	42101
N, atom	12	16	6
ρ, g/cm^2	0.7071	0.7204	0.6339
E_{total},eV(e.n.)	-21.1647	-2823.23	-1055.88
E_{total},eV(*BN*)	-352.75	-352.90	-351.96
E_{subl},eV(*BN*)	17.45	17.61	16.67
Δ, eV	3.156	3.896	3.166
E_F, eV	-3.9967	-3.9399	-4.0960

The crystal lattice of the BN-$L_{4\text{-}10}$ layer belongs to the oblique Bravais lattices. The elementary translation vectors of the unit cell of this layer are 4.64 Å, the angle between the vectors is 115.12°, and the number of atoms in the unit cell is 6. Atomic positions in the BN layers are characterized by Wells ring parameters (Rng). The BN-$L_{4\text{-}6\text{-}8a}$ layer is characterized by two different values of the parameter Rng 416181 and 6182, in the BN-$L_{4\text{-}6\text{-}8b}$ layer Rng of the first atomic position 416181 and the second - 6281, and in the BN-$L_{4\text{-}10}$ layer the values of the ring parameter 41102 and 42101 for each of two different atomic positions. The ratio of the number of atomic positions of the first and second types in boron nitride monolayers is 2:1, 1:1, and 2:1 for the BN-$L_{4\text{-}6\text{-}8a}$, BN-$L_{4\text{-}6\text{-}8b}$, and BN-$L_{4\text{-}10}$ layers, respectively. Polygons 4, 6, 8, 10,

Table2
Coordinates of atoms in unit cells of layered polymorphic varieties of boron nitride

Number	Atom	X,Å	Y,Å	Number	Atom	X,Å	Y,Å
BN-$L_{4\text{-}6\text{-}8a}$							
1	B	0.7309	0.6651	7	N	4.5591	0.8222
2	N	0.7258	3.7388	8	B	4.5654	3.8959
3	N	1.9373	1.4759	9	B	5.7508	1.6222
4	B	1.9176	2.9384	10	N	5.7511	3.0847
5	B	3.1029	0.6647	11	N	6.9425	0.8218
6	N	3.1093	3.7384	12	B	6.9375	3.8955
BN-$L_{4\text{-}6\text{-}8b}$							
1	N	0.6209	1.2308	9	N	5.7185	0.6244
2	B	0.6363	2.7063	10	B	5.7334	3.6384
3	B	1.8071	0.4549	11	B	6.9045	1.4010
4	N	1.8279	3.4794	12	N	6.9253	2.8660
5	N	3.0645	1.2345	13	N	8.1619	0.6210
6	B	3.0853	2.6995	14	B	8.1827	3.6455
7	B	4.2565	0.4621	15	B	9.3535	1.3941
8	N	4.2713	3.4762	16	N	9.3689	2.8696
BN-$L_{4\text{-}10}$							
1	B	-0.2439	2.3033	4	B	1.6886	2.6589
2	N	0.5760	3.5972	5	B	2.1897	0.7599
3	N	8.7808	1.3819	6	N	3.0119	2.0523

of which the layers are formally not ideal and significantly deformed (Fig. 1). This is due to the nonequivalence of the atomic positions in which the boron and nitrogen atoms are located. The coordinates of atoms in the unit cells of boron nitride polymorphs are shown in **Table 2**.

As parameters characterizing the structure of the layers, the lengths of interatomic distances in the boron nitride layers and the angles between the bonds were also determined, the values of which are given in **Table 3.** The structure of boron nitride BN-$L_{4\text{-}10}$ is characterized by the lengths of three types of bonds for each atomic position and varies in range from 1.4059 Å to 1.5318 Å, and the angles between bonds vary in the range from 82.22° to 165.98°. The maximum and minimum bond lengths are observed for the BN-$L_{4\text{-}10}$ monolayer, which indicates strong deformations of the structure of this layer. To assess the degree of deformation of the layer structure, the values of the deformation parameters were calculated, which were found as the sum of the moduli of the differences in

Table 3
Lengths of interatomic bonds and the angles between them in boron nitride layers

Atom	Layer	BN-$L_{4\text{-}6\text{-}8a}$	BN-$L_{4\text{-}6\text{-}8b}$	BN-$L_{4\text{-}10}$
N	L_1(I), Å	1.4863	1.4752	1.5125
	L_2(I), Å	1.4353	1.4711	1.4519
	L_3(I), Å	1.4647	1.4176	1.4516
	L_1(II), Å	1.4626	1.4652	1.5318
	L_2(II), Å	1.4370	1.4203	1.4059
	L_3(II), Å	1.4366	1.4795	1.4554
B	L_1(I), Å	1.4864	1.4752	1.5125
	L_2(I), Å	1.4370	1.4203	1.4554
	L_3(I), Å	1.4653	1.4711	1.4557
	L_1(II), Å	1.4626	1.4652	1.5318
	L_2(II), Å	1.4353	1.4176	1.4063
	L_3(II), Å	1.4356	1.4796	1.4519
N	φ_1(I), °	84.05	122.64	83.012
	φ_2(I), °	123.69	84.24	82.97
	φ_3(I), °	152.26	153.11	168.98
	Def_N(I), °	71.89	71.51	120.00
	φ_1(II), °	124.36	122.61	132.73
	φ_2(II), °	124.37	122.13	82.22
	φ_3(II), °	111.27	115.26	145.04
	Def_N(II), °	17.46	9.48	75.56
B	φ_1(I), °	95/93	123.57	97.74
	φ_2(I), °	124.62	95.77	97.78
	φ_3(I), °	139.45	140.66	164.48
	Def_B(I), °	48.14	48.45	88.96
	φ_1(II), °	123.88	120.98	132.65
	φ_1(II), °	123.87	124.01	97.03
	φ_1(II), °	112.24	115.01	130.33
	Def_B(II), °	15.52	9.98	45.94
	Def, °	38.25	34.86	82.62

the angles between bonds and the equilibrium value of the angle of 120° in an ideal hexagonal structure. The range of variation of the deformation parameters (Def(I) and Def(II)) of various atomic positions is from 45.94° to 120.00°. The maximum average value of the deformation parameters (Def) equal to 82.62° is observed for the BN-$L_{4\text{-}10}$ layer, for the remaining layers the deformation is more than two times less (Table 3). This indicates that layers BN-$L_{4\text{-}6\text{-}8a}$ and BN-$L_{4\text{-}6\text{-}8b}$ have a less deformed structure and should be more stable compared to layer BN-$L_{4\text{-}10}$. This is confirmed by the fact that the calculated value of the sublimation energy E_{sub} for the BN-$L_{4\text{-}10}$ layer is minimal and amounts

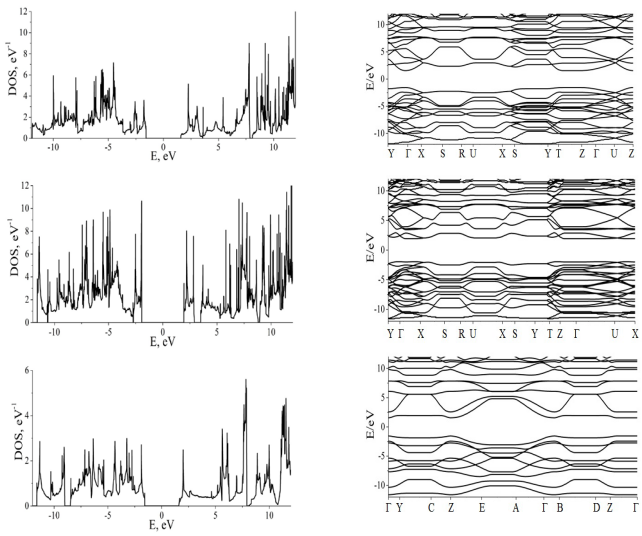

a *b*

Fig. 2. *Density of electronic states (a) and band structure (b) of new layered BN polymorphs.*

to 16.67 eV/(BN), i.e. about 5 percent less than the sublimation energy of other layers (Table 1).

The results of DFT-GGA calculations of the electronic structure of new polymorphic varieties of boron nitride are shown in **Fig. 2**. A band gap is observed in the images of the band structure of BN layers and graphs of changes in the density of electronic states at the Fermi energy (E_F) level, whose width varies from 3.156 eV for the BN-$L_{4\text{-}6\text{-}8a}$ layer, to 3.896 eV for the BN-$L_{4\text{-}6\text{-}8b}$ layer. This indicates that the conducting properties of boron nitride layers must be semiconducting and the band gap in them can vary depending on the features of the structure.

4. CONCLUSION

As a result of theoretical studies of the structure and properties of new polymorphic varieties of boron nitride monolayers, the possibility of stable existence of three layers - BN-$L_{4\text{-}6\text{-}8a}$, BN-$L_{4\text{-}6\text{-}8b}$ and BN-$L_{4\text{-}10}$ - was established. The structure of the BN-$L4_{\text{-}12}$ layer turned out to be unstable during geometric optimization. Of the three layers with a stable structure, the maximum sublimation energy (17.61 eV) and the minimum value of the deformation parameter (34.86°) are observed for the BN-$L_{4\text{-}6\text{-}8b}$ layer, which, apparently, should have the highest stability, and it is precisely this layer that should be attempted to be synthesized experimentally. Firstly new polymorphs of boron nitride with a layered structure can find practical application in nanoelectronics [16].

REFERENCES

1. Perevislov SN. Structure, properties and fields of application of graphite-like hexagonal boron nitride. *Research and Development,* 2019, 6:35-40 (in Russ.).
2. Zhou Ch, Lai C, Zhang Ch, Zeng G, Huang D, Cheng M, Hu L, Xiong W, Chen M, Wang J, Yang Y, Jiang L. Semiconductor/boron nitride composites: Synthesis, properties, and photocatalysis applications. *Applied Catalysis B: Environmental,* 2018, 238:6-18.
3. Rodríguez-Hernández P, González-Diaz M, Muñoz A. Electronic and structural properties of cubic BN and BP. *Physical Review B.*, 1995, 51(20):14705-14708.
4. Kim JH, Pham TV, Hwang JH, Kim CS, Kim MJ. Boron nitride nanotubes: synthesis and applications. *Nano Convergence*, 2018, 5(17):1-13.
5. Duo P, Fengmei S, Hu L, Yong M, Rajib D, Qian H, Chuntai L, Zhanhu G. The Properties and Preparation Methods of Different Boron Nitride Nanostructures and Applications of Related Nanocomposites. *The Chemical Record,* 2020, 20(11):1-25.
6. Zhang Y, Yun J, Wang K, Chen X, Yang Z, Zhang Z, Yan J, Zhao W. First-principle study of graphyne-like BN sheet: Electronic structure and optical properties. *Computational Materials Science,* 2017, 136:12-19.
7. Li X-D, Cheng X-L. Predicting the structural and electronic properties of two-dimensional single layer boron nitride sheets. *Chemical Physics Letters,* 2018, 694:102-106.
8. Belenkov EA, Kochengin AE. Structure and electronic properties of crystals consisting of graphene layers L_6, $L_{4–8}$, $L_{3–12}$, and $L_{4–6–12}$. *Physics of the Solid State*, 2015, 57(10):2126-2133.

9. Belenkov ME, Chernov VM, Belenkov EA, Morilova VM. Structure and electronic properties of 5-7 graphene. *IOP Conference Series: Materials Science and Engineering*, 2018, 447:012005.
10. Belenkov ME, Kochengin AE, Chernov VM, Belenkov EA. Graphene polymorphs. *Journal of Physics: Conference Series*, 2019, 1399:022024.
11. Ryashnetsev DS, Belenkov EA. New BN polymorphs with two-dimensional structure. *IOP Conference Series: Materials Science and Engineering,* 2019, 537:022060.
12. Ryashnetsev DS, Belenkov EA. Structure and electronic properties of 4-8 and 4-6-12 layered varieties of boron nitride. *Journal of Physics: Conference Series,* 2019, 1410:012016.
13. Koch WA, Holthausen MC. *Chemist's Guide to Density Functional Theory*. Weinheim, Wiley-VCH, 2002, 313 p.
14. Gisnnozzi P, Baroni S, Bonini N, Calandra M, Car R, Cavazzoni C, Ceresoli D, Chiarotti GL, Cococcioni M, Dabo I, Corso AD, Gironcoli S, Fabris S, Fratesi G, Gebauer R, Gerstmann U, Gougoussis C, Kokalj A, Lazzeri M, Martin-Samos L, Marzari N, Mauri F, Mazzarello R, Paolini S, Pasquarello A, Paulatto L, Sbraccia C, Scandolo S, Sclauzero G, Seitsonen AP, Smogunov A, Umari P, Wentzcovitch RMM. Quantum Espresso: a modular and open-source software project for quantum simulations of materials. *Journal of Physics: Condensed Matter,* 2009, 21:395502.
15. Langreth DC, Mehl MJ. Beyond the local-density approximation in calculations of ground-state electronic properties. *Physical Review B.*, 1983, 28(4):1809.
16. Katoch J, Ulstrup S, Koch RJ, Moser S, McCreary KM, Singh S, Xu J, Jonker BT, Kawakami RK, Bostwick A, Rotenberg E, Jozwiak C. Giant spin-splitting and gap renormalization driven by trions in single-layer WS2/h-BN heterostructures. *Nature Physics*, 2018, 14(4):355-359.

DOI: 10.17725/rensit.2021.13.355

Tracks on films and multi-charged clusters

Anatoly I. Nikitin, Vadim A. Nikitin, Alexander M. Velichko, Tamara F. Nikitina

V.L. Talrose Institute for Energy Problems of Chemical Physics at N.N. Semenov Federal Research Center for Chemical Physics, Russian Academy of Sciences, https ://www.chph.ras.ru/
Moscow 119334, Russian Federation

E-mail: anikitin@chph.ras.ru, vadim333@mail.ru, avelichko@chph.ras.ru, tnikitina1938@gmail.com

Received April 01, 2021, peer-reviewed April 12, 2021, accepted April 19, 2021

Abstract: **When conducting experiments on the electric explosion of titanium foil in water, a "strange" radiation was detected, leaving dotted traces on the film. The velocity of the carriers of this radiation was estimated as 20–40 m/s, and their energy, estimated by the Coulomb drag mechanism, turned out to be equal to 700 MeV. Subsequently, it was found that similar traces are formed at various types of high-current arc discharges, both of artificial and natural origin. Many solutions have been proposed to explain the nature of "strange" radiation, but none of them describes the details of the process of formation of dotted traces. We believe that these traces on the film could appear due to the action of charged micron-sized clusters. The possibility of the existence of clusters in the form of a nucleus from a certain number of similarly charged ions enclosed in a spherical shell of water molecules is shown. The force of the Coulomb repulsion of ions is compensated by the compression force of the shell polarized by the inhomogeneous electric field created by the nuclear charge. As the cluster approaches the surface of the film, a cluster with a small charge separates from it. It is accelerated in the electric field of a "large" cluster to energy of about 1 GeV. Having received a recoil momentum, a large cluster moves away from the film, braking in an inhomogeneous electric field, and then "falls" onto it again, and the process is repeated.**

Keywords: **"strange" particles, traces on films, multi-charged clusters, interaction with dielectrics, computer modeling**

PACS: 36.40.Wa; 52.80.Mg

Acknowledgements: This work was developed within the framework of the Program for Basic Research of the Russian State Academy of Sciences for 2013-2020 and supported by the Ministry of Sciences and Higher Education (agreement GZ No.007-00269-18-00).

For citation: Anatoly I. Nikitin, Vadim A. Nikitin, Alexander M. Velichko, Tamara F. Nikitina. Tracks on films and multi-charged clusters. *RENSIT*, 2021, 13(3):355-368. DOI: 10/17725/rensit.2021.13.355.

Contents

1. INTRODUCTION

In 2000, a group of researchers [1,2] discovered the particles with a "strange" radiation that appear at electric explosion of titanium foil in distilled water. Particles flew out of the luminous "cloud" arising above the plastic cover of the sealed explosive chamber when a voltage of 4.5 kV from a capacitor with an energy reserve of 50 kJ was applied to the titanium foil contained in it. The velocity of these

"strange" particles was estimated as 20-40 m/s. "RF-ZMP" fluorographic film with a 10 μm thick emulsion and a sensitivity of 1100 R^{-1} at a level 0.85 above the haze served as a detector of "strange" radiation. The film was wrapped in two layers of black paper. Exposed films were processed in the developer D-19 at a temperature of 20°C for 6 minutes. After manifestation on the films, traces were found with a length of 0.1 mm to 3 mm of various shapes – continuous and intermittent. The width of the trace was about 20 μm, and the "step" of the dotted trace was about 12 μm. The carrier energy of the "strange" radiation, estimated from the blackening area under the assumption of the Coulomb drag mechanism, turned out to be about 700 MeV. Traces ("tracks") were located inside the emulsion layer, this led to the conclusion that the source that caused the blackening of the film flew in a plane parallel to the plane of the emulsion.

Traces similar to tracks in the experiments of Urutskoyev et al. [1,2] were repeatedly observed by other researchers. Matsumoto [3,4] saw them at electric discharges in water, and Ken Shoulders [5] saw them during discharges along the surface of metals and insulators. Savvatimova reported the detection of tracks on *X*-ray films placed inside a chamber with a glow discharge in an atmosphere of hydrogen or deuterium [6-8]. Many traces from a millimeter to one tenth of a millimeter thick were recorded - straight and winding, consisting of black dots. Tracks appeared not only on films inside a discharge chamber made of 5 mm thick stainless steel sheet, but also on films outside the chamber. It has been found that intermittent traces appear not only on photographic films, but also on any objects with a smooth surface – on polycarbonate disks or mica plates [9,10]. In this case, traces of surface destruction look as if they were scratched by a solid object, which periodically fell and raked part of the material. It suddenly turned out that the appearance of "strange" particles is an ordinary phenomenon that accompanies the formation of plasma in a medium [11-28]. Moreover, it turned out that these particles (the properties of which are not yet known to us) can present a danger to human health [29-31].

In [32], the "strange" particles that appear during tests of industrial high-voltage equipment accompanied by the formation of an open electric arc are described. Test parameters with currents and voltages (I = 30 kA, U = 5 kV) close to those of the experiments of Urutskoyev et al. [1,2] were chosen. A short circuit of the elements of high-voltage installations was initiated by installing a jumper – a copper wire with a diameter less than 0.5 mm. The explosion safety of surge arresters, consisting of series-connected metal oxide varistors located inside the housing from the insulator, was tested. In this case, the wire passed along the surface of the insulator. To detect "strange" radiation, as in [1,2], the authors used an RF-ZMP *X*-ray film with an emulsion layer thickness of 10 μm. The film was placed in a plastic bag and wrapped in two layers of black paper. The detectors were installed at a distance 1.8 - 3.8 m from the site of the electric explosion. In the experiments, more than 500 tracks were recorded, similar to those obtained in [1,2]. Traces were located in the emulsion layer, their transverse dimensions were from 5 to 30 microns, and their length was from 100 microns to several millimeters. The farther the detector was from the test site, the narrower the track width. At currents I = 1-2 kA, no traces were observed. **Fig. 1***a* shows a view of a direct trace. If we take into account the remark of Agapov et al. [32] on the decrease in the thickness of the wake when the detector is removed from the location of the arc discharge, we can assume that the particle that left the wake moved from left

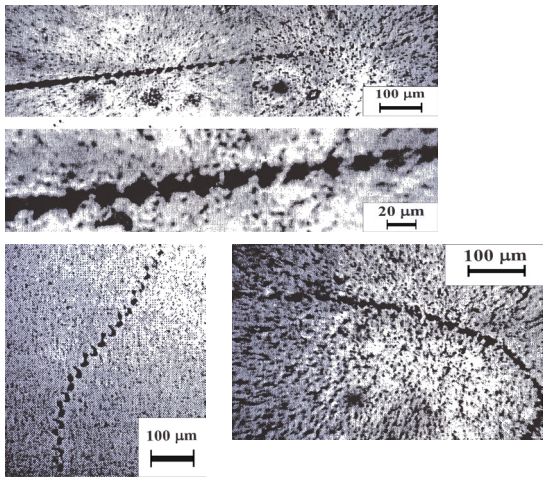

Fig. 1. *Traces of "strange" particles on photographic films* [32].

to right. Figs. 1*b,c* show curved tracks consisting of elements of complex shape (arcs, "birds", etc.). The authors found that the number of recorded traces increased with increasing volume and energy of the open arc, and no traces were found when testing the vacuum circuit breakers. This allowed them to conclude that "tracks appear only during electric discharges in the medium".

After realizing the reality of the existence of unusual particles with "strange" properties, attempts were made to explain their nature. Takaaki Matsumoto [3,4], who discovered negatively charged particles emanating from the cathode, suggested that they are "extremely compressed hydrogen-clusters" formed due to the pinch effect. Such clusters are in a certain connected "itonic state". Savvatimova also notes that particles emitted from the cathode of the discharge chamber have a negative charge [6-8]. Ken Shoulders [5], who devoted much time to researching microscopic particles that can make holes in metal foils (called EVO = Exotic Vacuum Objects), considers them "highly organized micro-sized clusters, having soliton behavior with electron populations on the order of Avogadro number". He thinks that "as long as the spacing between electrons is as close as one atomic diameter, they join each other. That is what happens when an abrupt, high field process, like a gas discharge ... forcible ejects electrons from a conductor at sufficient high current density. Having once achieved this uncommon union for our portion of space the electrons stick together until the marriage is violated by a sufficient quantity of conductor where they are forced to return to their more common state as a part of atom". The ideas of Matsumoto and Schoulders, apparently, suggest the presence of a process of plasma compression by a magnetic current field. However, it is known that this process is possible only at high currents (I > 200-500 kA) [33]. How such currents can occur in low-current discharges in the described experiments is not clear. Urutskoev et al. [1,2,34] believe that "strange" particles are magnetic monopoles. The idea of magnetic monopoles is supported also by Daviau et al. [35], Adamenko and Vysotsky [36] and Shakhparonov and Chicherin [37]. According to the theory of Lochak [38], a magnetic monopole is treated as a magnetically excited state of a neutrino. Skvortsov and Vogel [22] suggest that when aluminum was irradiated with neodymium laser pulses (λ = 1.064 μm, τ_p = 100 ps, E = 100 mJ), they observed the formation of "plasma drops" with a diameter of 10-20 μm containing 1-5 elementary magnetic dipoles. Lutz Jaitner [39] believes that the observed "condensed plasmoids" are threadlike structures with a diameter of $40 \cdot 10^{-12}$ m. The electrons in these structures are decoupled from the nuclei and move around them at a speed of $(0.3\text{-}2.4) \cdot 10^8$ m/s. Their movement creates a current 9 kA with a density $2.5 \cdot 10^{24}$ A/m^2. The magnetic field of this current reaches a value of 50 MT and creates a pressure more than 10^{21} Pa. Other models of the device of "strange" particles are also proposed. Fredericks [40] identifies them with tachyons (particles capable to move at a speed greater than the speed of light in a vacuum). Bazhutov [41] considers them to be stable heavy mesons with an energy of 200 GeV ("erzions"), and Rodionov and Savvatimova [12] – "fluxes" (cylindrical atoms with a nucleus in the form of a quark-gluon filament and a shell with a diameter of $60 \cdot 10^{-15}$ m from electron Bose fluid). It has been also suggested that "strange" radiation consists of dark matter particles, giant molecules from nuclei, exotic "neutronium" atoms (neutron-neutrino pairs) [11,42]. According to Shishkin and Tatur [31], magneto-toro-electric clusters in the form of string-vortex solitons produce effects on the film.

However, the authors of the proposed models do not even try to answer simple questions: 1) Why these particles fly strictly along the emulsion? 2) Why, moving at a speed of only 20 m/s, they are able to act on the emulsion as particles having energy of about 1 GeV? 3) What is the mechanism of their action on the emulsion? 4) Why does the appearance of the tracks look like prints on the ground of car tire treads? 5) Why does the spot area change along the track? 6) Why curved tracks are recorded along with direct tracks? The common thing that unites the authors of the models is that almost all of them emphasize the analogy of the behavior of objects with the behavior of ball

lightning and even call them "microscopic ball lightning".

Indeed, there is such an analogy. Natural ball lightnings have an energy reserve, an uncompensated electric charge and are able to move along the surface of conductors and dielectrics [43-48]. In 1998, we proposed a model of ball lightning in the form of a unipolarly charged core surrounded by a dielectric shell [49-60]. Owing to the electric field of the core, polarization of the shell material occurs and a force $F_a \sim Q$ arises, pulling the shell toward the center. The magnitude of this force is proportional to the first degree of the core charge Q. The force of stretching of the shell by charge carriers is proportional to the square of Q, $F_r \sim Q^2$. In the range of charge values from $Q = 0$ to Q_{max}, the force F_a is greater than F_r. Ball lightning continuously loses charge. As ball lightning approaches the conductor, this charge flows in the direction of this conductor. A mechanical impulse acquired by carriers of a falling charge when moving in the field of the main charge is transmitted to ball lightning. This allows it to "push off" from the conductor and move at a certain distance from it [60-62].

2. FORCES ACTING IN CHARGED CLUSTERS

Based on the analogy noted above, we can assume that "strange" particles are multiply charged clusters similar to microscopic ball lightning: a certain number of ions inside a shell formed from water molecules. In the electric field of the charge inside the shell, the dipole water molecules are oriented towards the center of the sphere, and a force arises that compresses the shell. At the same time, the molecules in the shell tend to push out their "neighbors", which leads to a decrease in the shell compression force. The calculation showed that the force F_r of pushing out water molecule from the shell of such a cluster is described by the formula [63,64]

$$F_r = 2.69 \cdot 10^9 (R - R_0)^{-1.3} \text{(H)}, \quad (1)$$

where R (inner radius of the sphere) is in angstroms (10^{-10} m), and $R_0 = -4.5$. Let us compare the force F_r with the force F_a of the attraction of the dipole with a moment $p_w = 6.327 \cdot 10^{-30}$ C·m to the central charge $q = 1.6 \cdot 10^{-19}$ C. $F_a = p_w \cdot \text{grad}\, E$, where E is the electric field created by the charge q:

$$F_a = p_w grad(q / 4\pi\varepsilon_0 R^2) = -2 p_w q / 4\pi\varepsilon_0 R^3. \quad (2)$$

The force F_a is directed toward the center of the cluster and decreases more steeply with increasing R than $F_r(R)$. At $R = 4 \cdot 10^{-10}$ m, $F_a = 2.84 \cdot 10^{-10}$ N, which is 1.65 times greater than F_r, but already at $R = 6 \cdot 10^{-10}$ m, $F_a = 0.843 \cdot 10^{-10}$ N, which less than the value of F_r ($1.27 \cdot 10^{-10}$ N).

Another reason that prevents the formation of an ordered cluster structure due to the action of the electric field of the ion is the thermal motion of the molecules of the surrounding gas. According to the Langevin formula [65], the noticeable action of the electric field on the dipole orientation with moment p_w ceases at a strength $E_{min} = 3\, k_B T / p_w$. (Here $k_B = 1.38 \cdot 10^{-23}$ J/K is the Boltzmann constant, and T is the absolute temperature). At $p_w = 6.327 \cdot 10^{-30}$ C·m and $T = 300$ K, the value of $E_{min} \approx 2 \cdot 10^9$ V/m. The electric field of the ion takes such a value at a distance of $R = 8 \cdot 10^{-10}$ m, that is, at the location of the second layer of water molecules in the cluster. Thus, we conclude that a cluster with $R = 4 \cdot 10^{-10}$ m can be formed in the electric field of an elementary charge, however, further cluster growth, apparently, occurs without significant participation of the electric field of the central charge.

Let us discuss whether it is possible to retain a large number of ions inside the shell of an aqueous cluster. The hope that this possibility can be realized is given by the fact that the force F_a of attraction of a water molecule to the charge can be increased due to an increase in the total charge of ions Q, but the force F_r does not depend on the charge (however, its value must be greater than a certain critical value determined by the condition for the need for polarization of molecules in the shell). To accommodate a large number of ions, the size of the internal cavity of the cluster must be increased in comparison with the case of a singly charged cluster (the radius R must be increased). This should simultaneously reduce the value of the force F_r.

Let us consider what a cluster can be with a total charge of ions $Q_1 = 4.5 \cdot 10^{-12}$ C. Such a

charge, for example, is possessed by $n = 2.8 \cdot 10^7$ hydroxyl ions $(OH)^-$. Let the ion diameter be $4 \cdot 10^{-10}$ m, the area occupied by one ion, $s = 16 \cdot 10^{-20}$ m^2, and the ions are placed on the surface of a sphere of radius R. The surface area of the sphere is $S = 4\pi R^2 = s \cdot n$, hence $R = (s \cdot n/4\pi)^{1/2} = 6 \cdot 10^{-7}$ m. The electric field created by the charge $Q = 4.5 \cdot 10^{-12}$ C at a distance $R = 6 \cdot 10^{-7}$ m, $E = Q/4\pi\varepsilon_0 R^2 = 10^{11}$ V/m, which is greater than $E_{min} = 2 \cdot 10^9$ V/m, determined by the Langevin criterion. This means that the water molecules in the shell are completely polarized. Ions stretch the shell with the force $F_Q = Q^2/8\pi\varepsilon_0 R^2 = 2.53 \cdot 10^{-1}$ N. The water molecule is attracted to the charge placed in the center of the sphere with the force $F_a = p_w Q/2\pi\varepsilon_0 R^3 = 2.37 \cdot 10^{-12}$ N. At the same time, it is pushed out from the shell by neighboring molecules with a force $F_r = 2.69 \cdot 10^{-9} \cdot (6004.5)^{-1.3} = 3.3 \cdot 10^{-14}$ N. The resulting force acting on the molecule, $F_t = F_a - F_r = 2.337 \cdot 10^{-12}$ N. On the surface of the shell with a radius $R = 6 \cdot 10^{-7}$ m, $n_w = 2.82 \cdot 10^7$ water molecules can fit (we consider the molecule to be a ball with a diameter $4 \cdot 10^{-10}$ m). The compression force of the shell with one layer of water molecules is $F_\Sigma = F_t \cdot n_w = 6.59 \cdot 10^{-5}$ N. This force is 3840 times less than the force F_Q. The F_Q force can be compensated if the number of layers of water molecules in the shell is equal to 3840, and its thickness is $a = 4 \cdot 10^{-10} \times 3840 = 1.54 \cdot 10^{-6}$ m. As a result, we obtained a cluster with a cavity radius $R = 6 \cdot 10^{-7}$ m and an outer radius of $R_1 = R + a = 2.14 \cdot 10^{-6}$ m. The mass of the cluster M_1 is equal to the mass of the shell. Its volume is $V_{sh} = 4\pi\,[(R + a)^3 - R^3]/3 = 4 \cdot 10^{-17}$ m^3, and the mass $M_{sh} = \varrho_w V_{sh} = 4 \cdot 10^{-14}$ kg. (Here $\varrho_w = 10^3$ kg/m^3 is the density of water). Carrying out similar calculations for a cluster with a cavity radius $R = 6 \cdot 10^{-6}$ m, inside which there are ions with a total charge of $Q_2 = 4.5 \cdot 10^{-11}$ C, we find its radius $R_2 = 3.75 \cdot 10^{-6}$ m and mass $M_2 = 8.62 \cdot 10^{-13}$ kg.

3. TESTING THE STABILITY OF A MULTIPLY CHARGED CLUSTER

The question of the stability conditions for ball lightning was considered in [66]. A multiply charged cluster can be thought of as a small ball lightning. When carrying out calculations, we will take into account the fact that ions can move inside the shell, thereby creating additional pressure, and the shell, in addition to the "gradient" force, is additionally compressed by the force of atmospheric pressure. Let us assume that the ions are inside a spherical shell with an inner radius R and have a kinetic energy E_k. We find the density of this energy by dividing E_k by the volume of the cavity inside the shell: $\varrho_E = 3E_k/4\pi R^3$. The energy density is related to the pressure P of the ion "gas" on the shell as $P = (2/3)\,\varrho_E = E_k/2\pi R^3$ [67]. The force of pressure of moving ions on the shell is $F_k = P \cdot 4\pi R^2 = 2E_k/R$. Stretching force of the shell by the total charge Q of ions is

$$F_{el} = \frac{kQ^2}{8\pi\varepsilon_0 R^2}, \tag{3}$$

where it is taken into account that not only the force of the Coulomb repulsion of charges, but also the magnetic forces that appeared due to the movement of charges, participates in the creation of a force that stretches the shell [68]. Coefficient $k \approx 2$. Let the charge density of dipole water molecules on the shell be equal to σ, and the shell thickness a. In this case, the force of compression of the shell by the "gradient" force is equal to:

$$F_{sh} = \frac{4\sigma a Q}{\varepsilon_0 (2R + a)}. \tag{4}$$

In the above numerical examples, it is shown that even at values of the radius of the cluster cavity $R > 5$ μm, the force F_r of pushing out water molecules from the shell becomes so small that it can be neglected.

The second force compressing the shell is the force of atmospheric pressure p: $F_a = 4\pi p R^2$. The condition for the equilibrium of the shell is the balance of all forces acting on it:

$$F = F_k + F_{el} + F_{sh} + F_a = \\ = \frac{2E_k}{R} + \frac{kQ^2}{8\pi\varepsilon_0 R^2} - \frac{4\sigma a Q}{\varepsilon_0 (2R + a)} - 4\pi p R^2 = 0. \tag{5}$$

The equilibrium of the system will be stable if the derivative dF/dR (at $F = 0$) is negative, that is, as the shell radius R increases, the force stretching it, will decrease [69]. Differentiating F with respect to R, we obtain:

$$\frac{dF}{dR} = -\frac{2E_k}{R^2} + \frac{2}{R}\frac{dE_k}{dR} - \frac{2kQ^2}{8\pi\varepsilon_0 R^3} + \\ + \frac{8\sigma aQ}{\varepsilon_0(2R+a)^2} - \frac{8\sigma RQ}{\varepsilon_0(2R+a)^2}\frac{da}{dR} - 8\pi pR. \quad (6)$$

From the condition of constancy of the shell volume $V_{en} = (4\pi/3)\,[(R+a)^3 - R^3]$, $(dV_{en}/dR = 0)$ we find:

$$\frac{da}{dR} = -\frac{a(2R+a)}{(R+a)^2}. \quad (7)$$

According to formula (5), under equilibrium conditions $F = 0$ and

$$\frac{2E_k}{R^2} = \frac{4\sigma aQ}{\varepsilon_0(2R+a)R} + 4\pi pR - \frac{kQ^2}{8\pi\varepsilon_0 R^3}. \quad (8)$$

With an increase in the inner radius of the shell R by dR, the kinetic energy of the ions decreases by an amount equal to the work against the forces compressing the shell:

$$-dE_k = \left[\frac{4\sigma aQ}{\varepsilon_0(2R+a)} + 4\pi pR^2\right]dR. \quad (9)$$

Substituting (7) - (9) into (6), we obtain:

$$\frac{dF}{dR} = -\frac{kQ^2}{8\pi\varepsilon_0 R^3} - 20\pi\rho R - \frac{4\sigma Qa(9R^2a + 10Ra^2 + 3a^3)}{\varepsilon_0(2R+a)^2(R+a)^2R}. \quad (10)$$

As you can see, all the terms of this sum are negative, therefore $dF/dR < 0$. It follows that the system described by equation (5) is in a state of stable equilibrium for any values of k, Q, a, and R.

4. PROPERTIES OF THE CHARGED CLUSTER

The cluster is a nonequilibrium system, so its lifetime is limited. Due to the conductivity of the shell material, ions will "leak" through it and drain to the ground. The characteristic time of charge drainage can be considered equivalent to the cluster lifetime. Due to the action of cosmic rays, the radioactivity of the earth and ultraviolet radiation, $N_i = 3\cdot10^8$ ions of different signs are permanently located in one cubic meter of air [70]. In the electric field of the cluster, half of these ions will move towards it and precipitate on the outer surface of the shell. Finally, the number of ions on the outer side of the shell will become equal to the number of ions on its inner side, and the cluster will become an uncharged body. The characteristic time of the process of "deposition" of ions from the atmosphere can also be considered the equivalent of the cluster lifetime (though, if at the same time there is no recombination of charges, it cannot be considered completely destroyed). Let us estimate the characteristic times of the indicated processes.

Let the total charge of ions inside the cluster shell be equal to Q, ions "leak" through the shell and gradually flow to the ground. We assume that the current value is limited only by air conductivity $\lambda_a = 3.5\cdot10^{-14}$ (Ohm·m)$^{-1}$ [71]. The current density on the surface of a cluster of radius R is $j = E\lambda_a = Q\lambda_a/4\pi\varepsilon_0R^2$. The total current flowing into the atmosphere is $I = dQ/dt = j\cdot4\pi R^2 = Q\cdot\lambda_a/\varepsilon_0$. Hence, $dQ/Q = (\lambda_a/\varepsilon_0)dt$, $Q = Q_0\exp(-\lambda_a/\varepsilon_0)t$ and the time of decreasing the charge by e times $\tau = \varepsilon_0/\lambda_a = 250$ s. Let us consider the process of "collecting" by a cluster charges from the atmosphere. In an electric field E, ions move at a speed $v_{dr} = K_iE$, where K_i is the mobility of ions. For air, $K_i = 2.8\cdot10^{-4}$ m^2/V·s [72]. The electric field strength and, consequently, the ion drift velocity are different at different distances from the cluster. If for v_{dr} we take its value on the cluster surface, then this will correspond to the maximum rate of "deposition" of ions and, therefore, the minimum time of "discharge" of the cluster. The rate of charge decrease Q due to the ion flux to the cluster surface is $dQ/dt = -(N_i/2)\cdot ev_{dr}\cdot4\pi R^2 = -(N_i\,e\,K_i\,Q)/2\varepsilon_0$. Here $e = 1.6\cdot10^{-19}$ C is the ion charge, and it is also taken into account that only half of N_i ions of the same polarity participate in the process. From here we find $dQ/Q = -[(N_i\,e\,K_i)/2\varepsilon_0]dt$ and $Q = Q_0\exp[-(N_i\,e\,K_i)/2\varepsilon_0]t$. The characteristic time of charge decrease is $\tau_i = 2\varepsilon_0/(N_i\,e\,K_i) = 1300$ *s*. We draw attention to the fact that the characteristic times of destruction and discharge of a cluster do not depend on the magnitude of its charge, but are determined only by the characteristics of environment, into which the cluster is "immersed". Therefore, these expressions are also valid for macroscopic charged objects – ball lightnings [52,59].

In experiments on recording "traces" on photographic films, targets were located at a distance about 4 m from the region of the electric

discharge under study [1,2,32]. At a particle velocity 20 m/s, its flight time is 0.2 *s*, which is noticeably less than τ and τ_i. Therefore, we can assume that during this period the cluster had an initial charge.

For a cluster with a charge $Q = 4.5\cdot10^{-11}$ C and radius $R = 3.75\cdot10^{-6}$ m, the electric field strength on its surface is $E = 2.88\cdot10^{10}$ V/m and the potential is $U = 10^5$ V. The distance R_{br} from the center of the cluster, where the electric field of the charge Q exceeds the air breakdown strength $E_{br} = 3\cdot10^6$ V/m, $R_{br} = 3.67\cdot10^{-4}$ m. We can assume that an ion approaching the ion for a distance less than R_{br} will be able to ionize the air in the vicinity of the ion. The average value of the current created by the movement of ions, is $I = Q/\tau = (4.5 – 18)\cdot10^{-14}$ A. Given the potential $U = 10^5$ V on the cluster surface, we find the power released by ions in the vicinity of the cluster is $P = I\cdot U = (4.5 – 18)\cdot10^{-9}$ $W = (2.8 – 11)\cdot10^{10}$ eV/s. If we assume that it is necessary to spend 10^3 eV on the formation of one quantum of light, we can expect that a region of 1 mm around the cluster can be a source of radiation of 10^8 quanta per second. Similarly the ion flow passing through the cluster shell will also participate in the process of air ionization. The interaction of counter-flows of ions with different signs is likely to lead to the emergence of an unsteady process of light emission, similar to the pulsed regime of corona discharge optical radiation, discovered by Trichel [73]. The repetition rate of the "Trichel" pulses increases with increasing discharge current; at small currents, it is equal to f = 5-50 kHz. If a cluster flies with a speed v = 20 m/s, and the intensity of its glow changes with a frequency *f,* then the path will look like a dashed line, the bright points of which are located at a distance $d = v/f$ = 4 – 0.4 mm. Such traces, indeed, were observed in the paths of particles generated in erosion discharges [25].

5. THE PROCESS OF THE FORMATION OF TRACES ON FILMS

Let us consider a possible scenario for the formation of traces on photographic films. Suppose that a cluster with a radius $R_1 = 2.14\cdot10^{-6}$ m, with a charge $Q_1 = 4.5\cdot10^{-12}$ C and a mass M_1 = $4\cdot10^{-14}$ kg moves in the direction of the film. When the edge of the cluster is at a distance L = $15\cdot10^{-6}$ m from the film surface, a small cluster is separated from it with a charge $q_1 = 4.5\cdot10^{-14}$ C and a mass $m_1 = 4\cdot10^{-16}$ kg and begins to move to the film. This cluster moves under the action of the force $F_{q1} = Q_{1q1}/[4\pi\varepsilon_0(R_1 + x)]^2$, where x varies from 0 to L. Having passed the path L, the small cluster will gain energy $W_{q1} = (Q_{1q1}/4\pi\varepsilon_0)[1/R_1 – 1/(R_1 + L)] = 7.447\cdot10^{-10}$ J = $4.65\cdot10^9$ eV. Its speed is $v_1 = (2W_{q1}/m_1)^{1/2} = 1.929\cdot10^3$ m/s, and the linear moment is $m_1v_1 = 7.7184\cdot10^{-13}$ kg·m/s. The large cluster will acquire the same moment, it will begin to move upward from the film at a speed $V_1 = (m_1v_1)/M_1 = 19.296$ m/s and gain energy $W_{Q1} = M_1V_1^2/2 = 7.447\cdot10^{-12}$ J. Calculation for an ion with $R_2 = 7.5\cdot10^{-6}$ m, $Q_2 = 4.5\cdot10^{-11}$ C, M_2 = $8.62\cdot10^{-13}$ kg, from which at a height $L = 15\cdot10^{-6}$ m a small cluster with a charge $q_2 = 4.5\cdot10^{-13}$ C and mass $m_2 = 8.62\cdot10^{-15}$ kg is separated, leads to the results: $W_{q2} = 1.619\cdot10^{-8}$ J = $1.012\cdot10^{11}$ eV, $v_2 = 1.938\cdot10^3$ m/s, $V_2 = 19.379$ m/s, $W_{Q2} = 1.619\cdot10^{-10}$ J.

A cluster with a charge $Q_1 = 4.5\cdot10^{-12}$ C creates an electric field at a distance $L = 15\cdot10^{-6}$ m E_1 = $Q_1/4\pi\varepsilon_0L^2 = 1.8\cdot10^8$ V/m, and a cluster with a charge $Q_2 = 4.5\cdot10^{-11}$ C at the same distance creates a field $E_2 = 1.8\cdot10^9$ V/m. Such fields are comparable in magnitude with the intensity E_{min} = $2\cdot10^9$ V/m, determined by the Langevin criterion. Therefore, we can assume that there will be a polarization of the film material, and a force will act on the cluster, which will inhibit its movement. When the work of this force becomes equal to the kinetic energy of the cluster, it will stop and begin to "fall" onto the film. The force acting on the cluster from the side of the polarized film is $F_d = P_1Q_1/2\pi\varepsilon_0R^3$ (see formula 2), where P_1 is the dipole moment of the polarized film section, and R is the distance between the center of charge and the film. The work of this force on the portion of the trajectory dR is equal to $dA = Fd\cdot dR$, and the full work until the cluster stops

$$A = \int_{R_0}^{R} F_a dR = -\frac{P_1Q_1}{4\pi\varepsilon_0}\frac{1}{R^2} = \frac{P_1Q_1}{4\pi\varepsilon_0}\left[\frac{1}{R_0^2} - \frac{1}{(R_0+\Delta R)^2}\right]. \quad (11)$$

Here $R_0 = 10^{-4}$ m is the cluster height above the film surface at the moment of the beginning of the upward movement, and $R = (R_0 + \Delta R)$ is the height that it will reach. In this problem, the

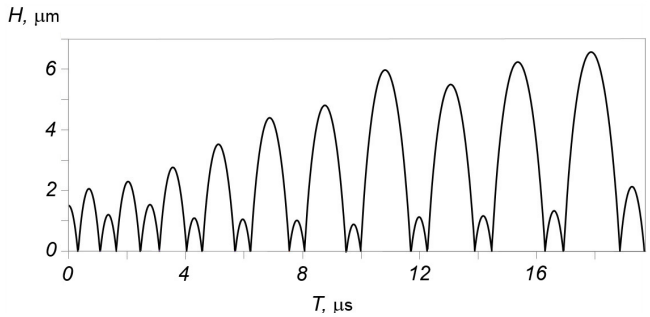

Fig. 2. *Dependence of the cluster elevation height above the level L = 15 μm of separation of a small charge from it. Cluster parameters: charge $Q_1 = 4.5 \cdot 10^{-12}$ C, mass $M_1 = 4 \cdot 10^{-14}$ kg, diameter $D_1 = 4.28 \cdot 10^{-6}$ m (Calculation results).*

unknown parameter is the dipole moment of the film P_1 induced by the charge Q_1. To evaluate it, suppose that the cluster was able to rise to a height $(R_0 + \Delta R) = 10.25 \cdot 10^{-4}$ m ($\Delta R = 25 \cdot 10^{-6}$ m) before falling. Equating the work A of the kinetic energy of the cluster $W_{Q1} = 7.447 \cdot 10^{-12}$ J, we find $P_1 = 5 \cdot 10^{-18}$ C·m. For a cluster with $Q_2 = 4.5 \cdot 10^{-11}$ C with kinetic energy $W_{Q2} = 1.62 \cdot 10^{-10}$ J, the value $\Delta R = 25 \cdot 10^{-6}$ m is obtained at $P_2 = 10^{-17}$ C·m. The specific polarization of the medium P (C·m/m^3) is related to the field strength E by the relation $P = \varepsilon_0(\varsigma - 1)E$ [65]. Assuming the dielectric constant $\varsigma = 2.6$ for the film material, we obtain $P = 1.6 \cdot \varepsilon_0 E$. This magnitude of the dipole moment of the film material is ensured by a "cube" of substance with an edge length of about 10 μm.

Fig. 2 shows the result of a numerical calculation of the change in cluster height above the level of separation of a small cluster from it $L = 15 \cdot 10^{-10}$ m. For the parameters of the cluster and the film, the values $Q_1 = 4.5 \cdot 10^{-12}$ C, $M_1 = 4 \cdot 10^{-14}$ kg, $D_1 = 4.28 \cdot 10^{-6}$ m are assumed. It is believed that for a separated small cluster, the charge $q_1 = Q_1/100 = 4.5 \cdot 10^{-14}$ C and the mass $m_1 = M_1/100 = 4 \cdot 10^{-16}$ kg are one a percentage of the initial values of the charge and mass of the main cluster, and these values remain unchanged despite the fact that Q_1 and M_1 decrease with each "jump". For the dipole moment of the polarized film, the value $P_1(t) = Q_1(t) \times 2 \cdot 10^{-8}$ C·m (the decrease in charge Q_1 is taken into account for each act of separation of a small cluster). It is accepted that at $t = 0$ the lower edge of the cluster is at a distance of $1.5 \cdot 10^{-6}$ m from the emission height of the small

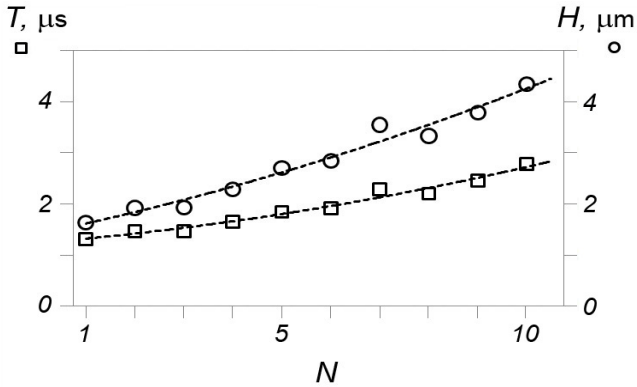

Fig. 3. *Dependence of the period of repetition of steps T (μs) (□) and height H (μm) (○) of the "jumps" of the cluster on the step number N for the cluster with the parameters indicated in Fig. 2 (Calculation results).*

cluster and its velocity is zero. You can notice that after five "jumps" the system switches to the alternating mode of short (0.5 μs long) and long (1.4 μs long) jumps with an average period of 1.86 μs. The height of the "jump" and the duration of the "flight" increases with time (see **Fig. 3**). This can be explained by a gradual decrease in the charge of a large cluster and the magnitude of the induced dipole moment of the film. The reason for the alternation of long (high) and short (low) "jumps" is as follows. When a cluster "falls" from a great height, it acquires a great speed. To stop the cluster and reverse the direction of its velocity vector, it is necessary to spend a significant part of the pulse acquired by it when a small cluster is emitted. As a result, the cluster begins to move up at a low speed and, accordingly, "falls" also at a low speed. The next impulse of interaction of

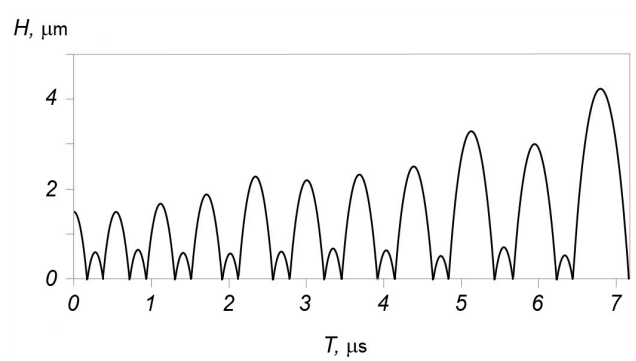

Fig. 4. *The time dependence of the cluster elevation height above the level L = 15 μm of separation of a small charge from it. Cluster parameters: charge $Q_2 = 4.5 \cdot 10^{-11}$ C, mass $M_2 = 8.62 \cdot 10^{-13}$ kg, diameter $D_2 = 15 \cdot 10^{-6}$ m. (Calculation results).*

charges of a large and small cluster "throws" it to a large height. If a charged cluster has a velocity component directed along the film plane, it will leave a chain of double spots on it, separated by large intervals. These spots can merge due to the spreading of the charge and form complex traces of the type shown in Fig. 1*a-c*. **Fig. 4** shows the motion diagram of a cluster with an initial charge of $Q_2 = 4.5 \cdot 10^{-11}$ C, mass $M_2 = 8.62 \cdot 10^{-13}$ kg and diameter $D_2 = 15 \cdot 10^{-6}$ m at the initial value of the film dipole moment $P_2 = Q_2 \times 2 \cdot 10^{-8}$ m, from which at a height $15 \cdot 10^{-6}$ m above the film a cluster is separated with a charge $q_2 = Q_2/100$ and a mass $m_2 = M_2/100$. As one can see, the nature of the cluster motion has not changed, the period of the "jumps" has decreased to 1.5 μs, and the height of the "jumps" has also become less (2 μm).

Fig. 1*b* shows the trace when the particle path deviated to the right. Let us make the assumption that this happened due to the action of the electric field E_x, whose vector was directed perpendicular to the trajectory of the cluster. Let the cluster charge be $Q_2 = 4.5 \cdot 10^{-11}$ C, and its diameter $D_2 = 7.5 \cdot 10^{-6}$ m. According to Fig. 1*b* for 8 "jumps" the cluster deviated from the direction of the initial trajectory by 158 μm. If we assume that the period of "jumps" is $1.5 \cdot 10^{-6}$ s, then the velocity of its lateral displacement is $v_1 = 13$ m/s. For a ball with a diameter of $7.5 \cdot 10^{-6}$ m, moving in air at a speed 13 m/s, the Reynolds number Re = 6.4. The strength of air resistance to the movement of the ball [74]:

$$F_D = (\pi C_D \rho_m D_1^2 v_1^2)/8, \quad (12)$$

where $\varrho_m = 1.205$ kg/m^3 is the air density, and $C_D = 5.8$ is the coefficient of resistance of the medium at Re = 6.4 [74]. Substituting the numerical values into formula (12), we obtain $F_D = 2.6 \cdot 10^{-8}$N. Equating F_D to the force $F_e = Q_1 E_x$, we find $E_x = 580$ V/m. For a cluster with a charge $Q = 4.5 \cdot 10^{-10}$C $E_x = 60$ V/m. The presence of such fields during experiments is likely. Let us consider an alternative possibility of curving the trajectory of a charged cluster by a magnetic field. For example, in Fig. 1*c*, the cluster moves along an arc of a circle with a radius $R = 190$ μm. Let the cluster mass $M = 3.78 \cdot 10^{-14}$ kg, its charge $Q = 4.5 \cdot 10^{-12}$ C and it moves at a speed of $v = 30$ m/s. In this case, the magnetic induction causing such a motion is $B = Mv/QR = 1.3 \cdot 10^3$ T. The presence of such strong fields in the laboratory is unlikely.

Let us list in concise form our results.

1. The "strange" particles are multiply charged clusters consisting of ions enclosed in a shell of a dielectric or other substance.
2. When the cluster approaches the surface of a solid, a small particle separates from it, which carries away part of the charge and mass of the cluster.
3. This particle is accelerated in the electric field of a "large" cluster to energy 10^9 eV and, when it hits a film, creates a latent image in the emulsion.
4. The "large" cluster receives a recoil impulsive moment, takes off above the film, and then, drawn by a polarized film, falls on it again.
5. When the cluster moves along the surface of the film, a trace chain is formed on it.
6. The height of the "jumps" of the cluster above the film turned out to be various, this leads to the formation of traces of a complex shape.
7. Due to a decrease in the charge and mass of the cluster, the period of the spots following on the film increases, and their size decreases.
8. An external electric field bends the trajectory of the cluster.

6. CONCLUSION

There have been the cases in the history of science when the epithet "strange", "unknown", and "mysterious" was assigned to a newly discovered phenomenon. The rays, discovered in 1895 by W.K. Roentgen, which in Western literature are still called *X*-rays ("unknown" rays) are clear examples of this. There were several options for interpreting the nature of these rays, until it turned out that *X*-rays are "ordinary" light with a short wavelength. The same after the discovery of radioactive radiation: it turned out that the "mysterious" γ rays are also light, and α and β rays are helium nuclei and electrons. Similar events related to the discovery of new particles with incomprehensible properties have occurred in the last 20 years: a whole "bunch" of explanations for this "strange" radiation has appeared with no less "strange" theories – dark matter, tachyons,

and nuclear particles with unusual properties (erzions). History teaches that of all the possible explanations, the simplest "survives" (the so-called principle of "Ockham's razor" works). It's like the nature "loves" to use one principle of "construction" for objects of different scales (atom → Solar system → Galaxy) – the systems based on the dynamic equilibrium of their parts. We applied a similar principle to the construction of a model of "strange" particles – we used the repeatedly mentioned analogy with ball lightning, which was built on the basis of the equality of the Coulomb repulsion force of particles of its core to the compressive strength of a polarized dielectric shell. It turned out that this principle can be used both for macroscopic ball lightning and micro-sized ball lightning. The mechanism of levitation of ball lightning above the surface of conductors (due to asymmetric runoff of the charge) turned out to be applicable to explain the movement of "strange" particles (micro-sized ball lightning) above the surface of film. The natural explanation was given to the details of this process: an unusual form of traces on photographic films, a decrease in the degree of blackening of the film along the trail, the reason for the appearance of charged particles with high energy.

REFERENCES

1. Urutskoev LI, Liksonov VI, Tsinoev VG. Experimentalnoye obnaruzhenie "strannogo" izlucheniya i transformatsii khimicheskikh elementov [Experimental finding of "strange" radiation and transformation of chemical elements]. *Prikladnaya fizika*, 2000, (4):83-100 (in Russ.).
2. Urutskoev LI, Liksonov VI, Tsinoev VG, Observation of transmutation of chemical elements during electric discharge. *Annales de la Fondation Louis de Brogle*, 2002, 27(4):701-726.
3. Matsumoto T. Ball lightning during underwater spark discharges and the Matsumae earth-quarks. In: *Proc. 5th International Symposium on Ball Lightning* (*ISBL97*). Tsugawa-Town, Niigata, Japan, 1997, p. 193-201.
4. Matsumoto T. Micro ball lightning during underwater spark discharge. In: *Proceedings of 6th International Symposium on Ball Lightning* (*ISBL-99*). Antwerp, Belgium, 1999, p. 249-254.
5. Shoulders K. *EV – A Tale of Discovery*. Austin, Texas, USA. Jupiter Technologies, 1987.
6. Savvatimova I, Kucherov Y, Karabut A. Cathode material change after deuterium glow discharge. *Transactions of Fusion Technology,* 1994, 26:389-384.
7. Savvatimova IB, Karabut AB. Produkty yadernykh reaktsiy, registriruemye na catode posle experimentov v tleyuschem razryade v deyterii [Products of nuclear reactions registrated on the cathode after experiments in glow discharge in deuterium]. *Poverkhnost,* 1996, 1:63-75 (in Russ.).
8. Savvatimova IB, Karabut AB. Radioaktivnost palladievykh catodov posle oblucheniya v tleyuschem razryade [Radioactivity of palladium cathodes after irradiation in a glow discharge]. *Poverkhnost*, 1996, 1:76-81 (in Russ.).
9. Zhigalov VA. Treki na fotoplyonke ot strannogo izlucheniya: replikatsiya [Tracks on photo film from a strange radiation: replication]. *Zhurnal formiruyushchikhsya napravleniy nauki* (*ZhFNN*). 2015, 3(9):55-62 (in Russ.).
10. Zhigalov VA, Zabavin SN, Parkhomov AG, Sobolev AG, Timerbulatov TR. Struktura trekov strannogo izlucheniya ot dvukh tipov reactorov LENR [Structure of strange radiation tracks from two types of LENR reactors]. In: *Proc. 25th Russian Conference on Cold Nuclear Transmutation of Chemical Elements and Ball Lightning*, p. 63-75. Moscow, NIC FTP "Erzion" Publ., 2019, (in Russ.).
11. Prosvirnov AA. Obobschenie i klassificatsiya nizkoenergeticheskikh yadernykh reaktsiy [Synthesis and classification of low energy nuclear reactions]. In: *Proc. 20th Russian Conference on Cold Nuclear Transmutation of Chemical Elements and Ball Lightning,* p. 93-109. Moscow, NIC FTP "Erzion" Publ., 2014, (in Russ.).
12. Rodionov BU, Savvatimova IB. O prirode strannykh trekov [About a nature of the "strange" tracks]. In: *Proc. 13th Russian Conference on Cold Nuclear Transmutation of Chemical Elements and Ball Lightning,* p. 187-205.

Moscow, NIC FTP "Erzion" Publ., 2006 (in Russ.).
13. Rodionov B, Savvatimova I. Unusual structures on the material surfaces irradiated by low-energy ions. *J. Condensed Matter Nucl. Sci*., 2006, p. 421-429.
14. Fox H, Jin SX. Low energy nuclear reactions and high density charge clusters. *Journ. of New Energy,* 1998, 3(213):56-67.
15. Fox H, Savvatimova I, Sarkisov V. Transmutation and Earth elements. In: *Proc. 9th Russian Conference on Cold Nuclear Transmutation of Chemical Elements and Ball Lightning,* p. 146-149. 2002, Moscow, NIC FTP "Erzion" Publ.
16. Nesterovich AV, Rodionov BU, Savvatimova IB. Formirovanie trekov pri kholodnykh transmutatsiyakh atomnykh yader [Forming of tracks at cold transmutation of atomic nuclei]. In: *Proc. 8th Russian Conference on Cold Nuclear Transmutation of Chemical Elements and Ball Lightning,* p. 211-215. Moscow, NIC FTP "Erzion" Publ., 2001 (in Russ.).
17. Bogdanovich BY, Volkov NV, Kostochko YP, Len NA, Nesterovich AV, Starostin AI. Experimentalnoye issledovanie kvaziperiodicheskogo impulsnogo razryada, initsiiruemogo v potoke zhidkosti v prielectrodnom prostranstve [Experimental investigation of quasi-periodical pulse discharge, initiated in the liquid flow in near-electrode space]. *Ingenernaya fizika,* 2000, (1):19-23, Moscow, MEPHI Publ. (in Russ.).
18. Golubnichi PI, Gromenko VM, Krutov VM. Obrazovanie dolgozhivuschikh svetyaschikhsya ob'ektov pri raspade plotnoy nizkotemperaturnoy vodnoy plasmy [Creation of long-living sining objects at decomposition of a dense low-temperature water plasma] *Jurnal tekhnicheskoi fiziki*, 1990, 60(1):183-186 (in Russ.).
19. Mesyats GA. *Ectony. Chast 1*. [Ectons. Part 1]. Ekaterinburg, Nauka Publ., 1993, 184 p.
20. Avramenko RF, Nikolaeva VI, Poskascheeva LP. Energoyomkie plazmennye obrazovaniya, initsiiruemye erozionnym razryadom – laboratornyi analog sharovoi molnii [Energy-capacious objects, initiated by erosion discharge, as a laboratory analog of ball lighting], p. 15-56. In: Avramenko RF, Bychkov VL, Klimov AI, Sinkevich OA (Eds). *Sharovaya molniya v laboratorii*. Moscow, Khimiya Publ., 1994, 256 p. (in Russ.).
21. Ivoilov NG. Nizkoenergetichescaya generatsiya "strannogo" izlucheniya [Low energy generation of "strange" radiation]. *Georesursy*, 2005, 2(17):84-92 (in Russ.).
22. Skvortsov VA, Vogel NI. Fizika generatsii ekzoticheskikh kvazichastits i ikh vzaimodeystviya s veschestvom, electricheskimi i magninymi polyami [Physics of generation of exotic quasi-particles and their interaction with substance, electric and magnetic fields]. *Preprint 2015-1 of Moscow Radio-technical Institute of Russian Academy of Sciences*. Moscow, 2015 (in Russ.).
23. Klimov AI. Vortex plasmoids created by high-frequency discharges. In: Bychkov VL, Golubkov GV, Nikitin AI (Eds). *The Atmosphere and Ionosphere. Elementary Processes, Discharges and Plasmoids*. Springer, Dordrecht, 2012, pp. 251-273.
24. Klimov A, Baranov D, Kutlaliev V, Zhirnov K, Moralev I, Tolkunov B. Izuchenie anomalnyukh trekov dvizhuschikhsya yarkosvetyaschikhsya chastits, sozdannykh erozionnym plsamogeneratorom [Study of anomalous "traces" of moving bright particles created by erosive pulsed plasma generator]. In: *Proc. 14th Russian Conference on Cold Nuclear Transmutation of Chemical Elements and Ball Lightning,* p. 199-208. Moscow, NIC FTP "Erzion" Publ., 2008 (in Russ.).
25. Klimov AI, Belov NK, Tolkunov BN. Myagkoye rentgenovscoye izluchenie, sozdannoe nano-klasternymi plazmoidami [Soft *X*-radiation created by heterogeneous cluster plasmoid]. In: *Proc. 23th Russian Conference on Cold Nuclear Transmutation of Chemical Elements and Ball Lightning,* p. 127-138. Moscow, NIC FTP "Erzion"Publ., 2017 (in Russ.).
26. Belov NK, Gerasimova AI, Godin SM, Klimov AI, Temirbulatov VS, Tolkunov BN. Registratsiya razlichnykh tipov izlucheniy v geterogennom vikhrevom plazmennom

reactore PVR [Registration of the different types of radiations from a heterogeneous plasmoid created in plasma vortex reactor PVR]. In: *Proc. 25th Russian Conference on Cold Nuclear Transmutation of Chemical Elements and Ball Lightning,* p. 24-32. Moscow, NIC FTP "Erzion" Publ., 2019 (in Russ.).

27. Baranov DS, Baranova OD. Issledovanie elementnogo sostava v vybrosakh klasterov iz nitrata vismuta [Investigation of elements composition in the cluster emissions from bismuth nitrate]. In: *Proc. 18th Russian Conference on Cold Nuclear Transmutation of Chemical Elements and Ball Lightning,* p. 62-69. Moscow, NIC FTP "Erzion" Publ., 2012 (in Russ.).
28. Bazhutov YN, Egorov OK, Kashkarov LL. Novye rezultaty yadernykh issledovaniy anodoplazmennogo electroliza [New results of nuclear phenomena researches of anode plasma electrolysis]. In: *Proc. 18th Russian Conference on Cold Nuclear Transmutation of Chemical Elements and Ball Lightning,* p. 37-47. Moscow, NIC FTP "Erzion" Publ., 2012 (in Russ.).
29. Lewis EH. Traces of ball lightning in apparatus? *J. Condenced Matter Nucl. Sci.*, 2009, 2:13-32.
30. Pryakhin EA, Tryapitsina GA, Urutskoev LI, Akleyev AV. Assessment of the biological effects of "strange" radiation. *Annales de la Fondation Louis de Broglie*, 2006, 31(4):17-23.
31. Shishkin AL, Tatur VY. Otsenka vozdeystviya strannogo izlucheniya na biologicheskie ob'ekty [Evaluation of the effects of strange radiation on biological objects]. In: *Proc. 25th Russian Conference on Cold Nuclear Transmutation of Chemical Elements and Ball Lightning,* p. 76-80. Moscow, NIC FTP "Erzion" Publ., 2019 (in Russ.).
32. Agapov AS, Kalensky VA, Kaitukov IB, Malyshev AV, Ryabova RV, Steblevsky AV, Urutskoev LI, Filippov DV. Obnaruzhenie "strannogo" izlucheniya i izotopnogo iscazheniya titana pri ispytaniyakh promyshlennogo electrotekhnicheskogo oborudovaniya [Observation of "strange emission" and titan isotopes distortion at testing of the industrial electric equipment]. In: *Proc. 12th Russian Conference on Cold Nuclear Transmutation of Chemical Elements and Ball Lightning,* p. 24-40. Moscow, NIC FTP "Erzion" Publ., 2005 (in Russ.).
33. Meyerovich BE. *Kanal silnogo toka* [The channel of a strong current]. Moscow, FIMA Publ., 1999, 376 p.
34. Urutskoev LI, Filippov DV, Gulyaev AA, Klykov DL, Kuznetsov VL, Stolyarov VL, Steblevsky AV. Experimentalnaya proverca fenomenologicheskoy modeli nizkoenergeticheskoy transformatsii yader khimichskikh elementov [Experimental testing of the phenomenological model of low-energy transformation of chemical elements]. In: *Proc. 10th Russian Conference on Cold Nuclear Transmutation of Chemical Elements and Ball Lightning,* p. 76-83. Moscow, NIC FTP "Erzion" Publ., 2003 (in Russ.).
35. Daviau C, Fargue D, Priem D, Racineux G. Tracks of magnetic monopoles. *Annales de la Fondation Louis de Broglie*, 2013, 38:139-153.
36. Adamenko SV, Vysotsky VI. Experimentalnoye obnaruzhenie i modelirovanie orientatsionnogo dvizheniya gipoteticheskikh magnitozaryazhennykh chastits na mnogosloynoy poverkhnosti [Experimental finding and modeling of the oriented motion of hypothetic magneto-charged particles on the multi-layer surface]. *Poverkhnost*, 2006, (3):84-92 (in Russ.).
37. Shakhparonov IM, Chicherin VG. Vzaimodeystvie potokov magnitnykh monopoley c veschestvom [The interaction of magnetic monopoles flow with matter]. In: *Proc. 19th Russian Conference on Cold Nuclear Transmutation of Chemical Elements and Ball Lightning,* p. 154-167. Moscow, NIC FTP "Erzion" Publ., 2013 (in Russ.).
38. G. Lochak, The symmetry between electricity and magnetism and the problem of the existence of magnetic monopole. In: TW Barnett and DM Grimes (eds.). *Advanced Electromagnetism*. Singapore, World Scientific Publishing Co., 1995, p. 105-147.
39. L. Jaitner, The physics of condensed plasmoids (CPs) and low-energy nuclear reactions

(LENR). 2018. Lutz.jaitner@t-online.de; www.condenced plasmoids.com.
40. Fredericks KA. Possibility of tachyon monopoles detected in photographic emulsions? *Condensed Matter Nuclear Science,* 2015, 15:203-230.
41. Bazhutov YN. Experiment Rossi-Focardy i ego erzionnaya interpretatsiya [Rossi-Focardy experiment and its erzion interpretation]. In: *Proc. 18th Russian Conference on Cold Nuclear Transmutation of Chemical Elements and Ball Lightning,* p. 48-61. Moscow, NIC FTP "Erzion" Publ., 2012 (in Russ.).
42. Baranov DS, Baranova OD. Evidence the formation and decay of giant long-lived nuclear molecules. *Proc. Intern. Symp. on Exotic Nuclei* (*EXON 2012*), p. 204-212. Vladivostok, 2012, http://exon2012.jinr.ru.
43. Brand W. *Der Kugelblitz.* Hamburg, Henry Grand, 1923, 170 p.
44. Singer S. *The Nature of Ball Lightning.* New York, Plenum, 1971, 239 p.
45. Imianitov I, Tikhiy D. *Za Gran'yu Zakonov Nauki* [Beyond the Border of Laws of Science]. Moscow, Atomizdat Publ., 1980, 191 p.
46. Stakhanov IP. *O Fizicheskoy Prirode Sharovoy Molnii* [About the Physical Nature of Ball Lightning]. Moscow, Nauchnyi Mir Publ., 1996, 264 p.
47. Stenhoff M. *Ball Lightning: an Unsolved Problem in Atmospheric Physics.* London, Kluwer Acad., 1999, 349 p.
48. Grigoriev AI. *Sharovaya Molniya* [Ball Lightning]. Yaroslavl, Yaroslavl State University Publ., 2006, 200 p.
49. Nikitin AI. Elektricheskiy kondensator kak element energeticheskogo yadra sharovoy molnii [An electric capacitor as an element of energy core of ball lightning]. *Electrichestvo,* 1998, (11):14-23 (in Russ.).
50. Nikitin AI. An electrical capacitor as the element of the power core of ball lightning. *Electrical Technol. Russ.,* 1998, (4):70-85.
51. Nikitin AI. The dynamic capacitor model of ball lightning. In: *Proceedings of 6th International Symposium on Ball Lightning* (*ISBL-99*). Antwerp, Belgium, 1999, p. 91-95.
52. Nikitin AI. Electrodinamicheskaya model sharovoy molnii [Electrodynamic model of ball lightning]. *Khimicheskaya fizika,* 2006, 25(3):38-62 (in Russ.).
53. Nikitin AI. Novyi podkhod k resheniyu problemy sharovoy molnii – smena paradigmy [A new approach for solving of ball lightning problem – change of the paradigm]. *Vestnik RAEN,* 2012, (3):15-26 (in Russ.).
54. Nikitin AI. Small-sized and composite ball lightning. *Intern. Journ. "Unconvented Electromagnetics and Plasmas* (*UEP*)". 2012, 4(1-2):105-116.
55. Nikitin AI. Possible process of ball lightning training in nature. *Journ. Atm. Solar-Terr. Phys.,* 2019, 190:54-61.
56. Nikitin AI, Velichko AM, Nikitina TF. Printsipy poiska usloviy sozdaniya uporyadochennykh plazmennykh struktur [Principles of the search of conditions for creating of ordered plasma structures]. *Izvestiya Academii nauk. Energetica*, 2008, (2):115-132 (in Russ.).
57. Nikitin AI, Bychkov VL, Nikitina TF, Velichko AM. High-energy ball lightning observations. *IEEE Trans. Plasma Sci.*, 2014, 42(12):3906-3911.
58. Nikitin AI, Bychkov VL, Nikitina TF, Velichko AM, Abakumov VI. Sources and components of ball lightning theory. *J. Phys. Conf. Ser.,* 2018, 996:012011.
59. Bychkov VL, Nikitin AI, Dijkhuis GC. Ball lightning investigations. In: Bychkov VL, Golubkov GV, Nikitin AI (Eds). *The Atmosphere and Ionosphere. Dynamics, Processes, and Monitoring,* p. 201-373. Springer, Dordrecht, 2010.
60. Bychkov VL, Nikitin AI. Ball lightning. A new step in understanding. In: Bychkov VL, Golubkov GV, Nikitin AI (Eds). *The Atmosphere and Ionosphere. Elementary Processes, Monitoring, and Ball Lightning.* Springer, Cham, 2014, p. 201-367.
61. Nikitin AI, Leipunsky IO, Nikitina TF. Rol vikhrevykh tokov v sozdanii podyomnoy sily avtonomnogo izluchatelya radiovoln [Role of eddy currents in lifting force creating for an autonomous emitter of radio-waves]. *Prikladnaya fizika*, 2010, 2:15-22 (in Russ.).

62. Nikitin AI, Nikitina TF, Velichko AM. Coronnyi razryad i levitatsiya sharovoy molnii [Corona discharge and levitation of ball lightning]. *Electrichestvo*, 2010, (3):16-22 (in Russ.).
63. Nikitin AI, Nikitin VA, Velichko AM, Nikitina TF. "Strange" particles and micro-sized ball lightning in some electric discharges. *Journ. Atm. Solar-Terr. Phys.*, 2021, 218:105525.
64. Nikitin AI, Nikitin VA, Velichko AM, Nikitina TF. "Strannye" chastitsy i microrasmernye sharovye molnii ["Strange" particles and micro-sized ball lightning] In: *Proc. 26th Russian Conference on Cold Nuclear Transmutation of Chemical Elements and Ball Lightning,* p. 226-244. Moscow, DeLibri.Publ., 2020 (in Russ.).
65. Blakemore JS. *Solid State Physics.* Cambridge, Cambridge University Press, 1985, 608 p.
66. Nikitin AI. Ustoichivost i predelnoe energosoderjanie avtonomnoi sharovoi molnii [Stability and a limit energy content of autonomous ball lightning]. *Electrichestvo*, 2004, (3):29-36 (in Russ.).
67. Frish SE, Timoreva AV. Kurs obschey fiziki. T. 1 [Course of general physics. V. 1] Moscow, GITTL, 1955, 463 c.
68. Sarantsev VP, Perelshtein EA. *Kollectivnoe uskorenie ionov electronnymi koltsami* [Collective acceleration of ions by electron rings]. Moscow, Atomizdat Publ., 1979, 216 p.
69. Zeldovich YB, Yaglom IM. *Vysshaya matematika dlya nachinayuschikh fizikov i tekhnikov* [High mathematics for beginning physicians and technicians] Moscow, Nauka Publ., 1982, 512 p.
70. Smirnov BM. Electricheskiy tsikl v atmosphere Zemli [Electrical cycle in the Earth's atmosphere]. *Uspekhi Fizicheskikh Nauk,* 2014, 184(11):1153-1176 (in Russ.).
71. Chalmers JA. *Atmospheric Electricity*. Oxford, Clarendon Press, 1949.
72. Raizer YP. *Fizika gazovogo razryada* [Physics of Gas Discharge]. Dolgoprudny, Intellect Publ., 2009, 736 p.
73. Trichel GW. The mechanism of the negative point to plane corona near onset. *Phys. Rev.,* 1938, 54:1078-1084.
74. Reist PC. *Introduction to Aerosol Science*. New York/London, Macmillan Publishing Company, 1984.

DOI: 10.17725/rensit.2021.13.369

Graphene-polyethylene high pressure composites and their properties

Ekaterina G. Rustamova
SPO "GRAPHENIKA", https://www.grafenika.com/
Moscow 107143, Russian Federation
Sergey P. Gubin
N.S. Kurnakov Institute of General and Inorganic Chemistry of RAS, http://www.igic.ras.ru/
Moscow 119991, Russian Federation
E-mail: nebukina@yandex.ru, gubin@igic.ras.ru
Received July 28, 2021, peer-reviewed August 09, 2021, accepted August 23, 2021

Abstract: **A method for the introduction graphene into high-pressure polyethylene (HPPE) has been developed. Samples of graphene-HPPE were obtained with the content of graphene filler: 0.25%; 0.5%; 1.0%; 1.5%; 3.0%; 5.0% wt. The structural, morphological and deformation-strength properties of the obtained samples have been investigated. It was established that the increase of the elastic modulus value for the samples with the filler concentration of 3% wt and more.**

Keywords: **graphene, high-pressure polyethylene, polymeric nanocomposite materials**

UDC 54.03'05'06

Acknowledgments: The authors express their gratitude and deep appreciation to the staff of the Laboratory of Inorganic and Hybrid Polymers and Composites at the Semenov Institute of Chemical Physics, Russian Academy of Sciences for the help in the investigation of the rheological and deformation-strength properties of graphene-HPPE composites.

For citation: Ekaterina G. Rustamova, Sergey P. Gubin. Graphene-polyethylene high pressure composites and their properties. *RENSIT*, 2021, 13 (3):369-376. DOI: 10.17725/rensit.2021.13.369.

Contents

1. INTRODUCTION

Currently, nanocomposites represent a new direction in the field of filled systems. Due to the special properties of nanoscale fillers, the most attention of scientists is focused on the development of polymer nanocomposite materials [1-5].

Carbon nanostructures, and graphene in particular, are promising fillers, which attract the special interest of researchers..

Graphene is a two-dimensional unit layer of carbon, only one sp^2-carbon atom thick and has many unique physical properties [6-13]. Experimental data show that the values of Young's modulus – 1 TPa, the maximum current density – 10^8 A·cm^{-2}, the coefficient of thermal conductivity of up to 5000 m^{-1}K^{-1}, the charge carrier mobility at room temperature of 10^4 cm^{2}K^{-1s-1}[14-17].

Due to the introduction of a graphene filler into various polymers, the obtained composites acquire improved characteristics in terms of strength, rigidity, electrical and thermal conductivity [18-20].

In turn, high-pressure polyethylene (HPPE) is one of the most common, widely available and cheap polymers, the expansion of the areas of

its application by modifying its properties is a currently important direction.

In this regard, the aim of this work was to develop a method of introducing graphene into high-pressure polyethylene, to obtain polymer composites of graphene-HPPE, and to study their properties.

2. EXPERIMENTAL

The following were used as precursors for the synthesis of graphene and composite materials: Chinese natural graphite (99.9% C, crushed in a ball mill to a size of 200-300 μm), sulfuric acids (ACS, "Sigma Tech" LLC), potassium permanganate (p.a., "NevaReaktiv" LLC), hydrogen peroxide (p.a., "NevaReaktiv" LLC), isopropyl alcohol (ACS, "EKOS-1" JSC), high pressure polyethylene (CAS-No: 9002-88-4, Sigma Aldrich), vacuum oil BM1 (industry standard OST 38.101402-86, "GSM Group" LLC), distilled water.

The samples of the graphene-HPPE composites were obtained in two stages. At the first stage graphene was synthesized. For this purpose, the natural graphite used as a starting material, was oxidized to graphite oxide by a modified Hummers' method [21-23]. The obtained oxidized product was dispersed in distilled water using an ultrasonic unit (20.4 kHz frequency, 0.1–1 W/cm^3 specific power) for 15 minutes until formation of graphene oxide. After that, the aqueous dispersion was centrifuged (6000 rpm for 10 min), a precipitate was isolated and dried at a temperature of 60°C for 24 h. Then, the powdered graphene oxide was reduced to graphene with isopropanol under supercritical conditions [24].

At the second stage the obtained graphene was dispersed in isopropyl alcohol in the ratio of 1mg/1ml for 1 h by ultrasonic treatment. The obtained graphene dispersion was introduced in small portions into solution-melt HPPE-BM1 oil at a temperature of 200°C under the condition of constant stirring (1200 rpm). The removal of isopropanol vapors from the reaction vessel was carried out by an argon flow.

At the end of the synthesis, the reaction mixture was cooled to room temperature. The obtained composite was purified from oil by extraction with hexane in a Soxhlet's apparatus for 16 h.

Thus, the samples of graphene-HPPE containing 0.25, 0.5, 1, 1.5, 3 and 5% wt of graphene, which are powders, were obtained. **Fig. 1** shows a sample of the graphene-HPPE composite containing 5 wt.% of graphene.

By the method of hot pressing from the samples, with different content of the carbon filler, the films were obtained. For this purpose, powdered samples (m = 5 g) were evenly distributed over the volume of copper frames (100×100×0.041 mm) and kept for 30 sec at 180°C and pressure of 20 kg/cm^2. Fixation of the shape of the products occurred as a result of cooling the samples to room temperature.

The structural characteristics of the samples were investigated using powder diffractometry and Raman spectroscopy. *X*-ray phase analysis (XRD) was carried out on DRON-7 unit with graphite monochromator on CuKα-radiation

Fig. 1. *A sample of the graphene-HPPE composite.*

(λ = 1.54056 Å) with Ni filters. The Raman spectroscopy signals were recorded using a photomultiplier (PMT) operating in the photon counting mode. The spectra were accumulated on a personal computer.

The morphology of graphene flakes in isopropanol and in a HPPE matrix was determined by analytical processing of microphotographs obtained by transmission electron microscopy (TEM) on a Leo 912 AB Omega unit at an accelerating voltage of 100 kV.

Before imaging, the samples were placed on carbon-film-coated copper grids 3.05 mm in diameter. Translucent images were acquired at magnifications up to 500,000×. A restriction aperture with a diameter of 0.4 μm was used to obtain electron diffraction images.

Atomic force microscopy (AFM) was used to determine the lateral size and height of the graphene particles. The samples were imaged using a Solver P47 microscope (Solver scanner, sonde NSG01) at a nominal cantilever resonance frequency of 150 kHz, cantilever stiffness constant of 5.1 N/m, sonde radius of 10 nm, scanning speed of 1 Hz, and resolution of 512x512 points.

Before the AFM study, a 10 *μl* drop of graphene dispersion in isopropanol was placed on freshly pierced mica and incubated at room temperature until complete evaporation of the solvent.

Deformation-strength studies of graphene-HPPE samples were performed on an Instron 5540 series testing machine. Blades of standard sizes (11×80 mm) were cut from the manufactured graphene-HPPE composite films and tested at room temperature, pressure of 620 kPa, and speed of 50 mm/min.

The rheological properties of the samples of graphene-HPPE composites were studied using a capillary viscometer.

3. RESULTS AND DISCUSSION

Before the introduction of graphene, obtained from natural graphite by chemical processes (oxidation, dispersion, reduction), into high pressure polyethylene, it was characterized by a complex of methods of physical and chemical analysis.

X-ray phase analysis (XRF) and Raman spectroscopy were used to obtain data on the structure of graphene.

The diffractogram of the initial graphite (**Fig. 2***a*) shows characteristic reflexes of low (at the angles of 2θ: 12.5, 25, 55 deg) and strong intensity (at 2θ – 26.6 deg) corresponding to the graphite phase with the hexagonal lattice structure.

The transition from the densely packed, compact source material to the nano-object, graphene, resulted in a decrease in the intensity and significant broadening of the diffraction maximum in the region of 26.6 deg. (Fig. 2*b*). In addition, there is a disappearance of low-intensity reflexes characteristic of graphite. These results indicate an increase in the sample dispersion (reduction of the size of graphene particles).

Additional information about the graphene structure was obtained using Raman spectroscopy. Raman spectroscopy is a powerful tool for the identification of non-destructive carbonaceous materials, in particular, for the determination of ordered and disordered crystal structures of carbon.

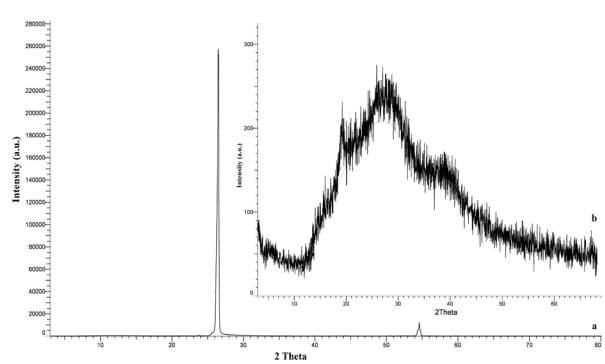

Fig. 2. *Diffractograms of samples: a - original graphite, b - graphene.*

G (≈1582cm^{-1}) and *D* (≈1350cm^{-1}) lines are characteristic features for carbon in Raman scattering spectra. The *G*-line is usually attributed to the E_{g2} phonon sp^2-hybridized carbon atoms, whereas the *D*-line constitutes the fully symmetric valence vibration $\varkappa$-point phonons of A_{1g} symmetry [25-28]. The overtones of these lines are 2*G* and 2*D*, located at 3248 cm^{-1} and 2700 cm^{-1} respectively.

The Raman spectrum of natural graphite (**Fig. 3***a*), used as a feedstock for graphene production, is represented by a strong *G*-line (1582 cm^{-1}), a broad 2*D*-line (2700 cm^{-1}), and a very weak 2*G* line at 3245 cm^{-1}. In the Raman spectrum signals of graphene (Fig. 3*b*), the *G* band broadens and shifts to 1590 cm^{-1}, an intense *D* band at 1350 cm^{-1} appears, there is a slight shift of the 2D and disappearance of the 2*G* bands. These phenomena can be attributed to the significant size reduction in the sp^2 plane of the domains due to exfoliation of the graphite crystal structure by oxidation and ultrasonic treatment to graphene oxide followed by its reduction [29,30].

The morphology of graphene was analyzed by transmission electron microscopy. Microphotographs show graphene sheets with a thin, transparent, slightly folded structure, resistant to the electron beam action.

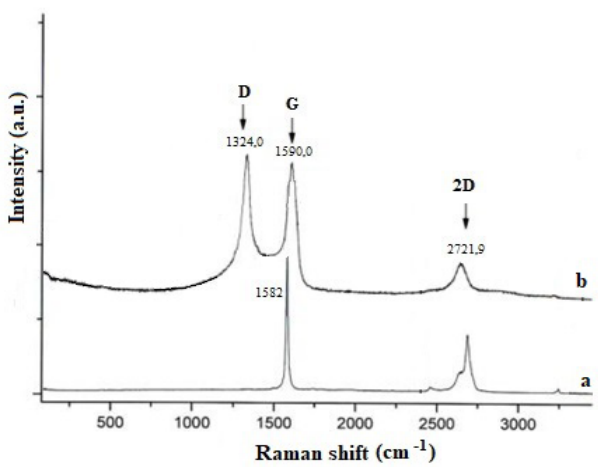

Fig. 3. *Raman spectrum: a-graphite, b-graphene.*

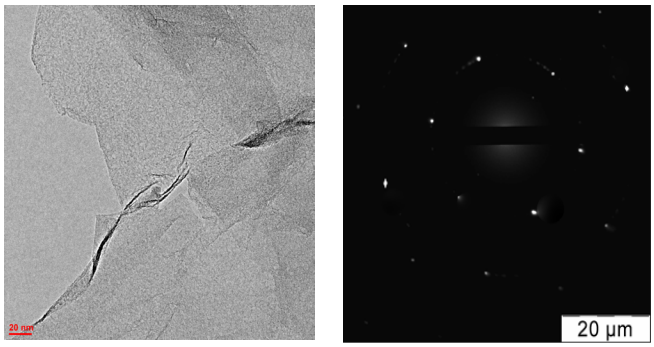

Fig. 4. *TEM image and electron diffraction of graphene.*

Electron diffraction was performed from the selected area of the graphene particle. **Fig. 4** shows the diffraction pattern in which clearly defined point reflexes confirm the crystalline structure of the graphene sheets.

By the AFM method the geometric parameters of the studied graphene were established. The AFM images show flat particles with lateral sizes from 1.5 to 3 μm and thickness of 1-2 nm, which corresponds to 3-5 layers of graphene. **Fig. 5** shows a single sheet of graphene.

After the basic structural and morphological characteristics of graphene were found out, it was used as a nanofiller for polyethylene.

High-pressure polyethylene has a rather rigid and complex structure, consisting of molecules, tightly stacked in parallel one to another to form lamellae. The introduction of graphene into the polymer could be accompanied by aggregation and uneven distribution of the filler particles, due to their difficult penetration between the lamellae.

In order to "activate" polyethylene, i.e. to make its structure available for the introduction and uniform fixation of the graphene particles,

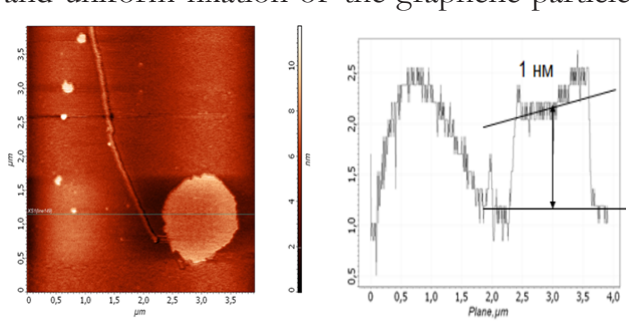

Fig. 5. *AFM–image and cross-section of a graphene sheet.*

vacuum oil was used. Vacuum oil mixed well with polyethylene, allowed to move apart the lamellae and create a very mobile reaction environment, allowing the filler to freely penetrate into the structure of polyethylene.

The obtained samples of graphene-HPPE in powder form contained from 0.25 to 5 wt% of the graphene filler and differed little from each other in color. However, after transforming the powders into films, a gamma from light to dark gray hue was formed. The degree of color saturation of the samples increased with increasing concentration of graphene in the HPPE.

Fig. 6 shows the TEM-image of the graphene-HPPE sample. The microphotograph shows a curved graphene sheet with lateral dimensions of 2 μm, which has entered the polymer structure. The authors of [31] argue that the surface relief and twisting are inherent to the graphene sheets, as the thermodynamic stability of the 2*D* structures occurs as a result of microscopic folds due to bending and deformation.

The electronogram (Fig. 6) for this sample is represented by blurred weakly pronounced ring reflexes due to the amorphous component of the polymer and signals in the form of single points characterizing the graphene crystal structure.

The results of Raman-spectra study of HPPE samples without the filler and with it showed that the filler introduction into the polymer is

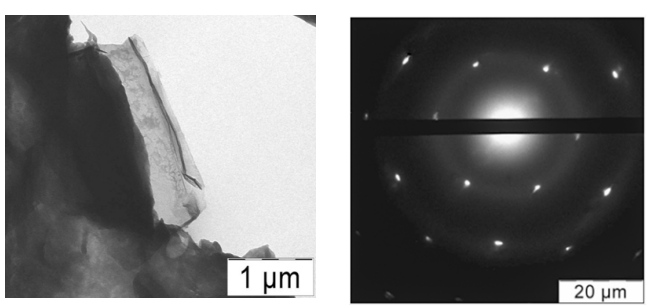

Fig. 6. *TEM-image and electron diffraction of the graphene-HPPE composite sample.*

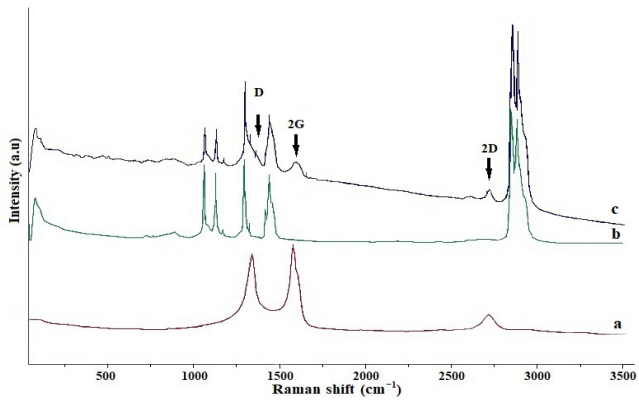

Fig. 7. *Image of the Raman spectroscopy of the studied samples: a - graphene, b - HPPE, c - graphene-HPPE composite.*

accompanied by the appearance of *G, D* and 2*D* lines typical for the carbon structures in the Raman spectra (**Fig. 7**).

Further stage of the work consisted in the study of the graphene-HPPE film samples properties.

Fig. 8 shows the results of the study of the films surface using an optical microscope. The image (Fig. 8) shows a uniform distribution of the filler particles of large (5-10 microns) and small (1-2 microns) size. Besides, the presence of light strips - defects (microcracks) is noted on the surface of the films.

A possible reason for such defects may be the presence of macroparticles located at the boundary of the crystallites, which behave as stress concentrators and contribute to the film surface continuity breaking.

The measurement of the deformation-strength characteristics of the graphene-HPPE nanocomposites made it possible to obtain the

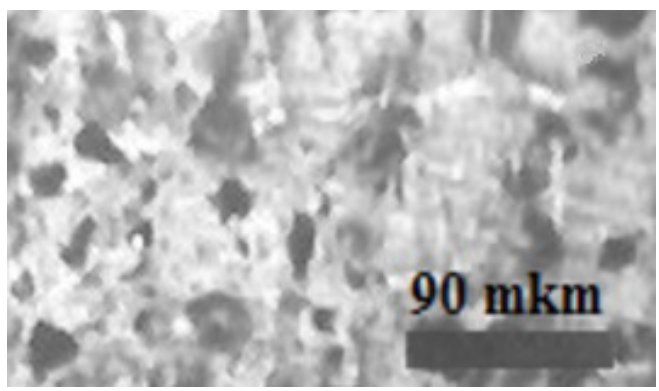

Fig. 8. *Image of the graphene-HPPE film surface.*

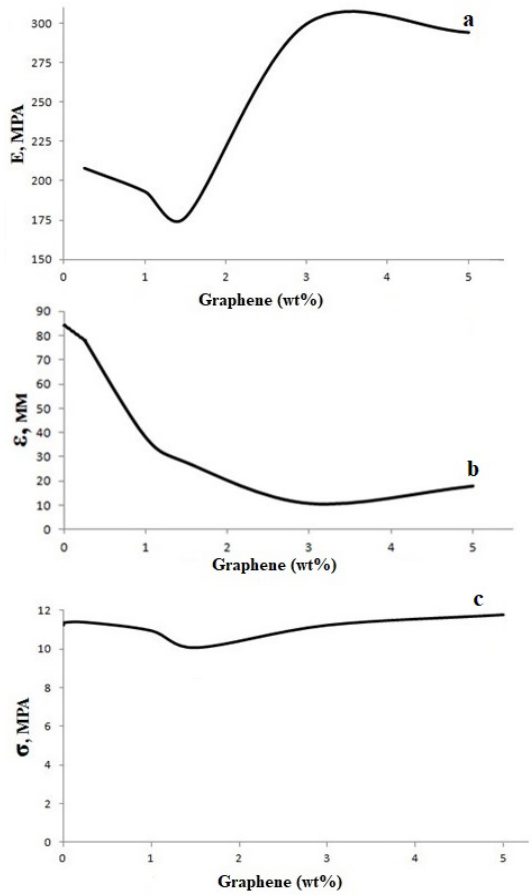

Fig. 9. *Concentration dependences: a - elastic modulus, b - elongation at break, c - strength of the graphene-HPPE samples.*

concentration dependences of the strength, modulus of elasticity, and elongation at rupture for the samples under study (**Fig. 9**).

According to the above presented data, the strength and elongation at break of the graphene-HPPE composites decrease, which is typical for the introduction of rigid anisotropic particles into polyolefin polymers.

The values of the elastic modulus remain unchanged for the samples with the filler concentration up to 1,5 wt.% and increase by 100 MPa at the graphene filling by 3% and more wt.%.

In addition to the deformation-strength characteristics for the graphene-HPPE samples, the rheological properties were studied.

Fig. 10 shows the flow curves of the studied samples. There is a directly proportional growth of the composites' viscosity with the increase

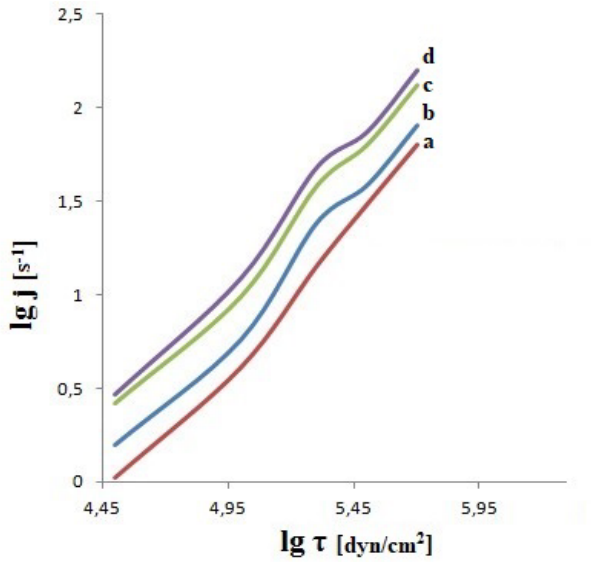

Fig. 10. *Flow curves of graphene-HPPE composite samples: a - HPPE, b - graphene- HPPE (1.5% wt.), c - graphene-HPPE (3% wt.), d - graphene-HPPE (5% wt.)*

in the graphene concentration from 1.5 to 5 wt.%. For the samples of graphene-HPPE with a lower filler content the values of the measured characteristics are comparable with the result obtained for HPPE without graphene. The viscosity growth is accompanied by the increase in the pseudomolecular weight of the graphene-HPPE samples. It is possible that this effect can be due to the increased interaction of the graphene sheets with the carbon chains of polyethylene.

4. CONCLUSION

During the conducted research work the method of graphene introduction into polyolefin polymer was developed, the samples of graphene-HPPE with different filler content (0.25-5 wt.%) were obtained. The structural and morphological characteristics of the graphene and the composite material were studied. Strain-strain characteristics of graphene-HPPE composite films with the thickness of 41 microns were measured and their rheological properties were investigated. It was found that the ultimate strength of the samples does not depend on the filler concentration, while the increase in its content in the composites leads to a decrease in the value of the relative elongation. There

is an increase in the elastic modulus relative to the values obtained for polyethylene without the filler by 100 mPa for the graphene-HPPE samples at the concentration of graphene 3 and more wt%. The results of the study of the rheological properties of the graphene-HPPE films, led to the conclusion about the growth of the interaction of graphene sheets with the carbon chains of polyethylene.

REFERENCES

1. Krishnamoorti R, Vaia RA. Polymer nanocomposites. J*ournal of Polymer Science Part B: Polymer Physics,* 2007, 45(24):3252–3256.
2. Jordan J, Jacob KI, Tannenbaum R, Sharaf MA, Jasiuk I. Experimental trends in polymer nanocomposites - a review. *Materials Science and Engineering: A*, 2005, 393:1–11.
3. Kim H, Abdala AA, Macosko CW. Graphene/Polymer Nanocomposites. *Macromolecules,* 2010, 43:6515-6530.
4. Nikolaichik VI, Gertsen MA, Avilov AS, Kornilov DY, Gubin SP. Pentagonal cobalt boride nanoparticles on the polystyrene granule surface. *Crystallography Reports,* 2019, 64(3):461-465.
5. Yasnaya MA, Kornilov DYu, Sytnikov EV, Sinel'nikov BM, Kargin NI, Khoroshilova SE. Metal-polymer nanocomposites as materials for ion-selective sensors. I*norganic Materials*, 2008, 44(3):230-238.
6. Novoselov KS, Geim AK, Morozov SV, Jiang D, Zhang Y, Dubonos SV, Grigorieva IV, Firsov AA. Two-dimensional gas of massless Dirac fermions in graphene. *Science,* 2004, 306:666-669.
7. Worsley MA, Olson TY, Lee JR. High surface area, sp^2-cross-linked three-dimensional graphene monoliths. *The Journal of Physical Chemistry Letters,* 2011, 2(8):921-925.
8. Papageorgiou DG. Mechanical properties of graphene and graphene-based nanocomposites. *Progress in Materials Science,* 2017, 90:75-127.
9. Babaev AA, Zobov ME, Kornilov DY, Tkachev SV, Terukov EI, Levitskii VS. Temperature dependence of electrical resistance of graphene oxide. *High Temperature,* 2019, 57(2):198-202.
10. Babaev AA, Zobov ME, Kornilov DY, Tkachev SV, Terukov EI, Levitskii VS. Specific features of temperature dependence of graphene oxide resistance. *Protection of Metals and Physical Chemistry of Surfaces,* 2019, 55(1):50-54.
11. Babaev AA, Zobov ME, Kornilov DY, Tkachev SV, Terukov EI, Levitskii VS. Optical and electrical properties of graphene oxide. *Optics and Spectroscopy,* 2018, 125(6):1014-1018.
12. Rychagov AY, Gubin SP, Chuprov PN, Kornilov DY, Karaseva AS, Krasnova ES, Voronov VA, Tkachev SV. Electrochemical reduction and electric conductivity of graphene oxide films. *Russian Journal of Electrochemistry,* 2017, 53(7):721-727.
13. Zaytsev EV, Bukunov KA, Bocharov GS, Chuprov PN, Tkachev SV, Kornilov DYu, Kurkina E S, Gubin SP, Eletskii AV. Graphene microtubes - new type of carbon materials. *RENSIT*, 2018, 10(1):59-64.
14. Mudryan VE, Sokolov EA, Piven NP, Babenko SD, Allayarov SR Anomalous behavior of the dielectric constant of a polymer composite with the addition of graphene. *ZhTF Letters,* 2010, 36(23):106-110.
15. Ferrari A et al. Science and technology roadmap for graphene, related two-dimensional crystals, and hybrid systems. *Nanoscale,* 2015, 7:4598-4810.
16. Wick P. Classification framework for graphene-based materials. *Chem. Int. Ed,* 2014, 53:7714-7718.
17. Bianco A. All in the graphene family - a recommended nomenclature for two-dimensional carbon materials. *Carbon*, 2013, 65:1-6.

18. Huang G, Gao J, Wang X, Liang H, Ge C. How can graphene reduce the flammability of polymer nanocomposites? *Materials Letters,* 2012, 66:187-189.
19. Zaitsev EV, Chuprov PN, Tkachev SV, Kornilov DY, Gubin SP, Kurkina ES, Bocharov GS, Eletskii AV. Preparation of graphene on copper substrates of various geometries by chemical vapor deposition. *Inorganic Materials*, 2018, 54(12):1205-1215.
20. Tkachev SV, Kornilov DY, Voronov VA, Gubin SP, Kraevskii SV. Graphene oxide on the surface of basalt fiber. *Inorganic Materials,* 2016, 52(12):1254-1258.
21. Hummers WS, Offeman RE. Preparation of graphitic oxide. *J. Am. Chem. Soc*, 1958, 80:1339.
22. Kornilov DY, Gubin SP. Graphene Oxide: Structure, Properties, Synthesis, and Reduction (A Review). *Russ. J. Inorg. Chem*, 2020, 65:1965-1976.
23. Yang D Chemical analysis of graphene oxide films after heat and chemical treatments by x-ray photoelectron and micro-Raman spectroscopy. *Carbon*, 2009, 47:45-52.
24. Tkachev SV, Buslaeva EYu, Gubin SP. Graphene: A novel carbon nanomaterial. *Inorg. Mater*, 2011, 47(1):1.
25. Tuinstra F. Koenig JL. Raman spectrum of graphite. *J. Chem. Phys*, 1970, 53:1126-1130.
26. Ferrari AC, Robertson J. Interpretation of Raman spectra of disordered and amorphous carbon. *Phys. Rev. B*, 2000, 61:14095-14107.
27. Ni Z, Wang Y, Yu T. et al. Raman spectroscopy and imaging of graphene. *Nano Res*, 2008, 1:273-291.
28. Muzyka R, Drewniak S, Pustelny T, Chrubasik M, Gryglewicz G. Characterization of graphite oxide and reduced graphene oxide obtained from different graphite precursors and oxidized by different methods using Raman spectroscopy. *Materials,* 2018, 11:1050.
29. Wang G, Yang J, Park J, Gou X, Wang B, Liu H. et al. Facile synthesis and characterization of graphene nanosheets. *J. Phys. Chem. C*, 2008, 112:8192–8195.
30. Kornilov DY, Kasharina LA. Effect of preparation and reduction on specific surface electrical resistance of thin films obtained from graphene oxide dispersion. *Inorganic Materials: Applied Research,* 2019, 10(5):1072-1077.
31. Meyer JC, Geim AK, Katsnelson MI, Novoselov KS, Booth TJ. Roth S. The structure of suspended graphene sheets. *Nature,* 2007, 446:60-63.

DOI: 10.17725/rensit.2021.13.377

Application of spectral and spatial processing methods to sonar images

Alexander V. Kokoshkin, Evgeny P. Novichikhin, Ilia V. Smolyaninov

Kotelnikov Institute of Radioengineering and Electronics of RAS, Fryazino Branch, http://fire.relarn.ru/
Fryazino 141190, Moscow Region, Russian Federation

E-mail: shvarts65@mail.ru, epnov@mail.ru, ilia159@mail.ru

Received May 26.2021, peer-reviewed June 07.2021, accepted June 21.2021

Abstract: **The paper proposes the use of the method of renormalization with limitation (MRL) for suppressing the speckle noise of images obtained using sonar. The method is tested on real images obtained by the interferometric side-view sonar. The principal possibility of a significant reduction in the speckle noise level is found due to the fact that the MRL renormalizes the spectrum of the sonar image to the universal reference spectrum (URS) model, which is a model of the spectrum of a "good" quality grayscale image. To increase the overall sharpness of the image, after applying the MRL, it is proposed to use spatial brightness transformations. The study allows us to conclude that the application of MRL to sonar images can significantly reduce speckle noise.**

Keywords: **sonar, remote sensing, sonar images, image processing, speckle noise, method of renormalization with limitation.**

UDC 621.369

Acknowledgments: The work was performed within the framework of the state assignment of the Ministry of Science and Higher Education of the Russian Federation

For citation: Alexander V. Kokoshkin, Evgeny P. Novichikhin, Ilia V. Smolyaninov. Application of spectral and spatial processing methods to sonar images. *RENSIT*, 2021, 13(3):377-382. DOI: 10/17725/rensit.2021.13.377.

Contents

1. INTRODUCTION

Currently, sonar systems are extremely widely used to solve applied problems in a large number of applications. Such as: environmental monitoring, search for natural resources, archeology, emergencies, industrial and defense security. Sonar images are a special case of synthetic aperture radar (SAR) images. Such images are characterized by the presence of multiplicative speckle noise. It arises due to wave interference caused by multiple scattering from reflectors small relative to the resolution element. Speckle noise appears as bright spots and bright dots randomly scattered throughout the image field.

Unlike SARs used for sounding the Earth from space, in sonar systems, the change in the relief from point to point can be commensurate with the distance to the sounding object. This increases the likelihood that a signal will be reflected from targets at different angles of arrival at the same range. This leads to the averaging of signals reflected from different areas [1]. This feature increases the likelihood of additional speckle noise.

Speckle noise suppression techniques are aimed at freeing the image from parasitic artifacts, removing graininess, and defining the

boundaries of areas and objects in the image. The fight against speckles is carried out in two directions. The first is to improve the design of sonars, i.e. the quality of visualization is improved with the help of various technical means. The second is the digital processing of an already obtained image.

This work is devoted to digital image processing. Frequently used methods of dealing with speckle noise are methods ranging from a simple locally averaging spatial filter and median filtering to Wiener, Kalman or homomorphic filtering algorithms applied to the entire image. Wavelet transforms or fractal coding are also used [2-5].

When testing the method of renormalization with limitation (MRL) on various types of images, in particular, a significant reduction in speckle noise was found [6,7]. Thus, the idea arose to apply MRL to sonar images in order to improve their quality. It is proposed to process the original acoustic images using the method of renormalization with limitation. It is assumed that after applying the MRL, on average, the axially symmetric (isotropic) part of the amplitude spatial spectrum of the studied images will correspond to the Universal Reference Spectrum (URS) model, i.e. models of the image spectrum of "good" quality [8,9]. It should be noted that the most significant information about the contours of regions and objects in the image is contained not in the amplitude, but in the phase part of the spectrum. Thus, while eliminating possible noise and distortions, all boundaries of the areas and the localization of objects in the images will be preserved. The aim of this work is to test the effect of suppressing speckle noise using MRL on real sonar images.

2. APPLICATION OF MRL TO SONAR IMAGES

The application of the renormalization method with limitation to sonar images is demonstrated by the example of **Fig. 1** - images of a fragment of the seabed with a sunken ship.

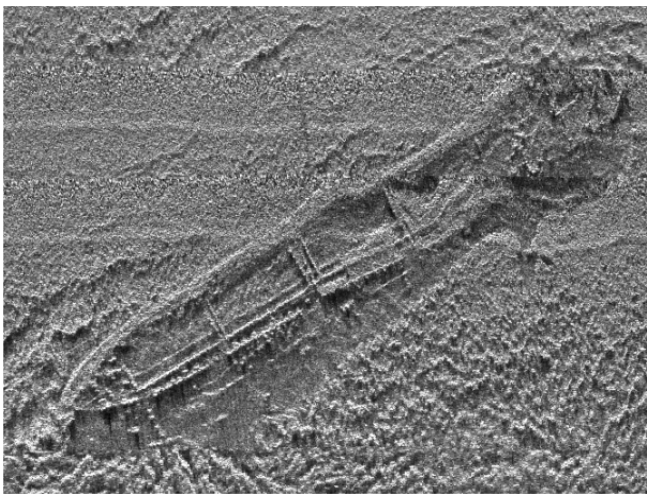

Fig. 1. *Original sonar image.*

The image with a size of 668 by 512 pixels, shown in Fig. 1, was obtained using the interferometric side-scan sonar (ISSS), which is part of the AGKPS 100 multifunctional sonar complex and has the following technical characteristics [10]:

1. The resolution of the ISSS in the direction of movement is 1.5 degrees. Slant range resolution - 0.03 m.
2. The working frequency of the ISSS is 450 kHz.
3. The root-mean-square error of measuring the depths of the ISSS in the swath up to 3 depths is not worse than 1% of the depth of survey, the sensitivity to changes in the coefficient of backscattering of soils is not less than 10%.
4. Band of survey (overview) ISSS up to 300 m on one side.
5. Probing signal is pulsed with linear-frequency modulation.

The multifunctional sonar complex AGKPS 100 also included additional sensors:

1. Satellite navigation receiver.
2. Trim roll and vertical displacement sensors.
3. Gyrocompass.
4. Sound speed meter in water.

The sonar survey was carried out while the vessel was moving in parallel directions (tacks) at a distance of 20 meters between them. Acoustic images obtained on parallel tacks are applied to a geographic map, taking into account the

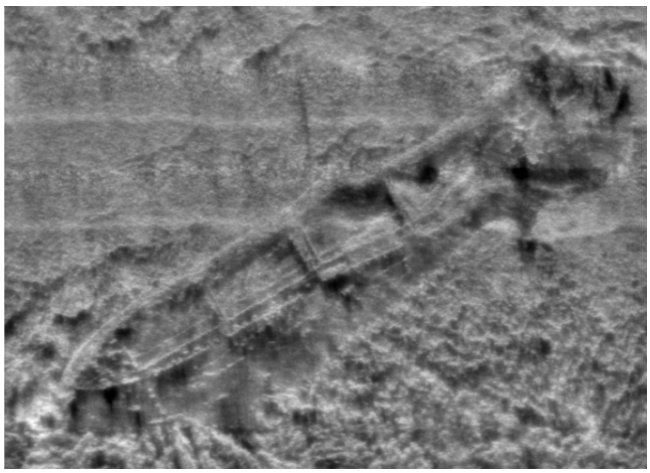

Fig. 2. *Applying the MRL to the image Fig. 1.*

indications included in the complex of sensors [11]. The peculiarity of the map construction is that the images from the adjacent tacks do not overlap (the images from the adjacent tracks are not averaged).

Shown in Fig. 1, the sunken ship has a length of 40 m and lies at a depth of 17 m.

We use the renormalization method with restriction in our "classical" version, i.e. the same as it was presented in [8,9] and registered in the certificate of state registration of a computer program [12]. Since it is assumed that the original image was not subjected to any blurring, the distorting hardware function is assumed to be "needle-like" (much less than one pixel wide). **Fig. 2** shows the application of the MRL to the image Fig. 1.

In a comparative analysis Fig. 1 and Fig. 2, it can be noted that, together with the suppression of speckle noise, there is a slight decrease in the

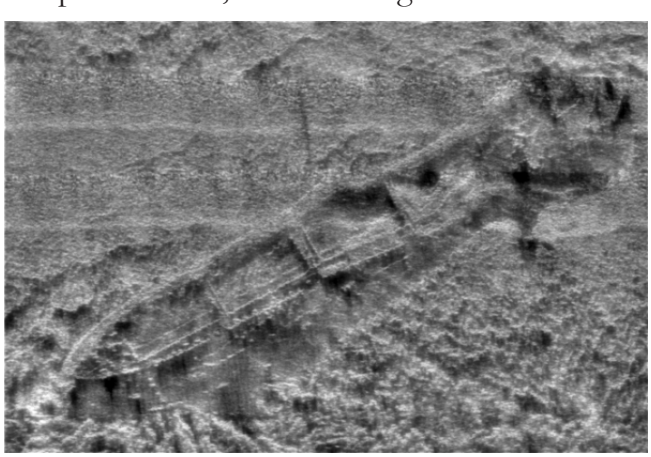

Fig. 3. *The result of applying the Laplacian to the image in Fig. 2.*

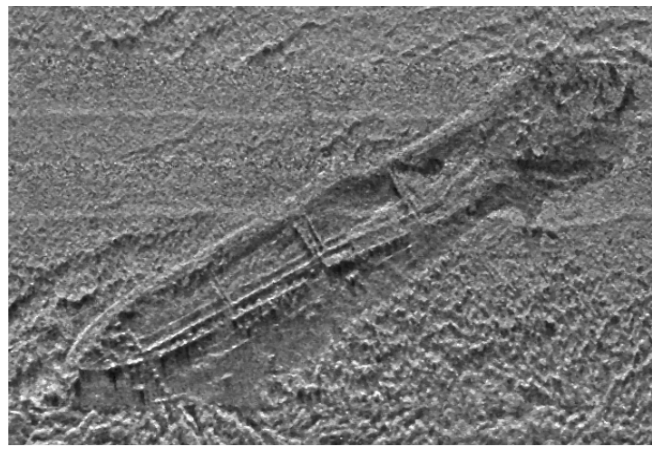

Fig. 4. *The result of applying median filtering to the image in Fig.1.*

overall contrast of the image. Therefore, as an additional step, we will sharpen Fig. 2 using the Laplacian [13]. The result of this operation is shown in **Fig. 3**.

For comparative analysis, as an alternative method for combating speckle noise, we use the commonly used median filtering with a square kernel of 3 by 3 pixels. The processing result is shown in **Fig. 4**.

Volumetric views of spatial brightness for images of Figures 1-4 are shown in **Fig. 5**.

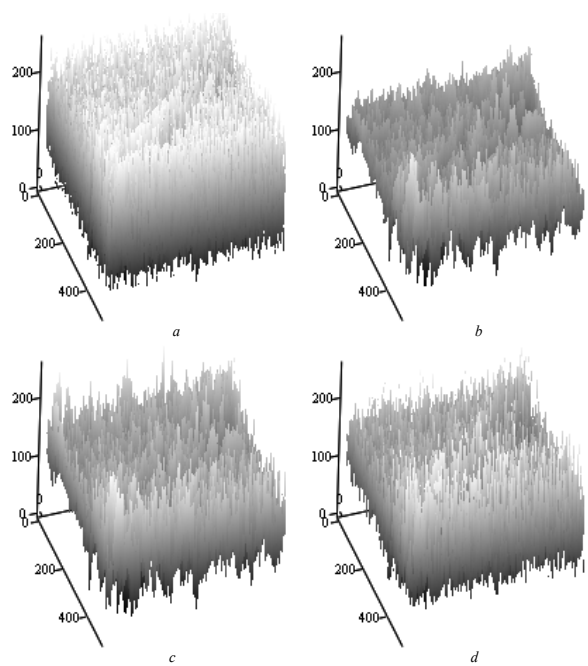

Fig. 5. *Volumetric view of the corresponding spatial brightness of the original sonar image (Fig. 1) - (a); original image processed by MRL (Fig. 2) - (b); original image processed by MPL and Laplacian (Fig. 3) - (c); original image after median filtering (Fig. 4) - (d).*

Along the vertical axis, the values of pixel brightness are plotted in grayscale (from zero - black, to 255 - white). The two remaining axes of the volumetric Fig. 5 show the coordinates of the brightness pixels on the image field. Fig. 5*b* - the result of using the MRL, clearly demonstrates a significant decrease in the level of speckle noise relative to the initial sonar image - Fig. 5*a*. This can be seen in the structure of the volumetric drawings. The original image is noisy with speckles all over the field, while the MRL processing, removing bright spots, leaves the contours of the sunken ship and the bottom topography intact. **Table 1** shows the statistical characteristics of the spatial brightness of the images. The root mean square deviation (RMSD) of the brightness in the image of the processed MRL is equal to 29, which is significantly less than the RMSD of the original one which is 49.

Fig. 5*c* is the action of the Laplacian in Fig. 5*b*. As mentioned above, this improves the sharpness after applying MRL to the original sonar image. Table 1 shows that the statistical characteristics of the MRL processing plus the Laplacian (Fig.5*c*) are very close to the alternative method - median filtering (Fig.5*d*) of the initial sonar image. The standard deviations are, respectively, 33 and 34. However, the use of median filtering is less preferable, since this procedure, together with speckles, can remove useful information [6,13].

Table 1

Statistical characteristics of spatial brightness in images

	Original sonar image	Sonar image, MRL processing	Sonar image, MRL processing and Laplacian	Sonar image, Median filter processing
Average brightness value	117	118	117	113
Root mean square deviation of Brightness	49	29	33	34

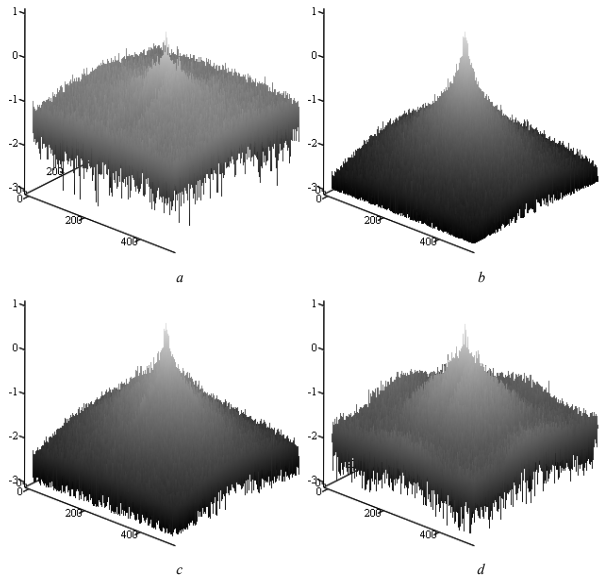

Fig. 6. *Amplitude spatial spectra on a logarithmic scale corresponding to the volumetric images in Fig.5. Spectra: initial sonar image (Fig. 1) - (a); the original image of the processed MRL (Fig. 2) - (b); the original image processed by MRL and Laplacian (Fig. 3) - (c); original image after median filtering (Fig. 4) - (d).*

Fig. 6 shows in a logarithmic scale the amplitude spatial spectra of the studied images with a size of 668 by 512 pixels. The indexing of Fig. 6 corresponds to the letters of Fig. 5.

The spectrum of the original image of the processed MRL (Fig. 6*b*), within the framework of the technique, was renormalized to the model of the universal reference spectrum (URS), i.e. to a model of the spectrum of a "good" quality grayscale optical image [8,9]. And, since sonar images are very different in structure from optical images, then as a "payment" for noise reduction, as a result of applying the MRL to the original figure 1, the effect of "fogging" or "blurring" of the image appears - Fig. 2. On the spectra, this can be seen as a decrease in the level of high frequencies in Fig. 6*b* relative to Fig. 6*a*. To increase the overall sharpness of the image, the Laplacian was then applied, which caused some increase in high frequencies - Fig. 6*c*. The spectrum after median filtering turns out to be slightly modulated (Fig. 6*d*), which may indirectly indicate possible undesirable changes in the image structure.

3. CONCLUSION

This article is devoted to testing the application of MRL to sonar images in order to improve their quality. It was found that the application of MRL to sonar images significantly reduces speckle noise. This is because the method of renormalization with limitation, by definition, renormalized the sonar image spectrum to a universal reference spectrum (URS) model, which is a model of the spectrum of a "good" quality grayscale image [8,9]. Due to the fact that sonar images in their structure differ significantly from optical images, as a "payment" for suppression of speckle, as a result of the use of MRL, the effect of "fogging" or slight "blur" of the image appears. To increase the overall sharpness of the image, it is proposed to use luminance transformations (for example, Laplacian) [13]. The use of median filtering in this problem is less preferable, since this procedure, together with speckles, can also remove useful information. All of the above allows us to conclude that the application of MRL to sonar images can significantly reduce speckle noise.

REFERENCES

1. Razmanov VM, Krivtsov AP, Dolotov SA. Specific features of measuring seafloor topography with an interferometric side-looking sonar. *Journal of Communications Technology and Electronics*, 2006, 51(1):52–58. DOI: 10.1134/S1064226906010074.
2. Alexandru Isar, Ioana Firoiu, Corina Nafornita and Sorin Moga SONAR Images Denoising. September 2011. DOI: 10.5772/19190. In book: *Sonar Systems,* https://www.intechopen.com/books/sonar-systems/sonar-images-denoising.
3. Achim A, Bezerianos A, Tsakalides P. Novel Bayesian Multiscale Method for Speckle Removal in Medical Ultrasound Images. *IEEE Transactions on Medical Imaging,* 2001, 20(8):772-783.
4. Ghazel M, Freeman GH, Vrscay ER. Fractal image denoising. I*EEE Transactions on Image Processing*, 2003, 12:1560-1578.
5. Ilyushin SV. Speckle suppression in medical ultrasound images using fractal coding. *T-Comm: Telekommunikatsii i transport*, 2011, 3:22–26 (in Russ.).
6. Kokoshkin AV. Using the method of renormalization with limitation for medical ultrasound image processing. *Journal of Radioelectronics* [*electronic journal*], 2020, №10, https://doi.org/10.30898/1684-1719.2020.10.1 (in Russ.).
7. Kokoshkin AV. Application of the method of renormalization with limitation to remote sensing images obtained with synthetic aperture radars. *Journal of Radioelectronics* [*electronic journal*], 2021, №3, https://doi.org/10.30898/1684-1719.2021.3.4 (in Russ.).
8. Gulyaev YuV, Zrazhevsky ÀYu, Kokoshkin AV, Korotkov VA, Cherepenin VA. Correction of the spacial spectrum distorted by the optical system using the reference image method. Part 3. General-purpose reference spectrum. *Journal of Radioelectronics* [*electronic journal*], 2013, №12, http://jre.cplire.ru/jre/dec13/3/text.html (in Russ.).
9. Kokoshkin AV, Korotkov VA, Korotkov KV, Novichihin EP. Using the method of renormalization limited to restore the distorted image in the presence of interference and noise with unknown parameters. *Journal of Radioelectronics* [*electronic journal*], 2015, №7, http://jre.cplire.ru/jre/jul15/4/text.html (in Russ.)
10. Kaevitser VI, Krivtsov AP, Razmanov VM, Smolyaninov IV, Elbakidze AV, Denisov EY. Development and test results of hydroacoustic system for studying the bottom of the shelf zone of the Arctic sea. *Journal of Radioelectronics* [*electronic journal*], 2016, №11. http://jre.cplire.ru/jre/nov16/1/text.pdf (in Russ.)
11. Smolyaninov IV. Program for drawing a sonar image of the sea floor on a geographical

map. *Certificate of state registration of a computer program №2018618950* от 21.08.2018.

12. Kokoshkin AV, Korotkov VA. Program for the implementation of the renormalization method with a limitation for processing radio images. *Certificate of state registration of a computer program № 2016661952* dated 26.10.2016.
13. Gonzalez RC and Woods RE. *Digital Image Processing*. Prentice Hall, International Version 3rd Edition, NJ, 2012:1071.

DOI: 10.17725/rensit.2021.13.383

The exploration of wave processes in the Arctics geological layers in the presence of the ice field

Polina V. Stognii

Educational Scientific and Experimental Center of Moscow Institute of Physics and Technology, https://kmipt.ru/
Dolgoprudny 141701, Moscow region, Russian Federation

E-mail: stognii@phystech.edu

Igor B. Petrov, Nikolay I. Khokhlov

Scientific Research Institute for System Analysis of Russian Academy of Sciences, https://www.niisi.ru/
Moscow 117218, Russian Federation

E-mail: petrov@mipt.ru, k_h@inbox.ru

Received 09.03.2021, peer-reviewed 09.13.2021, accepted 09.20.2021

Abstract: **The Arctic shelf zone is a very important region in our country due to the huge amounts of hydrocarbons, located there. The exploration of this region is difficult because of the presence of lots of various ice constructions, in particular, ice fields. While carrying out the seismic prospecting works, the reflected waves from the ice field contribute much to the seismograms. It sufficiently complicates the process of further interpretation of the seismograms. Only a few works are devoted to modelling the seismic waves spread through the geological layers of the Arctics in the presence of an ice field as this theme is rather new and needs deeper investigation. In this work we present the results of the investigation of the seismic waves spread in models with an ice field for the 3D case using the grid-characteristic method. The modelling results (wave fields of the velocity distribution and seismograms) allow to identify the reflected waves from the ice field from other waves. In addition, we carried out the comparative analysis of the wave fields and seismograms for the 2D model with an ice field on the surface of the calculated area for the problem description from the work of other authors. The results demonstrate a good qualitative coincidence under different approaches to the solution of the problem.**

Keywords: **seismic prospecting, numerical modelling, grid-characteristic method, ice field.**

UDC 519.63

Acknowledgments: The study was carried out with the financial support of the Russian Foundation for Basic Research within the framework of the scientific project No. 20-31-90034.

For citation: Polina V. Stogniy, Igor B. Petrov, Nikolay I. Khokhlov. The exploration of wave processes in the Arctics geological layers in the presence of the ice field. *RENSIT*, 2021, 13(3):383-388. DOI: 10.17725/rensit.2021.13.383.

Contents

1. INTRODUCTION

Ice and different ice structures (icebergs, ice hummocks) bring in the significant noise into seismograms in the form of additional seismic waves [1,2]. Then, the seismograms are hard to interpret and separate the useful information about the reflected waves from hydrocarbon deposits from the noise, presented by the reflections from ice constructions. Besides, in

the ice field additional waves spread along the whole surface of ice, which contribute much to the seismograms in the form of numerous reflections from the borders ice-air and ice-water.

In this work we carry out the research of influence of the ice field on the results of modeling – wave fields of the velocity distribution and seismograms. The ice field in the Arctic shelf zone is characterized by a small layer width in comparison with the length of the spreading waves, which demands the particular approach to the research conduction. The analytical solutions to the problems of the seismic waves spread in the models ice-water do not take into account all types of waves (Rayleigh waves, Scholte waves [3]), which appear in the ice layer in this kind of problems, and it leads to the incorrect or incomplete solution. In this work the solution to the problem of the seismic waves spread from the impulse source, located on the surface of the ice field, is carried out with the use of the direct numerical modeling by the grid-characteristic method of the third order of accuracy.

We conducted the computations of the model from [4] in order to compare the applied approach with the approach of other authors to the exploration of similar problems. The results demonstrated a good qualitative coincidence.

2. THE DETERMINANT EQUATIONS

For describing the seismic waves spread in geological media, we used the linear-elastic system of equations [5]:

$$\rho\frac{\partial \mathbf{v}}{\partial t}=\left(\nabla\cdot\boldsymbol{\sigma}\right)^{\mathrm{T}},$$
$$\frac{\partial \boldsymbol{\sigma}}{\partial t}=\lambda(\nabla\cdot\mathbf{v})\mathbf{I}+\mu\left((\nabla\times\mathbf{v})+(\nabla+\mathbf{v})^{T}\right), \quad (1)$$

where υ is the velocity of the seismic waves spread in the medium, σ is the Caushy stress tensor, t is the time, ϱ is the medium density, λ and μ are the Lame parameters, determining the elastic properties of the material.

3. NUMERICAL METHOD

The system of equations (1) was solved using the grid-characteristic method of the third order of accuracy [6,7]. We present the system (1) in the form:

$$\frac{\partial \mathbf{q}}{\partial t}+\mathbf{A}_x\frac{\partial \mathbf{q}}{\partial t}+\mathbf{A}_y\frac{\partial \mathbf{q}}{\partial t}=0. \quad (2)$$

where matrixes $\mathbf{A}_x$ and $\mathbf{A}_y$ are made out of the coefficients of the system (1), the vector $\mathbf{q}$ consists of three components of the Caushy stress tensor and two components of the velocity vector: $q=\{\sigma_{xx},\sigma_{yy},\sigma_{xy},v_x,v_y\}$..

Then, we apply the method of splitting by the space coordinates and obtain two 1D systems of equations:

$$\frac{\partial \mathbf{q}}{\partial t}+\mathbf{A}_i\frac{\partial \mathbf{q}}{\partial i}=0,\ i\in\{x,y\}. \quad (3)$$

Now we examine the system (3), for example, for the x coordinate:

$$\frac{\partial \mathbf{q}}{\partial t}+\mathbf{A}_x\frac{\partial \mathbf{q}}{\partial x}=0. \quad (4)$$

The system (4) is hyperbolic, then it can be presented in the form:

$$\frac{\partial \mathbf{q}}{\partial t}+\boldsymbol{\Omega}_x\boldsymbol{\Lambda}_x\boldsymbol{\Omega}_x^{-1}\frac{\partial \mathbf{q}}{\partial x}=0. \quad (5)$$

In (5) $\boldsymbol{\Omega}_x$ is the matrix, made out of the eigen vectors of the matrix $\mathbf{A}_x$, $\boldsymbol{\Lambda}_x$ is the diagonal matrix with the eigen values $\{-c_p, c_p, -c_s, c_s, 0\}$ on the diagonal, c_p and c_s are the longitudinal and the transverse sound velocities, correspondingly:

$$c_p=\sqrt{(\lambda+2\mu)/\rho},\ \ c_s=\sqrt{\mu/\rho}. \quad (6)$$

The similar transformations can be made for the system (3) for the coordinate y.

After the variable change $\omega=\boldsymbol{\Omega}_x^{-1}q$, the system (5) will look as:

$$\frac{\partial \omega}{\partial t}+\Lambda_x\frac{\partial \omega}{\partial x}=0. \quad (7)$$

The system (7) consists of five equations, each of which can be solved by any finite-difference scheme. In this work we solved the system (7) with the help of the Rusanov scheme of the third order of accuracy [8]:

$$(p_i)_m^{n+1} = (p_i)_m^n + \\ + \lambda_i \tau \frac{6(p_i)_{m-1}^n - 3(p_i)_m^n - 2(p_i)_{m+1}^n - (p_i)_{m-2}^n}{6h} + \\ + \frac{(\lambda_i \tau)^2}{2} \frac{(p_i)_{m+1}^n - 2(p_i)_m^n + (p_i)_{m-1}^n}{h^2} + \\ + \frac{(\lambda_i \tau)^3}{6} \frac{(p_i)_{m-2}^n - 3(p_i)_{m-1}^n + 3(p_i)_m^n - (p_i)_{m+1}^n}{h^3}. \quad (8)$$

The system (8) is represented for the positive eigen values.

4. THE BORDER AND CONTACT CONDITIONS

On the side and low borders of the model we established the non-reflective boundary condition. On the upper contact border between ice and air the free boundary condition was used [9, 10].

Between the ice layer and the water layer the free slip contact condition was established.

$$v_n^1 = v_n^2 = V_n. \quad (9)$$

$$f_n^1 = -f_n^2. \quad (10)$$

$$f_\tau^1 = -f_\tau^2 = 0. \quad (11)$$

The condition (9) means the equality of the normal components of the velocity on the contact border between the layers 1, 2. The condition (10) means the equality of the normal components of stress tensor on the border, the condition (11) means the equality of the tangential components of stress tensor to zero on the border.

5. RESULTS

We examined the model of a heterogeneous medium with an ice field. The model consisted of the water layer 200 m high and the ice layer 3 m high. We computed the spread of the seismic waves from the impulse source, located on the surface of ice in the center of the calculated area. The central frequency of the impulse source was equal to 30 Hz.

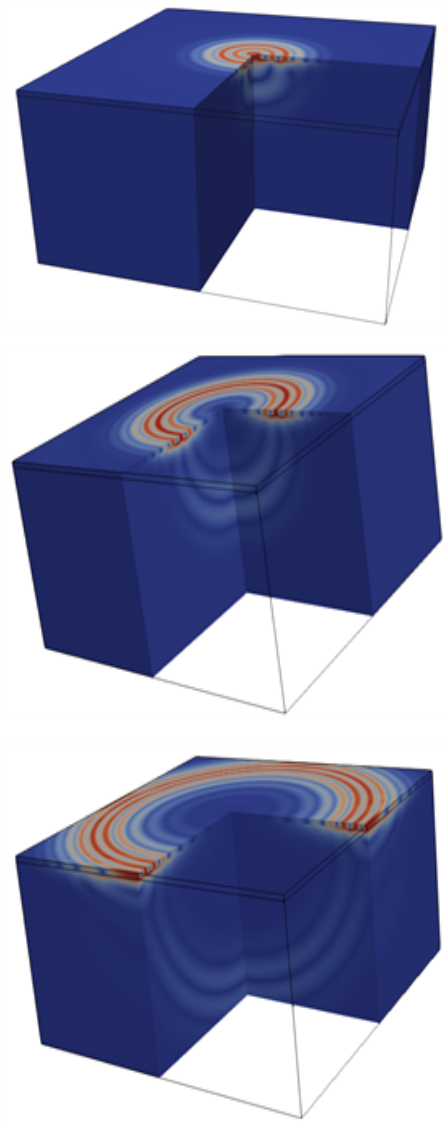

Fig. 1. *The wave fields of distribution of the velocity module for the model with an ice field at time moments 0.05 s, 0.07 s, 0.1 s.*

Fig. 1 presents the wave fields of the velocity module distribution for the model with an ice field. The wave fields give the opportunity to watch the consistent wave spread from the impulse source deep into the water layer. In the ice field the so-called multiple waves appear, which are obtained as a result of numerous reflections from the contact border ice-water and from the free border ice-air.

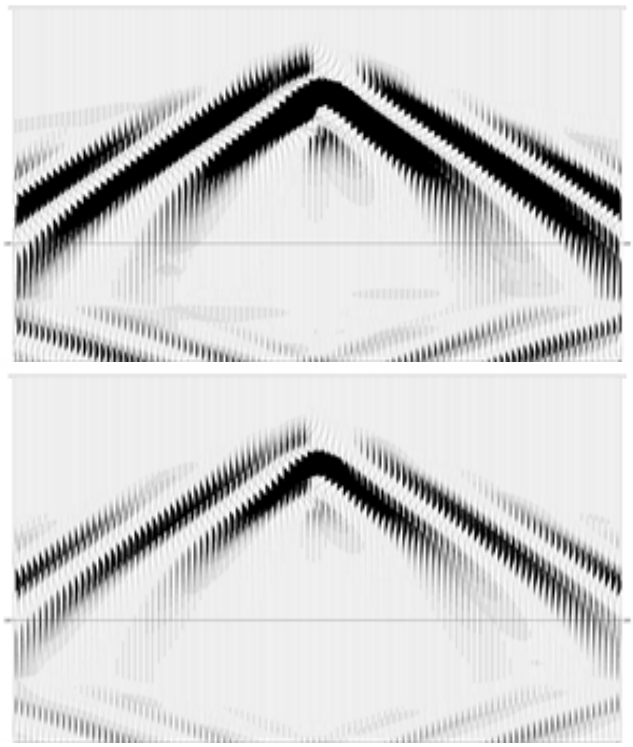

Fig. 2. *The seismograms of the recordings on the receivers for the velocity components V_x, V_z.*

On the surface of ice a row of seismic receivers was established for the registration of the reflected waves. The seismograms of the collected data on the receivers for the velocity components V_x, V_z are presented in **Fig. 2**. The number of the receiver (0-200) is depicted along the *x*-axis, the time of the arriving signal at the receiver is depicted along the y-axis. It follows from the seismograms that the spreading waves in the ice field contribute little to the result field of the reflected waves for the model, which further will allow to identify the reflected waves from oil, gas and other hydrocarbon deposits.

Next, we examined the model of a heterogeneous medium with the ice layer, the water layer and the soil layer, similar to the model from the work [4]. The density of ice was 931 kg/m^3, the density of water was 1004 kg/m^3, the soil density was 2700 kg/m^3. The longitudinal sound speed in ice was 3289 m/s, the longitudinal sound speed in water was 1448 m/s, and in soil it was equal to 1800 m/s. The transverse sound velocity in ice was 1657 m/s, and in soil it was equal to 1040 m/s. The height of the ice layer was 0.75 m, the height of the water layer was 22 m, the soil height was equal to 50 m.

The parameters of calculations were the following. The space step was 5 cm in order to consider the small height of the ice layer in the model correctly. The width of the model was equal to 800 m in order to avoid the reflections from the side borders of the model.

The seismic source of impulse with 100 Hz central frequency was located in the center of the calculated area on the surface of ice. 120 receivers of the reflected signals were located on the left from the impulse source with the distance of 3.125 m between them.

The wave field of the distribution of the velocity component V_x at 0.1 s time momemt for the described model is presented in the upper picture of **Fig. 3**, the wave field of the distribution of the velocity component V_y at the same time momemt is presented in the lower picture of Fig. 3.

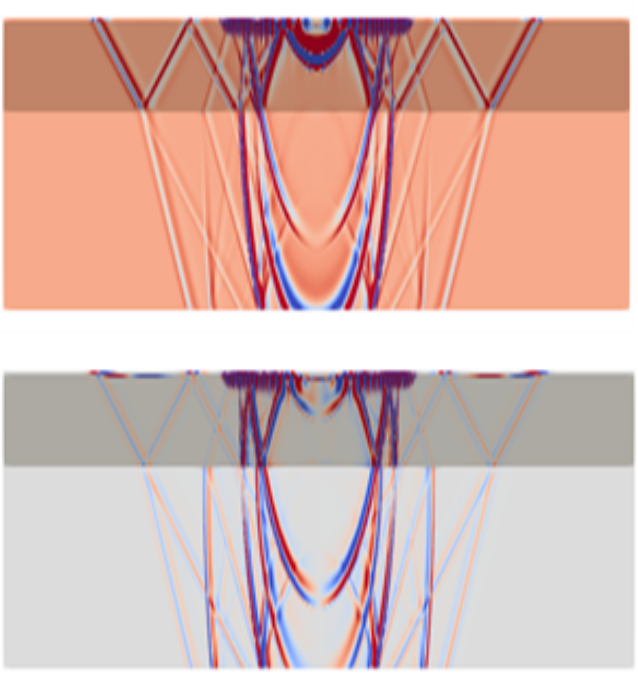

Fig. 3. *The wave fields of distribution of the velocity components V_x, V_y for the model with an ice field at time moment 0.1 s.*

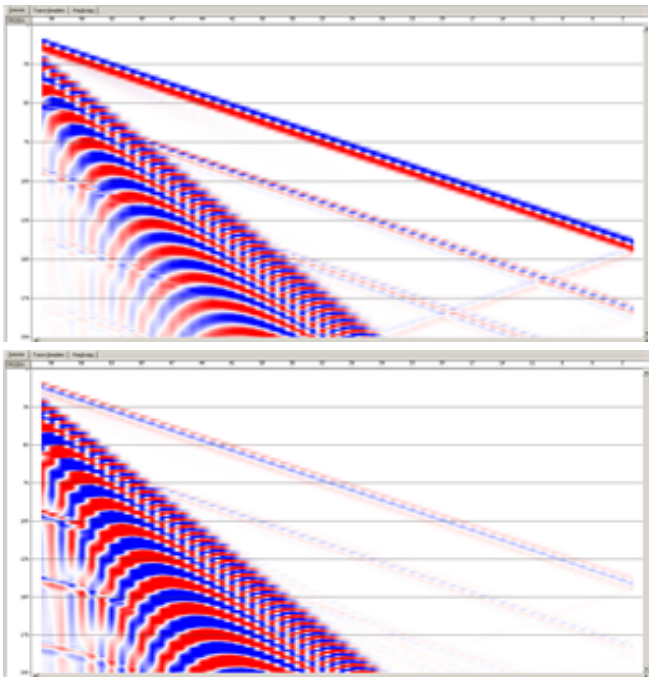

Fig. 4. *The seismograms of the recordings on the receivers for the velocity components V_x, V_y.*

The seismograms of the recordings on the receivers for the velocity components V_x, V_y for the model are presented in the upper and lower pictures of **Fig. 4**, accordingly.

The wave fields, presented in Fig. 3, and seismograms in Fig. 4 have a good qualitative coincidence with the similar modeling results from [4]. In the wave fields, different types of waves, spreading in the ice layer and in the water layer (flexural wave, longitudinal wave, Rayleigh wave and Sholte wave in the ice layer) can be detected.

6. CONCLUSION

In this work we presented the results of exploration of the seismic waves spread in the models with geological media in the presence of the ice field on the surface. The results of modeling, using the grid-characteristic method, showed the opportunity of identification of the reflected waves in the ice field from other reflected waves. We calculated the model with an ice field with the characteristics of the model from the work by other authors. The analysis of the modeling results showed a good qualitative coincidence of the results — wave fields of the velocity module distribution and seismograms. Further, we are going to carry out the research of models with other ice formations — icebergs, ice hummocks.

REFERENCES

1. Jensen K. Modelling and processing of flexural wave noise in sea ice. *Master's thesis*, 2016.
2. Landschulze M. Full wave field simulation of flexural waves in an Acoustic–Viscoelastic medium. *Arctic Technology Conference*, October 24-26, 2016. St. John's, Newfoundland and Labrador, Canada, Society of Petroleum Engineers (SPE) Publ., 2016. DOI: 10.4043/27420-MS.
3. Cherednichenko KD. On propagation of Scholte–Gogoladze surface waves along a fluid-solid interface of arbitrary shape. *Journal of Mathematical Sciences,* 2006, 138(2):5613-5622.
4. Landschulze M. Seismic wave propagation in floating ice sheets - A comparison of numerical approaches and forward modelling. *Near Surface Geophysics*, 2018, 16(5):493-505.
5. Savin GN, Rushchitskii YY, Novatskii V. The theory of elasticity. *Soviet Applied Mechanics,* 1971, 7:808-811.
6. Magomedov KM, Kholodov AS. *Grid-Characteristic Numerical Methods.* Moscow, Nauka Publ., 1988.
7. Petrov IB, Lobanov AI. *Lektsii po vychislitel'noy matematike* [Computational mathematics lectures]. Moscow, Internet-University of Informational Technologies Publ., 2006, 523 p.
8. Kholodov AS, Kholodov YaA. Monotonicity criteria for difference schemes designed for hyperbolic equations. *Comput. Math. and Math. Phys.,* 2006, 46(9):1560-1588.
9. Favorskaya AV, Zhdanov MS, Khokhlov NI, Petrov IB. Modelling the wave phenomena

in acoustic and elastic media with sharp variations of physical properties using the grid-characteristic method. *Geophys. Prospecting,* 2018, 66(8):1485-1502.

10. Favorskaya AV, Petrov IB. Grid-characteristic method. *Smart Innovation, Systems and Technologies*, 2018, 90:117-160.

DOI: 10.17725/rensit.2021.13.389

Physiological aspects of visual information perception of the oculomotor apparatus

Vladimir I. Grachev, Vladimir V. Kolesov, Viktor I. Ryabenkov

Kotelnikov Institute of Radioengineering and Electronics, Russian Academy of Sciences, http://www.cplire.ru/
Moscow 125009, Russian Federation

E-mail: grachev@cplire.ru, kvv@cplire.ru, ryabenkov.vi@list.ru

Galina Ya. Menshikova

Lomonosov Moscow State University, http://www.psy.msu.ru/
Moscow 125009, Russian Federation

E-mail: menshikova@psy.msu.ru

Received Sept. 06. 2021, peer-reviewed Sept. 13. 2021, accepted Sept. 20. 2021

Abstract: **The individual characteristics of the human visual apparatus are associated with the anatomical and psychophysiological parameters of his body. Based on the EyeTracking technology, the physiological aspects of the perception of visual information by the oculomotor apparatus, which are not associated with active cognitive activity, have been investigated. The individual features in the size of fixation when reading text and examining halftone graphic objects in various people have been investigated. The time durations of fixations in different people, associated with the process of accommodation, as well as the internal structure of fixations, were investigated. It is shown that the trajectory of the gaze shift in fixation has an internal heterogeneous structure. The total trajectory of eye movement in the fixation area is determined by a set of successive clusters. This fixation structure is apparently associated with the processes of restoration of the photosensitivity of rhodopsin in the photoreceptors of the retina. All the above studies of the fixations of various subjects on the basis of various images showed that the oculomotor system, taking into account the physiological characteristics of the visual apparatus, is equally controlled by the "video processor" of the brain when the eye is accommodated to the image elements. And the only objective individual feature of human vision, which uniquely characterizes the perception of graphic information, is the value of the average displacement in fixation. It is she who is the "visiting card" of the subject and remains practically unchanged both when reading and when examining halftone images and in test validation with forced fixation of the gaze.**

Keywords: **oculomotor reactions (oculomotorics), technology of eye-tracking, fixation, saccades, reading text, perception of graphics, individual characteristics of the visual apparatus**

UDC 004.932.2; 159.931

Acknowledgments: This work was financially supported by the Russian Ministry of Science and Higher Education (No. 0030-2019-0016) and Russian Foundation for Basic Research (grant No. 19-29-07392).

For citation: Vladimir I. Grachev, Vladimir V. Kolesov, Galina Ya. Menshikova, Viktor I. Ryabenkov. Physiological aspects of visual information perception of the oculomotor apparatus. RENSIT, 2021, 13(3):389-402. DOI: 10.17725/rensit.2021.13.389.

Contents

1. INTRODUCTION

In the perception of the external world, the leading place belongs to the organ of vision. It takes light to see. The human organ of vision is able to perceive light of different wavelengths, its different brightness, shape and size of objects, to orient itself in space, can estimate the distance between objects, their volume.

It has now been proven that we see not with our eyes, but with our brain. Those. object recognition takes place in the brain, which receives only "raw" information about the distribution of light spots in space from the retina. A large number of brain structures are involved in the processing of visual signals, the interconnections of which are numerous and not fully understood.

The combined function of the oculomotor apparatus is to provide a focused, clear image of the outside world on the two retinas. For both eyes, the task of tracking an object must be performed with an accuracy of several arc minutes - otherwise, the visible image will be doubled.

All oculomotor reactions are designed to provide the main task of the visual apparatus - the maximum human perception of visual information. The physiology of vision is provided by various systems that make up the visual apparatus. The optical system of the eyeball focuses images on the retina, the pupil regulates the amount of light falling on the retina, and the muscles of the eyeball ensure its continuous movement.

The human visual system consists of a peripheral part, represented by the optical visual tract in the eyeball, pathways that include the optic nerve, the axons of the optic neurons, and the central part of the system in the brain. The central section consists of the subcortical centers and the cortical visual center of the occipital lobe of the brain.

For the perception of electromagnetic radiation in the visible range, which is the basis of vision, are the receptors of a protein nature contained in the photoreceptor membrane of the cells of the retina of the eye - rhodopsin and iodopsin. The visual pigments of the cones are iodopsins, which are tuned to different parts of the spectrum, and the rods have only rhodopsin, which can distinguish only the emerald part of the spectrum from colors.

The retina is formed by two main types of visual cells - rods with light-sensitive rhodopsin (about 120 million cells per human retina) and cones with light-sensitive iodopsin (about 7 million cells). Cones, concentrated predominantly in the central region of the retina (called the fovea), function only in bright light and are responsible for color vision and sensitivity to small details, while the more numerous rods are responsible for vision in low light and turn off in bright light. Thus, of all existing mammals, only the higher primates, including humans, have trichromatic vision. The presence of two photoreceptor systems (cones and rods), differing in light sensitivity, provides adjustment to the changing level of external illumination.

The absorption of a light quantum by rhodopsin leads to a number of its photochemical transformations - photolysis. Photolysis occurs in several successive stages, each of which has a corresponding duration. The primary event associated with the absorption of a photon by rhodopsin takes about 200 fs. This event is followed by the formation within milliseconds of several intermediate forms of rhodopsin, each of which is characterized by its own absorption spectrum.

Light activation of rhodopsin is the only light-dependent process. All other stages of photolysis are light-independent; they are associated with molecular conformational rearrangements and are a consequence of this primary act of light absorption. The electrophysiological response of a photoreceptor cell to a light stimulus lasts for hundreds of milliseconds and then stops due to the existence of mechanisms responsible

for turning off the light-dependent cascade and restoring the dark state.

The cones located in the central part of the retina provide central shaped vision and color perception. Central shaped vision is the ability to discern the shape and details of the object in question due to visual acuity. The retina of the mammalian eye is called an inverted organ because photoreceptors, which are the first working link of the retina, are located in the lower layer, and above them are two layers of neurons that collect information from photoreceptors and transmit it to the brain.

The most important area of the retina is the macula or macula, which determines visual acuity. The spot diameter is 5-5.5 mm, it differs in color from the surrounding tissues, since the underlying pigment epithelium is more intensely colored here. In the center of the macula is the fovea, or fovea, which forms as a result of the thinning of the retina. The central fossa makes up 5% of the optic part of the retina, but up to 10% of all cones are concentrated in it. In the middle of the central fovea lies a dimple - a depression with a diameter of 0.2-0.4 mm, it is the place of the greatest visual acuity, it contains only cones (about 2500 cells).

In humans and other great primates (but not all mammals), the fovea reaches about 700 micrometers in diameter. In the fovea, the greatest visual activity is observed in comparison with other parts of the retina, which is caused by structural and compositional changes in this region. A feature of this zone is the shift of the cells of the proximal retinal neurons to the side, so that the light reaches the photoreceptors with minimal distortion. Fovea consists mainly of cones, the number of which increases as it moves towards the foveola (light point in the center of the fovea). This system provides a very high resolution of visual information, which is caused by another interesting mechanism: each cone in the fovea is connected to only one bipolar and one ganglionic cell. In other parts of the retina, each bipolar and ganglionic cell works with multiple photoreceptors, rather than one, as in the fovea.

An unusual anatomical feature of the retina is that it is directed by photoreceptors to the pigment epithelium. This enables photoreceptors to efficiently restore visual pigments. Photoreceptors are very sensitive to the environment, as they constantly have to deal with the effects of a large stream of photons and free radicals. Stacking photosensitive elements in the outer segment of photoreceptors makes possible the daily planned restoration (renewal) of these elements. In this case, new structures are collected at the base of the photoreceptors, while the old elements at the apex are destroyed by neighboring cells of the retinal pigment epithelium. Complete renewal of the outer segment takes ~ 10 days in higher vertebrates and 6-9 weeks in lower vertebrates.

Visual acuity is the ability of the eye to perceive two points located at a minimum distance from each other as separate. The minimum distance at which two points are visible separately depends on the anatomical and physiological properties of the retina. If the images of two points fall on two adjacent cones, they will merge into a short line. Two points will be perceived separately if their images on the retina (two excited cones) are separated by one unexcited cone. Thus, the diameter of the cone determines the magnitude of the maximum visual acuity. The smaller the diameter of the cones, the greater the visual acuity. For most people, the threshold angle of view (angular size of an object) corresponds to one minute. All tables for the study of visual acuity are built on this principle.

The electrophysiological effect of a photoreceptor cell on a light stimulus lasts for hundreds of milliseconds and then stops due to special mechanisms that "turn off" excitation and restore the "dark" state. The most difficult thing in the process of returning the photoreceptor to the dark state is the restoration

of the photosensitivity of rhodopsin. The slowest reaction is the breakdown of the rhodopsin complex.

From the retina, an electrical signal is transmitted along the optic nerve to a specialized cell cluster located deep in the brain - the so-called external (lateral) geniculate body. The signal then enters the visual cortex located in the back of the brain. Initially, information enters the primary visual zone, from where, after passing through several layers of synaptically connected cells, it is transmitted to neighboring zones of a higher order, where, ultimately, the image of the object we are looking at is formed.

Visual functions are closely related to each other and constitute a single whole, called the act of vision. At the same time, rods and cones cannot perceive and transmit information to neurons about the movement of a visual signal in one direction or another.

The oculomotor apparatus and binocular vision are a complex sensorimotor mechanism, the physiological significance of which is determined by its two main functions: motor (motor) and sensory (sensitive). The motor function ensures the guidance of both eyes, their visual axes and the central pits of the retinas to the object of fixation; sensory - fusion of two monocular (right and left) images into a single visual image.

The position of each eye is controlled by six separate muscles, two of them - the outer line and the inner line - control the horizontal rotation of the eyes, carried out when looking from left to right or from close objects to distant ones. The other eight muscles, four in each eye, control the raising and lowering of the eyes, i.e. turn in the vertical plane.

Any movement of one eye is almost always part of a more complex set of movements. If we look at an object very close, both eyes turn inward. If we look to the left, the right eye turns inward and the left eye turns outward. If we look up or down, both eyes turn up or down together. All these movements are controlled by the brain. Almost every movement that is performed is the result of the joint contraction of many muscles and the relaxation of many others.

It would be natural to expect that when examining the world around us, our eyes will smoothly scan the entire scene with continuous movements. In fact, when fixing an object, the eyes are set so that the image of this object falls into the region of the central fovea of both eyes. Then the eyes are held in this position for a short time, and then the eyes jump abruptly to a new position and fix a new target, which is located somewhere else in the visual field and attracts attention by moving somewhat relative to the background or having some then an interesting shape. During such a jump, or saccade, the speed of eye movement is so high that the visual system does not have time to respond to the movement of the image along the retina and we simply do not notice it. (It is possible that vision is disabled during the leap period by some kind of neural circuitry that links the oculomotor centers to the main visual pathway).

Jumping eye movements (saccades) occur when looking at stationary objects. Rapid turns of the eyeball (10-80 ms) alternate with periods of motionless fixation of the gaze at one point (200-600 ms).

Thus, the process of examining the visual field while reading or simply looking at the surrounding space consists of a series of rapid jumps from one point to another.

The task of the oculomotor system, apparently, is not to keep the image motionless on the retinas, but to prevent its smooth continuous displacement.

When tracing a moving scene, the gaze fixes some object and maintains its fixation by smoothly moving the eyes until the object leaves the field of view. Then a jump is made and a new object is fixed. This sequence of eye movements - a smooth tracing movement in

one direction, and then a saccade in the other is called nystagmus.

When considering a motionless scene and fixation at any point, this fixation is not absolutely motionless. Despite all attempts to rigidly fix the point, the eyes do not remain completely at rest, but perform continuous micromovements, called microsaccades. They occur several times per second and are directed more or less randomly, reaching an amplitude of 1–2 arc minutes [1].

It is known that if the image on the retina is artificially stabilized by special methods, eliminating its displacement relative to the retina, then the visual image after about a second seems to "fade" and the field of view becomes completely empty! (The simplest way to stabilize is to attach a point light source to a contact lens; when the eyes move, the light source also moves and the light spot quickly becomes invisible.) If, after stabilization, the image on the retina is even slightly displaced, the light spot immediately reappears.

Thus, the visual system ensures that cells are insensitive to stationary objects. At the same time, microsaccades are necessary in order to continuously see stationary objects. It can be assumed that complex cells of the cortex, which are especially sensitive to the movement of the stimulus, are involved in this process, but, probably, cells with directional selectivity are not involved, since microsaccades are clearly randomly distributed in directions.

On the other hand, the directional selectivity mechanism should be useful for detecting the movement of objects relative to a stationary background, signaling the presence of movement and its direction. In order to follow a moving object against a stationary background, you need to fix the object and move your gaze with it. In this case, the image of the entire scene will move along the retina. The movement of all the details of the stationary background along the retina should lead to a violent activity of the cells of the cerebral cortex.

Therefore, the mechanism of how the image of reality is formed in the brain is not only optics and chemical reactions occurring on the retina. Our brain plays the most important role in creating this picture - and not only the visual cortex, which makes the figures three-dimensional, separates them from the background and paints them in the desired colors, but also the other departments that are responsible for vital functions.

The purpose of this work is to study the individual characteristics of the human visual apparatus using a special technology for recording eye movements, which allows one to clearly demonstrate all the features of the behavior of the oculomotor apparatus. This technology is widely used in various tasks related to the visual system, research in the field of psychophysiology, psychology, cognitive linguistics, medicine and other areas of science, technology, and even sports, and even in marketing research to assess the effectiveness of print advertising and design.

2. EYETRACKING TECHNOLOGY

EyeTracking (eye tracking or tracking the movement of the eyes) is a method that determines the coordinates of the gaze: the point of intersection of the optical axis of the eyeball and the plane of the observed object or screen, on which some visual object is located. The Eye Tracker recognizes and records pupil positions and eye movements. It can be worn on the head (glasses) or stationary (a special stand in front of the monitor screen). There are several technologies available to record eye movements. Currently, a special high-precision infrared camera is most often used, which captures the pupil and the direction of the respondent's gaze [2].

The studies were carried out on the iView X ™ HiSpeed 1250/500 device of the German company SMI (HSSMI), designed for high-speed video recording of eye movements in the infrared range. It consists of a recording high-speed video camera, an infrared light source, a

column-column with a head rest and a chin rest, a monitor for displaying graphic objects, a personal computer, and a software package. Assessment of the directionality of eye movements is based on video information about the relative location of the centers of the pupil and corneal flare (Pupil center / corneal reflex method). The frequency of video recording of the surface of the eyes in monocular mode is 1250 or 500 Hz. In the video recording system, the subject's head is fixed using an ophthalmic frame, which avoids additional calculations associated with the subject's head movement [3].

Although, in general, the EyeTracking equipment satisfactorily reproduces micro- and macro-eye movements, there are disturbing influences that distort the picture of fixations and targeted saccadic eye rotations. The high frequency of video recording of the surface of the eyes is in itself insufficient for an adequate display of the oculomotor processes. A procedure is needed to separate the actual movements from the totality of events occurring inside the eye and on its surface. Analysis of the raw data of the coordinates of the center of the pupil and the center of the infrared flare shows that distortions are generated when the coordinates of the center of the pupil change, but with practically unchanged coordinates of the center of the flare. Since the flare mobility is considered as the main sign of the extraocular muscles work, the registered distortions are not of an oculomotor, but of some other nature. Most likely, they are caused by dynamic processes taking place inside the eyeball, for example, by the microdynamics of the structure of the pupil during sharp eye movements, or by the peculiarities of the operation of the mathematical model underlying the eye image processing program. In any case, we are talking about external factors that distort the actual picture of oculomotor activity [4].

Already the first studies have shown that the formal task assigned to the subject has a huge impact on the result of an eye-tracking experiment. A series of experiments showed that the result of the experiment depends not only on the visual stimulus, but also on the task assigned to the subject, as well as on the information that the subject expects to receive from the visual stimulus [5].

Recordings of the trajectories of eye movements showed that only a small part of the image elements attracts the subject's attention and his eyes fixate on these elements. The eye movement process reflects the human thinking process. The gaze, with some lag, follows the point where the subject's attention is directed. Thus, it is quite simple to determine which elements of the image attract the subject's attention, in what order and how often [6].

However, the records of the trajectory of eye movement show that the trajectory of the gaze and the fixation points often pass by the objects to which attention was actually drawn and only sometimes show short fixations. Thus, it was shown that it is impossible to unambiguously link directly the course of cognitive processes in the brain with the results of eye tracking experiments [7]. However, the analysis of eye movement trajectories associated with the process of accommodation in the fixation area allows one to investigate an algorithm that uses a "video processor" located in the brain to control involuntary movements of the oculomotor apparatus during visual perception of graphic information, as well as to investigate the individual physiological characteristics of the visual system of various people.

3. INDIVIDUAL FEATURES OF FIXATIONS IN THE PERCEPTION OF GRAPHIC IMAGES

Localization and identification of objects by the visual system occurs in the process of accommodation - the ability of the eye to focus on objects at different distances. At the same time, various accommodation mechanisms are triggered, providing good clear vision. The lens capsule is deformed, as a result of which the refractive power of the eye changes. The light

beams are focused on the retina, making objects clear. The oculomotor apparatus carries out micromovements of the eye in the region of the central part of the retina when the gaze fixes any object that attracts attention, while the fixation is not absolutely motionless [8].

It is known that oculomotor reactions have a decisive influence on visual acuity [9]. High visual acuity is extremely important in various life situations and for many professional tasks, from confident object recognition to driving cars and airplanes. It is well known that the optical and anatomical characteristics of the eye contribute to good vision and spatial resolution, however, the influence of individual characteristics of reflex eye movements on the characteristics of vision has hardly been studied.

3.1. Geometric parameters of fixations

An example of recording the trajectory of eye movement when examining an object is shown in **Fig. 1.** In the experiments, all graphic objects were demonstrated on a 295×520 mm monitor with a resolution of 1920×1080 pixels. In this case, the distance from the eyes to the screen was 800 mm.

Fig. 1. *The trajectory of eye movement when looking at a graphic object. The circles indicate the areas of eye fixation.*

There are various integral criteria for determining individual differences in eye movement of different observers when looking at identical images [10]. In turn, the size of the fixation in the perception of graphic images can also reflect the individual characteristics of the visual apparatus of various observers.

The external contours of fixations on real tracks have, as a rule, a rather complex configuration. In order to roughly estimate the area occupied by the fixture, it is necessary to simplify the geometry. In the first approximation, by the fixation area we mean the area of the rectangle described around the fixation, i.e. in each fix, you can find the maximum and minimum values for each coordinate, find the difference between them, and get the area of the rectangle. Estimates calculated in this way will be overestimated, but as a first approximation they give an objective idea of the real areas (sizes) of fixations and their ratio.

In **Fig. 2** shows the results of such studies in the form of area distributions for three subjects E, O and V, considering three different graphic images with different structures of T, F and W at eight different orientations, differing by rotation counterclockwise by 45° (total 24 images). The total number of fixations recorded on the tracking for all subjects is 1723. For individual subjects, this number was distributed as follows:

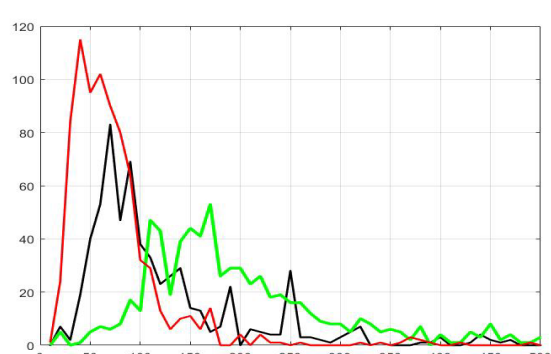

Fig. 2. *Distributions of fixations by area size for three subjects E (green), O (black) and V (red). The fixation area is plotted on the horizontal axis in mm².*

E - 551, O - 485, V - 687. It is natural to assume that the size of fixations is determined by the diameter of the fovea. when viewed, to provide a clear, specific portion of the image, it must be projected onto the fovea. In this case, a specific fragment of the image can have a variety of sizes and is not always projected onto the entire fovea area.

Fig. 2 demonstrates that all three distributions have a similar, very characteristic shape: a small number of fixations with a small area, a characteristic maximum, and a rather long tail.

If we estimate the diameter of a circular area with such an area, we get a value of about 30 mm. For the diameter of the fovea, taking into account the geometric data of the installation and considering the focal length of the lens of the order of 20 mm, we obtain approximately 750 μm, which is a somewhat overestimated value. The latter result is easily explained by a very crude method of calculating the areas of fixations.

The characteristic maxima of the distributions of individual fixation sizes for subjects E, O and V, taking into account the focal length of the lens of the eye of the order of 20 mm, fall on areas of 150, 75, and 50 mm^2. Estimation of the size of the fovea for these values of the areas of fixation gives values of the order of 400, 250, and 200 μm, respectively, which is close to its real size. The geometrical dimensions of the fixings are given in the screen coordinate system.

The size of the commits depends on the type of object being monitored. This can be shown by comparing the process of accommodation in the perception of graphic objects with different sizes. In **Fig. 3** shows the distributions of all fixations over the area for two subjects A and V. The subjects were asked to read 12 short texts. Fixations on the eye movement trajectory were analyzed. We also used the validation data before the start of measurements, when each subject undergoes an individual adjustment of the recording process by forcibly fixing

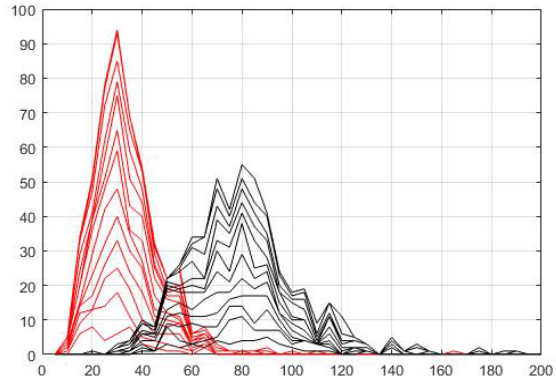

Fig. 3. *Distributions of fixations by area size for two subjects V (red) and A (black). The fixation area is plotted on the horizontal axis in mm^2.*

his gaze at the control points of the monitor screen. When plotting the graphs in Fig. 3, the distribution for fixations of the given text was added to the distribution for the previous text. The result is a cumulative distribution for the 12 texts and commits that took place in the validation. It can be seen from the figure that for each subject the distributions of fixations for all texts are extremely similar, the maxima of the distributions practically do not change their position, and the half-width of the distributions remains practically unchanged. If we compare the distribution for subject V, obtained by examining three graphic plots in eight different angular positions (Fig. 2 - red curve) with the distribution obtained for the same subject during reading, it can be noted that the maximum of the distribution has shifted towards smaller areas (from 50 to 30 mm2) and the distribution half-width also decreased from approximately 80 mm2 to 30 mm2. The decrease in the size of fixations can, apparently, be explained by the fact that when reading the text, only the central region of the fovea is involved - the foveola, because letters are significantly smaller than grayscale elements.

The case of perception in the absence of an image (imitation of fog), when the subject looks into the distance through a white sheet, is quite interesting. In **Fig. 4** shows the general distribution of lengths in fixations and saccades in the gaze trajectory for one subject in the case

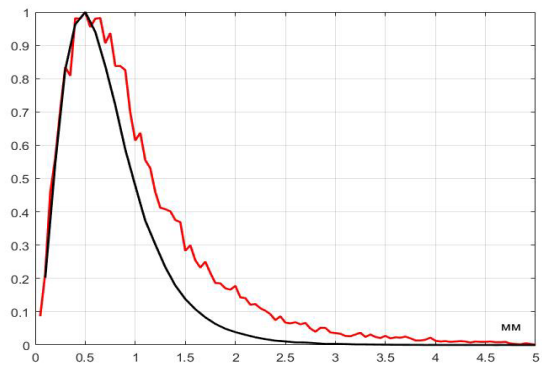

Fig. 4. *Distributions of displacements in all fixations along the length, normalized to their maximum, for one subject in the case of perception of a halftone image and in the absence of an image.*

of perception of a halftone image and in the absence of an image.

The figure shows that in the absence of an image, the video processor of the oculomotor apparatus works according to the standard algorithm, but the distribution of lengths in fixations and saccades becomes almost twice as narrow.

3.2. Duration of fixations

Various elements of the visual apparatus are involved in the perception of graphic information. In this case, the duration of fixations may be associated with some individual characteristics of the process due to both the physiological structure of the eyeball and the processes occurring in the brain [11].

From **Fig. 5** it can be seen that the maximum in the distribution of fixations by their duration for subjects in three half-tone graphic images for all subjects is approximately in the same place (0.25 s), which slightly exceeds the same value in the case of reading [12].

Fig. 6 shows the distribution of the number of fixations by their duration when reading six short texts by eleven subjects (*a, b, c, ... k*). At the same time, text no. 1 is grammatically flawless, while the rest were distorted in terms of increasing reading difficulties. Thus, 66 trajectories were processed and a separate distribution was constructed for each tracking.

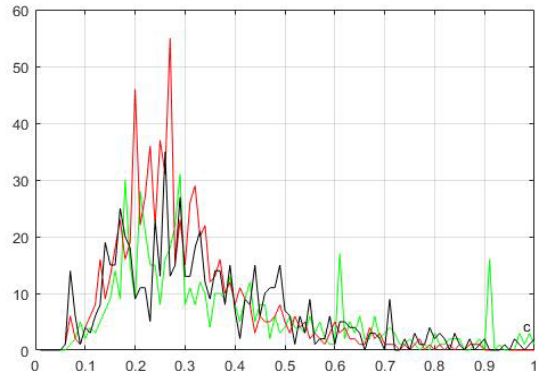

Fig. 5. *Distributions of fixations by their duration for subjects E (black), O (green) and V (red), in three graphic images rotated at eight different angles. Time is plotted along the horizontal axis in seconds.*

In this case, all distributions were the same (they contained 100 points with a step of 0.02 s), so they could be added. Such summation was performed for each text for all eleven subjects, and it is these total distributions that are shown in Fig. 6. It can be seen that due to the uniformity of the problem (reading the text) the maxima for all distributions lie within 0.2–0.25 s. At the same time, the distribution according to the first

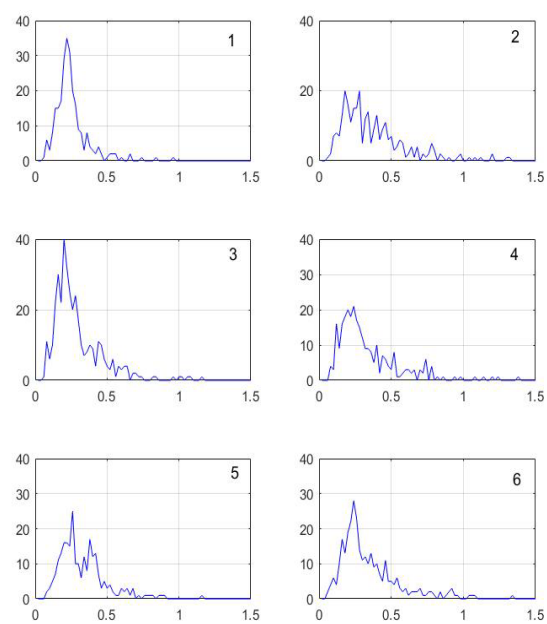

Fig. 6. *The total distribution of fixations by their duration when reading six short texts (the text number is indicated in the upper right corner) by eleven subjects (a, b, c,… k). On the horizontal axis - time in seconds.*

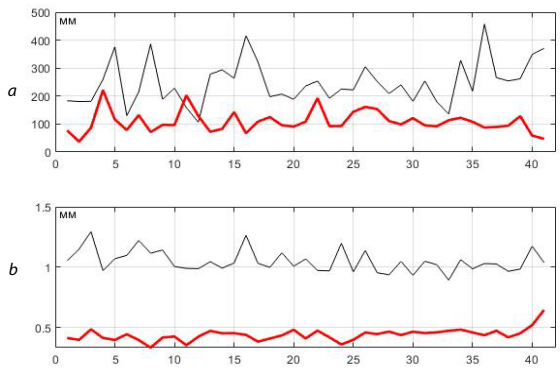

Fig. 7. *a - total length in each fixation, b - average value of displacement in each fixation for two subjects A (black) and V (red) when reading undistorted tex***t.**

(undistorted) text turned out to be the most compact. The analysis takes into account the total number of commits in the distribution.

In **Fig. 7** shows the results of fixation analysis for two subjects A and V when reading undistorted text. Shown is the total length for each fixation and the average offset for each fixation.

In **Fig. 8** shows the results of the analysis of fixations for subject V when reading the remaining five texts and points of forced fixation at checkpoints during the validation process. The figure shows that all fixation parameters for subject V are practically identical to the results and repeat the results obtained in the analysis of the first undistorted text.

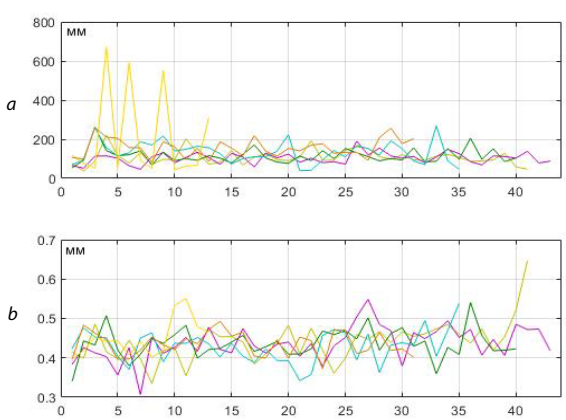

Fig. 8. *a is the total length in each fixation, b is the average value of the displacement in each fixation for the subject V when reading five texts and points of forced fixation at checkpoints and during the validation process.*

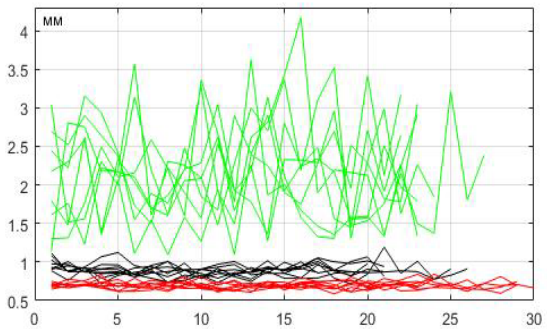

Fig. 9. *Average value of displacement in each fixation for three subjects E (green), O (black) and V (red) upon perception of eight variants of the test image Fig. 10 rotated at various angles.*

It should be noted that when performing the task of forced fixation, when the eye is deliberately held for some time at one point, the total fixation length increases several times (maxima in the initial section of the upper graph). Although forced fixation is fundamentally different from the reading process and requires additional efforts when fixing the eye, the average value of displacement in these fixations also remains practically unchanged.

In **Fig. 9** shows the results of the analysis of fixations on the trajectory of eye movement for three subjects E, O, and V when perceiving eight variants of the test grayscale image **Fig. 10** rotated at various angles. Explicit vertical and horizontal details of this drawing allow you to demonstrate the individual characteristics of the perception of a complex graphic image.

Fig. 10. *Test graphic image.*

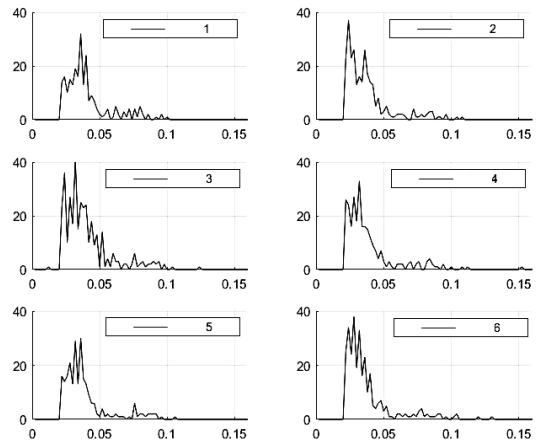

Fig. 11. *Distribution of the number of saccades in 6 texts by their duration for 11 subjects.*

All the above studies of the fixations of various subjects on the basis of various images showed that the oculomotor system, taking into account the physiological characteristics of the visual apparatus, is equally controlled by the "video processor" of the brain when the eye is accommodated to the image elements. The only objective individual feature of human vision that unambiguously characterizes the perception of graphic information is the value of the average displacement in fixation. It is she who is the "visiting card" of the subject and remains practically unchanged both when reading, and when examining halftone images, and in test validation with forced fixation of the gaze.

In **Fig. 11** shows the number of saccades in six texts according to their duration for eleven subjects [13]. Summation was performed for each text for all subjects. And in this case, the most compact is also the first cumulative distribution referring to the undistorted text. This distribution clearly shows two maximums. The first (0.03 s) is defined by lowercase saccades (intervals between words in a line). The second (0.06-0.08 s) is determined by interlinear or reverse saccades. It is also seen that due to the uniformity of the problem (reading the text), all distributions are quite similar.

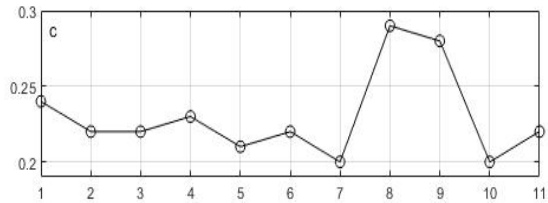

Рис. 12. *Average duration of fixation for each of 11 subjects.*

3.3. Dynamic features of the perception of graphic information

It is convenient to investigate the dynamic features of the perception of graphic information on tasks when reading texts. Apparently, the speed of reading is determined by the duration of the stay of the gaze in fixations, since the gaze is in them about 80% of the time and the main time saving can only be in fixations.

For example, analyzing the first (undistorted) text for eleven subjects, one can draw some conclusions about the individual characteristics of the reading speed. The research results are presented in **Fig. 12.** According to this parameter, subjects No. 7 and No. 10 are the best, respectively, their average gaze dwell time in fixations is 0.1965 and 0.1973 sec.

In **Fig. 13** shows the dependences of the duration of each fixation for all subjects. The figure shows that the number of fixations in subjects varies from 17 to 31, and the time spent on reading, from 4.94 to 10.2 sec.

From Fig. 13, it can be concluded that all subjects spend practically the same time on

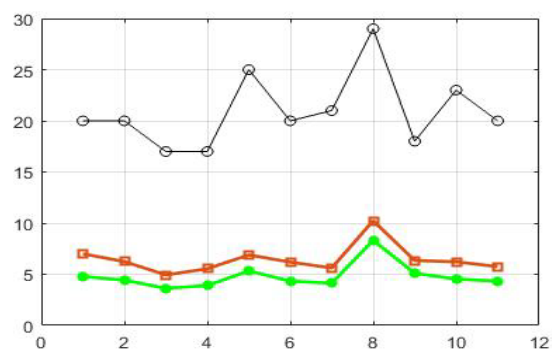

Fig. 13. *Eleven subjects read the same undistorted text. The black curve is the number of fixations in the text, the red curve is the reading duration, the green curve is the duration of all fixations in seconds.*

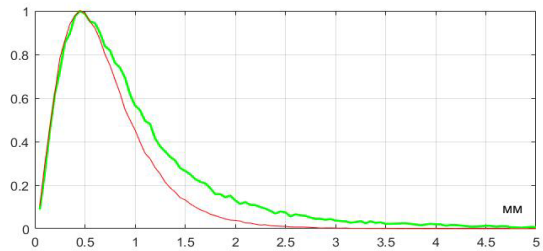

Fig. 14. *Total distributions of gaze displacements along the length in fixations, normalized to their maximum, for subject V from five different images with a break of six years.*

saccades, since the difference between the total reading time and the total duration of all fixations for them is almost constant and amounts to 1.5-2 sec.

In **Fig. 14** shows the total shift of gaze in fixations normalized to its maximum, for subject V from five different images with a break of six years [13]. It can be seen from the figure that the general nature of the perception of graphic information has not practically changed.

The duration of fixations is directly related to the total length of the gaze trajectory in fixation, which can be recorded with sufficient accuracy by the EyeTracking equipment.

In the upper images **Fig. 15** shows the gaze tracking of three subjects for the image in Fig. 10.

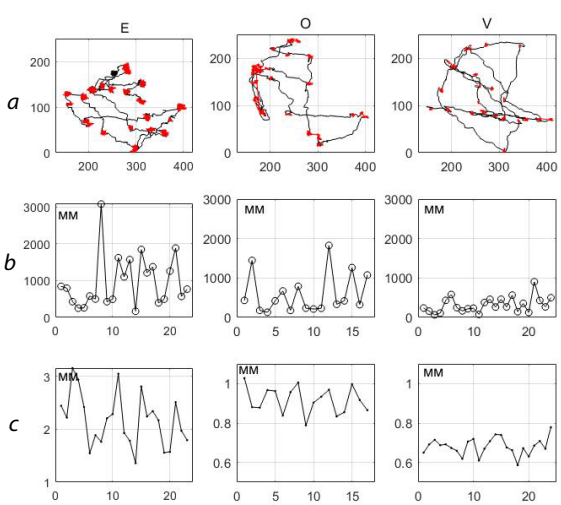

Рис. 15. *a - gaze tracking of three subjects for the image in Fig. 10, b - the total length of all displacements in a particular selected fixation, c - the value of the average gaze displacement in a specific selected fixation.*

The middle plots show the cumulative length of all displacements in a particular fixation selected, and the bottom plots show the amount of average gaze displacement at a specific fixation selected.

From Fig. 15 clearly shows the individual characteristics of the subjects in the perception of this image. In subject E, the area, the total average length of the track, and the average shift in gaze in fixation are significantly greater than in subjects O and V. The average shift in gaze in fixation for E is 2.1 mm, for O this value is 0.9 mm, and for V it is is approximately 0.7 mm.

3.4. Internal structure of fixations

The gaze trajectory in fixation has an internal heterogeneous structure, which is visible on the time base of the fixation track. This structure of reactions of the oculomotor apparatus, apparently, is completely determined by the physiological characteristics of the eyeball and the algorithm of the accommodation process, which is regulated by the "video processor" of the brain when perceiving graphic information.

In **Fig. 16** shows the trajectory of subject V's eye movement during forced fixation during the validation process.

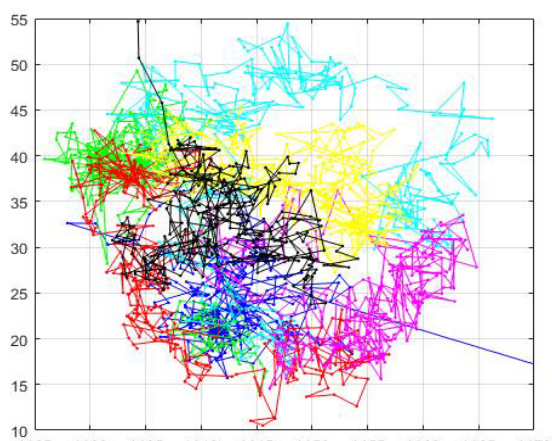

Рис. 16. *The trajectory of subject V's gaze movement during forced fixation during the validation process. The entire fixation is sequentially divided into 7 fragments of 314 points, the tracking of each fragment in the figure is represented by its own color. The sequence of colors from the first to the last fragment: blue, green, red, cyan, magenta, yellow, black.*

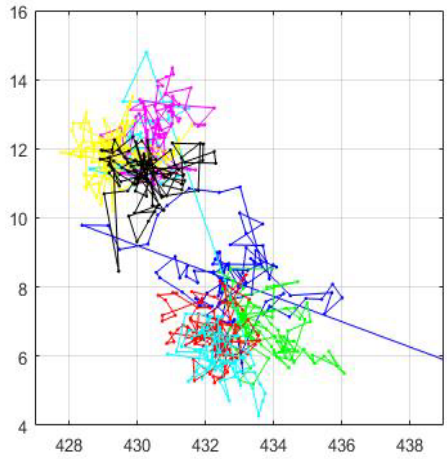

Fig. 17. *The initial segment of the gaze trajectory during forced fixation during the validation process. The segment is also divided into 7 fragments of 100 points, the tracking of each fragment in the figure is represented by its own color. The sequence of colors from the first to the last fragment: blue, green, red, cyan, magenta, yellow, black.*

In **Fig. 17** shows the initial portion of the eye movement trajectory during forced fixation during the validation process.

From Fig. 16 and 17, it can be seen that the trajectory of the shift of the gaze in fixation has an internal non-uniform structure. The total trajectory of eye movement in the fixation area is determined by a set of successive clusters, which are clearly visible in the figures. Such a fixation structure is apparently associated with the individual structure of the fovea and the processes of restoration of the photosensitivity of rhodopsin in the retinal photoreceptors.

4. CONCLUSION

The work is devoted to identifying the individual characteristics of the human visual apparatus associated with the anatomical and psychophysiological parameters of the body. Based on the EyeTracking technology, the physiological aspects of the perception of visual information by the oculomotor apparatus, which are not associated with active cognitive activity, have been investigated. The individual features in the size of fixation when reading text and examining halftone graphic objects in various people have been investigated. The time durations of fixations in different people, associated with the process of accommodation, as well as the internal structure of fixations, were investigated.

It is shown that the trajectory of the gaze shift in fixation has an internal heterogeneous structure. The total trajectory of eye movement in the fixation area is determined by a set of successive clusters. Such a fixation structure is apparently associated with the processes of restoration of the photosensitivity of rhodopsin in the photoreceptors of the retina.

All the above studies of the fixations of various subjects on the basis of various images showed that the oculomotor system, taking into account the physiological characteristics of the visual apparatus, is equally controlled by the "video processor" of the brain when the eye is accommodated to image elements and the only objective individual feature of human vision that uniquely characterizes the perception of graphic information is the amount of the average displacement in the fixation. It is she who is the long-term "visiting card" of the subject and remains practically unchanged both when reading and when examining halftone images and in test validation with forced fixation of the gaze.

REFERENCES

1. David H. Hubel. *Eye, Brain, and Vision*, W. H. Freeman 1995, ISBN/ASIN:0716760096, ISBN-13: 9780716760092, P. 256.
2. Barabanschikov VA, Zhegallo AV. Eye-Tracking Methods: Theory and Practice. *Psychological Science and Education*, 2010, 2(5). (psyedu.ru, ISSN: 2587-6139)
3. ViewPoint EyeTracker, Software User Guide, 2010 © Arrington Research, Inc.
4. Zhegallo AV. The SMI High Speed system of registration of eye movements: particular qualities of use. *Experimental Psychology,* 2009, 2(4):111-117.

5. Yarbus AL. *Eye Movements and Vision*. New York, Plenum Press, 1967.
6. Hoffman JE. Visual attention and eye movements. In: H. Pashler (ed.). *Attention*. 1998, pp. 119-154, Hove, UK, Psychology Press.
7. Holsanova J. How We Focus Attention in Image Viewing, Image Description, and during Mental Imagery. In: K. Sachs-Hombach and R. Totzke (eds). *Bilder, Sehen, Denken*. 2011, pp. 291-313. Cologne: Herbert von Halem Verlag.
8. Kirpichnikov AP. Eye video processor: Micromovements as a factor of accommodation and video processing. *Proc. 12 Intern. Conf. "Digital signal processing and its application, DSPA-2010, Image processing and transmission"*, Moscow, 2010, p. 170-172.
9. Janis Intoy, Michele Rucci. Finely tuned eye movements enhance visual acuity. *Nature Communications*, 2020, 11:795, doi: 10.1038/s41467-020-14616-2.
10. Rostislav V. Belyaev, Vladimir V. Kolesov, Galina Ya. Men'shikova, Alexander M. Popov, Viktor I. Ryabenkov, Quantitative criterion of individual differences of the eyes movement trajectories. *Radioelectronics. Nanosystems. Information Technologies (RENSIT)*, 2015, 7(1):25-33. DOI: 10.17725/rensit.2015.07.025.
11. Menshikova GY, Belyaev RV, Kolesov VV, Ryabenkov VI. The evaluation of individual differences using fractal analysis of scanpaths. *Journal of eye movement research*, 2015, 8(4) (Special issue ECEM 18) P. 282, https://doi.org/10.16910/jemr.8.4.1.
12. Belyaev RV, Grachev VI, Kolesov VV, Menshikova GYa, Popov AM, Ryabenkov VI. Oculomotor reactions in fixations and saccades with visual perception of information. *RENSIT,* 2020, 12(2):263-274. DOI: 10.17725/rensit.2020.12.263.
13. Rostislav V. Belyaev, Vladimir V. Kolesov, Galina Ya. Menshikova, Alexander M. Popov, Viktor I. Ryabenkov. Dynamics of reverse saccades of reading texts and its connection with the peculiarities of eye movement. *RENSIT*, 2018, 10(1):117-127. DOI: 10.17725/rensit.2018.10.117.

ALEXANDER ALEKSEEVICH POTAPOV

(to 70th Anniversary of Birth)

UDC 929.53

DOI: 10.17725/rensit.2021.13.403

Alexander A. Potapov is a doctor of physical and mathematical sciences, a well-known scientist in the field of radiophysics and radar, statistical radio engineering, recognition and processing of images and signals, fractal and texture analysis, fractional operators, fractal electrodynamics, fractal antennas and deterministic chaos.

Alexander Alekseevich Potapov was born on May 4, 1951 in the village of Lukino, Rzhaksinsky District, Tambov Region, Russia. After graduating from high school with a gold medal in 1968, he entered the radio engineering department at the Ryazan Radio Engineering Institute. Then in 1979 he graduated from the evening department (engineering flow) of the physics department of Lomonosov Moscow State University.

Since 1979 A.A. Potapov works at the Institute of Radioengineering and Electronics of the Russian Academy of Sciences. Aleksandr Alekseevich went through all the stages from junior to chief researcher. In 1989 he defended his Ph.D. thesis on a special topic at the Moscow Institute of Physics and Technology, and in 1994 - his doctoral dissertation at the IRE RAS on the topic: "Synthesis of images of the earth's covers in the optical and millimeter wave ranges".

Since 1979, the main scientific direction of A.A. Potapov - application of the theory of fractals, fractional operators, scaling effects and deterministic chaos in radiophysics, radar, radio electronics, electrodynamics, control theory and a wide range of related scientific and technical areas for the creation and development of breakthrough information technologies. He is currently working on combining fractals, photonics and nanotechnology. A.A. Potapov is the initiator of the first research and development work in Russia on radiophysical applications of the theory of fractals, scaling effects and fractional operators in radio systems.

The results of the scientific activity of A.A. Potapov on fractal information processing in intense interference, as well as on fractal radio systems, sensors and fractal radioelements were published in four reports of the Presidium of the Russian Academy of Sciences (Scientific achievements of the Russian Academy of Sciences. Moscow, Nauka Publ., 2008, 2010, 2012 and 2013), and also in a report to the Government of the Russian Federation - Moscow, Nauka Publ., 2012. All these priority results in the world make it possible to move to a new level of information structure of real non-Markov signals and fields.

At present, based on the pioneering work of A.A. Potapov and his students at the Kotelnikov IRE RAS, a new fundamental direction "Fractal radiophysics and fractal radio electronics: design of fractal radio systems" was formed and the Russian scientific school of fractal methods, well known in the world, was created.

A.A. Potapov - Scientific Secretary of the Dissertation Council at the Kotelnikov IRE RAS (1999-2018). Twice (1997 and 2000) he was awarded the State Scientific Scholarship. He is Deputy Chairman of the Scientific Qualification Seminar "Problems of Modern Radiophysics" and a member of the NKS "Informatics" at the Kotelnikov IRE RAS. In the period 2000-2002. A.A. Potapov is a professor at MIREA (SU), from 2008 to 2019 - a professor at the Tupolev Kazan State Technical University. Member of the Nizhny Novgorod Mathematical Society (2017). In 2015 A.A. Potapov was elected a full member of the Non-Departmental Expert Council on Aerospace Problems.

During the period of his work at the Kotelnikov IRE RAS gave a reliable physical substantiation of the practical application of fractal methods in modern fields of radiophysics, radio electronics and information-control systems; for the first time, the effectiveness and prospects of applying fractional measure theory, dimension theory and scaling relations (for textures and fractals) in the case of detecting and recognizing (filtering) one-dimensional and multidimensional radar signals from low-contrast targets against the background of intense non-Gaussian interference of various kinds was proposed and proved. He proposed the concept of creating fundamentally new

fractal radio systems, fractal sensors and fractal element base. In Kotelnikov IRE RAS in 2005, a working model of the world's first fractal nonparametric radar signal detector was created. A rigorous electrodynamic calculation of numerous types of fractal antennas has been carried out, the design principles of which underlie fractal frequency-selective surfaces and volumes (fractal "sandwiches"). For the first time, a model of a "fractal" capacitor was proposed and implemented as a fractal impedance and fractal labyrinths for the synthesis of microwave structures. In 1997, methods of fractal modulation and fractal broadband signals were developed for the first time. For the first time, a new class of informative features is proposed, based on the fine structure of reflected millimeter-wave radar signals. Also, for the first time, complete ensembles of textural features of optical and radar images of real earth covers have been investigated. The presence of a strange attractor is predicted to control radar scatter from vegetation. Subsequently (2002) the effect was discovered experimentally at a wavelength of 2.2 mm. In 2015 A.A. Potapov, for the first time in world practice, discovered, proposed, substantiated and developed the principles of a new type and a new method of radar, namely, fractal-scaling or scale-invariant radar. The efficiency of functionals, which are determined by the topology, fractional dimension and texture of the received multidimensional signal, for the synthesis of fundamentally new non-energy detectors of low-contrast objects against the background of noise has been proved. The postulates of fractal radar have been developed: 1 - intelligent signal/image processing based on the theory of fractional measures and scaling effects for calculating the field of fractal dimensions *D*; 2 - the sample of the received signal in noise belongs to the class of stable non-Gaussian probability distributions *D* of the signal; 3 - maximum topology with minimum energy of the input random signal (ie, maximum "deviation" from the energy of the received signal). This entails fundamental changes in the structure of theoretical radar, as well as in its mathematical apparatus.

A.A. Potapov - the author of the first in Russia monograph "Fractals in radiophysics and radar" (Moscow, Logos Publ., 2002, 664 p.), Which was revised and supplemented (Potapov A.A. Fractals in radiophysics and radar: sampling topology. Moscow, Universitetskaya kniga Publ., 2005, 848 p.). These two monographs have become the reference books of scientists of various specialties. A.A. Potapov - Author and co-author of a number of monographs on radar and the use of fractals in science and technology. Giving lectures on fractal technologies developed by him at the IRE RAS and reports on the ISTC project (together with the Almaz Central Design Bureau) in 2000 and 2005. in the USA (Washington, New York, Huntsville, Atlanta, Franklin), in China (2011 to the present) and at numerous international conferences (England, USA, Canada, Holland, Austria, Germany, France, Spain, Italy, Hungary, Greece, Turkey, Scotland, Switzerland, Sweden, Mexico, China, Serbia, Montenegro, Bulgaria, Kazakhstan, Belarus, Ukraine) brought him wide popularity in the international scientific community. In 2005, a significant meeting of A.A. Potapov with the founder of fractal geometry B.B. Mandelbrot, who warmly supported the work of A.A. Potapov.

A.A. Potapov published personally and in co-authorship over 1150 scientific papers in domestic and international publications, including over 45 monographs and chapters in books in Russian and English, 2 patents and 9 textbooks. He developed a course of lectures on the use of fractals and wavelets in radar for the Training Center of the Concern RTI Systems (A.L. Mints RTI and JSC NPK NIIDAR). Honorary Professor of the Eurasian National University (Astana, Kazakhstan, 2010), Honorary Professor of Jinan University, Guangzhou, China, 2011. In March 2012, A.A. Potapov was appointed President of the Sino-Russian Laboratory of Information Technologies and Fractal Signal Processing. A.A. Potapov is a member of the organizing committees of numerous international and Russian conferences. In 1997, he was awarded the medal "In Commemoration of the 850th Anniversary of Moscow". He was awarded the badge "Honorary Radio Operator of the Russian Federation" (2006) and eighteen medals. Laureate of the Prize. Academician A.M. Prokhorov (2013) and the WES VKS Prize (2016).

A.A. Potapov - organizer and editor-in-chief of the journal "Nonlinear World" (2003), member of the editorial boards and editorial boards of 13 Russian and international journals. The biography of Alexander Alekseevich was published in the encyclopedia "Who is Who in Russia" (Verlag fur Personenenzyklopadien AG - Switzerland) at the personal request of the Publisher (2009-2010).

A.A. Potapov - Academician of the Russian Academy of Natural Sciences in the Department of Problems of Radioelectronics, Nanophysics and Information Technologies and Academician of the A.M. Prokhorov Academy of Engineering Sciences.

A.A. Potapov has a well-deserved authority and is widely known among scientists.

Friends, colleagues and students congratulate Aleksandr Alekseevich Potapov on his glorious anniversary and sincerely wish him health, new successes, long years and fruitful work.

The editorial board of the journal of the RANS Branch cordially joins these wishes to their colleague.

RENSIT journal editorial board